A MOLECULAR APPROACH TO NANOPARTICLES: USING THE MOLECULAR-INTERFACE TO INFLUENCE GROWTH, ENHANCE ELECTROCHEMICAL BEHAVIOR AND DRIVE BIOCOMPATIBILITY

by

JACLYN EVE KELLON

A DISSERTATION

Presented to the Department of Chemistry and Biochemistry
and the Graduate School of the University of Oregon
in partial fulfillment of the requirements
for the degree of
Doctor of Philosophy

December 2019

DISSERTATION APPROVAL PAGE

Student: Jaclyn Eve Kellon

Title: A Molecular Approach to Nanoparticles: Using the Molecular-Interface to Influence Growth, Enhance Electrochemical Behavior and Drive Biocompatibility

This dissertation has been accepted and approved in partial fulfillment of the requirements for the Doctor of Philosophy degree in the Doctor of Philosophy degree in the Departments of Chemistry and Biochemistry by:

Shannon Boettcher	Chairperson
James Hutchison	Advisor
Mike Haley	Core Member
Stephanie Majewski	Institutional Representative

and

Kate Mondloch	Interim Vice Provost and Dean of the Graduate School

Original approval signatures are on file with the University of Oregon Graduate School.

Degree awarded December 2019

DISSERTATION ABSTRACT

Jaclyn Eve Kellon

Doctor of Philosophy

Departments of Chemistry and Biochemistry

December 2019

Title: A Molecular Approach to Nanoparticles: Using the Molecular-Interface to Influence Growth, Enhance Electrochemical Behavior and Drive Biocompatibility

Nanoparticles have garnered much interest over the past 30 years due to their unique size dependent properties. The majority of research initially focused on developing synthetic methods to produce uniform materials with a wide range of core compositions, sizes and morphologies. The second generation of nanoparticle research has focused on modifying and improving upon existing synthetic methods to access more complex nanoparticle compositions and morphologies. In addition, chemists have begun exploring methods of introducing functionality into the ligand shell and modifying the surface chemistry of nanoparticle cores to access or enhance desired properties. This dissertation focuses on this newer class of nanoparticles, specifically looking at the influence of the ligand shell as a molecular-interface between the nanoparticle core and its surroundings.

Three distinct areas of research are explored throughout this dissertation: 1) using the ligand shell to enhance electrochemical behavior, 2) understanding how coordinating molecules influence nanoparticle growth and 3) investigating the influence of a molecular coating on nanoparticle toxicity. The first two studies presented here explore how the molecular-interface can be employed to attach nanoparticles to conductive substrates.

Methods of fabricating nanoparticle-functionalized electrodes with a defined molecular interface are introduced in the first study while the second study demonstrates the enhanced electrochemical behavior achievable in these systems. The role of coordinating molecules and air in the formation of cobalt oxide nanoparticles are explored in the third study. Lastly, the fourth is a systematic study to determine which structural features of metal oxide nanoparticles drive nanoparticle toxicity. The structure-property relationships described in this dissertation can be used for the smart design of safer new materials.

This dissertation includes previously published and unpublished co-authored material.

CURRICULUM VITAE

NAME OF AUTHOR: Jaclyn Eve Kellon

GRADUATE AND UNDERGRADUATE SCHOOLS ATTENDED:

University of Oregon, Eugene, OR
Goucher College, Towson, MD

DEGREES AWARDED:

Doctor of Philosophy, Chemistry, 2019 University of Oregon
Master of Science, Chemistry, 2016, University of Oregon
Bachelor of Art, Chemistry, 2013, Goucher College

AREAS OF SPECIAL INTEREST:

Electrochemistry
Nanoparticle-functionalized electrode fabrication

Nanomaterial characterization
X-ray Photoelectron Spectroscopy
Transmission Electron Spectroscopy
Small Angle X-ray Scattering

Synthesis of Nanomaterials
Metal Oxide Nanocrystals

Green Chemistry

PROFESSIONAL EXPERIENCES:

Graduate Research Fellow, Department of Chemistry, University of Oregon
2015-2019

Science Intern, Environmental Law Alliance Worldwide, Eugene Oregon
2018-2019

Chemistry Short Course Instructor, Oregon Young Scholars Program, University of Oregon, 2016-2019

Founder and University Relations Officer, Creating Connections, University of Oregon, 2017-2019

Founder and President, A Community for Minorities in STEM, University of Oregon, 2015-2018

Teaching Assistant, General and Organic Chemistry Lab, University of Oregon 2014-2015

Chemistry Stock Room Manager, Department of Chemistry, Goucher College 2013-2014

Calculus Tutor, Goucher Prison Education Partnership, Goucher College 2012-2013

GRANTS, AWARDS, AND HONORS:

Julie and Rocky Dixon Graduate Student Innovation Award, University of Oregon 2018-2019

Karfilis Women in Leadership Award, Women in Graduate Science, University of Oregon 2016

Stimson-Duvall Graduate Fellowship, Goucher College 2014-2016

PUBLICATIONS:

1. **Kellon, J. E.**; Young, S. L.; Hutchison, J. E. Engineering the Nanoparticle-Electrode Interface *Chem. Mater.* **2019**, *31*, 2685-2701

2. Young, S. L.; **Kellon, J. E.**; Hutchison, J. E. Small Gold Nanoparticles Interfaced to Electrodes through Molecular Linkers: A Platform to Enhance Electron Transfer and Increase Electrochemically Active Surface Area *J. Am. Chem. Soc.* **2016**, *138*, 13975-13984

3. Schultz, K. P.; Spivey, D.; Loya, E. K.; **Kellon, J. E.**; Taylor, L. Photochemical Locking and Unlocking of an Acyl Nitroso Dienophile in the Diels-Alder Reaction *Tetrahedron Letters* **2015,** *57*, 1296-1299

4. Burke, M. S.; Zou, S.; Enman, L.; **Kellon, J. E.**; Gabor, C. A.; Pledger, E.; Boettcher, S. W. Revised Oxygen Evolution Reaction Activity Trends for First-Row Transition-Metal (Oxy)hydroxides in Alkaline Media *Phys Chem. Lett.* **2015**, *6*, 3737-3742

ACKNOWLEDGMENTS

I would not have completed this work without the support of others. First, I would like to thank my research advisor, Professor Jim Hutchison. Thank you for creating a welcoming environment and providing the space for me to explore my interests and passions outside of the laboratory. The support and guidance you offer your students to help them achieve their goals is unprecedented and I wish it were more common in academia. I truly do not think I would have made it through this program if you hadn't supported my efforts with CMiS. Thank you to all of you who helped make CMiS a reality, especially Meredith and Cathy. Meredith, CMiS would not exist if it weren't for you. I do not think you received the recognition you deserved for all of the hard work, time and effort you dedicated to the group. I would not even have made it to graduate school had it not been for two of my undergraduate professors, Professors Ahmed-Schofield and Schultz. Ruquia, thank you for believing in me and dragging me down the hall to tell Kevin that I would be his new research student! And thank you Kevin for agreeing and providing caring and supportive mentorship to a *very* inexperienced student.

People always ask if it is hard being a woman in the chemistry department, and I can honestly say that it wasn't that difficult. The *only* reason I can say that is because of the amazing lab culture we cultivated. Sam, you were such an amazing mentor and I am so glad that we got to write two papers together. Tawney, your sass and snarky comments will surely be missed. Thank you for making me laugh, listening to me complain and helping me drink all the grape juice. Aurora, thank you for unapologetically being yourself. Kenyon, Susan and Tatiana, thank you answering all of my science questions. You are the heart of the lab, so caring, supportive and empathetic.

One of my main goals in graduate school was to establish community outside of the chemistry department and I am proud to say that I achieved that goal. Thank you to all of you who offered me friendship, emotional support and fun times over the past five years. Creating Connections and Rehearsals for Life provided opportunities to connect with other graduate students and discuss topics important to me outside of chemistry. I want to acknowledge those of you who taught me that self-care is really important and not to feel guilty for taking time away from work. Mental health is not addressed enough in STEM and you all provided the space to be good to myself. I am so appreciative of my 'group' of friends that have made this past year not only manageable but fun. AnnaCecilia, Eric, Lauren and Phillip, spending time with you all playing games and exploring Oregon has brought me so much joy and happiness.

I have spent a lot of effort to establish a social support system for underrepresented minority graduate students at the UO. Having people around you that allow you to lower your guard and just be you is critical to navigating any difficult situation. A special thank you to the one person in the chemistry department who I felt I could truly be myself around, Erik Hadland. You just *get it* and I couldn't have asked for a better friend. I also could not have succeeded without the hee-haw gang and Leroy. Thank you for keeping me sane (most times!) and always being there to talk when I needed you. Without the unconditional love and support of my parents, brother and grandma I would not have made it through. I am so excited to be moving back east so that I can be closer to you! Lastly, I would not be who I am today without grandmother and grand-dad. I wish you were here to see me graduate. You always said we need another doctor in the family … well now we have one.

Dedicated to my Grandparents

Thank you for inspiring me to reach high, not let anything get in my way
and instilling in me a love of literature and learning

TABLE OF CONTENTS

LIST OF FIGURES

Figure Page

Figure Page

Figure Page

LIST OF TABLES

Table Page

LIST OF SCHEMES

Scheme Page

LIST OF CHARTS

Chart Page

CHAPTER I

INTRODUCTION

Note: I am the sole author of this chapter.

Dissertation Introduction

Nanomaterials are a newer class of materials that exist in a unique size regime having one dimension below 100 nm. In this size regime these materials exhibit properties different than their bulk counterparts but energetically do not resemble the quantized energy levels of molecules either. These unique materials have garnered much interest due to their morphology-dependent properties that make them promising candidates for applications in a wide range of technology sectors. As chemists, we are in the unique position to develop methods of manipulating matter to achieve new architectures within this regime to address key problems facing society today.

There are many types of nanomaterials, including 2-dimensional thin films,[1] 3-dimensional organic/polymeric,[2,3] and inorganic particles.[4,5] This dissertation will focus on 3-dimensional inorganic nanoparticles (NPs), specifically those with metallic and metal oxide cores. Inorganic NPs have two domains, the internal core which is comprised of the material by which the NP is referred (i.e. gold NP, iron oxide NP) and an organic molecular coating, which will be referred to as a ligand shell throughout this dissertation. The ligand shell serves to retain the core morphology by preventing the etching of atoms and/or the agglomeration of NPs.

The first generation of NP research focused on developing synthetic methods to produce NPs of varying core size, composition and morphology to access core material properties such as catalysis,[6] plasmonic resonance,[7] electrical conductivity[8] and magnetic properties.[9] The second generation of research has focused on enhancing existing synthetic methods to create NPs with more complex compositions to enhance the core properties.[10,11] Researchers have begun to apply insights from organic chemistry to manipulate the ligand shell to impart new chemical properties to the core materials,[12] and though much effort has gone into the synthesis of NP core materials with desired properties, the influence and role of the ligand shell has not been studied in as great of detail.

This dissertation focuses on the role of the NP ligand shell as a molecular interface between the NP core material and its environment. A deeper understanding of the molecular interface between the NP core and its surroundings aids in developing design principles for the safe, efficient and efficacious incorporation of new NPs into a wide variety of technology sectors. The structural features of the ligand shell can be adapted to produce different types of molecular interfaces between the NP core and its environment. The four structural components investigated in this dissertation are demonstrated in Figure 1.1: terminal functionality, bond strength, relative hydrophobicity and extent of surface passivation.

Synthetic organic handles can incorporate various functionalities into the ligand shell. Terminal ligand shell functionality has been used to direct NPs to a specific biological site, to bind NPs to a substrate and to build a generic building block for the

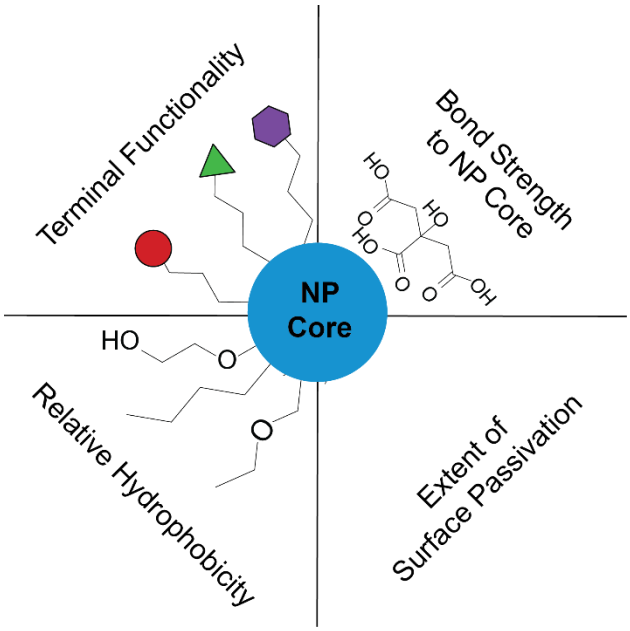

Figure 1.1: Different structural features of the nanoparticle ligand shell.

addition of synthetically challenging molecules. A wide range of methods have been developed to attach NPs to useful materials and molecules through their ligand shell: host-guest,[13–15] click',[16,17] grafting[18–21] and many others. The relative hydrophobicity can be altered to determine what media the NP cores will be soluble in.[22–24] Biological applications require a hydrophilic molecular interface that renders the core material biologically available. Conversely, it may be beneficial to have a hydrophobic molecular interface when attaching NPs to substrates for heterogenous applications such as sensing and catalysis. Developing synthetic routes to produce NPs with mixed ligand shells has become an important area of research as it can be beneficial to incorporate more than one type of functionality into the ligand shell.

Beyond the chemical structure of the ligand shell the interface between the ligand and the NP surface is also extremely important. The binding mode and bond strength between the ligand and the NP core can range from weakly ionic coordinating ligands[25,26] to covalently bound molecules.[27,28] The stability of the NP core material can be directly affected by the NP-ligand interface. While weakly coordinated ligands can easily be removed or replaced by other species in the environment,[28] covalently bound molecules form more robust interactions with the NP surface.[29] If the ligands are easily removed from the NP surface, the core material is made accessible for surface chemistry changes such as oxidation,[30] etching[31] and the adsorption of new molecules to the surface.[32] Lastly, the relative density of molecules on the surface, or extent of surface passivation can be manipulated to reveal reactive sites on the NP surface.[33] For electrochemical applications an exposed NP core material is usually beneficial. The desired redox reaction requires that the reactant come into direct contact with the NP surface. Conversely, for environmental and biomedical applications it is beneficial to prevent the highly reactive NP surface from coming into direct contact with biological species.

These four structural features of the ligand shell significantly influence the behavior the NP in various environments. In developing an understanding of how the ligand shell dictates behavior, we can employ synthetic tools to achieve desired architectures for certain applications. The following sections will discuss how this molecular interface can be manipulated to enhance the electronic behavior between NPs and a conductive substrate and the biocompatibility of metal oxide NPs.

Using a molecular interface to enhance the electronic communication between nanoparticles and a conductive substrate

Nanoparticles have shown promise for electrochemical applications in catalysis,[34–37] sensing[10,35,38,39] and energy conversion and storage.[40] In these applications NPs are attached to a conductive electrode support and the electrochemical response is monitored for a given reaction. The response has been shown to be influenced by core composition and morphology, which has been the subject of most of the research in this field.[6,41–43] In addition to core morphology, the chemical environment surrounding the NP can significantly influence electrochemical activity.[44–46] The surrounding chemical environment includes the ligand shell, the density of NP coverage and distribution of NPs on the electrode surface. These properties can significantly influence the electron transfer efficiency and the ability of the NPs to induce specific redox reactions and chemical transformations.[47]

The interface between the NP and the electrode is a component of the chemical environment that is often overlooked. However, this interface is important because it significantly influences the electronic communication between the NP and the electrode.[47] Numerous methods have been employed to interface NPs to electrode substrates. The type of interface generated greatly impacts the behavior and electrochemical activity of the NPs. Ideally, the interface would facilitate electron transfer while preserving desired NP properties such as the chemical environment and NP morphology. In addition, it would be beneficial if the interface was versatile enough to allow for different types of NPs to be attached to the electrode surface.

There are three main approaches to the fabrication of nanoparticle-functionalized electrodes: 1) physical deposition,[48–51] 2) solution deposition[34] and 3) use of a molecular tether.[47] Physical deposition methods include ion sputtering[52] and the electrochemical reduction of ions in solution to form NPs on the electrode surface,[53,54] among others. These methods provide limited control over NP morphology and size. Solution deposition prepares electrodes from NPs that were previously synthesized in solution and then are either drop-cast,[34,42,55,56] spin-coat or dip-coated[36,57] onto the electrode surface. Although this method provides better control over NP morphology and NP surface chemistry, the NP-electrode interface is often ill-defined and it is difficult to control NP surface coverage/density.[35,58] The use of a molecular tether to bind NPs directly to the electrode surface retains the benefits of control over NP morphology and surface chemistry while providing a defined NP-electrode interface and control over the extent of NP coverage on the electrode surface. Numerous strategies to produce a defined NP-electrode molecular interface have been demonstrated.[47]

A defined NP-electrode interface has three structural components, all of which influence electrochemical behavior: 1) the interface between the molecular linker and the electrode, 2) the chemical structure/identity of the molecular linker and 3) the interface between the molecular linker and the NP.[47] The linker-electrode interface influences the stability, density, and uniformity of the molecular monolayer. If the molecular monolayer is disordered and sparse, solution phase analytes may be able to interact directly with the underlying electrode and bypass the NPs. Additionally, the chemical identity of the molecular linker can directly impact the rates of electron transfer between the NP and the electrode. While some molecular linkers are electrochemically insulating,

others can enhance electronic communication between the solution analytes and the electrode substrate. Lastly, the type of bond between the NP and the molecular interface can influence NP stability, electron transfer rates, and the density of NPs on the surface. It has been shown that a bond between the NP and the molecular linker is necessary for efficient electron transfer. A strong molecular interface – NP bond can prevent NP desorption and provide a more robust electrochemical system while also influencing NP coverage density. Chapters II and III discuss in greater detail the current NP-functionalized electrode fabrication methods that utilize a molecular interface and the enhanced electrochemical behavior observed in two of these methods.

The role of coordinating molecules in the synthesis of metal oxide nanoparticles

Metal oxides are among the most widely investigated inorganic materials due to their abundance in nature and use in technological applications. In more recent years much research has focused on the nanoscale forms of metal oxides as promising materials for catalysis,[59] biomedical applications,[9] energy storage and conversion[60-62] and in electronic devices.[63] For use in a wide range of applications many different core materials and NP morphologies are required to provide the desired properties. In order to design systems that utilize NPs, it is necessary to understand how NP morphology influences properties. Reliable syntheses that produce uniform materials with variable morphology are necessary to develop a library of structure-property relationships for metal oxide NPs.

As previously stated, the NP core composition can have many different morphologies. The size,[64,65] shape[66] and surface chemistry of the core can be altered,[67] in addition to the ability to incorporate dopant atoms.[68] Variations in morphology can have a significant influence on the conductivity,[69] magnetic properties[70] and plasmonic

resonance[68] of the resulting NP. These property differences result from differences on the atomic level,[71,72] therefore synthetic approaches that provide control over the atomic-scale structure of these NPs is needed. Numerous synthetic approaches to metal oxide NPs have been developed with varying control over NP morphology. Although different syntheses of the same metal oxide core material my result in NPs of the same size and shape, the properties exhibited by these NPs can be drastically different.[69,70]

The lack of structural-behavior trends in literature for metal oxide NP conductivity,[69] magnetism[70] and other properties are attributed to atomic level differences such as surface defects and oxygen vacancies. These differences in surface chemistry are often a result of different synthetic methods and the lack of trends as a result make it impossible to discern any structure-property relationships. The synthetic methods used to produce metal oxide NPs use different reagents and therefore undergo different mechanisms of NP formation. The different mechanisms of NP formation result in differences in NP structure at the atomic level that then result in different properties.

Metal oxide NP syntheses can broadly be divided into two categories: aqueous and non-aqueous approaches. Methods based on hydrolysis and sol-gel chemistries in aqueous media produce monodisperse, large and often amorphous NPs.[73,74] In addition, the aqueous environment results in a complex series of reactions that are sensitive to pH, anion identity, concentration and temperature.[74] Nonaqueous sol-gel chemistry has fewer complexities than the aqueous counterpart yet still has a wide range of chemistries occurring during NP formation.[75–77] In these syntheses metal-organic precursors such as metal acetylacetonates, carboxylates of varying chain length and halides are combined with high-boiling, inert solvents, often in the presence of a coordinating/capping agent.[78]

The metal monomers/oligomers are produced through thermal decomposition, surface-catalyzed, and elimination reactions that decompose to produce metal oxide NPs.[79,80] The resulting NP morphology is typically controlled by the ratio of metal-organic precursor to coordinating agent, reaction temperature and/or concentration.[75,81] Thermal decomposition syntheses provide limited control over the incorporation of dopant atoms and the formation of core/shell architectures.[76] In addition, the variety of NP growth mechanisms often results in variability of the NP surface structure.

In order to observe the structure-property relationships of metal oxide NPs a synthetic method that provides control over the size, morphology, and core composition through the same mechanism of growth is necessary. This synthetic method should reliably produce NPs through an understood mechanism of formation with atomic-level control over the resulting NP. The Hutchison Lab has pioneered a slow injection synthesis that grows metal oxide NPs in a layer-by-layer fashion.[64,65] This synthesis provides access to a wide range of core sizes through the same mechanistic route with size control at the atomic level.

The slow injection synthesis occurs through the addition of a metal oleate precursor to hot oleyl alcohol. As the metal-oleate precursor is added, it undergoes an esterification reaction with the oleyl alcohol generating metal-hydroxyl monomers.[64] The monomers then condense to form M-O-M bonds with water as a byproduct. The monomers can either condense with other monomers in solution to nucleate new NPs (nucleation phase) or can condense on the surface of existing NPs thus growing the NPs (growth phase). The rate of monomer addition is kept below the rate of monomer condensation on existing NP surface in order to create a concentration gradient.[82] Once

the initial nucleation event occurs at a given monomer concentration, any additional metal oleate precursor introduced to the reaction is consumed in the growth phase. The higher concentration of NPs compared to monomer reduces the probability of new NP nucleation and results in uniform and monodisperse NPs. To date the slow injection growth mechanism has been explored for both In_2O_3 and Fe_2O_3 cores.[70,82,83] Extending this synthetic approach to additional metal oxide NPs is ongoing.

The influence of the molecular interface on metal oxide nanoparticle biocompatibility

As metal oxide NPs become more ubiquitous in technological applications it is important that we understand the relative safety of these materials. Much research has focused on understanding how NP size,[84–86] composition,[31,84,87] and surface chemistry[88–90] influence their toxicity. Unfortunately, there are many contradicting results in the literature which is often attributed to the different synthetic methods used to produce similar particles in different studies. Synthetic method used to make the same core material may result in atomic-layer differences that then influence the reactivity of the NP. In order to understand what and how different structural properties influence metal oxide NP toxicity, systematic studies of particles made through the same synthetic method are necessary.

For toxicity assays it is necessary for the NPs being tested to be available for interaction with the biological model being studied. This means the NPs must be soluble in the exposure media throughout the length of exposure. Most as-synthesized metal oxide NPs have a hydrophobic ligand shell and are therefore not soluble in aqueous environments. It is common to expose these NPs to sonication in the presence of additional surfactants to force the NPs to disperse in aqueous media. Unfortunately,

sonication can be harsh on NPs often leading to morphological changes. The use of surfactants also changes the surface chemistry and molecular interface between the NP core and its surrounding environment.[32] Such treatments are not often considered when interpreting the results. Additionally, the NPs are not fully characterized afterward even though the material may be fundamentally different after sonication in the presence of surfactants.

Research on metal and organic NPs have demonstrated that the terminal functionality in the ligand shell plays a significant role in dictating the toxicity of the material. Gold NPs have been used as a model system to study the influence of size and surface chemistry on NP toxicity.[86,91,92] For gold NPs, cationic ligands are highly toxic while neutrally charged ligands are benign.[93] The mechanism of toxicity for the cationic gold NPs is attributed to the increased interaction of the cationic ligand shell with biological proteins.[94] While much work has been done to understand the structural features that influence gold NP toxicity, the focus is starting to shift towards other core materials.

Metal oxide NP toxicity is most often attributed to either the generation of reactive oxygen species (ROS) or the leaching of toxic ions.[31,95] However, based on the influence of the ligand shell on gold NP toxicity, the ligand shell should also influence metal oxide NP toxicity. The toxicity mechanisms attributed to metal oxide NPs require that the NP surface be exposed to its surroundings in order to either leach toxic ions or induce redox reactions. Theoretically, if the reactive surface of the metal oxide NP is passivated these two toxicity mechanisms can be prevented, potentially rendering the NP biocompatible.

In order to investigate the influence of surface passivation on NP toxicity, a series of NPs with different core compositions and varying extents of surface passivation are required. The slow injection synthesis provides access to metal oxide NPs with different core compositions and the same surface chemistry/ligand shell.[64,68] The NPs produced in the slow injection synthesis have a hydrophobic oleate ligand shell. Previous work in the literature has developed methods to both remove and replace the oleate ligand shell.[28,96,97] The oleate ligand shell can be replaced with a hydrophilic polyethylene glycol ligand to create a water soluble, passivated metal oxide NP (Figure 1.2).[96,97] The same core material can alternatively be altered by removal of the oleate ligand to create an un-passivated metal oxide NP.[28] These chemistries enable a systematic study of the influence of both metal oxide NP core structure/composition and surface passivation on toxicity.

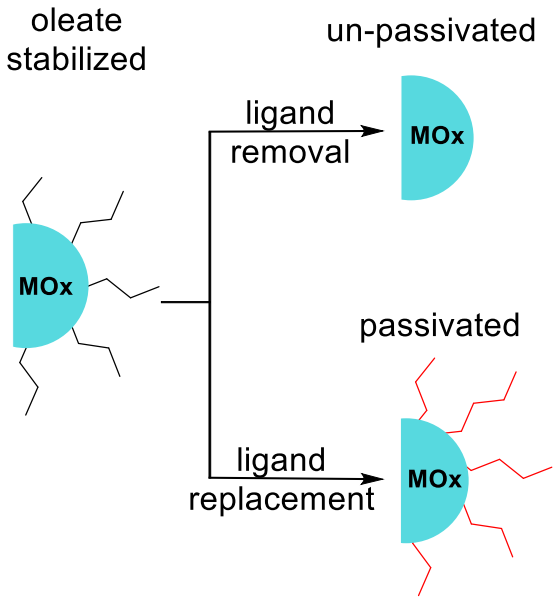

Figure 1.2: The removal and replacement of oleate to produce un-passivated and passivated NPs from the same starting metal oxide NP cores.

Dissertation Overview

Chapter II is from a previously published review article published in Chemistry of Materials (Kellon, J. E.; Young, S. L.; Hutchison, J. E. Engineering the Nanoparticle-Electrode Interface *Chem. Mater.* **2019**, *31*, 2685 – 2701). Chapter II reviews nanoparticle-functionalized electrode fabrication methods that utilize a molecular linker to interface NPs to an electrode substrate. Additionally, the structural features that influence electronic behavior are outlined. This work evaluates each design strategy and the resulting electrode composition with respect to behavioral attributes of broad interest for all applications. This work was written collaboratively by me and Samantha L. Young. Tawney A. Knecht aided in compiling references and editing the document. Jim Hutchison provided editorial assistance and guidance in conceptualizing this work.

Chapter III is from a previously published article in the Journal of the American Chemical Society (Young, S. L.; Kellon. J. E.; Hutchison, J. E. Small Gold Nanoparticles Interfaced to Electrodes through Molecular Linkers: A Platform to Enhance Electron Transfer and Increase Electrochemically Active Surface Area *J. Am. Chem. Soc.* **2016** *138* (42), 13975 – 13984). This work describes a new approach to tether pre-formed ligand stabilized small gold nanoparticles to a boron doped diamond electrode substrate. The photochemical grafting of terminal alkenes to boron doped diamond was employed to (1) graft NPs with a terminal alkene containing ligand shell and (2) assemble NPs onto previously functionalized electrodes through a ligand exchange reaction. The electrochemical behavior of both fabrication methods was investigated using a tethered ferrocene redox probe. Gold NP-functionalized electrodes were also fabricated using two additional strategies that produce a less defined interface. The electrochemical behavior

and electrochemically active surface area of each fabrication method was determined using cyclic voltammetry. The electrodes with a well-defined interface exhibited more efficient electron transfer and greater electrochemically active surface area compared to the physically adsorbed NP-functionalized electrodes. Experimental work and the writing of this chapter was performed equally between Samantha L. Young and me. Jim Hutchison provided guidance in the conceptualization of this work and editorial support.

Chapter IV discusses efforts to adapt the slow injection synthesis of metal oxide NPs to produce uniform and monodisperse cobalt oxide NPs. This chapter discusses the influence of air, temperature and precursor oxidation state on the resulting NP morphology. We observed that air is required for NP formation to occur at temperatures at or below 260^{o}C. Under all experimental conditions explored, the most reduced phase, CoO, in the rock salt crystal structure is formed. The resulting crystal structure was surprising given the necessary presence of air and the different oxidation state of the cobalt precursor. Our results suggest that the cobalt metal ions undergo one or more changes in oxidation state in the formation of CoO NPs. All experimental work was done by me.

Chapter V investigates the influence of metal oxide NP electronic structure and surface chemistry on NP toxicity. A series of six metal oxide NPs were synthesized: three different core materials each with an un-passivated surface and a passivated surface. The core materials were chosen because of their different electronic energy structures. The In_2O_3 and α-Fe_2O_3 NPs have conduction band energy minima that lie outside of the cellular redox window, above and below respectively. While the CoO NPs conduction band energy minimum lies within the cellular redox window. Each core materials surface

chemistry was modified to produce passivated and un-passivated NPs. Embryonic zebrafish were used as a biological model for the toxicity assays run. 18-morphological endpoints were monitored over five days including mortality. While all three un-passivated NPs resulted in mortality at 24 hours post fertilization at concentrations greater than 31.6 μg/mL, the passivated NPs did not yield any effects at the same concentration. However, unlike the passivated In_2O_3 and α-Fe_2O_3 NPs that did not have any adverse effects at any exposure concentrations, the passivated CoO NPs did induce mortality and morbidity at the highest concentration tested. This work was done in collaboration with the Tanguay Lab at Oregon State University. All materials synthesis and characterization were conducted by me. The toxicity assay was conducted by Lisa Truong and Robert L. Tanguay. Jim Hutchison and Robert L. Tanguay aided in the conceptualization of this work.

Bridge to Chapter II

Chapter II describes the structural features that comprise a nanoparticle-functionalized electrode with a defined molecular linker. The influence of each structural feature on electrochemical behavior is discussed. This work offers a literature review of existing nanoparticle-functionalized electrode fabrication methods that utilize a defined molecular interface. An evaluation of each method is conducted with respect to four universal attributes: stability, uniformity, electronic communication and tunability.

CHAPTER II

ENGINEERING THE NANOPARTICLE-ELECTRODE INTERFACE

Note: Reproduced with permission from Kellon, J, E.; Young, S. L.; Hutchison, J. E. This chapter was published previously in the following citation: Kellon, J. E.; Young, S. L.; Hutchison, J. E. Engineering the Nanoparticle-Electrode Interface. *Chem. Mater.* **2019**, *31*, 2685 – 2701.

Introduction

Chemically modifying electrodes has been an active research area for the last several decades. Murray's pioneering work using molecularly modified electrode surfaces laid the foundation for the functionalized electrode systems being studied today.[1] These modified electrodes were used to investigate the electron transfer processes for the design of improved molecular electrocatalysts.[2–6] Many of his insights and predictions from thirty years ago are still relevant as methods are being developed to modify electrode surfaces with more complex materials such as biomolecules,[7,8] polymers, and nanomaterials.[9–11] In particular, nanoparticle (NP)-functionalized electrodes are one class of modified electrodes that are being investigated for many important applications such as electrochemical energy conversion and storage,[12] sensors for biological and environmental applications,[13] and the electrosynthesis of molecules.[14]

The electrochemical activity of a NP-functionalized electrode can be tailored for a desired application and is influenced by many variables. In most cases, NP reactivity is strongly influenced by core size and shape. Variations in size and shape alter the

proportion of under-coordinated atoms at the NP surface, dictate which crystalline facets are dominant, and can drastically affect the electronic and optical properties, especially when core size is decreased below 2 nm. For example, the ratio of CO/H_2 produced by AuNP CO_2 electroreduction catalysts was reported to depend on the core size.[15] As the core size decreased, the higher ratio of under-coordinated atoms favored formation of H_2.

In addition to core morphology, the chemical environment surrounding the NP can significantly influence observed activity. The NP ligand shell can prevent and/or promote chemical reactions,[16–18] and the density of NP coverage and distribution on the electrode surface can influence the electrochemical activity. As an example, the mechanistic pathway and product selectivity for catalysts can depend upon interparticle distance: at higher NP densities, there is a greater likelihood of reaction intermediates generated at one NP undergoing further reaction at a neighboring NP on the electrode.[19] The oxygen electroreduction catalysis pathway was found to be influenced by the catalyst coverage on the electrode surface. The proportion of peroxide intermediates was found to decrease as the density of Pt nanodisk catalysts was increased.[20]

Finally, the interface between the NP and the electrode is important because it can dictate the electronic communication between the nanoparticle and the electrode.[21] There are numerous potential chemistries that can be employed to engineer the NP-electrode interface. The right tethering method can simultaneously integrate the NP and electrode system components and facilitate charge transfer while preserving the desired nanoparticle attributes (such as NP morphology and surface chemistry). Given the influence of the interface on electrochemical behavior and activity, the method of NP-functionalized electrode preparation is of the utmost importance. The ideal approach to

designing a NP-functionalized electrode makes it possible to systematically tune NP-functionalized electrode system variables to gain control over key electrochemical properties, such as facilitating electronic communication between the nanoparticle and electrode,[22–24] designing catalysts that are selective for a specific product,[25–27] or sensors that are selective for a target analyte.[28–30]

Over the years, a variety of physical deposition approaches have been explored to produce NP-functionalized electrodes. Simple strategies involve electrodeposition[31–36] or physical vapor deposition.[37–39] Electrodeposition was one of the earliest strategies used to modify electrode surfaces with nanostructures.[40] Metal ions can be deposited/precipitated out of solution directly onto the electrode surface by the application of a reducing potential. Some control over nanostructure size and density can be achieved by varying electroreduction potential and time. Physical vapor deposition involves the evaporation of a metal under vacuum that then selectively nucleates onto certain facets of a target substrate. Although both methods are convenient strategies to fabricate electrodes with un-passivated NP surfaces, they often yield disperse nanoparticle core sizes and have limited control over NP density on the electrode surface.

To address the limitation of physical deposition methods for the fabrication of electrodes with more highly engineered NPs, deposition of preformed NPs from solution has become a popular strategy. The use of preformed NPs allows for more rigorous characterization of the NP system being investigated through both solution and solid state analytical techniques before attachment to an electrode surface. The most common approaches for solution deposition include drop-casting,[41–44] spin-coating, and dip-coating.[45,46] It is typically assumed that the deposited NPs remain intact. Although these

methods utilize well-characterized NPs, the density of NP coverage and the chemical environment of the NPs on the electrode are not well defined. It can be challenging to reproducibly cover the electrode surface with NPs using solution deposition methods due to drying effects and sensitivity of coverage to the electrode surface preparation.[47,48]

Electronic communication between the NPs and the electrode is directly impacted by both the NP-electrode interface and the interactions between the NPs. Unless a defined electron transfer pathway is provided, the electron transfer between the NPs and an electrode can be hindered by the electrically insulating ligands that stabilize the NP core.[49] Although NPs have been successfully deployed in electrochemical applications such as fuel cells,[50] batteries,[51,52] electrocatalysis,[12] amperometric sensing,[13] and electrosynthesis,[14] more efficient communication between the NPs and the electrode could enhance the activity and/or selectivity for NP-functionalized electrode applications. Thus, the purpose of this review is to review and evaluate fabrication methods that produce defined NP-electrode interfaces to determine if they can increase electron transfer rates, prevent NP desorption, and control interparticle spacing.

The use of a molecular linker to directly bind NPs to an electrode substrate is a promising approach to engineering a well-defined NP-electrode interface. Over the past 30 years significant progress has been made in our ability to generate defined molecular monolayers on a wide variety of surfaces.[53–55] Additionally, our understanding of the behavior of these monolayers has led to the ability to tune their properties to achieve desired electrochemical behavior on a wide range of electrode substrates and electrochemical environments for various applications. Simultaneously, advancements in NP synthesis have led to increased control and tunability of NP surface chemistry (ligand

shell composition).[56–61] In fabricating NP-functionalized electrodes, researchers have acknowledged that it is the marrying of these two burgeoning fields that may provide enhanced system performance and deepen our understanding of the electrochemical properties of NPs (Figure 2.1). Significant effort has gone into the design and fabrication of NP-functionalized electrodes with a defined molecular interface. The use of a discrete molecular layer to bind a NP to an electrode surface allows for a higher degree of control over the chemical environment surrounding the NP while retaining the geometric control over the NP core offered through the use of preformed NPs.

Due to the increased variety in NP compositions and the ability to generate many different molecular monolayers on various electrode substrates, careful consideration must be taken when designing a NP-functionalized electrode. Figure 2.1 demonstrates the three commonly used NP surface chemistries: 1) a strongly bound and terminally functionalized ligand shell 2) ionic capping molecules and 3) a weakly bound, labile, ligand shell. Additionally, Figure 2.1 provides examples of the various molecular monolayers that can be formed on an electrode surface.

This review focuses on the various design strategies employed to generate NP-functionalized electrodes using the NP and electrode chemistries outlined in Figure 2.1. Each design strategy will be discussed and evaluated with respect to its resulting attributes, including electron transfer efficiency, synthetic accessibility, and overall defined structure. First, the chemistries employed in each strategy will be reviewed, followed by a comparison of each approach using universal attributes of interest for all applications of NP-functionalized electrodes: overall system stability, uniformity of the NP-electrode interface and resulting NP distribution, electronic communication between

the NP and electrode, and overall system tunability. Finally, we discuss future directions of molecularly linked NP-functionalized electrodes for creating advanced, multi-functional materials for important applications which will be enabled through the expansion of these design approaches coupled with improved analytical techniques.

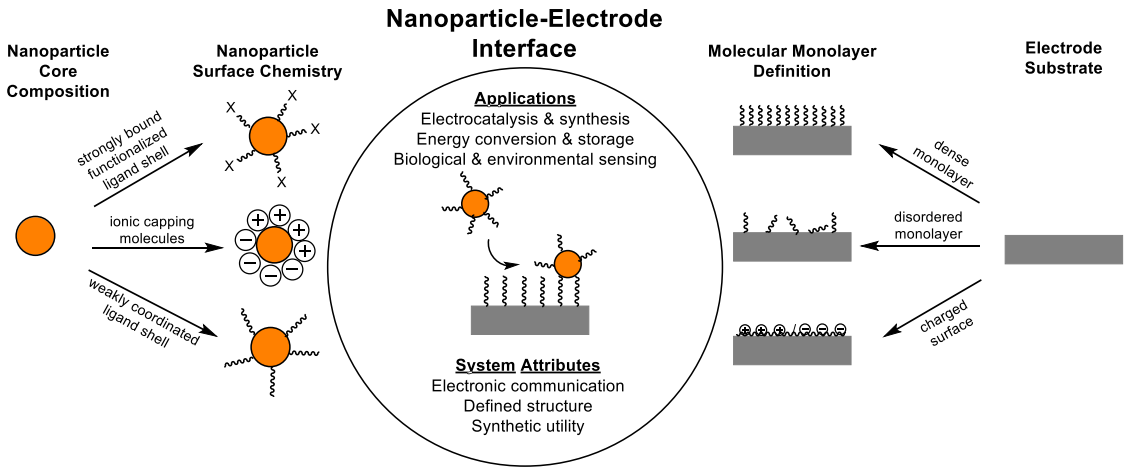

Figure 2.1. Engineering the nanoparticle-electrode interface with well-defined, ligand-stabilized NPs and molecularly-functionalized electrode substrates. The use of established synthetic methods to tune the surface chemistry (ligand shell) of NPs in combination with existing methods to molecularly modify electrode substrates allows one to construct a wide range of NP-linker-electrode architectures.

Design Strategies for the Engineering of NP-Functionalized Electrodes

There are four main approaches to produce a defined NP-electrode interface utilizing a molecular linker: 1) pre-functionalization of the electrode with a molecular monolayer capable of binding to the NP core via ligand exchange (Scheme 2.1a), 2) employing electrostatic interactions to assemble NPs with a charged surface chemistry onto a charged electrode surface (Scheme 2.1b), 3) utilizing the existing NP ligand shell to form a bond with a pre-functionalized electrode substrate (Scheme 2.1c) or 4) utilizing the existing NP ligand shell to form a bond to the electrode surface (Scheme 2.1d). It should be noted that although most of the existing chemistries discussed in this review

pertain to gold NPs and gold electrodes, the findings are still applicable to other NP core materials and molecularly functionalized electrodes due to the commonalities in molecular linker chemistries and tunability of terminal functionality. The few examples of molecular linkers used to assemble metal oxide, diamond and quantum dot nanomaterials to various electrode substrates, including boron-doped diamond, ITO and FTO, are also included in this review.

Scheme 2.1. General design strategies to engineer nanoparticle-functionalized electrodes with a defined NP-electrode interface.

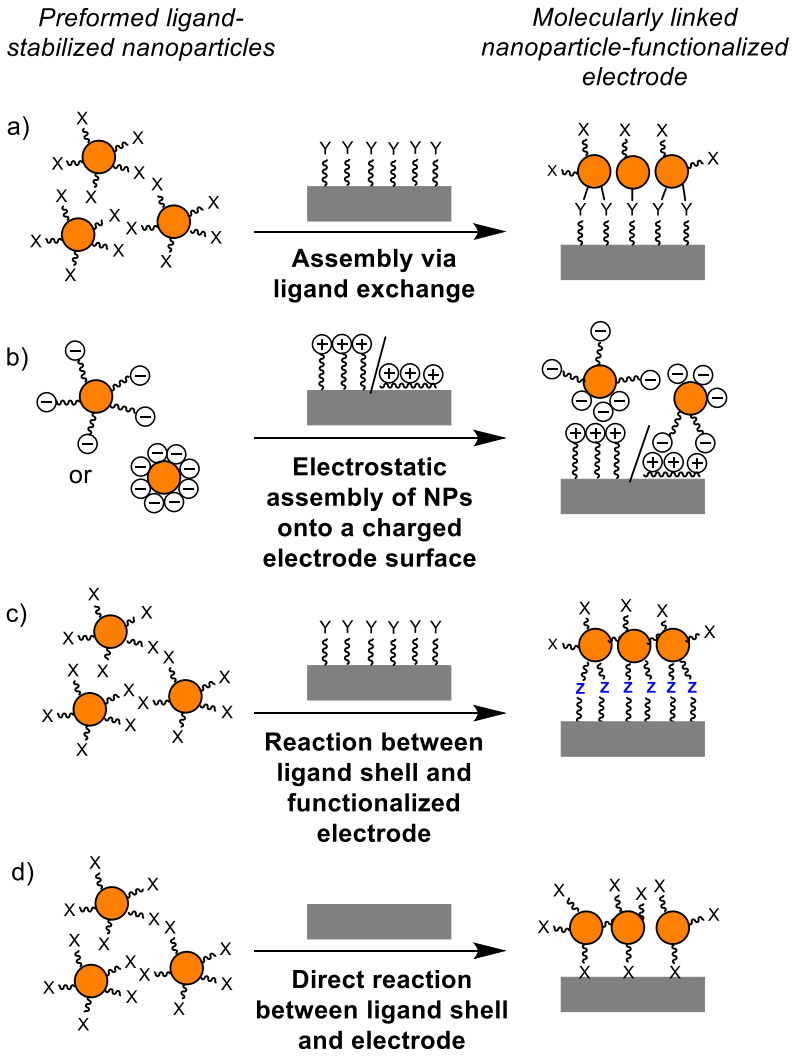

Assembly onto pre-functionalized electrodes through ligand exchange (Scheme 2.1a)

The most common approach to fabricating a NP-functionalized electrode with a molecularly defined interface is to first modify the electrode substrate with a molecular linker. This linker typically contains a terminal functional group or charged moiety capable of capturing preformed nanoparticles through either ligand exchange or electrostatic interactions, respectively. The functionalization of the electrode surface to enable subsequent NP assembly is typically accomplished through the formation of a self-assembled monolayer (SAM), the deposition of a polyelectrolyte onto an electrode substrate or a SAM, or grafting reactions. These functionalization methods will be discussed below in the context of NP assembly.

Self-assembled monolayers. Self-assembled monolayers (SAMs) can be formed on both metallic and non-metallic electrode substrates. Research done on SAMs has been extensively reviewed and will not be the subject of this review.[62,63] Three different molecular linker-electrode chemistries are commonly used to form SAMs on an electrode surface: thiol-noble metal electrode, alkoxysilane-non-metallic electrode, and polyelectrolyte or polyelectrolyte-SAM-electrode architectures. The most common terminal functionalities used to assemble a variety of NP materials are thiol, amine, and carboxylic acid moieties.

The use of thiol SAMs to functionalize electrodes is most often done on single crystal or polycrystalline noble metal electrodes (Pt, Ag, and most often Au). These electrodes are submerged in a solution of molecules containing a terminal thiol functional group which forms a strong bond with the electrode, resulting in a molecular monolayer. The other end of the SAM contains a functional group capable of assembling NPs such as

thiols,[64–66] amines,[67,68] and carboxylic acids.[69] For example, the size dependent electrochemical properties of Au nanorods were studied through their assembly on hexanedithiol modified gold electrodes (Figure 2.2).[70] Thiol SAMs with different terminal functionalities can be used together to form mixed molecular monolayers. These systems can be used to control the NP density on the SAM surface through the introduction of a diluent ligand, such as a hydroxy-terminal SAM which does not interact strongly with the NP core material.[69] A wide variety of molecular compositions can be introduced into the interior of the SAM such as conjugation,[71] aromatic moieties,[71,72] and redox active gates/bridges.[65,66] CdSe quantum dots were assembled onto a variety of dithiol SAM modified gold electrodes to investigate the electron tunneling rate dependence on linker length and interior composition.[72] Furthermore, three-dimensional

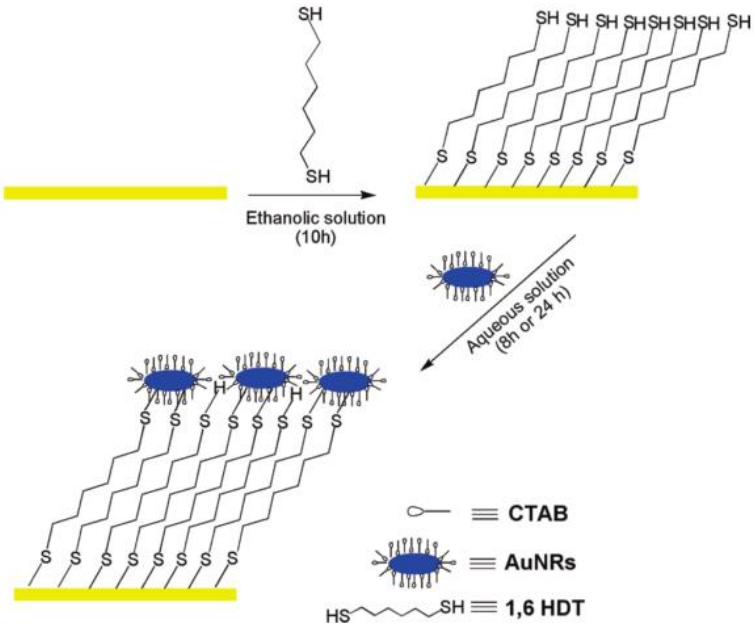

Figure 2.2. Schematic of the assembly of cetyltrimethylammonium bromide-stabilized gold nanorods onto a 1,6-hexanedithiol SAM on a planar gold electrode through ligand exchange. Reprinted with permission from ref 67. Copyright 2009 American Chemical Society.

architectures can be achieved through layer-by-layer assembly of alternating SAM-NP-SAM exposures.[69,73,74]

Functionalized alkoxysilanes are another class of molecules that have been widely used to form self-assembled monolayers on surfaces. These monolayers are formed through condensation reactions with hydroxyl groups on the electrode surface to form electrode-O-Si linkages between the electrode and the alkoxysilane. This chemistry is most commonly used to functionalize tin-doped indium oxide (ITO) electrodes[73,75–78] but has also been employed with surface oxidized silicon[73] and boron-doped diamond (BDD).[79] After molecular monolayer assembly, the distal functional group on the silane is used to assemble NPs. The most common alkoxysilanes used are 3-(aminopropyl)-triethoxysilane (APTES)[73,75,77,79] and 3-(mercaptopropyl)-trimethoxysilane (MPTMS),[73,75,78–81] both of which are commercially available. This chemistry was used to assemble AuNPs onto APTES or MPTMS-functionalized BDD, and the stability and electron transfer properties for the tethered systems were compared to physiadsorbed NPs on BDD.[79] AuNPs (d_{core} ~14 nm) were tethered to both APTES and MPTMS-functionalized ITO electrodes and the influence of the AuNP tethering chemistry on the electrocatalytic activity towards methanol electrooxidation was investigated (Figure 2.3).[75] Researchers found that the two molecular linkers led to different distributions of AuNPs on the functionalized electrode surface and that the APTES molecular linker resulted in significantly faster electron transfer and a higher current density for the electrooxidation of methanol than the MPTMS molecular linker.[75]

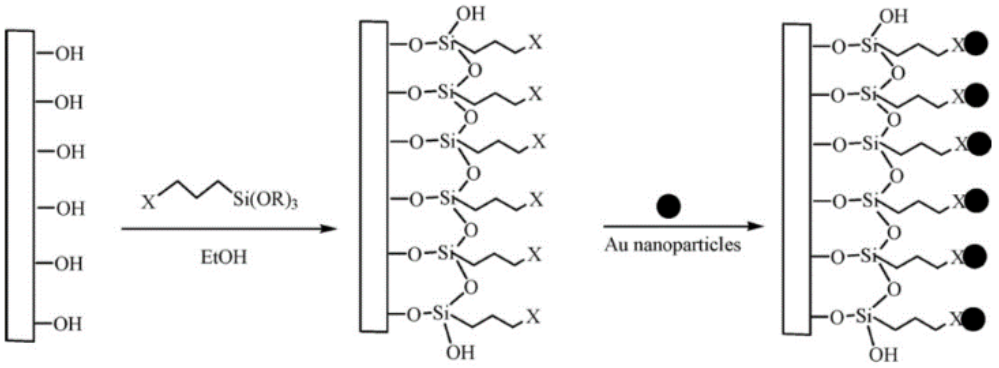

Figure 2.3. Assembly of citrate-stabilized AuNPs onto APTES and MPTMS functionalized ITO electrodes through ligand exchange. Reprinted with permission from ref 72. Copyright 2008 Elsevier.

Grafted Monolayers. Grafting chemistry is an alternative to self-assembly to modify surfaces with molecular tethers. Grafting reactions are initiated through electrochemical, photochemical, or thermal generation of a radical which can then bind to an electrode surface. This approach generally forms covalent carbon-electrode bonds between the linker and the electrode material.

Electrochemical grafting has been used to graft molecules to the surface of electrodes to produce functionalized electrodes that facilitate nanoparticle assembly. The reduction of aryl diazonium molecules has been used to functionalize electrode surfaces through grafting and has been the subject of several reviews.[82,83] Diazonium ions are generated *in situ* through the reaction of nitrite with substituted arylamines because most diazonium compounds are not shelf stable. The intermediate aryl diazonium molecule is then electrochemically reduced to produce a radical that reacts with the electrode surface. Electrode supports that can sufficiently reduce the diazonium molecule and react with the generated radical can be modified with this approach. This approach has been used to functionalize different carbon surfaces, noble metals, and metal oxide surfaces with aryl molecules possessing many different functional groups such as carboxylic acid,[5] amine,

azide,[84] thiol,[85,86] and nitro groups[87,88] which can be used to capture NPs. AuNPs (d_{core} ~ 16-30 nm) have been assembled onto aminophenyl and thiophenol-functionalized glassy carbon electrodes modified through the diazonium reduction to evaluate the stability of the interface[85] and its use as a biosensor to detect anti-biotin IgG which resulted in a detection limit of 5 ng/mL (Figure 2.4).[89]

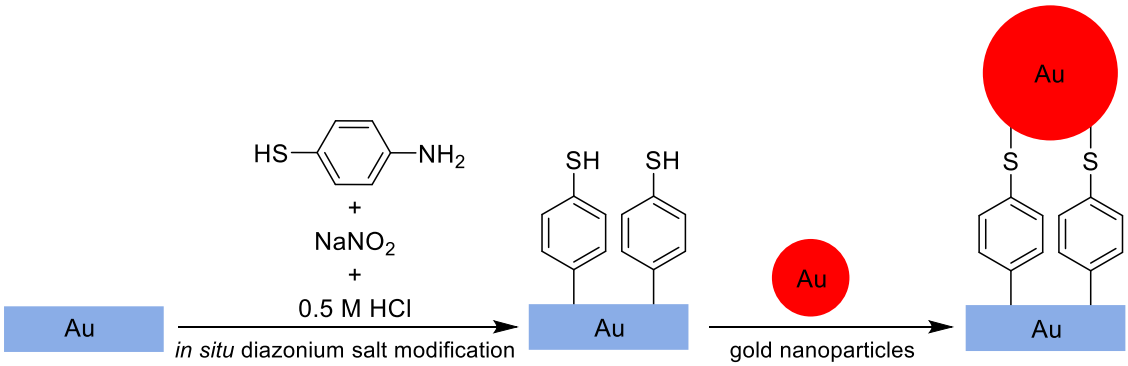

Figure 2.4. The *in situ* electrochemical reduction of aryl diazonium onto a gold electrode yielding a thiol-terminated molecular monolayer capable of assembling gold nanoparticles by binding to their core. Reprinted with permission from ref 86. Copyright 2011 Elsevier.

Electrochemical reduction techniques have been used to modify electrode surfaces with molecules other than aryl diazonium species. Poly(ethylenediamine) has been electrochemically grafted to glassy carbon and graphite electrodes to generate a series of samples with varying interface thicknesses to study NP-mediated electron transfer.[90] In addition to assembling NPs, the electrodeposition of these NPs onto an interface generated through electrochemical reduction has been reported.[86,88]

Photochemical grafting is another method used to functionalize electrode surfaces with a molecular interface to assemble NPs. The photochemical grafting of alkenes to boron doped diamond (BDD) electrodes was pioneered by the Hamers group and is generally accepted to occur through the photoemission of an electron from the substrate

into the acceptor level of the alkene.[54,91] This chemistry has been expanded to functionalize amorphous carbon, silicon, metal oxide, and metal nitride surfaces generally through the same mechanism.[54,92] Larger AuNPs (d_{core} ~15-40 nm) have been assembled onto amine functionalized BDD generated through photochemically grafting allylamine to study the stability of the interface and the electron transfer properties.[93] Smaller AuNPs (d_{core} < 2 nm) have also been assembled onto thioacetate or thiol molecular monolayers generated from grafting undecenyl-thioacetate to boron doped diamond electrodes.[21] Using this approach, the effect of core size and the interface on NP-mediated electron transfer was studied for this smaller NP core size regime. In contrast to the use of alkenes, irradiating elemental sulfur or carbon disulfide was reported to functionalize diamond surfaces with sulfur groups to facilitate the assembly of AuNPs.[94]

Silicon electrodes have been functionalized with alkenes or alkynes though hydrosilylation at elevated temperature. AuNPs were assembled onto thiol monolayers on silicon electrodes that had been heated with a trifluoroacetyl (TFA)-protected alkenylthiol to functionalize the electrode, followed by removal of the TFA protecting group to enable NP assembly through Au-thiolate bonds.[95] Alkyne monolayers on silicon were generated by heating the substrate with 1,8-nonadiyne. The monolayers were further functionalized through clicking an azide, containing a terminal amine, to the monolayer that was able to capture the AuNPs.[96]

Electrostatic assembly onto modified electrodes (Scheme 2.1b)

Another method utilizing a pre-functionalized electrode substrate to assemble NPs is the use of polyelectrolytes to form a charged electrode surface. Polyelectrolytes are

ionically charged polymers that electrostatically assemble either directly onto a bare electrode surface[97–99] or onto carboxylic acid terminated SAM-functionalized electrodes (Figure 2.5).[69,100–107] In contrast to assembling NPs onto the electrode through forming covalent bonds with the NPs as in the thiol or amine terminated SAMs, the polyelectrolyte layers capture NPs through electrostatic interactions. This strategy has been reported to capture a wide variety of NP core materials through electrostatic interactions including diamond,[97] gold,[98,99] palladium,[98,108] and semiconductor quantum dots.[62,100] Commonly used polyelectrolytes to assemble NPs are poly-L-lysine (PLL), poly(diallyldimethylammonium) chloride (PDADMAC), poly(amidoamine) (PAMAM) and poly-L-arginine (PLA), all of which are cationic. This method was used to assemble different sizes of CdTe and CdSe quantum dots onto PDADMAC modified carboxylic acid SAMs on planar Au electrodes to investigate the influence of core size on the charge transfer properties of these materials.[62] AuNPs and nanorods were assembled onto poly(styrenesulfonate)-APTES-functionalized ITO electrodes to study the influence of core size and shape on their electrocatalytic activity towards methanol electrooxidation and oxygen reduction.[109] The influence of the lattice strain of PdNPs on their ability to adsorb hydrogen was probed by assembling PdNPs onto PLL-modified ITO electrodes to inform future catalytic studies.[98] This approach has also been utilized to fabricate and investigate the electrochemical properties of nanocomposites, such as graphene-NP materials.[110]

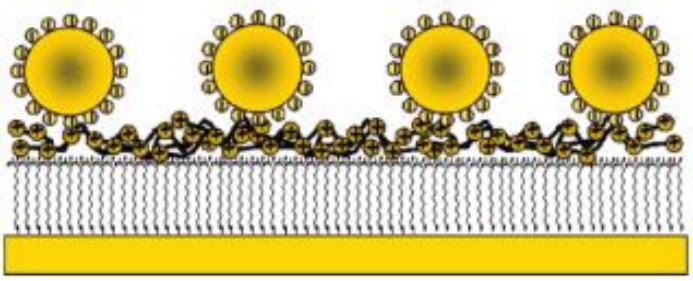

Figure 2.5. Poly-L-lysine polyelectrolyte on an 11-mercaptoundecanoic acid functionalized gold electrode is used to electrostatically assembly citrate-stabilized AuNPs. Reprinted with permission from ref 103. Copyright 2005 American Chemical

Nanoparticle ligand shell bound to a modified electrode (Scheme 2.1c)

This approach leverages terminal functionality in the NP stabilizing ligand shell to bind the NP to the electrode surface instead of assembling NPs onto molecularly modified electrodes through ligand exchange reactions. This is typically accomplished by a reaction between a functional group in the nanoparticle ligand shell with either an existing molecular tether on the electrode surface or the electrode substrate itself. Both strategies will be described in this section.

The development of efficient chemistries in organic synthesis such as click chemistry and host/guest supramolecular chemistry has been expanded to couple nanomaterials to surfaces. Improved nanoparticle syntheses have enabled the incorporation of functional groups that can undergo chemical reactions with an electrode containing an appropriate functional group. The combined use of these advances in synthesis have been used to link NPs to electrodes through several different approaches.

In synthetic organic chemistry, two different molecules are often bound to each other through coupling chemistry. Coupling reactions have also been applied to bind nanoparticles to functionalized electrodes through their ligand shells. The copper(I)-

catalyzed azide-alkyne cycloaddition, the most well recognized of the click chemistry reactions proposed by Sharpless et al.,[111] has been used to couple nanoparticles to functionalized electrode surfaces. Gold nanoparticles (d_{core} = 10-13 nm) with undecyn-1-thiolate ligands were bound to azide-functionalized glassy carbon electrodes through this azide-alkyne cycloaddition reaction, and these AuNP functionalized electrodes were demonstrated to selectively catalyze the electrooxidation of nitrite in the presence of competing pollutant ions.[84,112] Molecularly linked multilayer structures of Au, TiO_2 and SiO_2 nanoparticles were constructed on Au, silicon, ITO, and stainless steel electrodes through clicking azide-functionalized NPs and alkyne-functionalized NPs to each other in a layer by layer assembly approach (Figure 2.6).[113] These metallic and semiconductor NP heterostructures were demonstrated to be catalytically active towards the photochemical degradation of dyes, methanol electrooxidation, and electrochemical water splitting. In addition to observing increased stability of the NPs on the electrode through 150 cycles for methanol oxidation, Upadhyay et al.[113] found that the molecularly linked AuNPs yielded a higher current density for water splitting compared to a sputtered gold thin film. They attribute the higher current density to the increased surface area offered by the AuNPs. The azide-alkyne click chemistry has also been demonstrated without the copper catalyst by using strained alkynes. Magnetite (Fe_3O_4) NPs possessing strained cyclooctynes in their ligand shell were reacted with azide-functionalized silicon electrodes to tether the NPs to the surface.[114] The formation of amides through the reaction between carboxylic acids and amines has also been used to functionalize electrode surfaces with NPs. Carboxylic acid AuNPs (d_{core} ~3 nm) were reacted with amine-functionalized planar Au electrodes to link the AuNP to the electrode through

amide bonds.[115] Subsequently, a protein was bound to the AuNP surface to study its electron transfer properties using this electrode structure.

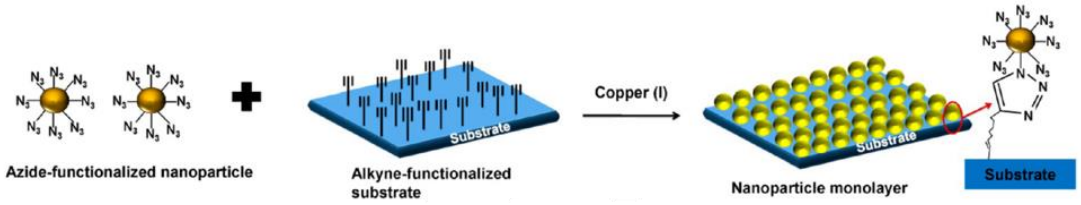

Figure 2.6. The copper catalyzed click reaction is used to bind azide-functionalized gold NPs with an alkyne-functionalized ITO electrode. Reprinted with permission from ref 110. Copyright 2013 American Chemical Society.

Another approach to attach NPs to functionalized electrodes though their ligand shells is to use strong non-covalent interactions such as host/guest chemistry or interactions of metal ions with molecules. The interaction of biotin ligands with the protein avidin is one of the strongest non-covalent interactions known in nature,[116] and this interaction has been used to bind NPs to electrode surfaces. Avidin or biotin were coupled to the carboxylic acid ligand shell of ~12 nm AgNPs, and these functionalized AgNPs were then bound to biotin or avidin functionalized planar Au electrodes respectively in order to study their electron transfer properties.[117] A similar strategy was used to assemble ~60 nm AgNPs onto planar Au electrodes through the biotin/avidin interaction in order to construct amperometric sensors to detect the pesticide dimethoate.[118] Strong non-covalent interactions have also been formed using synthetic host/guest supramolecular chemistry and have been used to tether NPs to electrodes. The ability of cyclodextrin and calixarene to strongly bind guest molecules has been used for this purpose. AuNPs with cyclodextrin terminal ligands were bound to a planar Au electrode functionalized with a monolayer possessing terminal iron porphyrin compounds

through supramolecular interactions between the cyclodextrin and the metalloporphyrin.[119] Similarly, cyclodextrin-functionalized AuNPs were bound through interactions between the cyclodextrin ligand and terminal ferrocenes on the functionalized ITO electrode.[120] This electrode was active towards the electrooxidation of ascorbic acid. The interactions between metal ions and carboxylic acids is another linking chemistry that has been used to bind NPs to electrodes using their ligand shells. Carboxylic acid-functionalized AuNPs (d_{core} ~ 2 nm) were bound to carboxylic acid SAMs on planar Au through the use of Zn^{2+} as a bridge.[9]

Direct binding of the nanoparticle ligand shell to the electrode (Scheme 2.1d)

Whereas the previous section described the binding of the NP ligand shell to a preformed molecular layer on the electrode surface, another strategy is to bind the ligand shell directly to the bare electrode surface. This has been typically accomplished using the grafting chemistry described previously. Alkenethiolate-stabilized AuNPs (d_{core} ~ 4 nm) have been interfaced to silicon substrates through Si-C bonds using thermal hydrosilylation reactions.[121] Photochemical grafting reactions were used to bind small alkenethiolate-stabilized AuNPs (d_{core} ~ 2.5 nm) to BDD through covalent C-C bonds and were used to study the electron transfer properties as a function of core size in this small size regime (Figure 2.7).[21] AuNP/graphene oxide nanocomposites were formed by the reduction of the diazonium group generated from phenylamine ligands.[122]

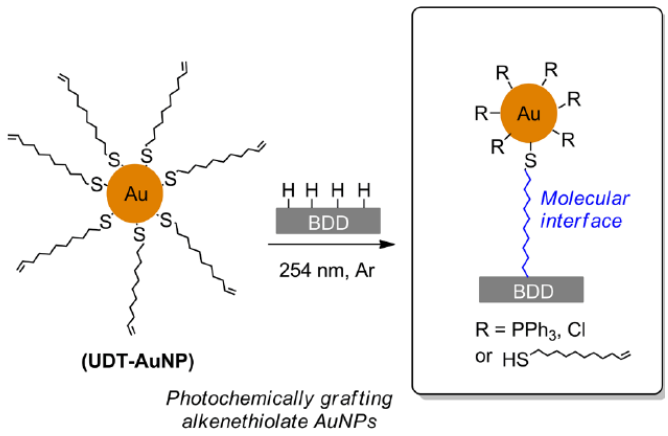

Figure 2.7. The photochemical grafting of alkenethiolate-stabilized AuNPs onto a boron-doped diamond electrode. Reprinted with permission from ref 21. Copyright 2016 American Chemical Society.

Structural Features of Nanoparticle-Functionalized Electrodes with Defined Molecular Interfaces

In order to design a NP-functionalized electrode system for a desired application using the methods discussed in the previous section, it is vital to understand how each structural system variable may influence the overall system properties. Although we briefly discussed how the structural attributes influence performance in the introduction, we will go into greater detail here to lay a foundation for how each method is evaluated in the following section. Figure 2.8 illustrates the structural attributes that influence overall performance of a NP-functionalized electrode.

The NP core material and composition is typically the driving variable for electrode design and fabrication (Figure 2.8a). The core composition dictates not only the types of reactions and chemistries available to the overall system but also the available core size range and ligand shell composition based on synthetic accessibility. As previously stated, nanoparticle size and shape have been shown to impact (photo)catalytic activity,[15,45] product selectivity,[15,45] and may influence electron transfer rates.[123]

Furthermore, the nanoparticle ligand shell (surface chemistry) influences the stability of the nanoparticle core and could prevent and/or enhance interactions between the nanoparticle and analytes.

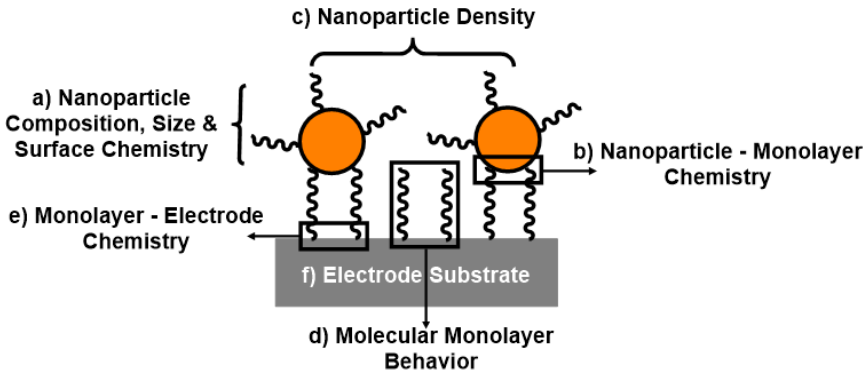

Figure 2.8. Schematic of the structural variables for a NP-functionalized electrode with a defined molecular interface. Each structural variable highlighted may influence the overall system performance and is used to evaluate each design strategy discussed in section 4.

In the previous section, we discussed numerous types of interactions used to link NPs to an electrode substrate. The type of chemical bond between the NP and the molecular monolayer (Figure 2.8b) can influence three main system properties: NP stability, electron transfer rates, and the density of NPs on the surface. NP desorption is less likely to occur if the NP-molecular monolayer chemical bond is robust. Weak ionically-coordinated NPs have the potential to readily desorb from the electrode surface, creating a more dynamic NP-electrode interface. Furthermore, it has been observed that nanoparticles that are physically adsorbed onto a molecular monolayer (i.e., no chemical bond) do not yield efficient electronic communication with the underlying electrode substrate.[68] Additionally, the density of NP coverage on the electrode surface (Figure 2.8c) has been shown to influence both catalytic activity and product selectivity. For example, the proportion of methane and ethylene products produced by CuNP CO_2

electroreduction catalysts was found to increase as the coverage on the electrode surface increased due to the ability of the CO intermediates to readsorb to the surface of neighboring CuNPs and undergo further reaction.[19]

Depending on the desired application, the electrochemical behavior of the molecular monolayer may be a critical structural attribute to consider (Figure 2.8d). While some molecular monolayers are electrochemically insulating (preventing faradaic charge transfer between solution analytes and the electrode surface), others enhance electronic communication between solution analytes and the underlying electrode. Each design strategy discussed yields molecular monolayers with varying degrees of electrochemically insulating behavior. Choosing a molecular monolayer that meets the needs of a desired application is critical to ensure that this structural feature does not complicate the data interpretation.

As previously stated, not only will the NP-linker interface influence electrochemical activity, but the linker-electrode interface influences the stability, density, and uniformity of the molecular monolayer (Figure 2.8e). If the molecular monolayer is disordered and sparse, solution phase analytes may be able to interact directly with the underlying electrode and bypass the nanoparticles. Lastly, choosing a substrate that is compatible with the necessary experimental conditions (i.e., electrolyte and potential window) is required (Figure 2.8f).

Evaluation of System Attributes and Electrochemical Behavior for Each Design Strategy

There are several attributes that are generally important across all applications of nanoparticle-functionalized electrodes. These attributes include: 1) stability of the

functionalized electrode 2) uniformity of the NP-electrode interface and the resulting distribution of NPs across the electrode surface, 3) sufficient electronic communication between the NP and the electrode, and 4) the ability to further modify the electrode after fabrication. For some attributes, the choice of general strategy to construct NP-functionalized electrodes, either through assembly onto molecular linkers or using the NP ligand shell for attachment, is the main factor in imparting the desired properties. In other cases, the choice of NP binding chemistry or electrode support material is the more important variable regardless of if the NPs are assembled through ligand exchange or bound through their ligand shell. The different methods of fabricating nanoparticle-functionalized electrodes will be evaluated and compared in the context of these universal attributes desired for electrochemical behavior. While analogous methods can be used to immobilize NPs on surfaces for other applications, such as surface-enhanced Raman spectroscopy (SERS)-active materials,[124–126] this discussion will be limited to electrochemical applications.

Stability

The NP, molecular interface, and electrode support of NP-functionalized electrodes need to be stable with respect to desorption, chemical degradation, and NP aggregation over long periods of time to realistically be useful for practical applications such as sensing or catalysis. In the context of nanoparticles linked to an electrode through a molecular interface, both the electrode-molecular interface and the NP-molecular interface should be evaluated for their ability to preserve the intended system morphology by preventing NP desorption and aggregation. Furthermore, the electrode substrate must be compatible with the desired operating conditions.

Both the stability of the electrode material and the electrode-interface are important for retaining sufficient electronic communication between the NP and the electrode over time. The electrolyte and potential window required for a study or application often dictate which electrode support is most appropriate. For example, silicon electrodes will dissolve in alkaline electrolytes limiting their application to acidic or non-aqueous electrolytes. Silicon can also easily form electrically insulating oxide layers in aqueous electrolytes unless the electrode surface is completely passivated by a molecular layer. A decrease in electron transfer rates for AuNP-functionalized silicon electrodes was observed over ~50 cycles in an aqueous solution of $Ru(NH_3)_6^{3+}$ which was attributed to the formation of insulating SiO_x underneath the molecular monolayer (Figure 2.9).[96] In contrast, carbon electrodes can be operated in acidic, alkaline, and non-aqueous electrolytes without concern of dissolution or oxidation of the surface. Boron doped diamond (BDD) in particular has been reported to have a remarkable stability across a wide potential window since it is inert towards hydrogen or oxygen evolution catalysis which can limit the available potential window for metallic electrodes or other carbon electrodes.[127]

Similarly, the choice of interface chemistry can also limit or enable operation of the electrode under certain conditions. The strength of the bond of the molecular monolayer to the electrode substrate will influence desorption of molecular layers and/or NPs from the interface. Covalent carbon-carbon bonds, which are formed in electrode modification methods such as aryl diazonium electrochemical reduction or photochemical grafting of alkenes, are anticipated to be stable since a significant amount of energy is required to break that bond. These interfaces have been reported to be stable

over many cycles as determined through preservation of the redox activity of the bound nanoparticle or organometallic catalysts.[85,128] In contrast, self-assembled monolayers of thiols on planar noble metal electrodes have been reported to desorb from the electrode surface under reducing potentials in alkaline media which could potentially limit applications under those conditions.[129,130]

The NP-molecular interface chemistry will determine the likelihood of NP desorption or aggregation during electrochemistry. In general, covalent bonds between the NP and the interface are anticipated to be more stable to both desorption and aggregation than electrostatic interactions. Furthermore, the presence of stabilizing

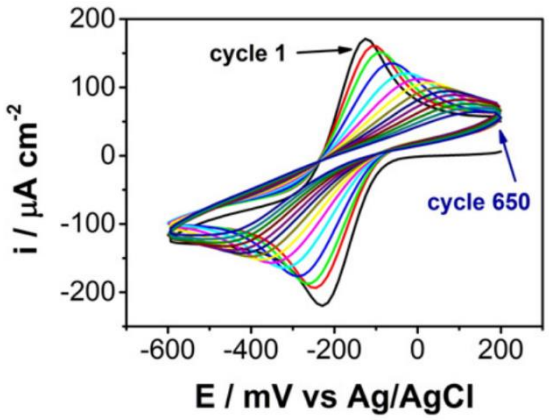

Figure 2.9. Cyclic voltammograms of a AuNP-functionalized Si electrode in an aqueous solution of $Ru(NH_3)_6^{3+}$ every 50 cycles up to 650 cycles. The diminished electrochemical response with increasing cycles is thought to be caused by the formation of an insulating SiO_x layer at the electrode surface. Reprinted with permission from ref 93. Copyright 2016 Elsevier.

ligands on the nanoparticle surface can also preserve the NP core by preventing core dissolution or fusion during electrochemistry. These ligands are present in many nanoparticles that are assembled onto or reacted with an interface, but not on NP-functionalized electrodes fabricated through electrodeposition or electrostatic adsorption. The interface chemistry can be sensitive to pH which can cause nanoparticle desorption or aggregation. The morphology and coverage of citrate-stabilized AuNPs assembled on

electrodes through Au-amine bonds have been observed to be influenced by pH with NP desorption occurring as the pH is increased due to deprotonation of the amine, which diminishes electrostatic interactions, allowing nanoparticle desorption (Figure 2.10).[93] AuNPs assembled onto amine-terminated silane monolayers have shown an increase in aggregation on the surface in contrast to assembly onto thiol-terminated silanes.[75,109]

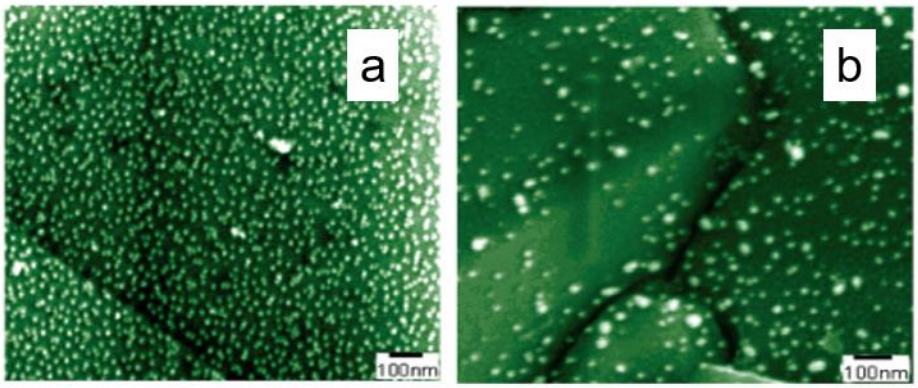

Figure 2.10. Scanning electron micrographs of AuNPs assembled onto amine-terminated BDD electrodes showing the relative degrees of NP desorption after being submerged into different pH Au colloidal solutions: (a) pH = 4, (b) pH = 5. Reprinted with permission from ref 90. Copyright 2006 American Chemical Society.

Uniformity

In order to extract reliable structure-property relationships for NP-functionalized electrodes, the NPs should all be in a uniform chemical environment. Specifically, NPs should be the same distance from the electrode and neighboring particles in order to attain uniform electron transfer rates and similar interparticle charging effects, respectively. While different applications may require different molecular monolayer features in terms of monolayer/NP density, methods to reproducibly produce a uniform molecular monolayer with a uniform NP distribution on this interface is typically desired for all applications.

Molecular monolayer. Some studies rely on a dense, insulating molecular monolayer to completely passivate the electrode surface. The systems that lead to the

highest molecular densities are fully-saturated alkanethiol SAMs on gold and electrochemically grafted ethylenediamine on glassy carbon. Both systems offer control over the extent of electrode passivation by altering the SAM length or organic layer thickness respectively. Alkanethiol SAMs on gold can form crystalline-like interfaces on single crystal gold electrodes that typically passivate the electrode substrate.[131–133] Although these SAMs generally lead to complete electrode passivation, defects in the electrode substrate can lead to pinholes and disorder in the SAM.[134,135] Gooding et al. were able to control the thickness of the poly(ethylenediamine) organic layer, ranging from 6.6 ± 1.3 Å to 37.7 ± 1.2 Å, through successive cycling at anodic potentials.[90] Although both methods provide tunability in the extent of electrode passivation, each has its limitations. SAMs offer a monolayer of uniform density and thickness, but bi-functionalized SAMs of greater than 18 methylene units are not achievable. Conversely, greater thicknesses can be achieved in poly(ethylenediamine) systems, but these layers suffer from variable thicknesses across the electrode surface leading to a non-uniform NP-electrode interface. Despite each method's limitations, both can yield a dense, completely passivated electrode surface.

It is not always necessary that the electrode surface be fully passivated. Depending on the nature of the study, the electrode material and electronic conductivity of the interface may be more important. Non-metallic electrodes require the use of either alkoxysilane, polyelectrolyte, or chemically grafted monolayers, each of which offer different levels of control over the interface uniformity. The two commonly used alkoxysilane molecular monolayers, APTES and MPTMS, yield different monolayer densities. APTES forms a sparse monolayer while the MPTMS is more dense, but still

not completely passivating.[75,79] Furthermore, silane chemistry is prone to polymerization/cross-linking thus leading to ambiguity in both interface thickness and chemical environment. Photochemical grafting of alkenes results in sparse, disordered monolayers with shorter alkenes being more ordered than longer alkenes.[136] Multilayer formation can occur during the electrochemical grafting of aryl diazonium molecules which can lead to variability of interface thickness.[137] Although this can be prevented by using radical scavengers during the grafting reaction[138,139] or by incorporating bulky substituents[140–142] into the linker molecule, there is a potential trade-off between interface density and uniformity.

Nanoparticles. When investigating the electrochemical properties of NPs, it is critical that the data are not convoluted by contributions from multiple NP-chemical environments. Although both a submonolayer of discrete NPs and a dense NP monolayer are desirable for different applications/studies, a surface with variations in NP distribution across the surface can lead to variability in the observed electrochemical properties. The formation of NP aggregates on the electrode surface can lead to irreproducible results because it is challenging to control the degree of aggregation. The terminal functionality of alkoxysilane SAMs have been reported to influence the molecular monolayer density and the overall distribution of NPs on the monolayer. The use of the MPTMS tether has been reported to yield uniform, submonolayer coverage of gold nanoparticles while the APTES tether results in an aggregated submonolayer of gold NPs (Figure 2.11).[75,79] Alkanethiol SAMs can be used to control NP density via two approaches: the use of mixed SAMs and variations in NP exposure time. The use of a non-coordinating, diluent ligand in combination with a SAM capable of NP assembly

serves to both prevent NP aggregation and control the NP density.[69] Additionally, Chirea et al. were able to control the density of gold nanorods on alkanethiol SAMs by altering the length of time the SAM-modified electrode was exposed to the solution of gold nanorods.[143]

Similar to alkanethiol/amine SAM systems, molecular monolayers formed through grafting reactions have been shown to yield uniform submonolayers of NPs on their surface.[21,85] Using the NP ligand shell to directly graft NPs to electrodes or to bind them to a molecular monolayer through coupling chemistry has also been shown to yield an evenly dispersed submonolayer of nanoparticles on the electrode surface given that the NP cores are stable to the reaction conditions.[21,84,121] In studies that grafted alkenethiolate-AuNPs to silicon electrodes through hydrosilylation reactions, significant core growth and aggregation was observed when reactions were performed at higher temperatures where the NPs were destabilized.[121]

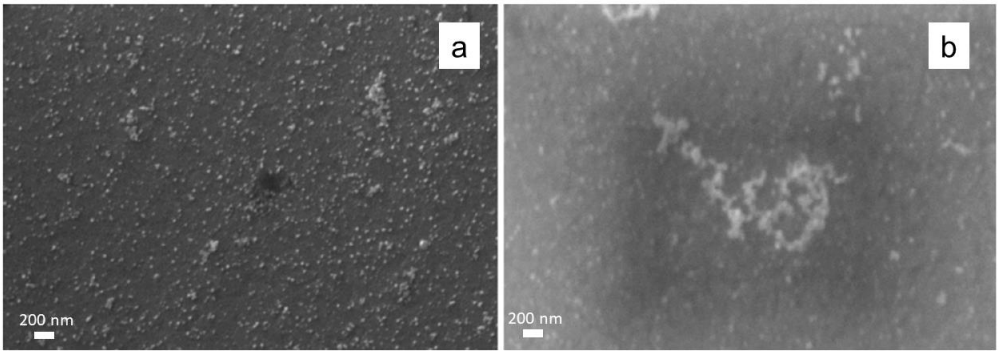

Figure 2.11. Scanning electron micrographs showing the differences in AuNP distribution on MPTMS (a) and APTES (b) modified ITO electrodes. Reprinted with permission from ref 72. Copyright 2008 Elsevier.

Electronic communication

When fabricating NP-functionalized electrodes for a given application, it is typically desirable that there not only be communication between the NP and the

electrode, but that this electron transfer is fast. Incorporating a molecular monolayer that separates the NP from the electrode substrate adds another barrier to electron transfer. Good electronic communication between the NP and the electrode may directly impact the sensitivity of amperometric sensors and the overpotential of electrocatalysts.[89,144–146] Additionally, for fundamental electron transfer studies, the observed rates of electron transfer should not be limited by the NP-electrode electron transfer step (unless that is what is being probed).[64] The electronic communication between a NP and the electrode surface is influenced by NP core size and the thickness/length and interior composition of the linker, which will be further discussed in the following sections.[75,79,90,101,123]

Studying NP-mediated electron transfer: solution phase vs surface bound redox probes. Regardless of application, understanding the NP-mediated electron transfer kinetics is important when investigating the electrochemical properties of NP-functionalized electrodes. When measuring the NP electrochemical activity, it is beneficial to be able to distinguish between the NP activity and that of the other system components, such as the underlying electrode substrate. Typically, redox probes are used to characterize the electronic properties of NP-functionalized electrodes. Redox probes can either be dissolved in the electrolyte solution, (solution phase probes), or directly bound to the NP surface, (surface bound probes). Although solution phase probes are most commonly used for characterization, they have some limitations. When using a solution phase probe, a dense, fully passivating molecular monolayer is required to ensure that any electrochemical response is NP-mediated and not a result of the probe interacting directly with the electrode material. These probes are appropriate when using thiol SAMs, MPTMS alkoxysilane SAMs, and electrochemical grafting methods that

suitably block the probe from approaching the electrode surface. APTES alkoxysilane SAMs and polyelectrolyte monolayers are known to enhance electron transfer between a solution phase redox probe and the electrode material, thus these probes are not suitable for studying NP-mediated charge transfer in these systems.[75,79,101] It is hypothesized that this enhancement is a result of the redox probe accumulating on the ionic surface of the monolayer, thus reducing diffusion limited electron transfer rates.

If the NP-electrode interface does not result in a fully passivated electrode, a NP-bound redox probe may be more appropriate to characterize NP-mediated electron transfer. When employing a NP-bound redox probe, there are a few considerations to be made. It is important that the probe only binds to the NP, not the underlying molecular interface or electrode substrate. The probe can either be bound directly to the NP core or through the NP ligand shell. In either case, the probe should not have an affinity for the electrode material. Furthermore, for fabrication methods that yield a sparse molecular monolayer that NPs are assembled onto, it is important that the redox probe cannot associate or bury itself into the molecular monolayer and come into direct contact with the electrode material which could result in measuring electron transfer that is not NP-mediated. This can be prevented through the incorporation of a hydrophobic/hydrophilic group within the redox probe that is not compatible with the relative hydrophobicity/hydrophilicity of the molecular monolayer. Unlike solution phase probes, appropriate surface bound probes may not be commercially available and may require synthesis. If the desired redox probe is synthetically accessible, and the chemical environment of the probe is taken into consideration, a surface bound probe is a great way to ensure any observed electrochemical activity is due to the NPs.

Redox probes have different mechanisms and rates of electron transfer. Solution phase probes can either undergo inner or outer sphere electron transfer, both of which are slower than electron transfer for surface bound redox probes. Liu et al. nicely demonstrated the importance of redox probe selection when studying NP-mediated electron transfer (Figure 2.12).[64] They looked at Au, Pt, and Pd NP-dithiol-gold electrode systems using both solution phase and surface bound redox probes. While minimal differences in electrochemical behavior were observed with the solution phase probe, differences in electrochemical behavior of both the NP core material and in SAM length were observed using a surface bound probe (Figure 2.12b). They concluded that the identity of the redox probe, solution versus surface bound, dictated the observed electrochemical behavior of these systems.

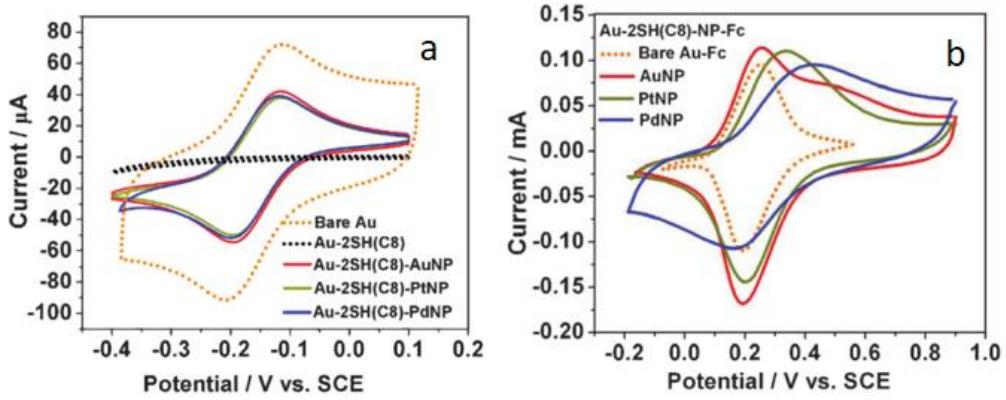

Figure 2.12. Cyclic voltammograms of a bare Au electrode, 1,8-dithiol-functionalized Au electrode and AuNPs, PdNPs and PtNPs assembled onto 1,8-dithiol-functionalized gold electrodes with a ruthenium hexamine solution phase redox probe (a) and a tethered ferrocenyl redox probe (b). The cyclic voltammograms in (a) versus (b) demonstrate how the observed electrochemical behavior is influenced by the type of redox probe used to study the system. Reprinted with permission from ref 61. Copyright 2013 WILEY-VCH.

Electron transfer efficiency. Prior to NP assembly, a molecularly functionalized electrode often impedes electronic communication between a redox probe and the

electrode surface. It has been well established that the addition of NPs to electrodes functionalized with an insulating molecular layer restores electronic communication between a solution phase redox probe and the electrode (Figure 2.12a).[64] Chazalviel and

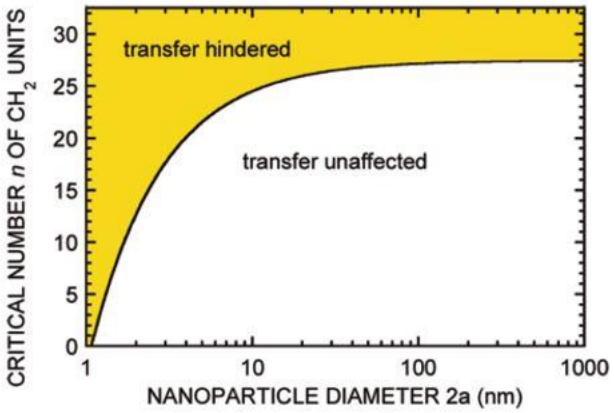

Figure 2.13. A theoretical relationship depicting the critical number *n* of CH_2 units above which a SAM coated with gold nanoparticles is expected to lead to a change in the voltammogram of a reversible redox system in solution (shaded area) as compared to that obtained on a bare gold electrode. Reprinted with permission from ref 120. Copyright 2011 American Chemical Society.

Allongue provided a theoretical framework explaining NP-mediated electron transfer through a molecular monolayer as a function of both the monolayer thickness and NP core size (Figure 2.13).[123] The rate of NP-mediated electron transfer across an insulating molecular monolayer is inversely proportional to the thickness/length of that monolayer. Barfidokht et al. provided the first experimental data to support this theory, showing the transition from thickness independent electron transfer kinetics to distance dependent kinetics using large AuNPs (d_{core} = 27 nm) assembled onto an electrochemically grafted poly(ethylenediamine) molecular monolayer.[90] Additionally, the effect of insulating molecular monolayer thickness/length on NP-mediated electron transfer may have greater impact for small NPs (d_{core} < 10 nm) than larger NPs.

It is important to take into consideration both the NP core size and linker length when designing a NP-functionalized electrode system with a defined molecular interface because of their potential impact on the overall electron transfer rates. Small NPs are of interest as active materials for many applications due to their unique electronic and structural properties compared to their larger counterparts. When small NPs are used, it is important to consider how those particles will interface with the electrode as to not unintentionally reduce NP-electrode electronic communication. For example, while the attachment of larger NPs through their ligand shell to a ligand-functionalized electrode has proven effective, the longer linker lengths associated with this method could hinder NP-mediated electron transfer when using small NPs. For applications where fast electron transfer is needed, methods that can incorporate shorter molecular linkers are beneficial to decrease the tunneling barrier. Another strategy to enhance the rate of electron transfer between the NP and electrode may be to use conjugated linkers. To incorporate conjugation or aromaticity into the molecular monolayer, either thiol SAMs or aryl diazonium electroreduction methods should be employed.

Flexibility in system design and tunability

For general use with many types of NPs and for different applications, it is desirable to have access to a number of different structures and/or have opportunities to manipulate the structure after fabrication in order to create more advanced materials. Such access affords the ability to vary the interface length/thickness, control over the density of NP coverage on the electrode surface, and incorporate additional functional ligands, metals, or nanoparticle layers onto the surface of the bound NP.

The length of the interface influences the electron transfer between the NP and the electrode as discussed above as well as the steric arrangement of the NPs on the surface. Consequently, for certain applications or studies, it is desirable to have the ability to vary this interface. For fabrication methods such as self-assembly of molecules such as thiols, amines, and silanes, or photochemically or thermally grafting alkenes onto electrode surfaces, there is no inherent limitation to the length of the molecular tether assuming it is stable and can be synthesized. The aryl diazonium grafting method is limited to an aryl group as the interface due to the inherent nature of the chemistry. Methods that utilize the ligand shell as part of the interface to the electrode will likely be limited to longer tethers since longer ligands are generally better at stabilizing the nanoparticle core.

The coverage of NPs on an electrode surface can influence the electrochemical properties as previously discussed making it desirable to have methods to control this variable. Assembly methods ultimately rely on the efficacy of ligand exchange with a surface bound ligand which is not always controllable. Some control over the coverage can be achieved by forming a mixed monolayer of a NP binding ligand and an inert, diluent ligand.[95] The use of efficient coupling chemistry like azide/alkyne click chemistry or directly binding nanoparticles to electrodes can make varying the coverage as a function of reaction time more reliable.[84,121]

In many cases, it is desirable to modify the NP surface after it is interfaced to an electrode to create new structures or compositions that would be challenging to synthesize otherwise. The addition of metals to a nanoparticle surface through methods such as underpotential deposition (UPD) which are typically selective for metallic surfaces such as noble metals, is a useful post-fabrication modification to create

multimetallic NP compositions (Figure 2.14a).[147,148] Since UPD can occur on metallic surfaces, the electrode must either be an inert material such as carbon or ITO, or it must be completely passivated. For biological applications, the addition of biomolecules such as enzymes or proteins to NP surfaces is often done after the initial electrode fabrication (Figure 2.14b).[115] Similarly, the electrode material should be inert towards the binding

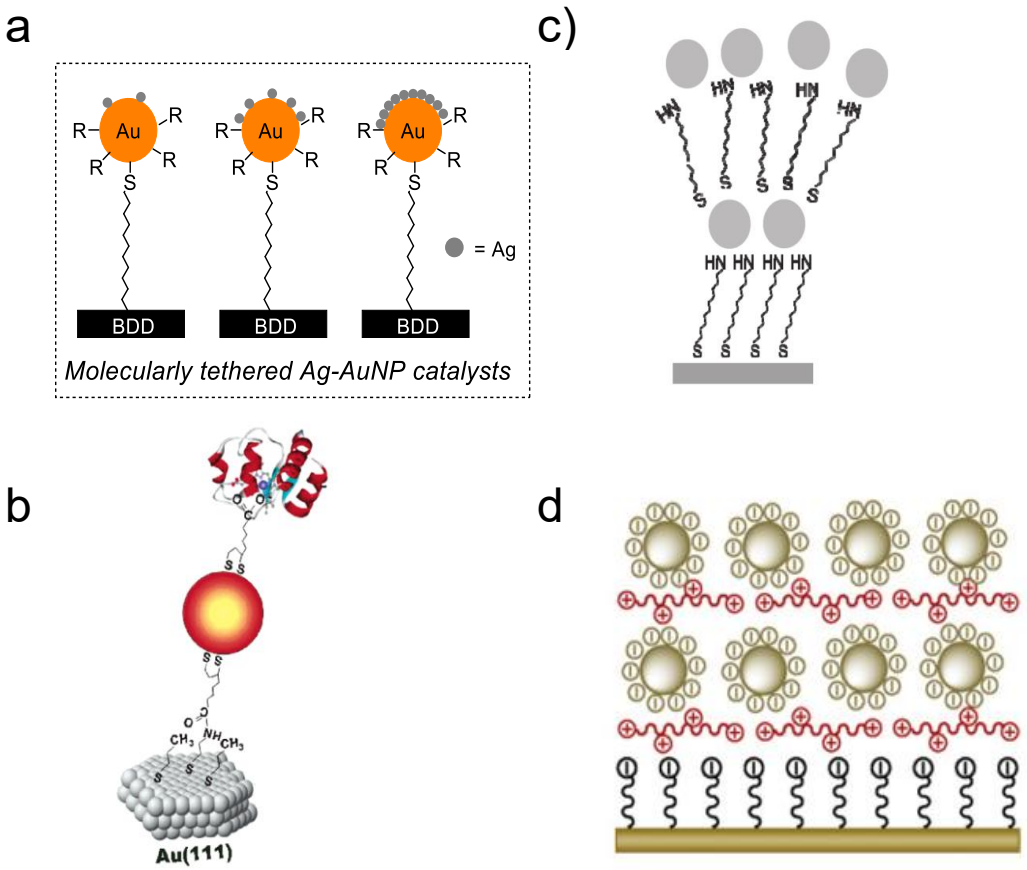

Figure 2.14. Depictions of post-fabrication manipulation of the NP-electrode structure and composition. (a) Post-modification of linked AuNPs with silver via galvanic exchange and/or underpotential deposition. Reprinted with permission from ref 148. (b) Schematic illustration of the molecular assembly of cyt *c*-NP hybrid structure on the Au(111) surface. Reprinted with permission from ref 115. Copyright 2007 American Chemical Society. (c) NP-multilayer architectures through layer-by-layer assembly using SAMs. Reprinted with permission from ref 68. Copyright 2009 American Chemical Society. (d) Multilayers of NPs formed using polyelectrolytes to electrostatically assemble ionically capped NPs. Adapted with permission from ref 104. Copyright 2012 Elsevier.

chemistry used to attach the biomolecule to the NP surface for it to occur selectively. Finally, molecularly linked multilayer nanoparticle structures are often desired to increase the overall surface area.

Multilayer structures are typically constructed in a layer by layer approach where an initial monolayer of NPs is attached to the electrode and then functionalized with a ligand that can facilitate an additional NP monolayer, and this process is continued iteratively (Figure 2.14c, d).[68,104] As with the previous modifications discussed, it is desirable that the binding chemistry used to form the nanoparticle multilayers is selective for the nanoparticle surface. For example, the use of dithiols to link multiple layers of AuNPs together while supported on a planar Au electrode could lead to complications unless the planar Au electrode is completely passivated. The ordering of the nanoparticles on the surface can also influence the quality of the resulting multilayer structures. It is known that longer chain SAMs on metallic electrodes are more dense and ordered than monolayers formed through grafting methods.[136] The uniformity and density of the initial monolayer should be considered when looking to create nanoparticle multilayer structures.

Outlook

Advances in the synthesis and characterization of nanomaterials, as well as the development of more efficient reaction chemistry, have provided the opportunity to design nanomaterial-functionalized electrodes with a greater degree of control over the system attributes. As this field continues to develop, there are several areas that will be important. While much of the work so far has been focused on tethering noble metal NPs or semiconductor quantum dots, there is interest in investigating more earth abundant

materials for applications such as electrocatalysis and photochemical energy conversion. Development of new tethering chemistries to couple materials such as metal oxide nanoparticles to electrodes while maintaining efficient electronic communication will be a next step in the field as precision syntheses of these materials are being established.[149]

While tethering NPs to an electrode through a molecular interface produces a defined structure which enables more precise and rigorous studies of these materials, it remains to be determined if this approach leads to significant improvements in practical electrochemical applications. Very few studies that directly compare electrodes with molecularly tethered NPs to deposited NPs have been reported. Improved electrochemical properties such as faster electron transfer and higher electrochemically active surface areas have been observed when comparing electrodes with molecularly tethered NPs to deposited NPs,[21] which suggests that defining the NP-electrode interface helps improve these materials, however more studies directly comparing the two approaches need to be done to understand the role of this interface on desired properties for applications.

While synthetic techniques to create advanced nanomaterials are being developed, another opportunity to access these structures is through modification of nanomaterials after attachment to electrode surfaces. Methods such as underpotential deposition, galvanic exchange, and anti-galvanic reduction that have previously been studied extensively with planar electrode surfaces are beginning to be used to modify NP surfaces to create multimetallic NPs.[147,150,151] This approach allows for the quick screening of different elemental compositions and potential access to nanomaterials that may be challenging to synthesize through traditional synthetic methods. Another

approach to access nanomaterials that are challenging to synthesize through traditional batch chemistry methods is the electrodeposition of nanomaterials onto a molecularly functionalized electrode. While traditional electrodeposition syntheses of NPs onto unfunctionalized electrodes can suffer from disperse core sizes and an ill-defined interface, deposition onto a molecular monolayer could provide more control over these variables. Currently, this method is mostly used to produce noble metal nanomaterials such as AuNPs[85,152] and bimetallic Ag/AuNPs.[153] By modifying existing methods that yield a defined NP-electrode interface for the electrodeposition of other nanomaterials, a new class of nanomaterials could be more precisely synthesized and studied for their electrochemical properties.

In addition to creating new nanomaterials, methods to precisely control the coverage of nanoparticles on an electrode surface will be important. The loading of a nanomaterial on an electrode substrate has been observed to influence product selectivity for electrocatalytic reactions.[19,20] By increasing the NP coverage, the probability of reaction intermediates to diffuse to a neighboring nanoparticle and be further transformed is also increased. Incorporating multiple types of NPs on the surface can be a strategy to efficiently access products that would be challenging to produce with a single catalyst. Improved methods to precisely control the nanomaterial coverage and construct mixed nanoparticle surfaces will be useful as more efficient and selective catalysts for complex reactions such as carbon dioxide electroreduction are being developed. Beyond use of only NP(s) in the electrochemical processes, design of hybrid and nanocomposite systems that can take advantage of the functionality of the NP ligand shell and the molecular

functionalization on the surface is another approach that will become more possible as this field advances.

As these synthetic and electrode fabrication methods are employed, more sophisticated analytical techniques will also be needed to continue to inform design of these materials. *In operando* x-ray techniques such as absorption spectroscopy,[154] scattering/diffraction,[155] and pair distribution function analysis[156] are helping identify catalytically active sites and structural changes in materials during electrochemistry which may not be apparent during standard *ex situ* measurements. Ambient pressure x-ray photoelectron spectroscopy is allowing the surfaces of materials to be observed in their operating conditions which is important for materials where typical ultra-high vacuum conditions may alter their surface chemistry.[157] Electron microscopy techniques will also be useful in assessing the nanoparticle structure. As liquid transmission electron microscopy (TEM) cells are becoming more available, electrochemical TEM measurements are being used to visualize the structure of battery materials in operando.[158] Through functionalization of a TEM electrode with a molecular tether that can bind NPs, multi-modal analysis can be performed for NP-functionalized electrodes.

The future is promising for the field of NP-functionalized electrodes. Significant progress has been made over the past forty years since the field of chemically modifying electrodes emerged. Through the incredible advancement of precision nanomaterial synthesis, development of tethering chemistries, understanding of electronic processes, and advancement of multi-modal analytical techniques, this interdisciplinary effort has provided opportunities to create materials that will make an important impact on the technological needs of society.

Bridge to Chapter III

Chapter II reviewed existing methods to fabricate nanoparticle-functionalized electrodes with a defined molecular interface. We discussed the resulting electrochemical behavior of each fabrication method in reference to four universal attributes: stability, uniformity, electronic communication and tunability. From this literature review it is clear that existing methods have focused on the attachment of large nanoparticles. However, previous research has suggested that small nanoparticles, $d_{core} < 2$ nm, offer enhanced catalytic activity and are therefore promising candidates for electrocatalytic applications. Due to the unique electronic properties that arise at smaller core sizes, establishing efficient electronic communication between small nanoparticles and an electrode substrate can be difficult.

Chapter III describes two new approaches to attaching small gold nanoparticles to an electrode substrate using a molecular linker. The electrochemical behavior of this new system is compared to solution depositions methods used to fabricate nanoparticle-functionalized electrodes with the same nanoparticles. Using a tethered redox probe, this research demonstrates the enhanced electrochemical behavior achieved when using a molecular linker to tether nanoparticles to an electrode. In addition, we observed that the electrochemically active surface area of the gold nanoparticles is greater in the molecularly tethered system. This platform provides another fabrication method that can be easily tuned to tether nanoparticles of varying core compositions to electrode substrates.

CHAPTER III

SMALL GOLD NANOPARTICLES INTERFACED TO ELECTRODES THROUGH MOLECULAR LINKERS: A PLATFORM TO ENHANCE ELECTRON TRANSFER AND INCREASE ELECTROCHEMICALLY ACTIVE SURFACE AREA

Note: Reproduced with permission from Young, S. L.; Kellon, J. E.; Hutchison, J. E. This chapter was published previously in the following citation: Young, S. L.; Kellon, J. E.; Hutchison, J. E. Small Gold Nanoparticles Interfaced to Electrodes Through Molecular Linkers: A Platform to Enhance Electron Transfer and Increase Electrochemically Active Surface Area. *J. Am. Chem. Soc.* **2016**, *138* (42), 13975-13984.

Introduction

Nanoparticles (NPs) have been employed in a wide range of applications including sensing[1,2], energy storage and conversion[3,4], catalysis[5], and electrochemical applications[6] due to their core size dependent properties and high surface area to volume ratio. NPs can impart chemical reactivity to otherwise inert, but abundant, materials and dramatically increase the surface area available for chemical transformations while minimizing the use of the active, often precious, metals.[7–9]

Nanoparticle-functionalized electrodes have been studied for electrochemical applications such as amperometric sensing,[10,11] photocatalysis,[12] and electrocatalysis.[4,13] In electrochemical applications, the addition of nanoparticles to an electrode surface

enhances the electrode's catalytic activity[4-8] and can promote electron transfer through otherwise insulating molecules.[14,15] The enhanced electrochemical properties of NP-functionalized electrodes have been attributed to the NP's electronic structure,[16] surface chemistry,[17] crystal facets,[18–21] density on the electrode surface,[22] as well as the interface between the NP and the support.[23–26]

A number of studies have attempted to correlate the electrochemical and/or electrocatalytic properties of NPs with nanoparticle composition and structure in the context of NP-functionalized electrodes.[13,16,18,27–29] These electrodes are often made by physical deposition methods such as vacuum evaporation or electrodeposition.[30–32] The structures of the NPs and their interfaces with the electrode are difficult to characterize, making it challenging to attribute observed electrochemical properties to specific structures. Such deposition methods also make it hard to control the resulting NP core size distribution or coverage on the electrode. In order to understand the electrochemical properties of specific nanoparticle structures, it is necessary to fabricate NP-functionalized electrodes with uniform NP core sizes, known surface chemistry, and a defined interface between the NP and the electrode support.

The solution deposition of preformed nanoparticles on electrodes is an alternative strategy to fabricate NP-functionalized electrodes that can help overcome the limitations of size control found in other deposition methods. The use of preformed NPs allows for more rigorous characterization of the NPs since solution-state characterization techniques are available in addition to solid-state techniques.[33] In addition, bonding such NPs to an electrode might be useful to control the NP-electrode interface. Several methods to deposit (or attach) ligand-stabilized NPs on electrode materials are presented in Scheme

3.1. The simplest approaches involve solution deposition techniques (e.g., drop-casting, spin-coating, dip-coating) to modify the electrode surface with preformed NPs, or mixing nanoparticles with a support material (i.e. carbon black) which is then fabricated into an electrode.[18,27] While these methods are admittedly convenient, there are several drawbacks making it difficult to directly relate NP morphology to observed electrochemical behavior. Solution deposition methods offer limited control of the NP surface coverage, the NP-electrode interface and/or interactions between the NPs, all of which influence electrochemical properties. NP coverage and attachment on electrodes prepared through solution deposition methods can also be sensitive to surface pretreatment steps. These pretreatment steps are not always easily identifiable and consequently, it is often challenging to reproduce reported results. NPs adhered to the electrode through weak Van der Waals forces may also desorb over time.[34]

To preserve the core size of preformed nanoparticles during deposition, a stabilizing ligand shell is required, typically composed of electrically insulating ligands. This can pose a barrier to electron transfer throughout the NP-functionalized electrode if efforts are not made to provide an electron-tunneling pathway. Two common ways to enhance electron transfer are to form bonds between the ligands and electrode surface or other NPs in the film, or to remove the ligands through thermal or chemical treatments. Such treatments can result in growth or destabilization of the NP core.[35–37]

A strategy to improve the NP-electrode interface while retaining NP morphology is to attach NPs to an electrode via a molecular monolayer, as shown in Scheme 3.1. These approaches provide a molecular interface between the NP and the electrode material and allow for more control over interactions between NPs while retaining the

core size control offered by use of preformed NPs. It has been shown that electron transfer from a redox probe to an electrode through a NP-molecular monolayer-electrode assemblies only occurs if the NP is bound to the monolayer through electrostatic or covalent interactions.[34] When AuNPs were solution deposited on methyl-terminated self-assembled monolayers, no faradaic current was observed between the NP and a solution-phase redox probe. Proximity to the surface alone does not seem sufficient to promote NP-mediated electron transfer. Two covalent attachment strategies are shown in Scheme 3.1. In the first, the NP ligand shell is used to graft the NP directly to the electrode through a functional group known to interact strongly with the electrode material (denoted X in Scheme 3.1). In the second case, NPs can be assembled onto chemically modified electrodes through ligand exchange with a functional group known to bind to the NP surface (denoted Y in Scheme 3.1). Each approach results in a defined interface for efficient electron transfer and should prevent NP desorption from the electrode surface compared to NPs that are non-specifically adsorbed.

Scheme 3.1. Methods of attaching preformed, ligand-stabilized nanoparticles to electrode substrates.

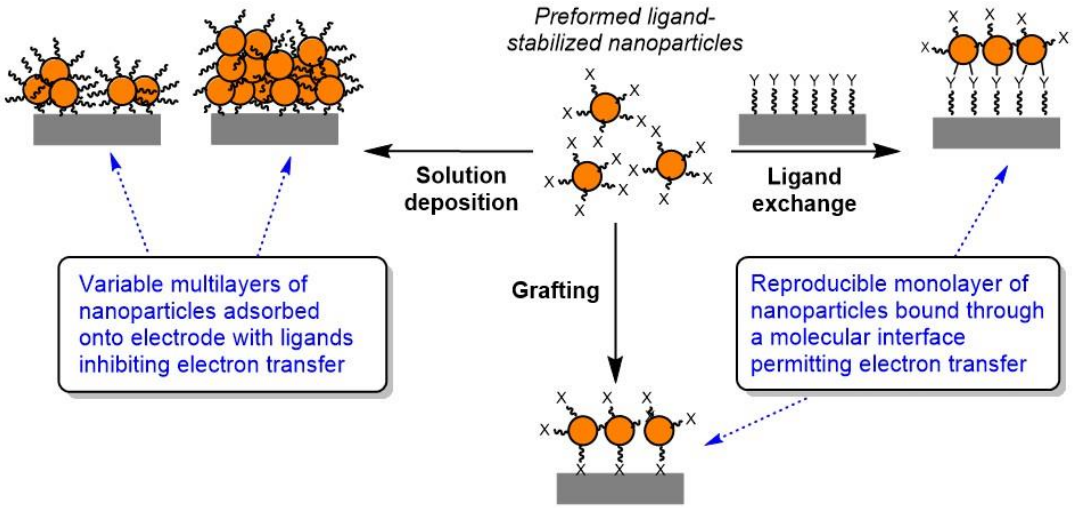

The assembly of nanoparticles onto a molecular monolayer has been demonstrated for larger (core diameter >10 nm) citrate-stabilized AuNPs. These AuNPs have been assembled on molecular monolayers on planar Au, [15,38–40] glassy carbon,[14,41,42] silicon, [43] and boron doped diamond. [44,45] However, the AuNP attachment chemistry can be sensitive to pH (e.g., AuNPs assembled through Au-amine bonds) and have limited electrochemical windows (e.g., thiol monolayer desorption from planar Au at cathodic potentials in alkaline conditions [46,47]). In some cases, the electrode supports are unstable in aqueous electrolytes (e.g., silicon) limiting their general use in electrochemical applications. The use of gold electrodes makes it difficult to characterize AuNPs and to distinguish the electrochemical properties of the AuNP from those of un-passivated areas of the electrode. Some methods used to functionalize other electrode supports, particularly for carbon electrodes, have been reported to yield linkers of non-uniform thicknesses, leading to uncertainty about the NP-electrode interface.[14,48] In addition, some electrode supports used have variable microstructure (e.g., glassy carbon[49]) that can result in irreproducible electrochemical responses. The challenges in controlling the NP-electrode interface, as well as the limited stability of these systems under electrochemical conditions, mean that these platforms are not ideal for general electrochemical study of NPs, particularly small NPs that are already more challenging to characterize.

Small NPs (d_{core} < 2.5 nm) are reported to have unique electronic and catalytic properties.[16,27,50] Small changes in NP size and surface chemistry in this regime can significantly affect these properties,[51] warranting the further investigation of NPs of uniform size, well-established surface chemistry, and a defined interface between the NP and the electrode. Murray and co-workers reported the few existing studies of small

AuNPs (d_{core} = 1.6 nm) stabilized by a mixed hexanethiolate/mercaptoundecanoic acid ligand shell adhered to a planar Au electrode through Zn^{2+}/carboxylate bridges.[52] In this system, it was challenging to avoid the formation of Zn^{2+}/carboxylate bridges between ligand shells of neighboring NPs, which would influence the electrochemical properties. Furthermore, the instability of the system under acidic conditions limits the ability for use in acidic electrolytes. In order to further understanding of NP-mediated electron transfer and electrocatalytic properties of NPs in this small size regime, a robust, versatile platform that allows for small, uniform NPs to be attached to an electrode through molecular monolayers is needed.

Herein, two approaches to interface small AuNPs ($d_{core} \leq 2.5$ nm) to boron doped diamond electrodes through molecular linkers have been developed and compared. These interfaces allow for control over NP morphology while providing a molecular pathway for electron transfer. In one approach, AuNPs are directly grafted to the electrode surface using the NP ligand shell as the covalently bound molecular linker. A second approach involves ligand exchange to link AuNPs to a molecular monolayer covalently bound to the electrode surface. The efficiency of the NP attachment chemistry was studied, showing that both methods yield monolayer coverage and that NP core size is not affected during the grafting and assembly processes. AuNPs with different core sizes and ligand shells were successfully assembled demonstrating the versatility of the platform. Using a redox probe tethered to the NP surface, the electrochemical properties of the different molecularly tethered AuNP systems were compared to one another and to those prepared by drop-casting AuNP films and depositing a AuNP monolayer formed at the air-water interface. The studies represent the first direct comparison of the

electrochemical properties of small (< 2.5 nm diameter) AuNPs as a function of their core size, ligand shell, and interface to an electrode support.

Experimental

Materials and characterization

Water (18.2 MΩ·cm) was obtained from a Barnstead Nanopure Diamond system. Chloroform was filtered through basic alumina before use with nanoparticles to remove any acidic impurities. All other reagents were used as received without further purification. Hydrogen tetrachloroaurate was obtained from Strem Chemicals. S-(10-undecenyl)-1-thioacetate was received from Sigma Aldrich. Electrochemical grade free-standing boron doped diamond (BDD) substrates (Element Six, 1 cm x 1 cm) were used for all experiments.

Nuclear magnetic resonance spectroscopy (^{1}H NMR) spectra were collected on a Varian Inova 300 MHz NMR to verify material purity. Ultraviolet-visible spectroscopy (UV-Vis) spectra were collected using an Ocean Optics USB2000 spectrometer and samples were measured in a quartz cuvette (1 cm path length). Small angle x-ray scattering (SAXS) patterns were collected on an Anton Paar SAXSess mc^2 instrument operating in line collimation mode. The samples were measured in an epoxy sealed quartz capillary (Charles Supper) and were exposed to a monochromated x-ray source (Cu Kα, 1.54Å) operating at 40 kV and 50 mA. Data were collected by averaging 50 scans of 5-20 second exposures. Scattered x-ray intensity was measured with a charge-coupled device (CCD) detector (Roper Scientific). Data were desmeared using the Anton Paar SAXSquant software to produce scattering patterns and were imported into the Irena macro within IGOR Pro for modeling.[53] Models were fit to the scattering patterns using a

Gaussian distribution, spherical form factor, and a dilute structure factor to determine the core size distribution of the AuNPs. All reported size distributions came from the Modeling II macro within Irena. Transmission electron microscopy (TEM) images were acquired on a FEI Titan 80-300 TEM. Samples were prepared by drop-casting a dilute solution of the nanoparticles on a lacey carbon coated copper TEM grid (Ted Pella).

X-ray photoelectron spectroscopy (XPS) was performed on a ThermoScientific ESCALAB 250 X-ray Photoelectron Spectrometer using an Al Kα monochromated source (150 W, 20 eV pass energy, 500 μm spot size). The spectra were analyzed using a Smart background and were calibrated to the C1s hydrocarbon peak (284.8 eV). Peak fitting was done using ThermoScientific Avantage 4.75 software. Scanning electron microscopy (SEM) images were collected on a Zeiss Ultra-55 Scanning Electron Microscope using a secondary electron detector at an accelerating voltage of 25 kV.

Cyclic voltammograms were collected using a BAS 100B Electrochemical Analyzer (Bioanalytical Systems). Ag|AgCl (3 M NaCl) reference electrodes and a platinum wire counter electrode (Bioanalytical Systems) were used for all measurements. The geometric surface area of the working electrode was defined using a Viton o-ring (0.6 cm inner diameter) in a custom glass electrochemical cell. Electrical contact to the BDD electrodes was made through a back contact with silver paint and copper wire.

Synthesis and characterization of gold nanoparticles

Undecenethiolate-stabilized gold nanoparticles (UDT-AuNPs) were synthesized following a modified two-phase Brust preparation.[54] $Au_{101}(PPh_3)_{21}Cl_5$ (TPP-Au_{101}) and $Au_{11}(PPh_3)_8Cl_3$ (TPP-Au_{11}) were synthesized using previously reported methods.[51,55]

Nanoparticles were characterized using ^{1}H NMR, UV-Vis spectroscopy, SAXS, and TEM.

Direct functionalization of boron doped diamond with UDT-AuNPs

Boron doped diamond (BDD) substrates were cleaned with aqua regia and piranha solution before hydrogen termination. Hydrogen termination, which was necessary for photochemical grafting, was performed in a tube furnace with flowing H_2 in a quartz tube under conditions reported to produce hydrogen terminated diamond surfaces.[56] The BDD was heated to 850° C and held at that temperature for 20 minutes before cooling back down to room temperature under H_2. Contact angle goniometry was used to verify that the thermal treatment effectively hydrogen terminated the BDD surface. The contact angle increased from 40° to 70° after hydrogen termination, indicating an increased hydrophobicity of the BDD. The sharpening of the peak at 284.8 eV in the x-ray photoelectron spectroscopy (XPS) C1s spectrum, attributed to C-H bonds, and the disappearance of the oxidized carbon shoulder at ~288.6 eV indicated that the BDD was successfully hydrogen terminated (Figure A1).

The procedure for photochemical grafting was adapted from Hamers and co-workers.[57,58] To graft the UDT-AuNPs to BDD (**Graft-UDT-AuNP**), a solution of UDT-AuNPs in heptane was sparged with argon to remove oxygen. The concentration of the nanoparticle solution, measured using the absorbance of the solution at 500 nm, was ~0.2 absorbance units. A hydrogen terminated BDD substrate was submerged in ~1 mL of the nanoparticle solution in a 10 mL beaker and irradiated through a quartz window with a UVP UVGL-58 Handheld UV lamp (254 nm, ~1 mW/cm^2) for 7 hours in an argon filled chamber. Photochemical grafting was performed in an argon filled chamber to minimize

ozone generation during irradiation. The substrate was rinsed extensively with dichloromethane and hexanes to yield the UDT-AuNP- functionalized BDD substrate (**Graft-UDT-AuNP)**.

Assembly of triphenylphosphine gold nanoparticles onto undecyl thioaceate modified BDD (UDTA-BDD).

Functionalization of boron doped diamond using S-10-(undecenyl) thioacetate. An undecyl thioacetate monolayer was formed on BDD by photochemically grafting S-10-(undecenyl) thioacetate to BDD using a procedure adapted from Hamers and co-workers.[57,58] Neat S-10-(undecenyl) thioacetate (~2 μL) was placed on a hydrogen terminated BDD substrate and sandwiched between a quartz slide to produce a film on the BDD substrate. This sample was irradiated at 254 nm for 5 hours under argon in a Novascan PSD Pro Series Digital UV Ozone System. The substrate was removed and sonicated in 30 mL chloroform (2 x 5 min) followed by sonication in toluene (2 x 5 min) to remove any physiadsorbed thioacetate to yield **UDTA-BDD**.

*Assembly of TPP-Au_{101} on UDTA-BDD (**TPP-Au_{101}-UDT**).* **UDTA-BDD** was submerged in a solution of TPP-Au_{101} in tetrahydrofuran (0.1 mg/mL). The solution was sparged with N_2 and kept under N_2 overnight to assemble the nanoparticles on the monolayer through ligand exchange. The sample was removed and vigorously shaken in dichloromethane for one minute (3x) to remove physiadsorbed TPP-Au_{101} and $AuClPPh_3$ from the ligand exchange.

*Assembly of TPP-Au_{11} on undecanethiol-functionalized BDD (**TPP-Au_{11}-UDT**).* Before assembly of TPP-Au_{11}, the thioacetate group on **UDTA-BDD** was deprotected to yield a thiol-functionalized surface. A mixture of K_2CO_3 (0.3 g, 2.2 mmol) in N_2-sparged

methanol (20 mL) was stirred for 10 minutes. **UDTA-BDD** was submerged in the mixture for 2 hours and kept under N_2 to prevent disulfide formation. HCl (10 mL, 0.2 M, N_2 sparged) was then added to the mixture to yield the deprotected undecanethiol-functionalized BDD (**UDT-BDD). UDT-BDD** was removed and rinsed with dichloromethane. **UDT-BDD** was then submerged in a solution of N_2-sparged TPP-Au_{11} in basic chloroform (0.1 mg/mL). The solution was heated to 55°C under N_2 and left to react overnight, conditions that have previously been used for ligand exchange of TPP-Au_{11}.[59] The sample was removed and vigorously rinsed in dichloromethane for one minute (3x) to remove physiadsorbed TPP-Au_{11} and free triphenylphosphine ligand from the ligand exchange.

Binding the redox probe 6-ferrocenyl(carbonyloxy)hexanethiol (FcCO$_2$HT) to the AuNP surface

The redox probe 6-ferrocenyl(carbonyloxy)hexanethiol (FcCO$_2$HT) was synthesized based on a method previously reported (details in the supporting information).[60] The **Graft-UDT-AuNP** electrodes were treated with ozone (50 ppm in N_2) for five minutes, followed by a ten minute soak in H_2O. This treatment is known to remove a portion of the thiolate ligand shell.[61] The sample was soaked in 1 mM FcCO$_2$HT (in dichloromethane) to assemble the redox probe on the open sites on the NP, followed by extensive rinses with dichloromethane and acetonitrile to remove non-specifically bound FcCO$_2$HT from the surface. The **TPP-Au$_x$-UDT** samples were soaked in 1 mM FcCO$_2$HT (in dichloromethane) to exchange some of the triphenylphosphine ligands for FcCO$_2$HT, followed by extensive rinses with dichloromethane to remove any unbound FcCO$_2$HT.

Deposition of monolayer films of AuNPs formed by self-assembly at the air-water interface onto BDD

A 10 mL beaker was filled with H_2O and the water surface was coated with a solution of NPs dispersed in dichloromethane. Once the dichloromethane had evaporated, the resulting monolayer of NPs was transferred to a bare BDD electrode by placing the BDD substrate on top of the NP monolayer at the air-water interface.

Results and Discussion

The aim of this study was to evaluate the electrochemical properties of small, uniform ligand-stabilized AuNPs at a molecularly defined electrode interface and to evaluate the role of the interface and core size on those properties. A NP-functionalized electrode possessing a monolayer of evenly distributed NPs bound through a well-defined interface that also retain their initial core size once assembled on the surface was required for this study. Boron doped diamond (BDD) was chosen as an electrode support because it is a robust material that is electrically conductive, stable in most common electrolytes, relatively inert towards most electrocatalytic transformations, and has a wide electrochemical window.[62] Furthermore, molecular monolayers can be generated through the photochemical grafting of alkenes to form covalent C-C bonds between the BDD and the grafted molecule.[57,58] Small ligand-stabilized AuNPs ($d_{core} \leq 2.5$ nm) were chosen as a model system to assemble due to their interesting electronic and catalytic properties and since well-established synthetic methods that afford both a narrow core size distribution and defined surface chemistry exist.

Scheme 3.2 outlines two routes used to obtain AuNPs bound through an undecanethiolate tether to a hydrogen terminated BDD substrate.[58] In Route 1, preformed undecenethiolate AuNPs (UDT-AuNPs) are covalently attached to the BDD through direct photochemical grafting of their ligand shell to the substrate (**Graft-UDT-AuNP**). This is a direct, single-step approach to attach synthetically accessible and stable alkene-modified AuNPs. In Route 2, two different core sizes of preformed triphenylphosphine-stabilized AuNPs (d_{core} = 0.8 nm and 1.9 nm) are assembled via ligand exchange onto an undecyl thioacetate-functionalized molecular monolayer covalently bound to BDD (**UDTA-BDD**). The thioacetate protecting group prevents disulfide formation and other undesired thiol-alkene reactions during the initial photochemical grafting of the linker to the substrate. The thioacetate group is easily deprotected to the free thiol prior to AuNP assembly, if needed. Triphenylphosphine AuNPs were used since they are known to readily undergo ligand exchange reactions with thiols.[59,63,64] An undecyl thioacetate monolayer was used to maintain a constant linker length across all three systems studied, allowing for direct comparisons to be made. The assembly approach provides a method

Scheme 3.2. Two strategies to prepare AuNP-functionalized electrodes with a molecular nanoparticle-electrode interface.

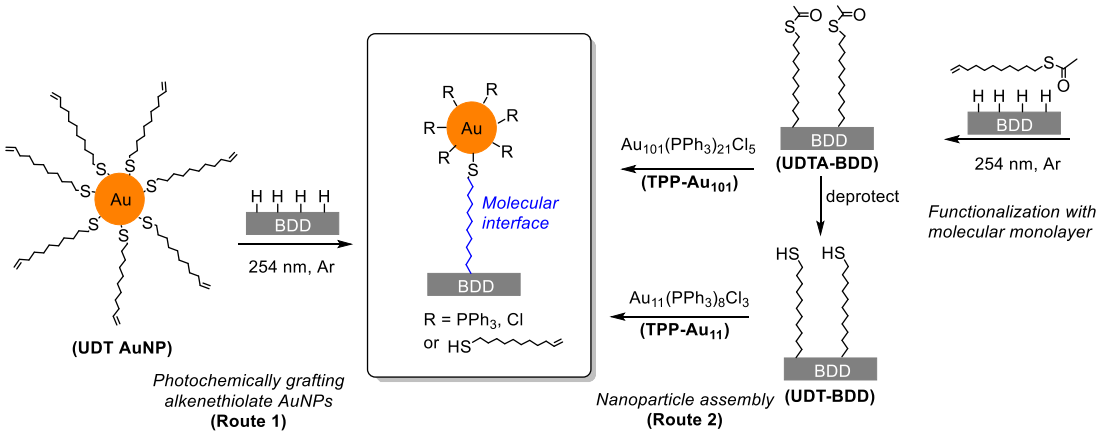

when shorter molecular linkers are desired, and/or when NPs of a desired core material/size cannot be synthesized with terminal alkenes in their ligand shell.

Synthesis and characterization of ligand-stabilized AuNPs for attachment

Undecenethiolate-stabilized AuNPs (UDT-AuNPs) were synthesized as previously reported and purified by sequential precipitations.[54] ^{1}H NMR verified that purification removed any free ligand or phase transfer catalyst (Figure A2). The UDT-AuNPs were found to be 2.1 ± 0.1 nm by small angle x-ray scattering (SAXS) and transmission electron microscopy (TEM) (Figure A3). The absence of a plasmon peak in the UV-Vis spectrum is consistent with this size (Figure A4).

Two types of triphenylphosphine-stabilized AuNPs (TPP-Au_x) were synthesized for use in ligand exchange reactions with the molecular monolayer. $Au_{101}(PPh_3)_{21}Cl_5$ (TPP-Au_{101}) was synthesized as previously reported.[55] The core size of TPP-Au_{101} was determined to be 1.9 ± 0.5 nm by SAXS, and was corroborated by TEM and UV-Vis (Figure A5, A6). $Au_{11}(PPh_3)_8Cl_3$ (TPP-Au_{11}) was synthesized by reduction of $AuClPPh_3$ with $NaBH_4$.[51] ^{1}H NMR and UV-Vis of TPP-Au_{11} confirmed that only $Au_{11}(PPh_3)_8Cl_3$ (d_{core} = 0.8 nm) was synthesized and not a mixture of $Au_{11}(PPh_3)_8Cl_3$ and the less stable form $Au_{11}(PPh_3)_7Cl_3$ (Figure A7, A8).[51] The core size of TPP-Au_{11} was determined to be 0.8 ± 0.2 nm by TEM (N = 530) (Figure A9).

Building the AuNP-molecular monolayer-BDD platform

*Route 1: Photochemically grafting undecenethiolate AuNPs to BDD (**Graft-UDT-AuNP**).* UDT-AuNPs were grafted to BDD upon irradiation of BDD in a dilute heptane solution of UDT-AuNPs at 254 nm under argon. X-ray photoelectron spectroscopy (XPS) of **Graft-UDT-AuNP** was performed to determine if the UDT-AuNPs were altered by

the grafting process (Figure A10). The elemental $Au_{84.5}$:$S_{162.5}$ ratio was used to compare the thiolate ligand shell before and after the grafting process, since 162.5 eV is the characteristic binding energy of a thiol. There was minimal change in the $Au_{84.5}$:$S_{162.5}$ ratio when the UDT-AuNPs are grafted versus when they were simply drop-cast onto a BDD substrate (Table 3.1) indicating the integrity of the ligand shell of the UDT-AuNPs is maintained throughout the grafting process. The difference in $Au_{84.5}$:$S_{162.5}$ ratios between the two samples can be explained by ozone generated in the grafting chamber from trace oxygen resulting in the oxidation of a small amount of the thiolate ligands in the **Graft-UDT-AuNP** sample.

A control experiment was performed to assess if the XPS Au4f signal was due to grafting UDT-AuNPs or simply AuNP physiadsorption to the BDD surface. A bare BDD substrate was treated in the same way as the **Graft-UDT-AuNP** samples except that it was not irradiated by 254 nm light. The $Au_{84.5}$:$C_{284.8}$ ratio obtained via XPS was used to compare AuNP surface coverage over the BDD substrate. The $Au_{84.5}$:$C_{284.8}$ ratio underestimates the true coverage since the C1s peak at 284.8 eV originates from both the BDD substrate as well as the alkenethiolate ligand shell. The **Graft-UDT-AuNP** sample has roughly an order of magnitude higher $Au_{84.5}$:$C_{284.8}$ ratio compared to the sample that was not irradiated (Table 3.1). This suggests that the majority of the Au4f XPS signal is not a result of physiadsorbed AuNPs, and that the UDT-AuNPs were successfully grafted to BDD.

Route 2: TPP-Au_x NP assembly onto undecanethiolate monolayers on BDD

Before AuNP assembly, an undecyl thioacetate molecular monolayer was grafted to BDD by irradiation at 254 nm under argon to produce **UDTA-BDD** as shown in Scheme 3.2.

XPS was used to evaluate the efficacy of the photochemical grafting method in forming an undecyl thioacetate monolayer on BDD. The S2p region of the XPS of **UDTA-BDD** showed a peak at 164.2 eV, characteristic of a thioacetate group (Figure A11). A control experiment was performed where a hydrogen terminated BDD (H-BDD) substrate was exposed to 10-undecene-1-thioacetate in the dark. The grafted **UDTA-BDD** and the control sample were compared with XPS using the $S_{164.2}$:$C_{284.8}$ elemental ratios as a metric to evaluate the extent of thioacetate grafting. The grafted thioacetate yielded a $S_{164.2}$:$C_{284.8}$ ratio of 0.023 ± 0.007 (determined from averaging four samples) while the control sample only had a $S_{164.2}$:$C_{284.8}$ ratio of 0.002. This verifies the efficacy of the photochemical grafting and confirms that the thioacetate signal observed in **UDTA-BDD** is due to primarily to grafting, not physiadsorption to the BDD surface.

Table 3.1. Comparison of elemental ratios of UDT-AuNPs on BDD by XPS

Sample	$Au_{84.5}$:$S_{162.5}$	$Au_{84.5}$:$C_{284.8}$
Drop-cast sample [a]	2.9 ± 0.1 [b]	-
Graft-UDT-AuNP	3.4 ± 0.2 [b]	0.12 ± 0.02 [b]
Control sample, no UV [c]	3.3 ± 0.1 [d]	0.020 ± 0.002 [d]

[a] Sample prepared by drop-casting UDT-AuNPs onto BDD substrate
[b] Average of two samples, three spots analyzed per sample
[c] Sample exposed to all grafting conditions except irradiation by 254 nm light
[d] Average of three spots on one sample

Cyclic voltammetry was used to assess the extent of BDD passivation. The **UDTA-BDD** electrode showed an 87% decrease in capacitive current and significant suppression of oxygen reduction current compared to the H-BDD electrode (Figure A12).

Ligand exchanges reactions were used to tether TPP-Au_{101} to **UDTA-BDD**. The $Au_{84.5}$:$C_{284.8}$ elemental ratios from XPS were used to compare AuNP surface coverage between samples. When **UDTA-BDD** was exposed to TPP-Au_{101}, XPS yielded a $Au_{84.5}$:$C_{284.8}$ ratio of 0.15 ± 0.07 whereas a bare BDD substrate exposed to TPP-Au_{101} yielded a $Au_{84.5}$:$C_{284.8}$ ratio of 0.05 ± 0.01. In addition, XPS provided evidence that TPP-Au_{101} is assembled on **UDTA-BDD** through Au-thiolate bonds from the appearance of a new peak in the S2p spectrum at a lower binding energy, ~162.8 eV, indicative of a Au-thiolate bond (Figure S12). In addition to the presence of the thiolate bond, a P2p peak at 131.2 eV and Cl2p peak at 197.8 eV are also present, indicating that TPP-Au_{101} remains intact throughout the assembly process (Figure A13).

TPP-Au_{11} could also be assembled on BDD through undecanethiolate linkers, but first required deprotection of the terminal thioacetate in **UDTA-BDD** to yield a surface rich in thiol groups (**UDT-BDD)**. When **UDT-BDD** was exposed to TPP-Au_{11}, XPS yielded a $Au_{84.5}$:$C_{284.8}$ ratio of 0.10 ± 0.06 while a bare BDD substrate exposed to TPP-Au_{11} yielded a $Au_{84.5}$:$C_{284.8}$ ratio of 0.005 ± 0.001. The characteristic peak for a Au-thiolate bond also appeared in the XPS S2p spectrum which suggests that TPP-Au_{11} is bound to the molecular monolayer surface through Au-thiolate bonds (Figure A14). The ability of the system to assemble both TPP-Au_{101} and TPP-Au_{11} exemplifies its versatility.

Assessing surface coverage of AuNPs on BDD. While $Au_{84.5}$:$C_{284.8}$ ratios from XPS provided a means of comparing the Au surface coverage between samples, a method was needed to determine NP surface coverage more directly. Figure 3.1a,b shows scanning electron microscopy (SEM) images of a **Graft-UDT-AuNP** and **TPP-Au_{101}-UDT** samples showing even AuNP coverage with no signs of NP aggregation. In comparison, the bare BDD and **UDTA-BDD** show no features in this size range at the same magnification (Figure 3.1c,d). Due to the small size of the AuNPs, the SEM is near its resolution limit, preventing quantitative size analysis of the AuNPs, however it is still possible to estimate the coverage of nanoparticles from these images. The coverage of AuNPs obtained via molecular tethering is estimated to be ~10^{11} NPs/cm^2 for both the **Graft-UDT-AuNP** and **TPP-Au_{101}-UDT** samples, determined by counting NPs on the SEM images. Assuming the NPs are monodisperse and the BDD is flat, using the NP core diameter and ligand shell contribution to determine the NP area, this method yields approximately 10% NP coverage relative to a theoretical hexagonally close packed monolayer of NPs. For comparison, other methods reported to assemble monolayers of ~ l3 nm citrate-stabilized AuNPs on planar supports through molecular tethers resulted in ~1-30% coverage of AuNPs.[34,44,45]

Assessing nanoparticle-mediated electron transfer using a AuNP tethered redox probe

A small amount of a redox probe, 6-ferrocenyl(carbonyloxy)hexanethiol ($FcCO_2HT$), was introduced into the ligand shell of the AuNPs through Au-thiolate bonds to electrochemically evaluate the AuNP-UDT systems. A redox probe bound to the NP surface was chosen to examine NP-mediated electron transfer instead of a redox probe in solution to minimize any direct electron transfer between the redox probe and the BDD

electrode support. $FcCO_2HT$ was chosen because of its fast electron transfer, allowing for the electron transfer from the NP to the electrode to be directly observed.[18] In addition, the hydrophilic ester moiety prevents the ferrocene from burying itself in the hydrophobic alkane monolayer. This probe also facilitates the comparison of this platform to existing reports of planar Au self-assembled monolayers of ferrocene thiols.[60]

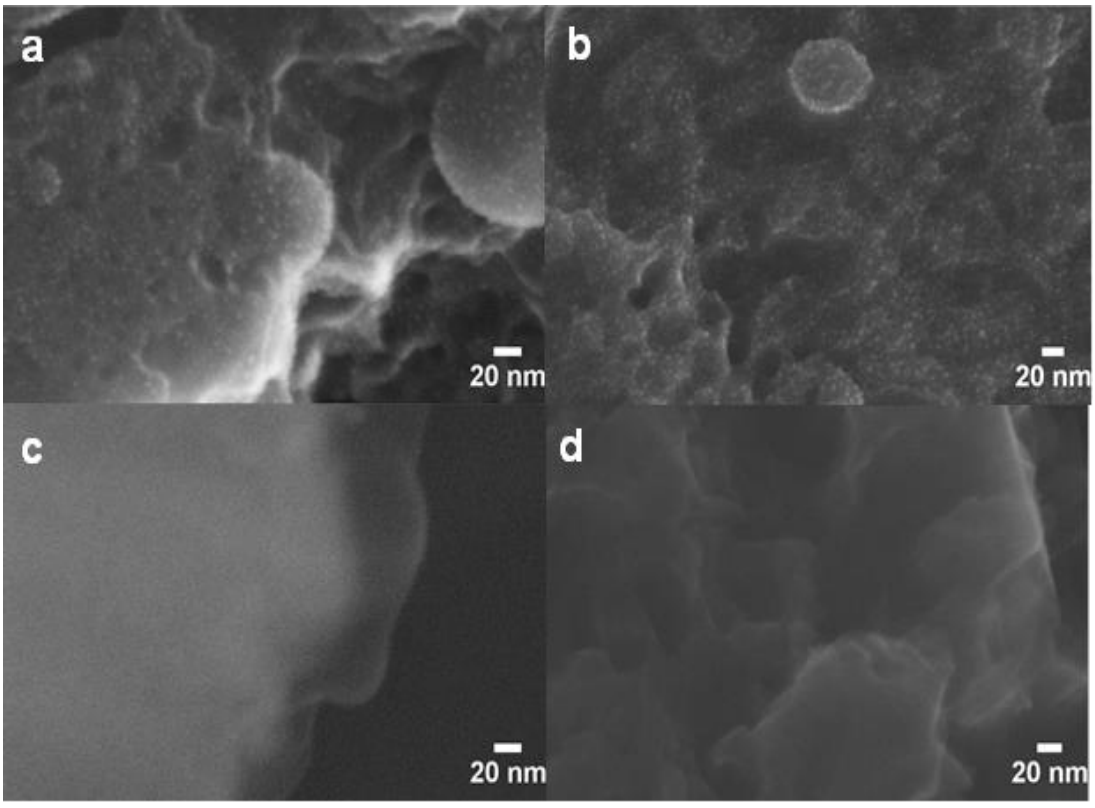

Figure 3.1. SEM images of a) **Graft-UDT-AuNP**, b) **TPP-Au_{101}-UDT,** c) a bare BDD substrate, and d) **UDTA-BDD.** The small, white features in a) and b) demonstrated the methods yielded monolayer coverage of nanoparticles, and the absence of these features in c) and d) verified that these features were indeed nanoparticles and did not originate from the substrate.

Two different methods were used to attach $FcCO_2HT$ to the AuNP surface for the **Graft- UDT-AuNP** samples and the **TPP-Au_x-UDT** samples. The **Graft-UDT-AuNP** sample was initially treated with dilute ozone to remove a portion of the thiolate ligand

shell. The $FcCO_2HT$ probe was then introduced to replace the partially removed thiolate ligand shell. This method was used in lieu of a direct ligand exchange between the $FcCO_2HT$ and the undecenethiolate ligands because thiol for thiol ligand exchanges do

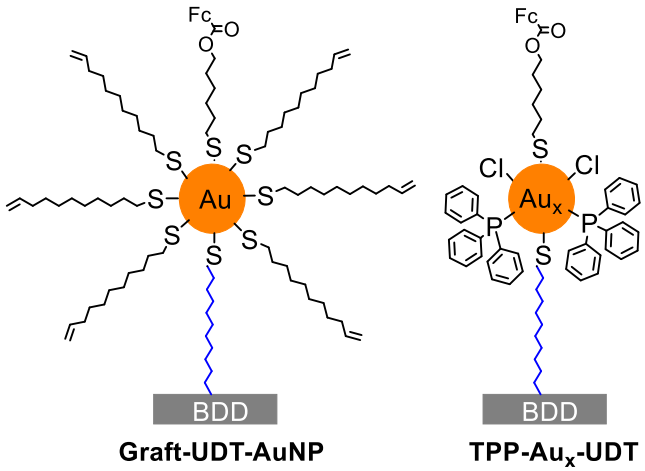

Chart 3.1. Molecularly tethered AuNP-functionalized boron doped diamond electrodes with bound ferrocene (Fc) redox probes

not always readily occur, especially when trying to replace a longer chain ligand with a shorter ligand.[65] This dilute ozone treatment was previously shown not to cause NP growth or destabilization.[61] $FcCO_2HT$ was attached to **TPP-Au$_x$-UDT** samples through simple ligand exchange with the triphenylphosphine ligands.[59,63] Chart 3.1 depicts the two molecularly tethered AuNP systems with bound $FcCO_2HT$ redox probe.

Several control experiments were performed to ensure the measured current was from redox probe bound to the NP surface. One concern was that the electrochemical response observed could be from redox probe adhered directly to the BDD electrode rather than from $FcCO_2HT$ bound to the NP surface. To ensure the $FcCO_2HT$ signal was only from that bound to the AuNPs, a bare BDD substrate underwent the same treatment to attach $FcCO_2HT$ to the **Graft-UDT-AuNP** samples (Figure A15). No $FcCO_2HT$ signal was detected, indicating that the electrochemical response is not from $FcCO_2HT$ attached

directly to the BDD surface. It was also possible that in the **TPP-Au$_x$-UDT** systems the $FcCO_2HT$ could form disulfide bonds with free terminal thioacetate or thiol functionalities in the molecular monolayer. To investigate whether the electrochemical response was influenced by disulfide bonds reacting with the probe, **UDTA-BDD**, **TPP-Au$_{101}$-UDT**, and **TPP-Au$_{11}$-UDT** were treated with known disulfide reducing agents (dithiothreitol or tris(2-carboxyethyl)phosphine (TCEP)) to reduce any disulfide bonds between the molecular monolayer and the redox probe (Figures A16, A17). A small reduction in faradaic current was observed, however, the peak potentials remained unchanged. Finally, to further confirm that the observed current only originated from probe bound to the NP, **Graft-UDT-AuNP** was treated with a 0.1 M KCN solution to decompose the AuNPs. Less than 10% of the initial $FcCO_2HT$ remained in the cyclic voltammograms of the decomposed sample, suggesting that the majority of the current in the original **Graft-UDT-AuNP** sample is from NP-bound redox probe (Figure A18).

Effect of molecular tethering method and NP core size on electrochemical properties. Cyclic voltammetry (CV) was used to investigate the electrochemical properties of the $FcCO_2HT$-AuNP-UDT systems (Figure 3.2, top row). All three systems exhibit behavior of a reversible, surface bound redox probe where the peak current scales linearly with the scan rate (Figure A19), and are stable over many electrochemical cycles. Slightly different peak-to-peak separations (ΔE_p), full width at half maximum (FWHM), and E^0 values were found for each system (Table 3.2). ΔE_p can be used to assess the barrier to electron transfer. For an ideal surface bound redox probe, the ΔE_p is 0 mV. The small $\Delta E_p \leq 41$ mV for all three $FcCO_2HT$-AuNP-UDT systems indicates the undecanethiolate molecular tether does not significantly inhibit electron transfer. The

Graft-UDT-AuNP (d_{core} = 2.1 ± 0.1 nm) and the **TPP-Au$_{101}$-UDT** (d_{core} = 1.9 ± 0.5 nm) systems had ΔE_p values within 2 mV of each other, 30 mV and 28 mV respectively, while the smaller **TPP-Au$_{11}$-UDT** (d_{core} = 0.8 nm) system had a ΔE_p of 41 mV. The larger ΔE_p suggests the **TPP-Au$_{11}$-UDT** system experiences a greater barrier to electron transfer than the **Graft-UDT-AuNP** and **TPP-Au$_{101}$-UDT** samples. Chazalviel and Allongue theorized that the rate of NP-mediated electron transfer across a molecular monolayer is dependent on both molecular layer thickness and NP core size, with electron transfer being more hindered as NP size is decreased.[66] The similar ΔE_p values for the similarly sized AuNP systems and larger ΔE_p exhibited by the smaller, **TPP-Au$_{11}$-UDT** system is in agreement with Chazalviel's theoretical model. The FWHM for all three systems are near 90 mV, the ideal value for a surface bound redox couple. This

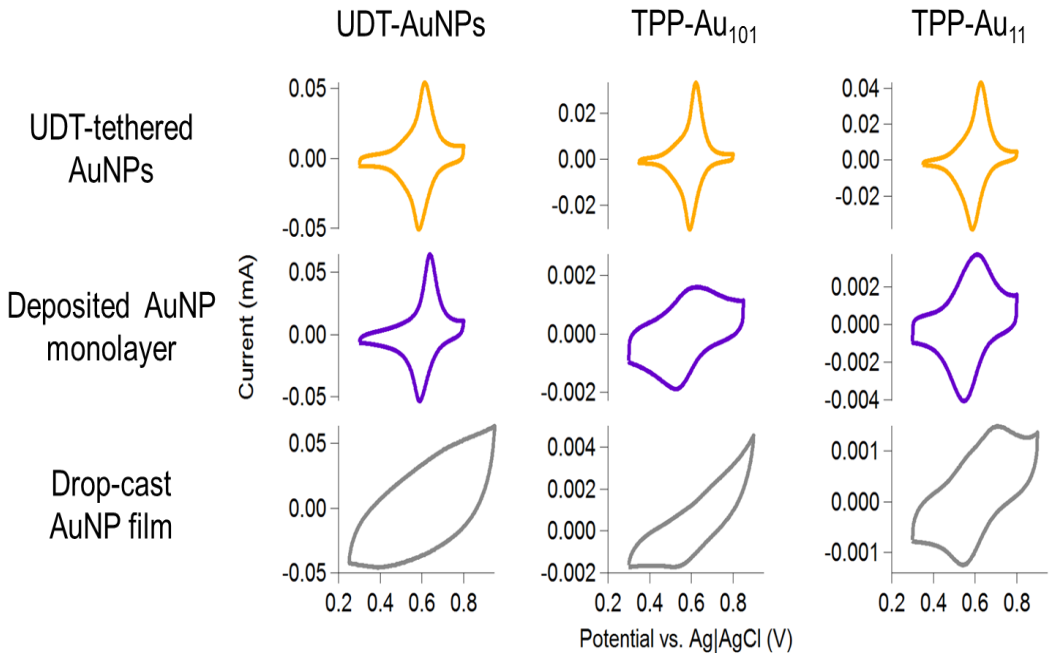

Figure 3.2. Comparison of cyclic voltammograms of the AuNP-BDD electrodes fabricated by different methods: binding a monolayer of AuNPs through an undecanethiolate monolayer (top row), depositing a AuNP monolayer film formed by self-assembly at the air-water interface (middle row), and drop-casting a AuNP film (bottom row). All samples were treated with $FcCO_2HT$. CVs were taken in 0.1 M $HClO_4$ at 100 mV/s.

suggests there are no major ferrocene-ferrocene interactions in the $FcCO_2HT$-AuNP-UDT systems as such interactions would broaden both the anodic and cathodic peaks. Lastly, both **TPP-Au$_x$-UDT** samples' E^0 values were within 2 mV of each other while the **Graft-UDT-AuNP** system's E^0 value was decreased by 6-8 mV. This could suggest that E^0 is ligand shell dependent and not dependent on core size. The variance in electrochemical properties with changing NP size is evidence that the observed electron transfer is NP-mediated. Both molecular tethering routes yield almost identical electrochemical properties, where E^0 is slightly affected by the ligand shell. Either route is suitable to fabricate a NP-functionalized electrode with a uniform monolayer of molecularly tethered NPs that exhibits reproducible electrochemical behavior.

Although it is tempting to compare the $FcCO_2HT$-AuNP-UDT systems to analogous AuNP-SAM-electrode systems, most AuNP-SAM-electrode systems employ passivating monolayers and thus are able to use solution phase redox probes for electrochemical characterization. Since the molecular monolayers formed on boron doped diamond are not completely passivating[67], the electrochemical response observed from a solution redox probe in the AuNP-UDT-BDD system arises from both AuNPs and the BDD substrate. Liu et al. reported an AuNP-SAM-electrode system studied with a tethered redox probe assembled AuNPs (d_{core} = 5-15 nm) on terminal thiol SAMs.[68] Although, they used a very fast scan rate, 50 V/s, preventing the comparison of ΔE_p values due to its scan rate dependence, sample preparation and peak shapes can be compared. The 6-(ferrocenyl) hexanethiol probe they used was diluted 1:9 with 1-pentanethiol to prevent major ferrocene-ferrocene interactions. Even with their use of a diluent ligand, the CV has a prominent anodic shoulder indicating the ferrocene probe

resides in different local environments. Similarly, Kondo et al. reported assembly of large AuNPs (~12 nm) on 3-mercaptopropyltrimethoxysilane linkers on boron doped diamond, also using bound 6-(ferrocenyl) hexanethiol to electrochemically evaluate their samples.[45] While they ran CVs in 0.1 M $NaHCO_3$, preventing direct comparison of E^0 values, the FWHM values of their system were almost double compared to the $FcCO_2HT$-AuNP-UDT samples reported in this work. They also observed small ΔE_p values (~17 mV). The slightly smaller ΔE_p values in their system are likely a result of the larger AuNP core size and that their molecular linker is a third of the length of the undecanethiolate linkers used in this work, both of which have been reported to influence electron transfer.[38,66] The $FcCO_2HT$-AuNP-UDT systems do not require the use of a diluent ligand to achieve narrow redox peaks. This could be due to the uniform spacing of AuNPs across the BDD, allowing for each $FcCO_2HT$ molecule to reside in chemically equivalent environments.

Effect of NP attachment method on electrochemical properties: molecular tethering, deposition of a monolayer, and drop-casting. To evaluate the effect of tethering NPs to electrodes through a molecular interface on the electrochemical properties, these samples were compared to electrodes prepared by other solution deposition techniques. One simple method often used to prepare NP monolayers on electrodes is NP self-assembly at the air-water interface, followed by transfer of the NP monolayer to the electrode.[69–71] A AuNP monolayer was formed through self-assembly at an air-water interface and then deposited on a BDD electrode. This sample was then treated with $FcCO_2HT$ to directly compare the effect of the molecular interface on the electrochemical properties (Figure 3.2, middle row). All three samples prepared through deposition of a AuNP monolayer to BDD had larger ΔE_p values than their respective

UDT-tethered samples (Table 3.2). These larger values suggest that the barrier to electron transfer increases in the absence of a covalent molecular interface. For the TPP-Au_x samples, the FWHMs were significantly broader than their tethered analogues, indicating that the environment of $FcCO_2HT$ is not uniform. The E^0 for both TPP-Au_x samples prepared by deposition of the NP monolayer decreased to 580 mV while the UDT-AuNP E^0 increased to 615 mV supporting the previous claim that redox potential is dependent on ligand shell.

To compare the electrochemically active surface area of these samples, the Au surface area was determined for each sample by integration of the gold oxide reduction peak at 0.9 V vs. Ag|AgCl in cyclic voltammograms (Figure A20).[72] For the molecularly tethered samples, the reduction peak did not disappear after multiple cycles, suggesting that the AuNPs are strongly tethered to the electrode. Additionally, the electrochemically active Au surface area of the TPP-Au_x deposited monolayer samples is an order of magnitude lower than their molecularly tethered analogues. This could indicate that the NPs are not as electrochemically accessible as the tethered NPs or that NP desorption occurs throughout the $FcCO_2HT$ treatment and/or electrochemical measurements. The broad redox peaks and subsequently ill-defined electrochemical properties of the physically adsorbed NP monolayer further demonstrate the necessity of strong interactions between the NP and the electrode to facilitate efficient electronic communication between the redox probe and electrode.

Table 3.2. Electrochemical properties of the $FcCO_2HT$-AuNP-BDD electrodes

AuNP sample	*NP-attachment method*	*ΔE_p (mV)*	*FWHM (anodic) (mV)*	*E^0 (mV)*	*Electrochemically active Au surface area (cm^2)*
UDT-AuNP					
	UDT-tethered	30	90	601	0.9 ± 0.3[c]
	Deposited monolayer	50	78	615	0.9
	Drop-cast	*N/A*[a]	*N/A*[a]	*N/A*[a]	1.2
TPP-Au_{101}					
	UDT-tethered	28	68	607	0.43 ± 0.03[c]
	Deposited monolayer	101	> 400	580	0.02
	Drop-cast	*N/A*[a]	*N/A*[a]	*N/A*[a]	*N/A*[b]
TPP-Au_{11}					
	UDT-tethered	41	84	609	0.5 ± 0.3[c]
	Deposited monolayer	65	170	580	0.01
	Drop-cast	168	> 300	627	0.02

[a] Unable to identify clear $FcCO_2HT$ signal

[b] Characteristic sharp Au oxide reduction peak not present

[c] Averaged over three samples

The electrochemical properties of molecularly tethered NPs were also compared to drop-cast NP samples. Drop-cast NP films were prepared from casting a solution of AuNPs in dichloromethane onto BDD resulting in ~2 mg of AuNPs on the BDD electrodes. Each sample was then treated with $FcCO_2HT$ for a direct comparison. CVs of drop-cast TPP-Au_{101} and the UDT-AuNPs showed no distinct $FcCO_2HT$ redox peaks while the drop-cast TPP-Au_{11} sample showed broad $FcCO_2HT$ redox peaks with a large ΔE_p of 170 mV (Figure 3.2, bottom row). There were significantly more AuNPs on the drop-cast samples than the samples prepared through NP grafting or assembly, thus a

much larger current response is expected if all of the NPs are available to perform electrochemistry. However, this is not observed in the CVs, presumably because only the NPs at the surface of the sample are accessible to the $FcCO_2HT$ probe and electrochemically. The ill-defined or absent $FcCO_2HT$ redox peaks for the drop-cast AuNP electrodes indicates an efficient electron transfer pathway is lacking between the redox probe and the electrode, either due to poor electrical contact between the NPs and the electrode or the physical distance between the $FcCO_2HT$-functionalized NPs and the electrode. Similar results were observed in previous work examining multi-layer films of ferrocenated AuNPs.[71] These results demonstrate that one cannot simply drop-cast thicker layers of ligand-stabilized NPs onto electrode substrates as a means of increasing NP loading, for applications such as electrocatalysis, since the NP-electrode interface greatly affects the electrochemical properties.

The clear differences between the deposited monolayer and the drop-cast samples demonstrated that the electrochemical properties of NP electrodes fabricated from solution deposition techniques are variable from sample to sample. Such variability is due to a lack of control over NP-NP interactions and the NP-electrode interface. In contrast, the molecularly tethered systems exhibit reproducible electrochemical properties. These results exemplify the importance of a defined interface when studying the electrochemical properties of NP-functionalized electrodes.

Conclusions

Two strategies were demonstrated for tethering small ($d_{core} \leq 2.5$ nm) ligand-stabilized AuNPs to a boron doped diamond electrode through a molecular interface. In one approach, undecenethiolate-stabilized AuNPs ($d_{core} = 2.1$ nm) were photochemically

grafted to BDD through the terminal alkene in the ligand shell. Alternatively, BDD was first functionalized with an undecyl thioacetate monolayer followed by assembly of triphenylphosphine-stabilized AuNPs onto the monolayer through ligand exchange. Using the ligand exchange approach, two different sizes (d_{core} = 0.8 and d_{core} = 1.9 nm) of AuNPs could be tethered to BDD. XPS analysis and electron microscopy show that the NPs retain their composition, initial core size and shape throughout the process and yield uniform monolayer NP assemblies with ~10^{11} NPs/cm^2 coverage resulting from either method.

Nanoparticle-mediated electron transfer through molecular monolayers was evaluated by attaching redox probes to the AuNP surfaces. All of the molecularly tethered AuNPs displayed cyclic voltammograms with narrow peak widths (≤ 90 mV FWHM) that were stable over many cycles. The smaller **TPP-Au$_{11}$-UDT** system exhibits a greater barrier to electron transfer than the larger **Graft-UDT-AuNP** and **TPP-Au$_{101}$-UDT** systems as might be expected if the nanoparticle core size influences electron transfer as theorized by Chazaviel and Allongue.[66] In all cases, the molecular NP-electrode interface results in more efficient electron transfer than the two solution deposited samples, and a greater proportion of the nanoparticles are electrochemically active when using a molecular tether. In contrast to samples produced by solution deposition methods where the electrochemical response depends strongly on the exact deposition conditions, the electrochemical properties of the molecularly tethered samples were reproducible across a number of preparations. Each of the molecularly tethered samples exhibited stability over many days as indicated by the electrochemical response, and could be re-exposed to the redox probe prior to reuse if needed. Compared to

analogous systems with larger AuNPs ($d_{core} \geq 10$ nm) the systems reported here exhibit nearly ideal, narrow redox peaks even when they are not diluted with a redox-inactive diluent ligand.

The molecular tethering strategy demonstrated here offers a versatile platform to interface nanoparticles with an otherwise inert electrode material. Because the platform yields samples with reproducible electrochemical responses, it provides the opportunity to quantitatively study NP-mediated electron transfer as a function of NP morphology and linker length. It also provides a system to study the influence of core size and the NP-electrode interface on the electrocatalytic behavior of preformed nanoparticles. Both will be the focus of future work with this platform. In addition, the platform should prove useful for grafting other nanomaterials stabilized by ligands possessing terminal alkenes or assembling other nanoparticle core materials onto an appropriate terminal functional group on the monolayer. The linker length could be easily varied, given that an alkene derivative can be synthesized. Although boron doped diamond was used for the electrochemical measurements in this work, this approach could be further expanded to attach nanoparticles to other substrates that alkenes can be photochemically grafted to, such as silicon, SiO_2, TiO_2, and amorphous carbon.[73–76]

Bridge to Chapter IV

The previous two chapters focused on how to enhance the electronic communication between nanoparticles and electrodes by employing a defined molecular interface to attach the nanoparticles. This work demonstrates how the molecules that bind to the nanoparticle core offer an additional architectural tool for the design of

nanomaterials with desired properties. Chapter IV looks at the influence these molecules have in the synthesis of cobalt oxide nanoparticles.

Cobalt oxide is a promising candidate for electrocatalytic applications such as CO_2 reduction and OER. Cobalt oxide nanoparticles may offer enhanced catalytic properties due to the high surface area to volume ratio in this size regime. In order to investigate cobalt oxide nanoparticles as electrocatalysts, uniform materials must be synthetically accessible. Current synthetic methods lack the size, morphology, composition and surface chemistry control required to produce a series of uniform materials for study.

Chapter IV expands on a synthetic approach, slow injection, of metal oxide nanoparticles that allows for control at the atomic level over nanoparticle size, composition and surface chemistry. Attempts to adapt the slow injection synthesis to the produce uniform cobalt oxide nanoparticles have produced surprising results. Unlike the In_2O_3 and Fe_2O_3 systems, the condensation reaction mechanism for the cobalt oxide system requires the presence of air for nanoparticle formation to occur. Furthermore, the cobalt system appears to have two competing mechanisms resulting in limited control over nanoparticle nucleation and growth. Speculation is provided as to why air is required for nanoparticle nucleation, and why, under the conditions explored, we are not able to separate the nucleation and growth phases in the synthesis.

CHAPTER IV

EFFORTS TOWARDS ADAPTING THE SLOW INJECTION SYNTHESIS TO MAKE UNIFORM COBALT OXIDE NANOCRYSTALS

Note: Portions of this chapter may appear in an upcoming publication authored by Jaclyn E. Kellon and James E. Hutchison. All experimental work and the writing of this chapter was done by J. E. Kellon. J. E. Hutchison aided in the conceptualization of this work and with editorial assistance.

Introduction

Metal oxide nanoparticles (NP) are being incorporated into a wide range of technology sectors due to their unique properties accessed at the nanometer size range and their high surface area to volume ratio. Many size,[1,2] composition,[3,4] structure,[4,5] surface chemistry,[6,7] and morphology[8–10] dependent properties of metal oxide NPs have been reported, making these promising materials for a broad suite of applications. Additionally, nanomaterials are more likely to exhibit properties different than their bulk counterparts at core diameters less than 15 nm.[11] As we move into a new stage of understanding the influence of NP structure on performance, systematic studies of NPs with the same core composition but with a different size, shape and surface chemistry are required. In order to conduct these systematic studies, a synthetic route that access small core sizes with tunable surface chemistry, morphology and core composition is necessary.

The Hutchison lab has pioneered a synthetic method for metal oxide NPs that grow in a layer-by-layer fashion.[12] The slow injection synthesis allows for the size of the NPs to be controlled and easily predicted by the amount of metal precursor added. In this living growth system, a metal oleate precursor is slowly added into hot oleyl alcohol at a constant rate.[13] The metal oleate precursor undergoes an esterification reaction with the oleyl alcohol, producing metal hydroxide monomers that then condense to grow NPs with low size dispersity. Although the slow injection approach was initially introduced for the synthesis of In_2O_3, Fe_2O_3 and CoO NPs, only the synthesis of In_2O_3 and Fe_2O_3 NPs been thoroughly investigated.[1,12,14] A significant advantage of this synthetic method is not only the ability to incorporate dopant elements into the NP, but to control their location within the NP.[14,15] It is extremely desirable to adapt the slow injection synthesis to access other transition metal oxide nanomaterials with precise control over size and core composition.

In Fe_2O_3 we found relatively elevated saturated magnetism to similar sized NPs that had been made by thermal decomposition.[1] We thought this could be related to two aspects of the slow injection synthesis: well defined chemistry and slow growth. Thus, one might be interested in examining the synthesis/properties for other magnetic materials. Cobalt oxide nanoparticles (NP) are promising materials for applications such as sensing,[16] energy storage,[17] catalysis[18] and magnetism.[19] The reduced form, CoO, has two possible crystal structures, cubic rock salt and hexagonal wurtzite. Both forms have garnered much attention because their magnetic properties; the hexagonal phase is paramagnetic while the rock salt phase is antiferromagnetic.[20]

The most common route to CoO NPs is by the thermal decomposition of cobalt surfactant complexes in long-chain hydrocarbon solvents in a reducing atmosphere at

temperatures ranging from 135 – 290ºC.[21–28] The long-chain hydrocarbons are either amines or a combination of carboxylate and alcohol molecules. Both Co (II) and Co (III) acetate and acetylacetone salts are the common sources of Cobalt.

Synthetic methods that utilize similar reagents to the slow injection synthesis exist and are able to produce CoO NPs with a variable morphology. For example, a synthesis developed by Zhang and co-workers is able to access a wide range of CoO NP morphologies with the rapid injection of dodecanol into a solution of Co (II) oleate and octadecene.[29] The NP morphology is altered by the relative ratios of excess oleic acid and dodecanol. The mechanism of NP formation in this route is most likely through the generation of cobalt hydroxyl species via an esterification reaction between the rapidly injected dodecanol and the Co (II) oleate, followed by condensation. Although synthetic routes for CoO NPs with similar chemistry to the slow injection synthesis exist, the resulting NPs are not well-defined below 15 nm.

In order to develop a better understanding of how the size of CoO NPs influences their magnetic and catalytic properties, a synthesis capable of accessing a wide size range is required. This work aims to adapt the slow injection synthesis to access cobalt oxide NPs with precise size control by using precursors with two different oxidation states: Co (II) and Co (III). This work has provided insights into what synthetic conditions are necessary to reliably produce CoO NPs. We examine the influence of temperature, cobalt precursor oxidation state and air on NP formation and provide a hypothesis for the specific role of air in NP formation.

Methods: Nanoparticle Synthesis

1 mmol (II) acetate (176 mg) or Co (III) acetylacetone (356 mg) was stirred with 2 mL oleic acid (6.0 mmol) under flowing N_2 or air at 150^{o}C for 30 – 60 minutes for Co (II) and Co (III) respectively. The resulting Co oleate was added dropwise to hot oleyl alcohol at a rate of 0.1 mL/min. The temperature of the oleyl alcohol ranged from 230 - 290^{o}C. The reaction was either under flowing N_2 or in a 1:3 air:N_2 flowing environment. After addition of the precursor was completed, the reaction was left to stir at temperature for 15 minutes, then cooled to room temperature. The NPs were washed twice with acetone and stored in toluene.

Results and Discussion

The slow injection synthesis of In_2O_3 and Fe_2O_3 produces nanoparticles through a two-step living growth mechanism: esterification and condensation.[1,14] Based on those findings it is expected that the slow injection synthesis of CoO previously achieved by Ito and co-workers should undergo the same growth mechanism.[12] The slow injection synthesis is carried out by injecting a metal oleate precursor at a constant rate into a flask of hot oleyl alcohol. The oleate precursor undergoes an esterification reaction with the hot oleyl alcohol to produce metal hydroxyl species. These metal hydroxyls then undergo an initial condensation reaction to nucleate metal oxide nanoparticles. After the initial nucleation event, addition metal hydroxyl species generated from the continual addition of metal oleate precursor, preferentially condense on the NP surface. What is unique about this living growth synthesis is that after the initial nucleation event, the slow injection rate ensures that the metal hydroxyl species condense on the NP surface and not

with other metal hydroxyl species in solution to nucleate new NPs. In this work both Co (II) and Co (III) oleate precursors were used in the synthesis of cobalt oxide NPs.

Influence of oleyl alcohol temperature on nanoparticle formation

Considering the reaction conditions used for the slow injection synthesis of In_2O_3 and Fe_2O_3 NPs, we began our syntheses at 260^{o}C in flowing N_2. To our surprise, at this temperature we did not observe the formation of any NPs. Previous CoO NP syntheses from other researchers indicate that the NPs produce either a brown or green solution indicating cubic or hexagonal morphology respectively.[21] Instead, at the end of the injection of the cobalt oleate precursor the reaction solution remained a deep blue/purple color. Once the reactions were cooled to room temperature, the solution formed a gelatinous purple product. The gelatinous purple product was not initially soluble in toluene but went into solution after a few days. Transmission electron microscopy (TEM) was used to determine whether any NP formation occurred at 260^{o}C. Few NPs were observed on the TEM grids in addition to what appears to be a polymeric species that so far is unidentified.

When the reaction temperature was increased to 290^{o}C, NP formation readily occurred. Roughly 45% of the way through the injection of the cobalt (II) oleate precursor, the reaction changed from a deep blue to brown in color, indicating NP formation. TEM confirmed the formation of NPs with a mostly tetrahedral morphology that ranged in core size from roughly 4 – 13 nm in diameter (Figure 4.1a). X-ray diffraction (XRD) confirmed that the NPs were predominantly the cubic-rock salt crystal phase (Figure 4.2). The XRD was collected six months after the NPs were synthesized and the NPs were stored in air allowing them to slowly undergo oxidation explaining the

broad peak at 19.5°. The same behavior was observed for the addition of Co (III) oleate at 290°C under flowing N_2.

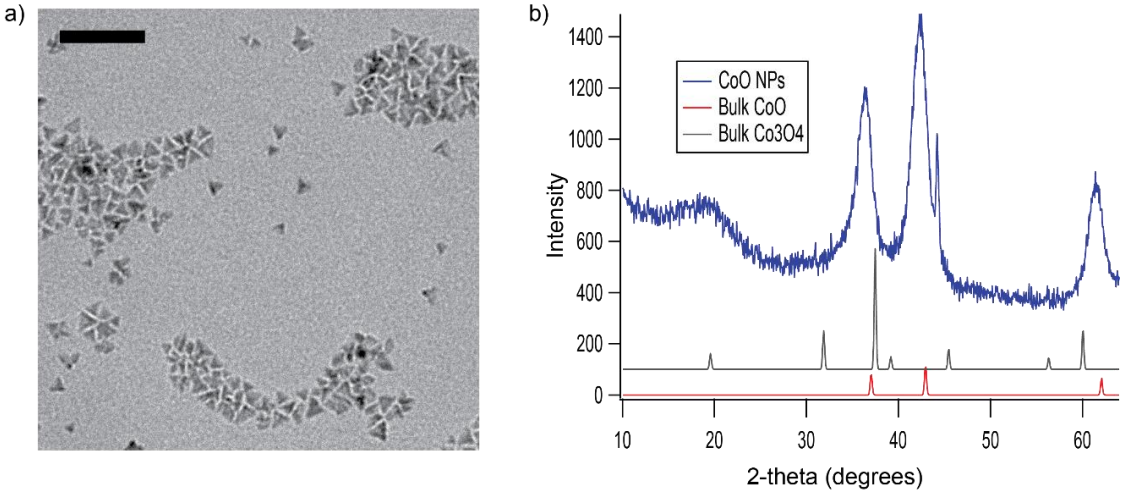

Figure 4.1: TEM micrograph, a, and XRD pattern, b, of the CoO NPs produced from the injection of Co (II) oleate into oleyl alcohol at 290°C under flowing N_2. The red and grey patterns in b correspond to bulk rock salt CoO and spinel Co_3O_4 respectively. Scale bar is 50 nm.

Considering that most CoO NP syntheses in the literature use reaction temperatures below 260°C, we were surprised that our system did not produce NPs below 290°C. Unlike the slow injection approach which is completed within 20 minutes, the other syntheses in literature that are conducted at lower temperatures, ≤ 260°C, occur over the course of a few hours. However, our findings do align with work done by Zhang and co-workers. Their synthetic approach is the most similar to our slow injection synthesis in that it uses similar reagents and temperatures for the rapid injection of dodecanol into a solution of Co (II) oleate and octadecene between 290 - 310°C.[29] The rapid color change at 45% of precursor addition and similarities in reaction conditions with the work by Zhang suggests that the slow injection of cobalt (II) oleate at 290°C results in a burst nucleation event that is responsible for the color change after 45% of the Co (II) oleate has been added. Additionally, the resulting NPs core sizes are

polydisperse indicating that the nucleation of new NPs continues throughout the addition of the remaining Co (II) oleate. Based on these observations, these synthetic conditions are not appropriate for the living growth synthesis of uniform CoO NPs with core diameters below 15 nm.

The influence of air in CoO nanoparticle formation

The results of the slow injection of Co (II) and Co (III) at 290^{o}C under flowing N_2 indicated that some variable in the synthetic conditions is not conducive to the growth of uniform CoO NPs. Based on the sudden color change observed at 290^{o}C, the following reactions were all conducted at 260^{o}C in an attempt prevent the nucleation of new NPs throughout the addition. As previously stated, NP formation and growth in the slow injection synthesis occurs in two steps. First, the cobalt oleate precursor must undergo an esterification reaction with the oleyl alcohol to produce cobalt hydroxyl species. Those cobalt hydroxyl species must then condense with each other to form Co-O-Co bonds to either nucleate new NPs or grow on the surface of existing cobalt oxide NPs. It is clear that below 290^{o}C, in N_2, that one or both of these reactions is not occurring.

In one synthesis, at the end of the addition of Co (II) at 260^{o}C in N_2, the deep blue/purple reaction was opened to air and within five minutes the reaction turned brown, suggesting the formation of NPs. TEM confirmed the presence of polydisperse CoO NPs in the brown reaction solution. We were surprised that the introduction of air resulted in the rapid formation of CoO NPs considering that the slow injection synthesis for other metal oxides and all other syntheses of CoO are done under N_2 or Ar. In order to understand what role air plays in the formation of CoO NPs, the same reaction was repeated with both Co (II) and Co (III) oleate injected at 260^{o}C in flowing N_2. After

addition, the flowing N_2 was switched to flowing air and within three minutes the dark blue reaction turned brown. The reaction was left to stir at 260°C in flowing air for one hour. Three aliquots were removed: 1) at the end of the cobalt oleate precursor addition, before the introduction of air, 2) three minutes after the introduction of air at which time the reaction turned brown and 3) 60 minutes after the introduction of air.

FTIR and TEM were used to understand the reaction progression at these specific color changes. FTIR showed the presence of ester both before and after the introduction of air into the system for both the Co (II) and Co (III) precursors (Figure 4.2). In addition to the presence of the carbonyl stretch from an ester at 1741 cm^{-1} before and after the air induced color change, the ratio of carbonyl stretch from the excess oleic acid at 1720 cm^{-1} to ester carbonyl is similar in relative intensity, indicating that the cobalt oleate

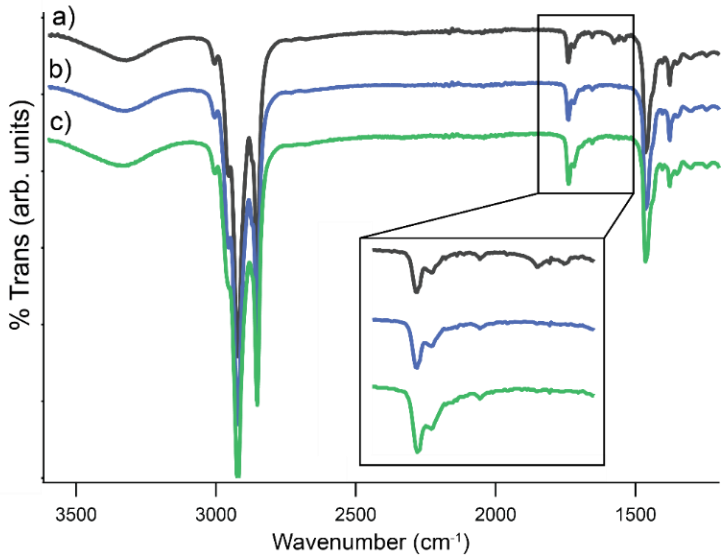

Figure 4.2: Infrared spectra of the reaction of Co (II) oleate after injection into oleyl alcohol at 260°C in flowing N_2 and flowing air. At the end of addition, prior to exposure to air, the reaction was a deep blue/purple in color, a. After 3 minutes of flowing air the reaction became a light brown, b, and stayed that color for the remaining 60 minutes, c. The inset shows the ester and oleic acid carbonyl stretches at 1741 cm^{-1} and 1720 cm^{-1} respectively in addition to the small peaks at 1578 cm^{-1} and 1540 cm^{-1} caused by cobalt – (COO^-) interactions.

precursors readily undergo the esterification reaction with oleyl alcohol to generate cobalt hydroxyl species.

FTIR indicates that the blue species present prior to the introduction of air is a cobalt hydroxyl species. The blue color is indicative of a Co (II) tetrahedral complex with hydroxyl ligands. Additionally, the FTIR spectra for the Co (II) reaction prior to the introduction of air has small peaks at 1578 cm^{-1} and 1540 cm^{-1} that are from the presence of cobalt – (COO^-) interactions. This species may be mono or multinuclear in nature and would most likely have the chemical formula $Co_x(O_2CR)2_{x-y}(OH)_y$. The subsequent condensation of the $Co_x(O_2CR)2_{x-y}(OH)_y$ to form Co-O-Co bonds would results in a decreased number of cobalt – (COO^-) interactions. The decrease of the cobalt – (COO^-) interactions is evidenced in the FTIR spectra after the introduction of air by the disappearance of the peaks at 1578 cm^{-1} and 1540 cm^{-1}. This same behavior was observed in the Co (III) system but instead of two peaks between 1580 – 1540 cm^{-1} a single broad peak is present before the introduction of air that then disappears once the reaction turns brown.

TEM was used to evaluate whether NP formation occurred at the three aliquots. Although very few NPs are present by TEM prior to the introduction of air, after the color change the TEM grid is covered with small CoO NPs (Figure 4.3). The NPs present three minutes after the introduction of air have a mostly tetrahedral morphology and are polydisperse for both the Co (II) and Co (III) reactions. Although some of the NPs appear to grow in size over the 60-minute period of air exposure, small NPs are also present, indicating that new nucleation continues to occur over the course of the hour.

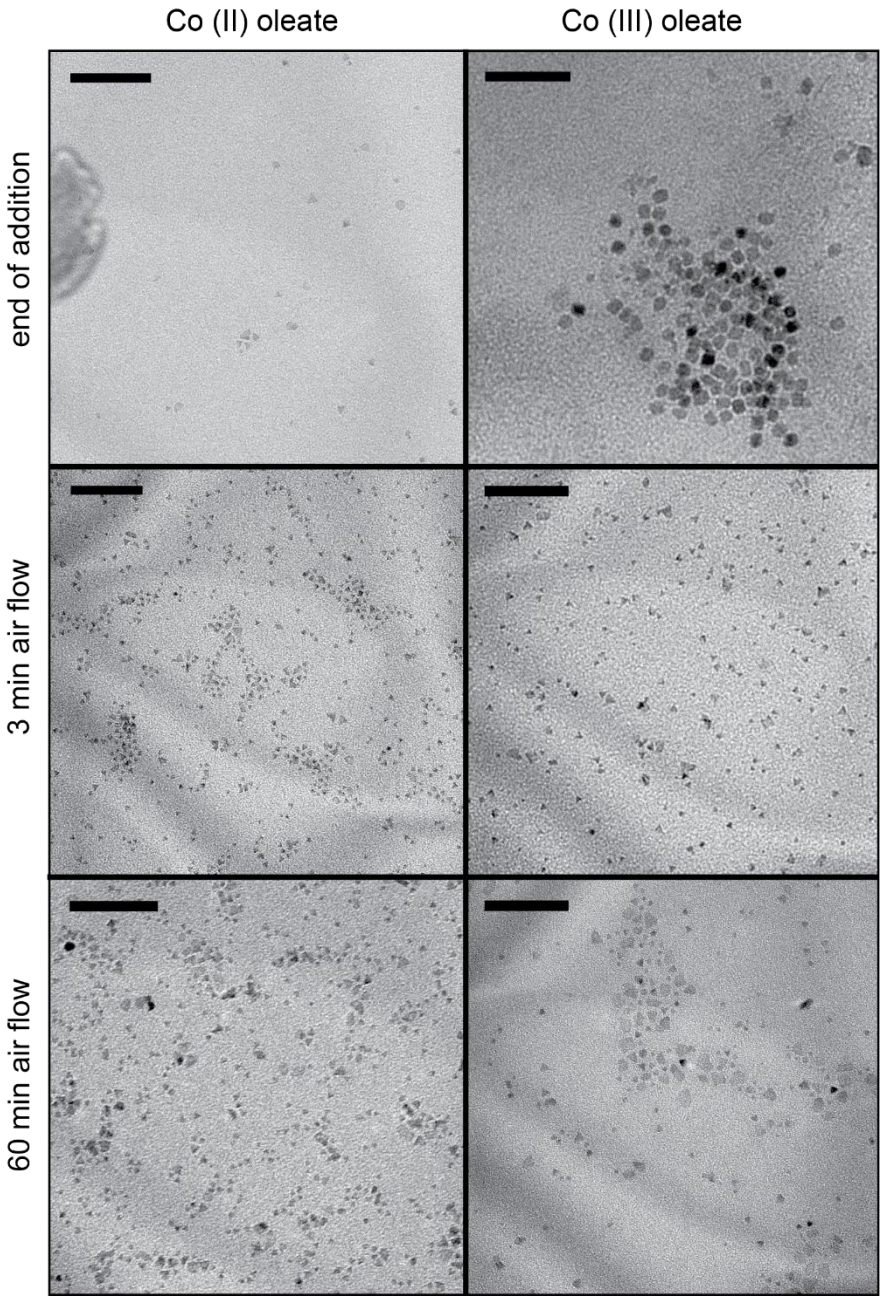

Figure 4.3: TEM images of the product of the slow injection of Co (II) oleate and Co (III) oleate into hot oleyl alcohol (260^{o}C) in a flowing N_2 environment (end of addition) and after exposure to air. Scale bars are 50 nm.

Considering the growth behavior of the NPs at 290^{o}C in flowing N_2 and the requirement of air for NP growth at lower temperatures, we continued to search for reaction conditions that would yield surface mediated growth at 260^{o}C. The atmosphere

of the reaction container was changed from 100% flowing N_2 to 75% N_2 and 25% air. The introduction of air into the reaction led to NP formation for both the Co (II) and Co (III) oleate precursors at 260°C. Similarly to what was observed at 290°C in N_2, after 45% of the cobalt oleate precursor was added the reaction solution changed from a deep blue to a light brown and the presence of bubbles was observed. Bubble formation is indicative of the cobalt hydroxyl species condensing and producing H_2O as a byproduct that is quickly evaporated at these elevated temperatures.

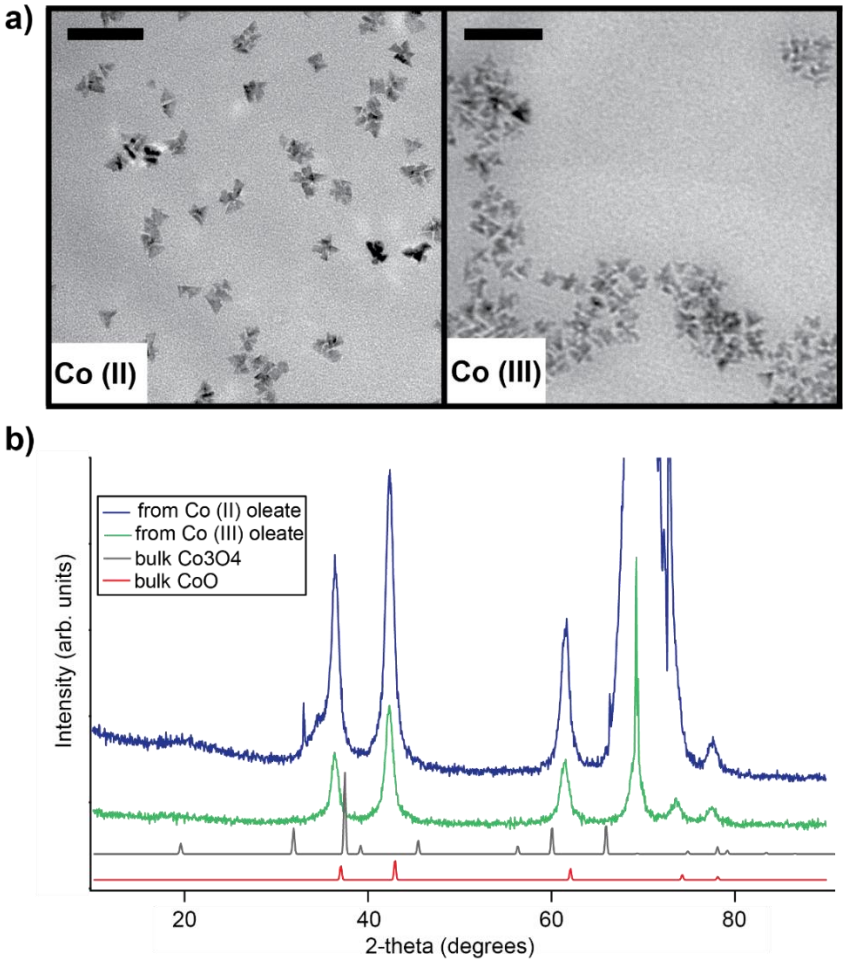

Figure 4.4: TEM micrographs (a) and XRD patterns (b) of the CoO nanoparticle formed from Co (II) and Co (III) oleate at 260°C in a 75% N_2 and 25% air environment. The scale bars are 50 nm. The strong peak at 68° is from the silicon substrate.

The resulting NP morphology was dependent on which cobalt precursor was used. Co (II) oleate produced mostly tetrahedral particles while the Co (III) oleate precursor produced NPs with irregular shapes resembling popcorn (Figure 4.4a). XRD confirmed that both the Co (II) and Co (III) oleate precursors led to the formation of cubic-CoO NPs (Figure 4.4b). It was initially puzzling to us why the Co (III) oleate precursor produced CoO NPs in the presence of air, but the reaction conditions are highly reducing, and we believe that the Co (III) oleate is being reduced *in situ*.

Based on the color changes, FTIR data and TEM images, it appears that air is required not for the esterification reaction, but for the condensation of the $Co_x(O_2CR)2_{x-y}(OH)_y$ species into CoO NPs (Figure 4.5). Considering that every other CoO NP synthesis is performed in a rigorously air free environment, it is surprising that the presence of air is necessary for CoO NP formation. The decomposition of cobaltous hydroxide *in vacuo* by Mehandjiev and Nikolova-Zhecheva found that CoO was the predominant product.30 Their results indicate that CoO froms from the decomposition of cobalt hydroxide and cobalt oxalate. By monitoring the magnetic properties throughout

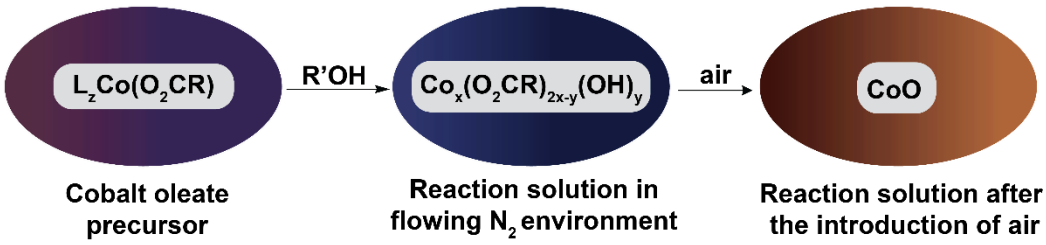

Figure 4.5: Color progression of the slow injection of Co (II) or Co (III) oleate precursor into oleyl alcohol at 260°C. The addition of the cobalt oleate precursor into the oleyl alcohol was completed in a flowing N_2 atmosphere, at which time the reaction was deep blue in color. After all the precursor was added, the flowing N_2 atmosphere was switched to flowing air and the reaction color changed to brown, indicating the nucleation of CoO nanoparticles.

the decomposition of cobalt hydroxide, they observed that the reaction proceeds through the formation of an octahedral Co (III) intermediate. Perhaps oxygen is required to oxidize the $Co_x(O_2CR)2_{x-y}(OH)_y$ species to a Co (III) intermediate which can then condense to form CoO NPs.

Using air to drive nanoparticle growth

The color changes observed throughout the slow injection synthesis of CoO NPs may offer insight into the NP growth mechanism. In order to discern what species were present in the reaction at different colors, a synthesis with Co (II) oleate precursor was carried out at 260^{o}C in a 25% flowing air environment. The addition of the Co (II) oleate precursor was halted at various points throughout the addition to monitor any color change and to remove aliquots for further analysis. Precursor addition was halted at 0.3 mL added, and an aliquot was removed from the reaction. After ~4 minutes the reaction changed to a light brown color, and another aliquot was removed. The precursor addition was resumed until the reaction returned to a dark blue color at 1 mL precursor added. The addition was again halted, an aliquot removed and within three minutes the reaction turned brown. The addition was resumed and by the end of addition the reaction was almost black in color. TEM was used to evaluate the extent of NP formation, NP morphology and NP core size for each aliquot removed (Figure 4.6).

The initial blue aliquot removed at 0.3 mL of precursor added potentially shows very small, ill-defined CoO NPs. The TEM grid was mostly covered with amorphous dark spots that appear to have small NPs within it. The large amorphous dark spots are no longer present in the next aliquot, when the reaction has turned brown. This sample shows clear signs of small NPs having formed but at this size their morphology is

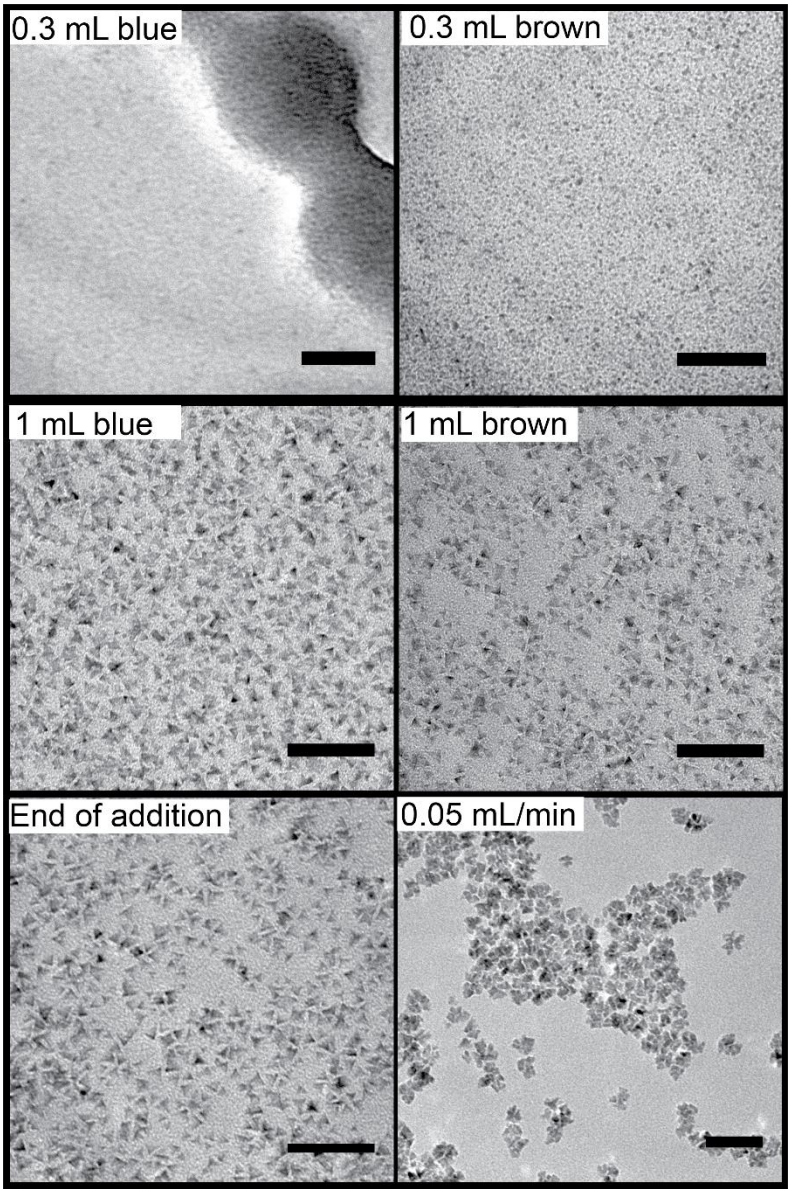

Figure 4.6: TEM images of aliquots taken during the slow injection of Co (II) oleate into hot oleyl alcohol at 260^{o}C in a flowing 25% air environment at a rate of 0.1 mL/min. The injection was halted at points corresponding to a change in color. The volumes indicate the amount of Co (II) oleate precursor added and the color of the reaction when the aliquot was removed. The bottom right TEM grid is the addition of Co (II) oleate at 260^{o}C in a flowing 25% air environment at 0.05 mL/min. The scale bars are 50 nm.

difficult to discern. At 1 mL of precursor added, tetrahedral NPs ranging in size from roughly 3 – 8 nm in diameter are present in the blue aliquot. After the halt in addition and the reaction changed to brown, the NP morphology and extent of core size dispersity are

unchanged. By the end of the reaction the NP cores may have slightly grown, but small NPs are still present.

The slow injection synthesis of Fe_2O_3 and In_2O_3 NPs grow via a living growth mechanism. After the initial nucleation of NPs, the In/Fe hydroxyl monomer species formed *in situ* via the esterification reaction rapidly condense on existing NP surfaces as opposed to reacting with each other in solution to continually nucleate new NPs. There are always two competing reactions, the nucleation of new NPs or growth of existing NPs via surface condensation. The slow injection synthesis is unique in its ability to separate the nucleation and growth stages, and this separation allows for the synthesis of uniform, monodisperse NPs. The slow injection of monomer species is what allows for this separation. After the nucleation of the initial NP cores, the reaction between the NP and monomer is high yielding and rapid, meaning that if the addition rate is sufficiently slow, the concentration of NPs is always greater than that of the monomer species.

It appears that we have not yet found the conditions to separate the nucleation and growth stages for the formation of CoO NPs. Throughout the course of the addition, two competing reactions appear to be occurring: 1) condensation of the cobalt hydroxyl monomers with other monomers in solution and 2) the condensation of monomers on the surface of existing NPs. The first case results in the nucleation of new NPs while the second results in the growth of existing NPs. The presence of small NPs and apparent growth of other NPs at each aliquot removed suggest that condensation of the cobalt hydroxyl species occurs both at existing NP surfaces and with other monomer species in solution thus continually nucleating new NPs.

Moving Forward

We hypothesize that multiple things could be preventing the separation of the nucleation and growth phases under these conditions. One possibility is that the condensation reaction is significantly slower than the esterification reaction. Cobalt hydroxyl species could be building up in solution throughout the course of precursor addition. If the cobalt hydroxyl species are not efficiently consumed, the concentration gradient necessary to drive NP growth is not reached. In this situation the concentration of cobalt hydroxyl species in solution is sufficiently high enough to continue nucleating new NPs in addition to growing existing ones.

There are multiple situations that could result in slow condensation. One possibility is that the surface of the CoO NPs is less reactive than the In_2O_3 and Fe_2O_3 NP surfaces. The rate of condensation of cobalt hydroxyl species at the NP surface may be inherently slower than both for In/Fe or the oleate ligands that passivate the NP surface may bind more strongly with the CoO NPs than with the Fe_2O_3 or In_2O_3 NPs. Alternatively, the cobalt precursor has to go through at least one intermediate that is associated with a change in oxidation state. It has been suggested that the Co (III) intermediate required for CoO formation is octahedral while the blue color of the reaction solution suggests a tetrahedral geometry for the cobalt hydroxyl species. The oxidation state and coordination change may slow down the condensation reaction relative to the esterification reaction. Slowing down the rate of precursor addition may lead to surface mediated growth by allowing enough time for condensation to occur. However, when we reduced the injection rate from 0.1 mL/min to 0.05 mL/min the resulting NPs appear to be more aggregated with less uniform morphology (Figure 4.6).

An alternative hypothesis is that unlike the In_2O_3 and Fe_2O_3 systems that produce In/Fe hydroxyl species with only one hydroxyl group, cobalt may readily produce $Co(OH)_4^{2-}$. We predict that $Co(OH)_4^{2-}$ would be highly reactive under these conditions and that the condensation reaction would then happen too rapidly to separate the nucleation and growth phases. It may be that the cobalt oleate precursor is esterified to $Co(OH)_4^{2-}$ immediately once it enters the reaction flask and then condenses before it gets homogenously mixed into the solution. If this is the case, it may be possible to slow the addition rate down enough and introduce better mixing to generate a true concentration gradient between the $Co(OH)_4^{2-}$ species and existing NPs.

Unfortunately the OH stretch from $Co(OH)_4^{2-}$ cannot be observed by FTIR because if present, it is buried in the OH stretch from the excess oleyl alcohol. Furthermore, the FTIR data do not suggest that only $Co(OH)_4^{2-}$ are being formed prior to the introduction of air. As can be seen in Figure 4.2a, metal carboxylate peaks are present at 1580 – 1540 cm^{-1} suggesting the presence of a hydroxylated Co with remaining oleate ligands. One could possible observe the presence of $Co(OH)_4^{2-}$ by FTIR if a reaction was carried out with a stoichiometric amount of oleyl alcohol. The complete addition of the cobalt oleate precursor would need to be carried out under flowing N_2. Following addition the atmosphere could be switched to flowing air to induce NP formation. If $Co(OH)_4^{2-}$ is present, it may be observable at the end of precursor addition prior to the introduction of air.

Bridge to Chapter V

Chapter IV discussed the nucleation and growth of cobalt oxide nanoparticles on a molecular level. Although work is still required to flesh out the appropriate conditions to

access the controlled growth of cobalt oxide nanoparticles, other metal oxide core materials are accessible via the slow injection synthesis. Chapters II – IV have discussed efforts in synthesizing uniform nanoparticles and integrating them into systems for a desired application. As chemists continue to develop ways of integrating new nanomaterials into a wide range of technology sectors it is important to understand what impact these materials will have on human health and the environment.

Chapter V investigates which structural features of metal oxide nanoparticles influence their toxicity. Specifically, the influence of the electronic structure and surface passivation is probed using embryonic zebrafish as a biologic model. Three different metal oxide core materials where chosen due to their differences in conduction band energy minima in relation to the cellular redox window. To probe surface passivation, the surface chemistry of each metal oxide core was modified to produce both an un-passivated nanoparticle and a passivated nanoparticle. While all three un-passivated nanoparticles resulted in mortality within 24 hours, at the same concentrations the passivated nanoparticles showed no adverse effects. The presence of a passivating molecular layer effectively turned off the toxicity of two of the materials and significantly reduced that of the third. These findings suggest that metal oxide nanoparticles, beyond just iron oxide, may be explored for biomedical applications.

CHAPTER V

SURFACE PASSIVATION, NOT CORE COMPOSITION, DRIVES METAL OXIDE NANOPARTILE *IN VIVO* BIOCOMPATABILITY

Note: Portions of this chapter are expected to appear as Kellon, J. E.; Truong, L.; Tanguay, R. L.; Hutchison, J. E. Surface Passivation, Not Core Composition, Drives Metal Oxide Nanoparticle *in vivo* Biocompatibility. All materials synthesis and characterization were performed by me. All toxicity assays were performed by L. Truong. J. E. Kellon was the primary author of this chapter and J. E. Hutchison and R. L. Tanguay provided editorial assistance.

Introduction

Metal oxides are among the most widely investigated inorganic materials due to their abundance in nature and use in technological applications. In more recent years much research has focused on the nanoscale forms of metal oxides as promising materials for a wide range of technology sectors including, electronics,[1–3] optics,[4,5] energy storage and production,[6,7] human health,[8] water remediation[9] and catalysis.[10,11] Their broad utility is derived from their size- and structure-dependent properties that arise due to the unique size regime they inhabit. As chemists continue to develop synthetic methods to tune the structural features of metal oxide nanomaterials, their distribution and range of applications will only continue to grow. As these materials continue to be incorporated

into our society, it is imperative that we develop an understanding of how structural features impact their overall toxicity.

Within the last decade there have been many attempts to correlated toxicity to specific structural properties, such as size,[12] shape,[12–14] surface chemistry[13,15–18] and NP electronic structure.[19–21] Despite much work in this area, contradictory trends in the literature have made it difficult to conclude any structure-property relationships. Although it is still unclear which structural features lead to a toxic response, it has been established that nanomaterials in general have three different mechanisms of toxicity: (1) the generation of reactive oxygen species (ROS),[22–24] (2) metal ion release[25–29] and (3) electrostatic interactions that disrupt the lipid bilayer.[30] Metal oxide NP toxicity is most commonly attributed to ROS generation and metal ion release. Wang et al showed that the mechanism of metal oxide NP toxicity is dependent on the behavior of the core material under exposure conditions and that all NPs tested fell into one of three categories: the presence of leached metal ions, the presence of the entire metal oxide NP or a combination of both.[27] Additionally, work by Zhang and co-workers observed that for metal oxide NPs that do not leach toxic ions, there was a correlation between the band-gap and toxicity. This correlation is attributed to the overlap of the conduction band minima, E_{CB}, with the cellular redox window. The cellular redox window is the range of energy levels where biomolecular redox couples occur. The proposed mechanism of toxicity is the generation of ROS by NPs with E_{CB} minima that overlapped with the cellular redox. In addition to core behavior, numerous studies on metal oxide NPs have found that the molecular coating of the particle impacts their behavior and resulting toxicity.[18,24,31–37] For example, a study by Yang and co-workers showed that the length of

the passivating ligand shell on copper oxide NPs influenced the extent of ROS generation.[23]

Although we know that both the behavior of the core material and the identity of a molecular coating impact metal oxide NP toxicity, there are several challenges that need to be addressed if we are to develop a structure-property relationship for toxicity. Because it is not common to characterize the materials being tested under relevant exposure conditions, contradictory toxicity results in the literature are often attributed to differences in the exposure concentrations, particle solubility, extent of aggregation, the presence of additives and the synthetic conditions used for particle formation.[38] Often the as synthesized metal oxide NPs are not available for exposure, meaning they are not soluble under relevant exposure conditions causing them to aggregate and precipitate out of solution leading to limited interaction with the biological system. To overcome this limitation, it is common to use additives or surfactants to produce well-dispersed suspensions of particles. When surfactants/additives are used, the NP suspension is typically sonicated to break up the NP aggregates and encourage the surfactants to coat the cores. Sonication can be harsh on NP cores by inducing etching, and one study even found that polymeric dispersants may be degraded under sonication and generate toxic byproducts.[39]

Another common route to disperse NPs is through the use of biocompatible materials such as protein serums.[31,32,40] It has been well-established that metal NPs, depending on their ligand shell, are readily coated with proteins adsorbed from the serum forming a protein corona over the NPs which then influences cellular responses.[41] The methods used to generate water soluble metal oxide NPs often results in a change in the

surface chemistry or morphology of the material. A previously un-passivated material may now have a weakly-coordinated molecular coating that passivates the NP surface. Previous studies on metal oxide NPs clearly suggest that the surface chemistry influences toxicity, however few studies rigorously characterize the NPs under relevant conditions. Often this new surface chemistry is not considered in the interpretation of the toxicity assay resulting in claims about a material that is structurally different than what was studied.

Although much work has been done to understand what structural features of metal oxide NPs influence toxicity, no clear trend has emerged. While some researches have reported that the cores electronic structure is the most influential, other studies suggest differences in surface chemistry or toxic ion release are the properties that dictate toxic response. Beyond empirical studies, efforts have been made to predict metal oxide NP toxicity using nano-quantitative structure activity relationships (nQSAR) modelling.[42–47] Predictive models like these would be extremely helpful in the rapid screening of engineered nanomaterials. However, contradictory observations in the literature prevent the construction of reliable models. In order to begin filling these knowledge gaps, systematic studies of well-characterized metal oxide NPs are required.

The goal of this study is to investigate the influence of both the electronic structure and surface passivation of metal oxide NPs. Three different core materials, each with different electronic energy profiles, were synthesized to range in core size between 7 – 10 nm with narrow dispersity among each core material. The surface chemistry of each core material was then modified to produce both passivated and un-passivated NPs, yielding six materials: un-passivated α-Fe_2O_3, passivated α-Fe_2O_3, un-passivated CoO,

passivated CoO, un-passivated In_2O_3 and passivated In_2O_3. Additionally, the NPs used in this study were characterized under relevant exposure conditions and are available for exposure without the use of surfactants, additives or sonication. By manipulating the ligand shell to achieve water-soluble, un-passivated and passivated NPs starting from the same NP core, we are able to systematically observe the influence of the electronic structure and surface chemistry on metal oxide NP toxicity.

Results and Discussion

Materials and experimental design

The lack of consensus in the literature around the mechanism of metal oxide NP toxicity calls for a systematic study to elucidate the influence of electronic structure, toxic ion release and surface passivation on toxic response. The materials being tested need to be roughly the same core size and dispersible in water. To elucidate the influence of the NP electronic structure, each core material must have a conduction band energy minima that lies in a different energetic relationship to the cellular redox window: above, within, or below. In addition to electronic structure, we wanted to observe the role of surface passivation. This requires that water-soluble passivated and un-passivated core materials are synthetically accessible. The NPs should also undergo the same treatment to render them water-soluble in order to ensure that only core composition, and not surface chemistry differences, are being observed. Lastly, we chose to avoid metal oxides that release toxic ions in order to simplify the analysis.

In selecting and designing the materials for this study, existing materials had limitations. Often, two different synthetic routes are required to make metal oxide NPs with different ligand shells. Unfortunately, different synthetic routes to make NPs with

the same core composition results in surface chemistry differences at the atomic-level that influence properties and toxicity.[18,48] In addition, the core materials need to be of similar size and made using similar synthetic methods. We needed to develop new routes to access un-passivated and passivated cores in order to avoid the unwanted influence of synthetic methods on experimental outcomes.

Three different core materials were chosen, α-Fe_2O_3, CoO and In_2O_3 because of their different electronic band structures and synthetic accessibility. The cellular redox window ranges from -4.2 to -4.8 eV. α-Fe_2O_3 and In_2O_3 cores were chosen because their reported E_{CB} values, -4.99 and -3.63 eV respectively, lie outside of the cellular redox window.[19] CoO was chosen because its E_{CB} value, -4.42 eV, lies within the cellular redox window (Figure 5.1). In addition, these materials are synthetically accessible in core size ranging from 7 – 10 nm with similar surface chemistries. To probe the influence of surface passivation the three core materials were further modified to produce a series of three passivated and three un-passivated NPs. Previous work on the removal and replacement of oleate ligands from the surface of metal oxide NPs has allowed for both

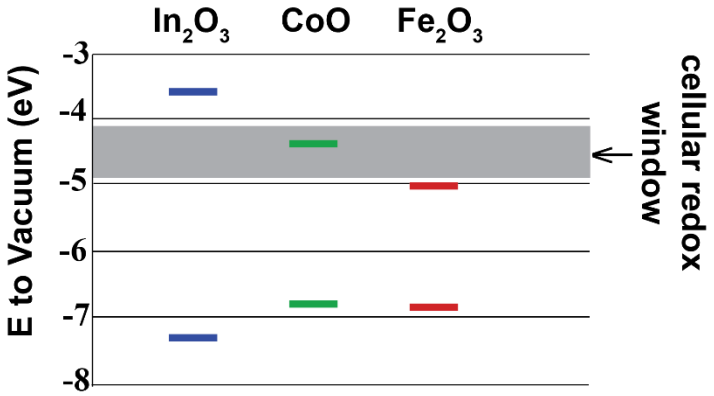

Figure 5.1: Proposed relationship of band gap energy to the cellular redox window (-4.12 to -4.84 eV). The conduction band and valence band energies were previously reported by Zhang *et al* and used for these core materials based on their experimentally determined crystal structures.

the passivated and un-passivated NPs to be made from the same starting NP cores.[49–51] The ability to retain the NP structure while modifying only the surface chemistry ensures that we are observing only the influence of surface passivation.

What is unique about our study is that we first synthesized the NP cores using the same or similar synthetic approaches and then modified their surface chemistry. This approach produces a set of passivated and un-passivated NPs with the same core composition, size and electronic structure for a complete series of six metal oxide NPs, Table 5.1. We assessed the toxicity of these six metal oxides NPs using the developmental zebrafish assay. The zebrafish model is a sensitive assay that is used to identify structure-bioactivity relationships in only five days.[15,52,53] Due to the ability of the zebrafish to develop in low to no ion media, the assay results are not hampered by media induced NP aggregation and/or precipitation. Additionally, this powerful model utilizes small volumes (100 µL), which is ideal when synthesizing precision NPs.

Table 5.1: Physicochemical properties of the semi-conducting metal oxide core materials.

Metal Oxide Nanoparticle Core	**Surface Chemistry**	**d_{core} by SAXS (nm)**	**Crystal Structure**	**E_C (eV) Lit. values**	**E_V (eV) Lit. values**
α-Fe_2O_3	un-passivated	7.3 ± 1	Spinel	-4.99	-6.99
	passivated	7.3 ± 1			
CoO	un-passivated	10 ± 3	Rock salt	-4.42	-6.83
	passivated	10 ± 3			
In_2O_3	un-passivated	7.5 ± 0.8	Bixbyite	-3.63	-7.32
	passivated	7.5 ± 0.8			

Nanoparticle synthesis

The In_2O_3 and α-Fe_2O_3NPs used in this study were synthesized using the slow injection synthesis developed by the Hutchison lab.[54] Briefly, indium (III) acetate and iron (II) acetate salts were stirred with oleic acid at 150^o C for 1.5 hours to yield the corresponding metal oleate precursors. These metal oleate precursors were slowly added to hot oleyl alcohol yielding oleate stabilized metal oxide nanocrystals of a predictable core size. The slow injection synthesis produces bixbyite In_2O_3 and spinel α-Fe_2O_3 nanocrystals as confirmed by the powder X-ray diffraction (pXRD) patterns (Figure B1). The CoO NPs were synthesized according to a previously published method where cobalt (III) acetylacetonate was stirred under an inert atmosphere in the presence of oleylamine for eight hours yielding oleylamine stabilized CoO NPs with the rock salt crystal structure confirmed by pXRD.[55]

Particle core sizes were measured using small angle x-ray scattering (SAXS) patterns (Figure B2), and all materials used in this study ranged in core diameter from 7 – 10 nm (Table 5.1). Transmission Electron Microscopy (TEM) was used to confirm the spherical particle morphology of the oleate/oleylamine stabilized NP cores before and after surface modification (Figure 5.2). The slow injection synthesis used to make the α-Fe_2O_3 and In_2O_3 cores produces single-crystal NPs having grown layer-by-layer from a single nuclei.[56] Unlike the slow injection synthesis, the thermal decomposition synthesis produces CoO NPs through oriented attachment, making less uniform NP cores. [57]

Nanoparticle surface modification

Un-passivated metal oxide nanoparticles. The hydrophobic oleate/oleylamine ligands were removed using a previously published ligand stripping method.[49] The NPs

were dispersed in hexanes and combined with 0.02 M nitrosyl tetrafluoroborate ($NOBF_4$) in dimethyl sulfoxide (DMSO) to form a bi-phasic mixture (Scheme 5.1). Upon vigorous stirring the oleate/oleylamine ligands were removed and the NPs transferred to the

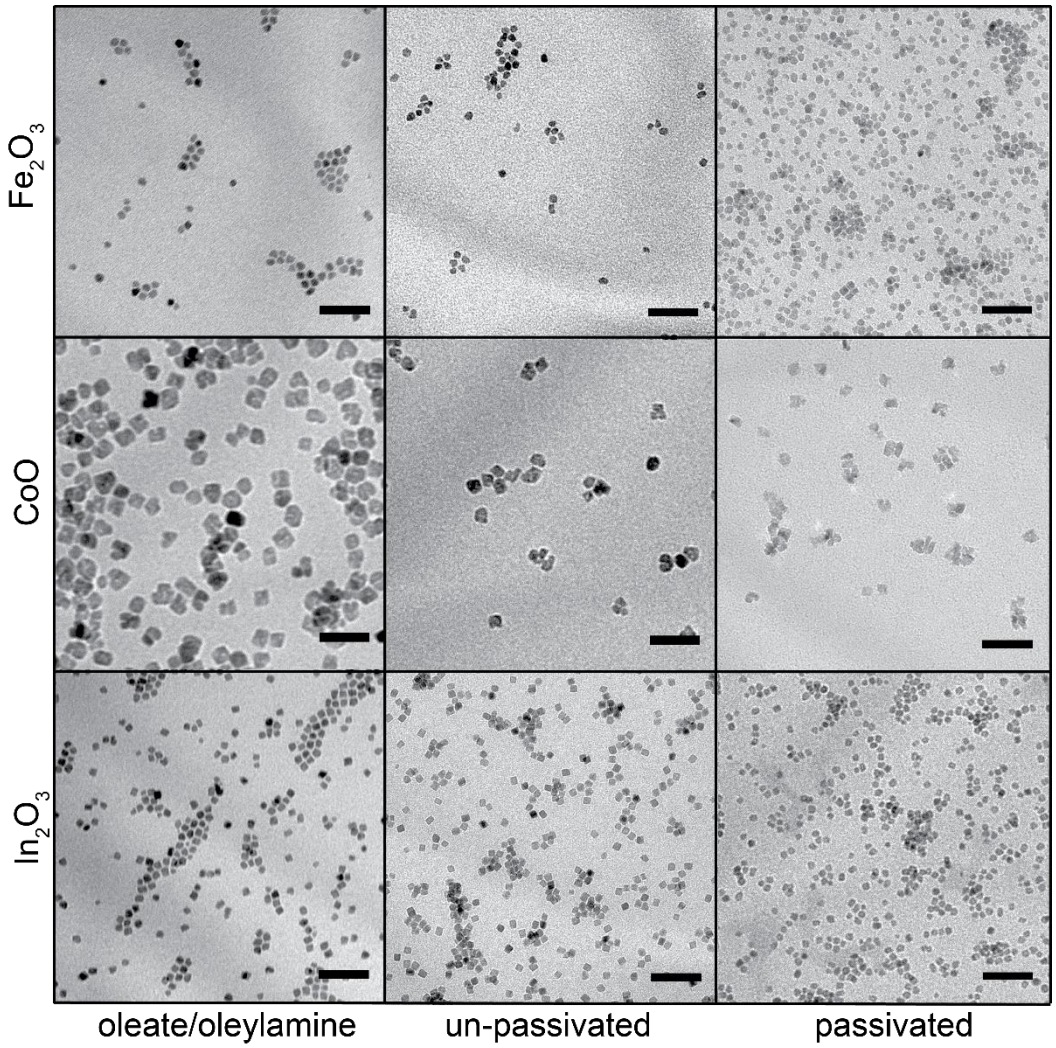

Figure 5.2: Transmission Electron Microscopy images of oleate/oleylamine, un-passivated and passivated NP cores with 50 nm scale bars.

DMSO phase. As can be seen in Figure 5.2, the removal of the oleate/oleylamine ligands with $NOBF_4$ does not change the NP core size or morphology.

X-Ray Photoelectron Spectroscopy (XPS) was used to characterize the surface chemistry of the un-passivated particles (Figures B3-B5). The presence of boron and

fluorine 1s peaks indicate the NPs are partially stabilized by tetrafluroborate (BF_4^-) anions. In addition, the atomic ratio of boron to fluorine is 0.23 which is close to the 0.25 expected for BF_4^- anion. A sulfur 2p peak at 167.1 eV suggests that the DMSO is participating in the core stabilization. The presence of solvent stabilization by dimethyl formamide was observed by Dong and co-workers.[49] Additionally, the carbon 1s spectra can be fit to a hydrocarbon peak at 284.8 eV, a peak at 286 eV originating from the methyl groups on the DMSO and an additional ester peak at 288.9 eV from remaining oleate ligands for the In_2O_3 and α-Fe_2O_3 NPs. The change in the atomic ratio of the C1s ester to Fe2p/In3d peak correlates to a 50% removal of the oleate ligands for the In_2O_3 and α-Fe_2O_3 NPs. The N1s peak from the oleylamine ligand was used to determine the

Scheme 5.1: Removal and replacement of hydrophobic oleate/oleylamine ligands from the same starting NP cores.

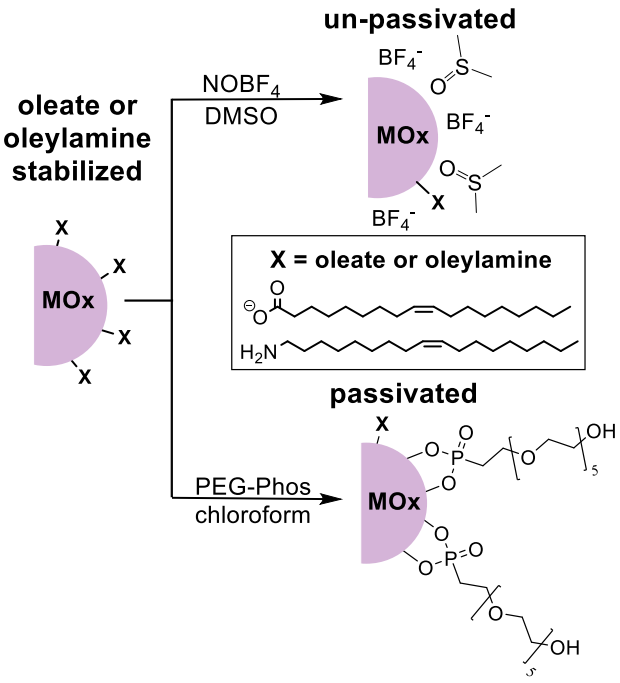

extent of ligand removal for the CoO NPs and corresponds to a 78% removal. Although this ligand stripping method does not remove 100% of the oleate/oleylamine, the phase

transfer indicates that enough oleate/oleylamine ligands were removed to render the NPs hydrophilic.

Passivated metal oxide nanoparticles. A pentaethylene glycol (PEG) with a phosphonic acid head was chosen to replace the oleate/oleylamine ligands because of the hydrophilicity of PEG and the affinity of phosphonic acid for metal oxide surfaces. A simple ligand exchange procedure developed by Davis and co-workers was utilized, where the NPs and the PEG-phosphonic acid (PEG-Phos) were stirred at room temperature in chloroform overnight.[50] After washing with diethyl ether, the NPs could easily be re-dispersed in ethanol. As illustrated in Figure 5.2, the NP core size and morphology is unchanged during the replacement of the oleate/oleylamine ligands with the PEG-Phos ligand. Similarly to the un-passivated NPs, the oleate/oleylamine ligands are not completely removed but enough ligand exchange occurred to solubilized the NPs in a polar solvent.

XPS was used to confirm that the oleate/oleylamine ligands were replaced by the PEG-phos (Figures B6-B8). The presence of a P2p peak at 132.5 eV and C1s ether peak at 286.2 eV indicates that the PEG-phos ligand is passivating the surface of the metal oxide NPs. The extent of ligand exchange cannot be determined for the In_2O_3 and α-Fe_2O_3 NP cores because the C1s ester peak lies within the C1s ether peak. The change in atomic ratios between the N1s amine and Co2p peaks correspond to a 51 % replacement of oleylamine ligands by PEG-phos.

Particle stability under exposure conditions

To prevent experimental artifacts, the NPs being tested must be dispersible throughout the length of the exposure. The materials used in this study are soluble under

relevant exposure conditions and the NPs remain dispersed in solution throughout the entirety of the toxicity assay. Previous toxicity studies of metal oxide NPs have been complicated by the fact that the materials under investigation are often not readily dispersed and available for interaction under relevant exposure conditions. It is typical for NPs to be ultra-sonicated in the presence of surfactants for extended periods of time in order to disperse the NPs in the exposure media. Although the use of sonication and additional surfactants may disperse the NPs briefly in the exposure media, they often crash out of solution and do not actually interact with the biological system as intended. Additionally, sonication is harsh on NP cores and can cause a change in their morphology often resulting in the study of a different set of materials.[39] Although it is well known that NP surface chemistry has a significant impact on the observed toxicity, the use of surfactants is often overlooked when interpreting the resulting toxicity. What is unique about the NPs tested in this study is that they are available for exposure without any additional surfactants or sonication.

UV-vis spectroscopy (Figure 5.3) in corroboration with TEM (Figures B9 and B10) was used to evaluate the stability of the NPs under the conditions in which they were exposed to the zebrafish. The stability studies were conducted at the highest concentration of NPs the zebrafish were exposed to, 100 μg/mL in 1% DMSO or ethanol in H_2O. UV-vis spectra and TEM micrographs were collected at the initial dilution time point, t = 0 h, and again after 18 hours under exposure conditions. The UV-vis spectra indicate that after 18 hours under exposure conditions the NPs are still available for interaction with the zebrafish.

By UV-vis the un-passivated α-Fe_2O_3 and In_2O_3 NPs behave similarly. Both the α-Fe_2O_3 and In_2O_3 traces retain their shape with 55% and 49% of the NPs remaining in solution after 18 hours, respectively. The increase in the baseline absorbance for both traces is indicative of light scattering caused by some NP aggregation. Additionally, TEM was used to observe whether the particle morphology changes under exposure conditions (Figure B9). By TEM, the un-passivated α-Fe_2O_3 and In_2O_3 NPs retain their morphology and core size throughout the experiment with no signs of etching.

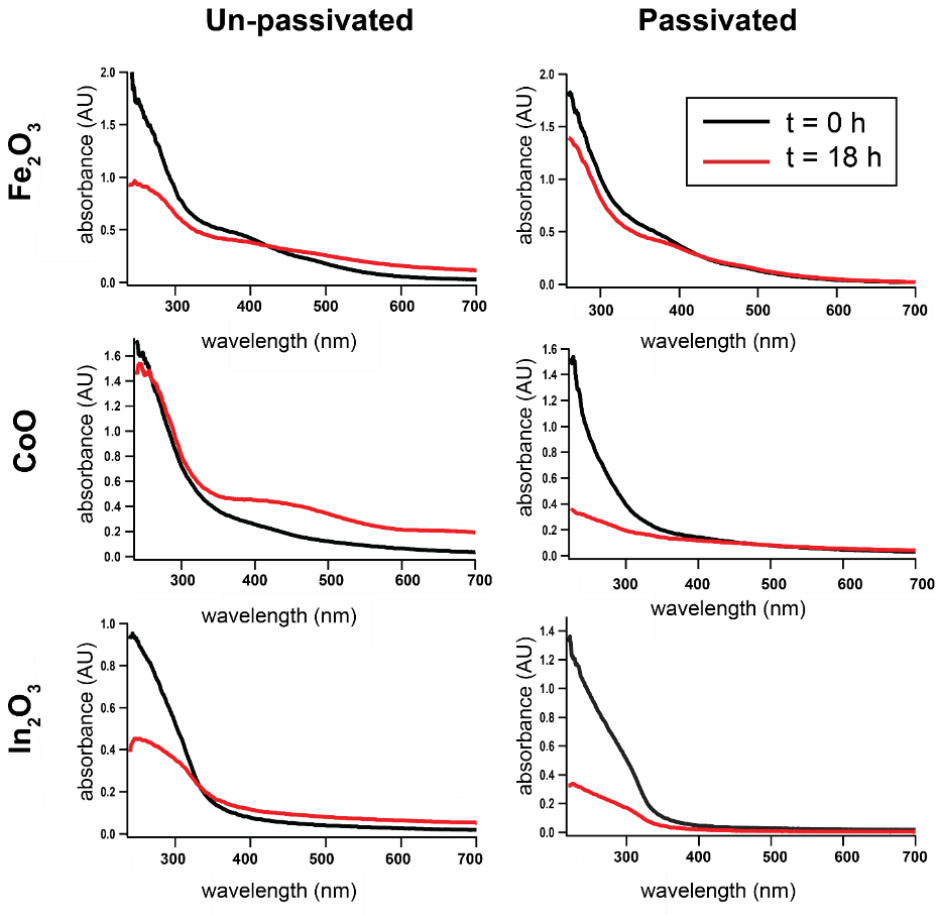

Figure 5.3: UV-vis spectra of 100 µg/mL solutions of un-passivated α-Fe_2O_3, CoO and In_2O_3 NPs in 1% DMSO in H_2O and 100 µg/mL solutions of passivated α-Fe_2O_3, CoO and In_2O_3 NPs in 1% ethanol in H_2O.

The un-passivated CoO NPs behave differently than the un-passivated α-Fe_2O_3 and In_2O_3 NPs under the same exposure conditions. By UV-vis 92% of the NPs remain in solution after 18-hours. Similar to the α-Fe_2O_3 and In_2O_3 NPs, the baseline absorbance increases, indicating some aggregation over 18 hours. The shape of the UV-vis trace changes after 18 hours indicating a change in NP morphology. The peak at 425 nm increases in its relative intensity while a new peak at 692 nm grows in. By TEM, the NP cores are smaller in size and have formed large networks of small NP aggregates. The different behavior observed by the un-passivated CoO cores may be due to the difference in core morphology. As previously stated, the synthesis used for the α-Fe_2O_3 and In_2O_3 produce single crystal particles while the CoO NPs appear less uniform by TEM.

Unlike the un-passivated NPs, the passivated NPs show no signs of aggregation or morphology changes by UV-vis, Figure 4, or TEM, Figure B10. The UV-vis traces for all three core materials retain their shape with no increased baseline absorbance after 18 hours. The passivated α-Fe_2O_3 NPs show the most stability to crashing out with 75% remaining in solution. Alternatively, 33% of the passivated In_2O_3 and CoO NPs remain in solution.

Elucidating metal oxide nanoparticle toxicity

The zebrafish embryos were statically exposed to a broad concentration range of NPs (1-100 μg/mL) with a final well concentration of 1% DMSO or ethanol in water. The exposure was initiated prior to organogenesis (6 hours post fertilization; hpf) until 120 hpf when most of the organs have been formed. Mortality and 18 morphological endpoints are assessed at two developmental time points: 24 and 120 hpf. At both endpoints, mortality is noted, and sublethal effects were assessed, a majority at 120 hpf.

Some of the morphological endpoints include malformations in the eye, jaw, snout, etc.[58,59]

Toxicity and bioactivity of the six metal oxide nanoparticles. When all six NPs were assessed in the developmental toxicity zebrafish model, a trend was revealed; the un-passivated NP cores lead to mortality while the passivated core materials did not. Figure 5 provides a developmental profile of the zebrafish from 6 – 120 hpf upon NP exposures ranging from 1 – 100 µg/mL. The red boxes present at exposure concentrations greater than 31 µg/mL for all three un-passivated NPs indicate a statistically significant effect. The un-passivated NPs, regardless of the core material, induced mortality at exposure concentrations greater than 31 µg/mL. Furthermore, the NPs resulted in mortality after only 24 hpf. The absence of statistically significant morbidity effects at the 120 hpf timepoint is a result of mortality after 24 hpf.

Largely, the passivated NPs are biocompatible at the same exposure concentrations, with the exception of CoO at the highest concentration tested. As illustrated in Figure 5.4, neither the passivated In_2O_3 and α-Fe_2O_3 NPs yield any statistically significant effects at any of the concentrations tested. The passivated CoO NPs did induce adverse effects at the highest concentration, 100 µg/mL. However, unlike the un-passivated CoO NPs that only induced mortality, the passivated CoO NPs resulted in a combination of mortality and morbidity. The statistically significant response in the any except MORT portion arises from malformations in the trunk, fin, axis and yolk sac edema (Figure B11).

For the un-passivated NPs and the passivated CoO NPs an effective concentration that induces 50% incidence, EC_{50}, value was calculated, and dose response curves were

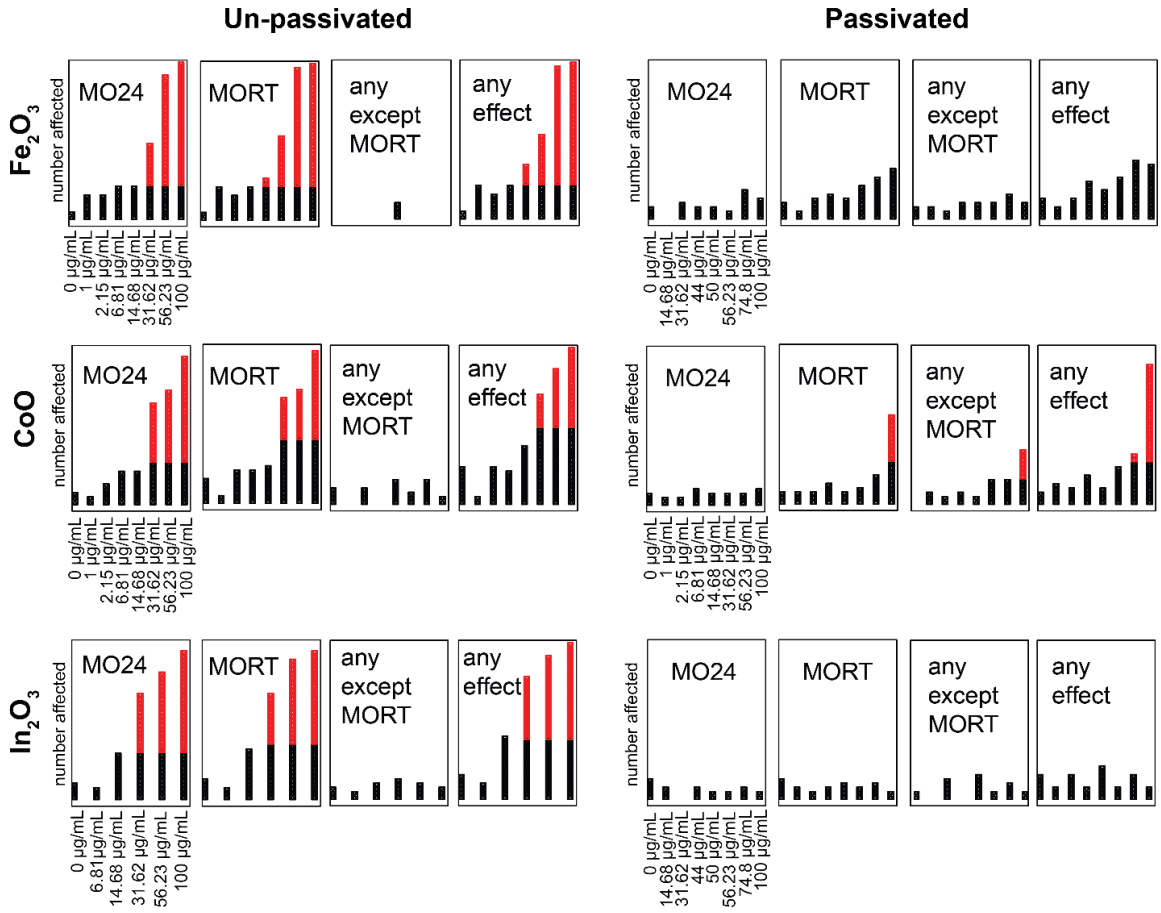

Figure 5.4: Developmental profile of un-passivated and passivated α-Fe_2O_3, CoO and In_2O_3 nanoparticles. Embryonic zebrafish are developmentally exposed from 6 to 120 hours post fertilization (hpf) to 6 concentrations (0-100 µg/mL) of each of the NPs. At 24 and 120 hpf, the embryos are evaluated for mortality and 18 morphological endpoints. For each endpoint, the number of embryos exhibiting that effect is denoted as a square, and once the accumulation of affected individuals passes a statistically significant threshold (a Fishers Exact Test, $p<0.05$), then the additional affected individuals are noted as red. A total of 32 animals are exposed per concentration. MO24: mortality observed at 24 hpf; MORT: cumulative mortality at 120 hpf; any except MORT: a summary endpoint representing individuals that had any of the 18 morphological endpoints; any effect: a summary endpoint of any effected individual (including mortality). All 18 morphological endpoints can be found in the supplemental information.

generated for all six materials (Figure 5.5). Instead of using a mass dose metric we used total NP surface area. Previous studies have demonstrated that it is more appropriate to use a total surface area dose-metric for NP toxicity assays.[60,61] For instance, all three un-

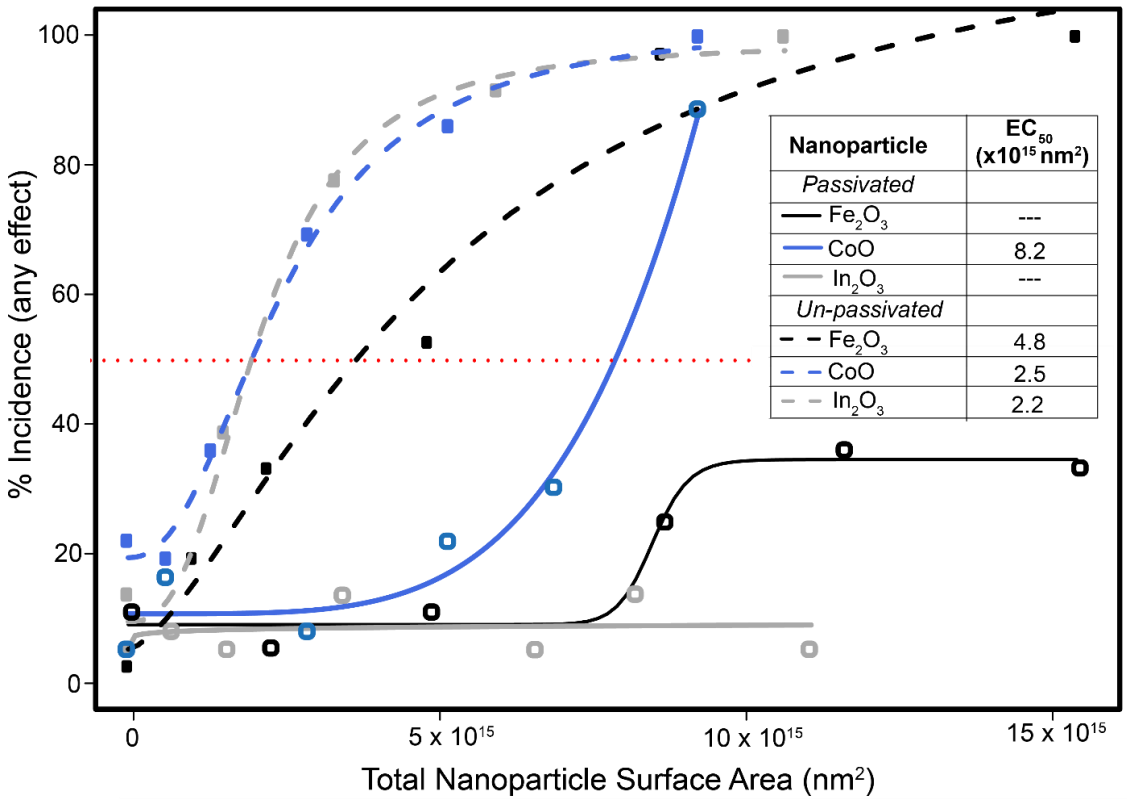

Figure 5.5: The concentration response profiles of the un-passivated and passivated metal oxide nanoparticles when the exposure medium is expressed in surface area (nm^2). The percent incidence of the affected animals (for any endpoint) are plotted for each of the NPs and curve of best fit is applied. The dotted lines represent the un-passivated samples, and the solid lines represent the passivated NP. The horizontal red link denotes the 50% affected threshold used to compute the EC_{50}.

passivated NPs induced mortality beginning at 31.6 µg/mL suggesting there is no difference in toxicity between the three core materials. However, when total NP surface area is used to calculate the EC_{50} values, differences in core material become evident. As illustrated in Figure 5.5, the line of best fit for the un-passivated α-Fe_2O_3 intersects the 50% incidence line (red; EC_{50}) at a higher surface area than the un-passivated CoO and In_2O_3. Additionally, the EC_{50} value for the un-passivated α-Fe_2O_3 NPs is almost twice that of the un-passivated CoO and In_2O_3 NPs (4.8 vs ~2.3 x 10^{15} nm^2).

EC_{50} values could not be calculated for the passivated In_2O_3 and α-Fe_2O_3 NPs because neither induced statistically significant effects. The EC_{50} value calculated for the passivated CoO NPs, 8.2 μg/mL, is 4-times greater than for the un-passivated CoO and In_2O_3 cores. These results suggest that although the passivated CoO NPs have adverse effects at the highest concentration, they are significantly more biocompatible than un-passivated cores. The data do not indicate a correlation between the electronic structure of the NP core materials and NP toxicity but clearly demonstrate the influence of surface passivation.

Potential mechanisms of toxicity

Our results clearly show that surface passivation has a greater influence on NP toxicity than the electronic structure of the core material. As previously stated, metal oxide NP toxicity is typically explained by either ROS generation, the leaching of toxic ions or the combination of both. All three un-passivated NPs induced mortality within 24 hours indicating that these un-passivated core materials are highly reactive. The materials chosen are known to only result in minimal (< 2%) ion release and are non-toxic at the concentrations tested,[19,27] suggesting that the un-passivated NPs readily generate ROS. We also considered that the observed toxicity could be due to the ionically coordinated BF_4^- ion. $NaBF_4$ was tested at a concentration assuming 100% coverage of the NP surface at the 100 μg/mL exposure concentration. No statistically significant effects were observed at this concentration of $NaBF_4$ (Figure B12).

Some researchers have correlated ROS generation from metal oxide NPs with the overlap of that materials E_{CB} with the cellular redox window.[19,20] They suggest that if the E_{CB} lies within the cellular redox window, redox reactions between biological redox

couples and the NP are facile leading to a toxic response while materials with E_{CB} minima that lie outside of the cellular redox window are non-toxic. However, our results show that the un-passivated NPs cause mortality within 24 hours regardless of the relation of the E_{CB} with the cellular redox window. Interestingly, the same core materials did not induce statically significant effects at the same concentrations once the NP surface was passivated with a tightly bound ligand shell. These data suggest that the NP surface is highly reactive and if that surface is available to come in direct contact with biological species, unfavorable redox reactions can occur leading to adverse outcomes.

A significant amount of research aimed at using iron oxide NPs for biomedical applications exists due to the belief the iron oxide is inherently non-toxic.[62–64] Despite these claims we expected to observe some threshold of toxicity for the un-passivated α-Fe_2O_3 NPs. Although, we did not expect the toxicity threshold to be at the same mass concentration as the un-passivated CoO and In_2O_3 NPs. However, when the results are presented with respect to total NP surface area, the α-Fe_2O_3 NPs are significantly less toxic than the other core materials.

The presence of a tightly bound, passivating ligand shell rendered the α-Fe_2O_3 and In_2O_3 NP cores biocompatible at all concentrations tested and the CoO NPs at concentrations below 100 μg/mL. Although other core materials are known to be biocompatible when passivated with a PEG ligand, these studies have compared the toxicity of NPs with different passivating ligand shells.[65–69] This is the first systematic study that compares un-passivated and passivated NPs and shows that surface passivation renders toxic core materials biocompatible. As previously stated, we believe the un-passivated NP surfaces are highly reactive. The presence of a surface passivating ligand

may prevent the core material from coming into direct contact with biological species. If the ligand shell fully passivates the core material, the highly reactive surface would not be able to undergo facile electron transfer to generate ROS.

Interestingly, the toxic response of the passivated CoO cores was different than the other passivated cores. The passivated CoO cores are toxic under the highest exposure conditions, but unlike the other NPs, mortality was not the only significant endpoint. The difference in toxicity between the passivated CoO NPs and the passivated α-Fe_2O_3 and In_2O_3 may result from either differences in surface chemistry and/or electronic structure. The different synthetic methods used to make the In_2O_3/α-Fe_2O_3 and the CoO NPs may produce differences in surface chemistry. Differences in the amount of surface defects and oxygen vacancies have been observed for the same metal oxide core materials prepared by different synthetic methods.[18,48] The α-Fe_2O_3 and In_2O_3 NPs grow as a uniform single crystal, while the thermal decomposition synthesis produces CoO NPs through oriented attachment. By TEM the CoO NP cores appear to be less uniform than the α-Fe_2O_3 and In_2O_3 cores (Figure 5.2). The uniformity of the α-Fe_2O_3 and In_2O_3 NP surfaces may result in tighter binding of the PEG-Phos ligand to their surface. If the passivated CoO NPs are losing their ligands over time, that would result in exposed areas on the NP surface that are then available to directly interact with biological species and generate ROS.

Another potential explanation for the toxic response of the passivated CoO NPs is because of their electronic structure. The E_{CB} of the CoO NPs lies within the cellular redox window, while that of the α-Fe_2O_3 and In_2O_3 NPs lie below and above, respectively. Although the electronic structure of the core did not influence toxicity for

the un-passivated NPs, perhaps when the highly reactive NP core surface is passivated, the electronic structure becomes influential. Despite the mechanism of toxicity for the passivated CoO NPs, it is clear that surface passivation has a greater influence on the relative biocompatibility of metal oxide NPs. While un-passivated metal oxide NP cores result in a toxic response, the presence of a surface passivating ligand shell renders the same core material biocompatible.

Conclusion

By careful control of both the nanoparticle core composition, size and surface chemistry we were able to systematically study the influence of both electronic structure and surface passivation on metal oxide NP toxicity. The surface chemistry of three metal oxide core materials was modified to produce a passivated and un-passivated NP, yielding a series of six materials total: passivated and un-passivated α-Fe_2O_3, In_2O_3 and CoO. The three different core materials were chosen because of their differences in electronic structure in relation to the cellular redox window and because they do not leach toxic ions. Our findings clearly show that surface passivation has a greater influence on toxicity than the electronic structure of the core material.

Although all three un-passivated core materials induced mortality within 24 hours at the three highest exposure concentrations, the α-Fe_2O_3 NPs were less toxic than the In_2O_3 and the CoO NP cores. The presence of a passivating PEG-phos ligand for the same core materials either completely turned off the toxicity for both the α-Fe_2O_3 and In_2O_3 NPs, or significantly reduced it for the CoO NP cores. This is the first systematic study showing that surface passivation renders toxic metal oxide NP core materials biocompatible. Previous work has attempted to compare the toxicity of un-passivated and

passivated iron oxide NPs, but synthetic limitations required that the NPs be pre-treated with surfactants, sonication and/or biological media to produce water dispersible materials.[31,32] The use of surfactants and biological media to render NPs available for exposure results in some molecular coordination of those species to the NP surface. Considering the influence of surface passivation on NP toxicity, it is necessary to take into consideration any potential for additional molecular coordination to the NP surface when conducting NP toxicity assays. The NPs being tested should always be well-characterized under the conditions in which the biological model will be exposed.

The insights gained regarding the influence of surface passivating and electronic structure on NP toxicity can be applied to the safer design of engineered metal oxide NPs. While electronic applications are most likely to require nanomaterials without a passivating molecular coating, biomedical and environmental applications will likely utilize a molecular coating that can be functionalized for a given application. Our results show that the electronic and structural properties of the core material do not effectively eliminate that material from use in biomedical applications. To date iron oxide is the most common metal oxide NP core material being explored for biomedical applications. However, the ability to significantly reduce the toxicity of other metal oxide core materials using a passivating ligand shell greatly expands the materials available for medicinal and environmental applications. Furthermore, although our study did not include NPs that release ions at toxic concentrations, the presence of a tightly bound ligand may prevent the leaching of toxic ions from NPs whose mechanism of toxicity is toxic ion release, such as ZnO and CuO.

Methods

Chemicals

Indium (III) acetate, Iron (II) acetate, Co (III) acetylacetonate, oleic acid (90% technical grade), oleyl alcohol (80-85% technical grade), oleylamine (70% technical grade) and nitrosyl tetrafluroborate were purchased from Sigma-Aldrich and used without further modification.

α-Fe_2O_3 nanoparticle synthesis

Iron (II) acetate (0.174 mg, 1 mmol) was added to 2 mL oleic acid and kept at 150^o C for an hour under N_2 to produce an iron oleate solution with a concentration of 0.5 mmol iron/mL oleic acid. The iron oleate solution was then added dropwise to 13.0 mL of oleyl alcohol heated to 230^o C in a 100 mL three-neck flask. The iron oleate solution was added using a 3 mL syringe and a syringe pump at a rate of 0.2 mL/min. During the addition, N_2 was flowing through the flask at a rate of 140 cc/min. After the addition ended, the reaction was cooled to room temperature and the NPs were precipitate with acetone and centrifuged at 7000 rpm for 10 min.

CoO nanoparticle synthesis

Cobalt (III) acetylacetone (0.3g, 0.8 mmol) was combined with oleylamine (55 mL) and heated to 135^o C in a N_2 atmosphere. The green slurry was stirred for five hours followed by a temperature increase to 200^o C for three hours. The reaction was then cooled to room temperature and the NPs were precipitated with acetone and centrifuged at 7000 rpm for 10 minutes.

In_2O_3 nanoparticle synthesis

Indium (III) acetate (0.292 mg, 1 mmol) was added to 2 mL oleic acid and kept at 150^o C for an hour under N_2 to produce an indium oleate solution with a concentration of 0.5 mmol indium/mL oleic acid. The indium oleate solution was then added dropwise to 13.0 mL of oleyl alcohol heated to 290^o C in a 100 mL three-neck flask. The metal oleate solution was added using a 3 mL syringe and a syringe pump at a rate of 0.35 mL/min. During the addition, N_2 was flowing through the flask at a rate of 140 cc/min. After the addition ended, the reaction was cooled to room temperature and the NPs were precipitated with acetone and centrifuged at 7000 rpm for 10 min.

Oleate/oleylamine ligand removal

The oleate/oleylamine stabilized NPs were dispersed in a 5 mg/mL hexane solution. This solution was combined in a biphasic mixture with a 0.02 M solution of $NOBF_4$ in DMSO. The reaction was stirred vigorously for an hour for the CoO NPs and overnight for the α-Fe_2O_3 and In_2O_3 NPs at which point the NPs transferred to the DMSO phase. The hexanes phase was removed via pipette and toluene was added to the DMSO phase to precipitate out the NPs. The NPs were washed twice with toluene via centrifugation at 7000 rpm for 10 min and could easily be redispersed in DMSO.

Oleate/oleylamine ligand replacement with PEG-Phosphonic acid

20 mg of the oleate/oleylamine NPs were dispersed in 2 mL of basic chloroform. In a separate 100 mL flask 18 mg of the pentaethyleneglycol-phosphonic acid (PEG-phos) ligand was combined with 40 mL of basic chloroform and sonicated for 2 minutes. Immediately after sonication the NP solution was added to the PEG-phos solution and

stirred vigorously for 48 hours. The NPs were washed with diethyl ether via centrifugation at 7000 rpm for 10 min and could easily be redispersed in ethanol.

Physical characterization

Transmission electron microscopy (TEM) images were collected on 400 mesh Cu grids (Ted Pella, Redding, CA) using a Tecnai Spirit TEM (FEI, Hillsboro, OR) operating at 120 kV equipped with a Bruker EDS detector. Samples were prepared by dip-coating the Cu grid into a dilute solution of NPs. Images were analyzed using ImageJ software, and following procedures outlined in literature. X-ray photoelectron spectroscopy (XPS) was acquired using a Thermo Scientific ESCALAB 250 X-ray photoelectron spectrometer using monochromatic Al Kα X-ray source at 20 kV. A range of scans (10 – 40) were collected on each sample at various binding energy ranges, depending on the elemental composition of the sample. Charge neutralization was used for all samples. Samples were prepared by drop-casting NP solutions onto boron-doped diamond substrates. Data reduction was done using the Avantage software package provided by the manufacturer. UV-vis spectra were collected on a JAZ spectrometer with a fixed slit width of 25 μm using 1 cm quartz cuvettes. X-ray diffraction (XRD) was carried out on a Rigaku Smartlab instrument using Bragg-Brentano geometry, Cu Kα radiation and a diffracted beam monochromator to eliminate background iron and cobalt fluorescence. Small-angle X-ray Scattering (SAXS) analysis was done on a lab-scale SAXS (SAXSess, Anton Paar, Austria). The system was attached to an X-ray generator equipped with a X-ray tube (Cu Kα X-rays with a wavelength $\lambda = 0.154$ nm) operating at 40 kV and 50 mA. The scattered X-ray intensities were measured with a charge-coupled device (CCD) detector (Roper Scientific, Germany). The raw data was processed with

SAXSquant software (version 2.0). Scattering curves were averaged over 50 individual curves for various acquisition times (2-20s).

Zebrafish husbandry and developmental toxicity test

Adult Tropical 5D zebrafish are raised at Oregon State University Sinnhuber Aquatic Research Laboratory. The fish were raised at 28^{o} C with 14 h light: 10 h dark photo cycle and fed twice daily with size appropriate Gemme Micro (Skretting Inc, Tooele, France). For the developmental toxicity testing, adult zebrafish were spawned and embryos were collected and stated according to Kimmel et al.[58] All stock solutions were provided as either 100% dimethyl sulfoxide (DMSO; un-passivated NP) or in 100% ethanol (passivated). Individual wells of a 96-well plate (Falcon U-Bottom Plate; VWR catalog #: 25382-200) prefilled with 90 µL of ultrapure water. At six hours post fertilization (hpf), embryos were dechorionated using an automated dechorionator and by adding 83 µL of 25.3 U/µL of pronase (Roche, Indianapolis, IN, USA).[59] At 6 hpf, the embryos were manually placed into the prefilled wells. A serial dilution was made to achieve 2.15, 6.81, 14.68, 31.62, 56.23 and 100.0 µg/mL for all for all but the passivated Fe_2O_3 and In_2O_3 – those were diluted at 14.68, 31.62, 44.00, 50.00, 56.23, 74.8 and 100.0 µg/mL. These working stocks contained 10% of either DMSO, or ethanol. For each NP, 10 µL of each concentration of the working stock was added to a row (n = 12) of a 96 well; this plate was replicated 3 times resulting in a total of 36 animals tested per concentration. The plates were sealed with parafilm sandwiched between the lid and the plate, then kept in the dark until 120 hpf. At 24 hpf and 120 hpf, a total of 22 endpoints are evaluate and stored in a laboratory information management system (ZAAP).[53] The developmental toxicity statistical significance was computed using a custom R script as

described in Truong et al.[53] The concentration response modeling was completed using the drm() function in drc package in R. The percent incidence for the any effect summary endpoint was used and a 4 parameter Hill model was used to establish a line of best fit and estimate the effective concentration to cause a 50% effect. All adult care and reproductive techniques follow the Oregon State University Institutional Animal Care and Use Committee protocols.

Bridge to Chapter VI

Chapter V demonstrated that surface passivation drives metal oxide nanoparticle toxicity, not core composition or electronic structure. Chapter VI summarized the key findings of this dissertation and provides an outlook to future studies and applications of this work for the smarter design of safe nanomaterials.

CHAPTER VI

CONCLUSION

Note: I am the sole author of this chapter.

Concluding Remarks

Nanoparticles will probably play an integral role in solving some of the most significant global challenges. While nanoparticle research has been a field of study for over 30 years, there are limited examples of applications involving nanomaterials. The initial phase of nanoparticle research focused on developing synthetic methods to access a wide variety of core compositions. As we move into the next phase, research efforts are shifting towards developing methods to apply these materials to address specific needs. In order to do so, three main things need to occur simultaneously. Chemists must continue investigating structure-property relationships, methods must be developed to integrate nanoparticles into new and existing technologies, and we must understand any harmful impacts these materials may have on the environment and human health and the end of their lifecycle.

This dissertation contains research in all three of the areas mentioned above. In order to understand how structure influences behavior and properties, synthetic methods are required that can access a wide range of nanoparticle sizes, composition and surface chemistry. The slow injection synthesis of metal oxide nanoparticles offers control over nanoparticle formation at the atomic-level. This level of control has enabled the

synthesis of precise metal oxide nanoparticles with predictable size, composition and surface chemistry. Efforts to expand this synthesis to form other metal oxide nanoparticles, such as cobalt oxide, will allow for systematic studies investigating the influence of nanoparticle structure to be conducted.

As chemists continue to gain atomic-level control over nanoparticle synthesis, methods of incorporating these materials into devices for a given application will need to be developed. Without the ability to integrate nanoparticles into larger systems, the promising properties of these materials are inaccessible. This dissertation has explored the existing methods of fabricating electronically conductive materials that contain discrete nanoparticles. Although the work presented here focuses on attaching small gold nanoparticles, the electrode fabrication methods outlined in Chapter II can be adapted for many different core materials, compositions and sizes.

Lastly, to prevent unintended consequences of introducing these materials into society, we must understand how they interact with the environment. Knowing which structural features influence nanoparticle toxicity is inherent to designing materials and systems that address specific needs without harming other systems downstream. The work in this dissertation is an example of what types of questions need to be addressed for nanoparticles to fulfill their potential to solve global problems.

APPENDIX A

SUPPORTING INFORMATION FOR CHAPTER III: SMALL GOLD NANOPARTICLES INTERFACED TO ELECTRODES THROUGH MOLECULAR LINKERS: A PLATFORM TO ENHANCE ELECTRON TRANSFER AND INCREASE ELECTROCHEMICALLY ACTIVE SURFACE AREA

Synthesis of 6-ferrocenyl(carbonyloxy)hexanethiol

Ferrocene carboxylic acid (2.3 g, 0.01 mol) and oxalyl chloride (4.3 mL, 0.05 mol) were dissolved in 50 mL heptane. The cloudy orange solution turned a deep brown with a small amount of white precipitate after stirring for an hour. The reaction was heated to 80°C to dissolve the remaining ferrocene carboxylic acid and stirred for an additional 30 minutes. The reaction was filtered and the filtrate condensed. Unreacted oxalyl chloride was dissolved in 40 mL heptane and removed via evaporation. The resulting ferrocene acyl chloride was combined with 6-bromohexanol (1.18 g, 0.01 mol), triethylamine (2.0 g, 0.02 mol) and 75 mL dichloromethane and stirred under nitrogen for 48 hours. The crude product was purified via column chromatography using dichloromethane as the eluent. The target compound was in the second colored, fraction (0.93 g, 25% yield).

6-(ferrocenylcarbonyloxy)hexyl bromide (0.459 g, 1.2 mmol) was dissolved in 250 mL acetone. Potassium thioacetate (0.229 g, 2.0 mmol) was added to the reaction solution and the resulting suspension was stirred for 15 hours under nitrogen. The volume of acetone was reduced and the crude compound was dissolved in 80 mL of dichloromethane. The organic layer was washed with water and brine and dried over sodium sulfate. The solvent was removed via rotary evaporation to yield 6-(ferrocenylcarbonyloxy)hexyl thioacetate (0.42 g, 90% yield).

Potassium carbonate (0.327 g, 2.3 mmol) was suspended in 15 mL methanol and stirred under nitrogen for 15 minutes. A portion of 6-(ferrocenylcarbonyloxy) hexyl thioacetate (0.42 g, 1 mmol) was dissolved in 10 mL methanol and sparged with nitrogen before adding to the potassium carbonate suspension. The reaction was allowed to stir under argon for 90 minutes. Nitrogen sparged HCl (0.2 M, 20 mL) was added to the reaction and allowed to stir for 5 minutes. The crude compound was extracted into dichloromethane. The organic layer was washed with water and brine and dried over sodium sulfate. The crude compound was purified via flash column chromatography

using dichloromethane as the eluent. The target compound was in the second colored fraction (red oil) (0.075g, 20% yield). ^{1}H NMR (300 MHz), $CDCl_3$ δ 4.81 (broad, 2H), .40 (broad, 2H), 4.20 (broad, 7H), 2.55 (q, 2H), 1.75-1.62 (broad , 4H), 1.55-1.40 (broad, 4H), 1.35 (t, 1H).

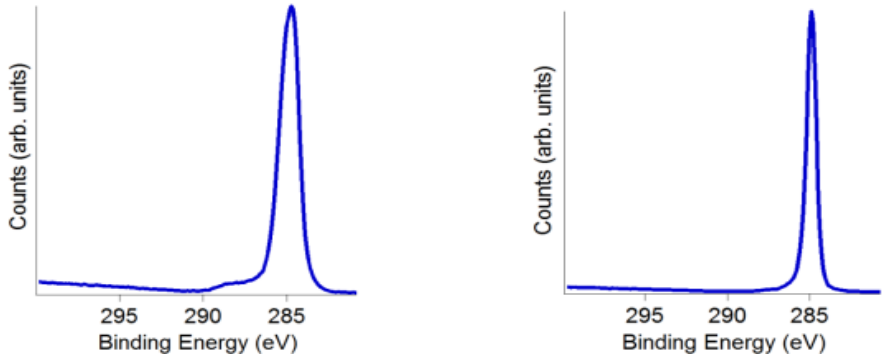

Figure A1. XPS C1s spectra of BDD before hydrogen termination (left) and after hydrogen termination (right). The sharpening of the peak at 284.8 eV and the loss of the shoulder at 288.6 eV was indicative of successful hydrogen termination of the BDD substrate.

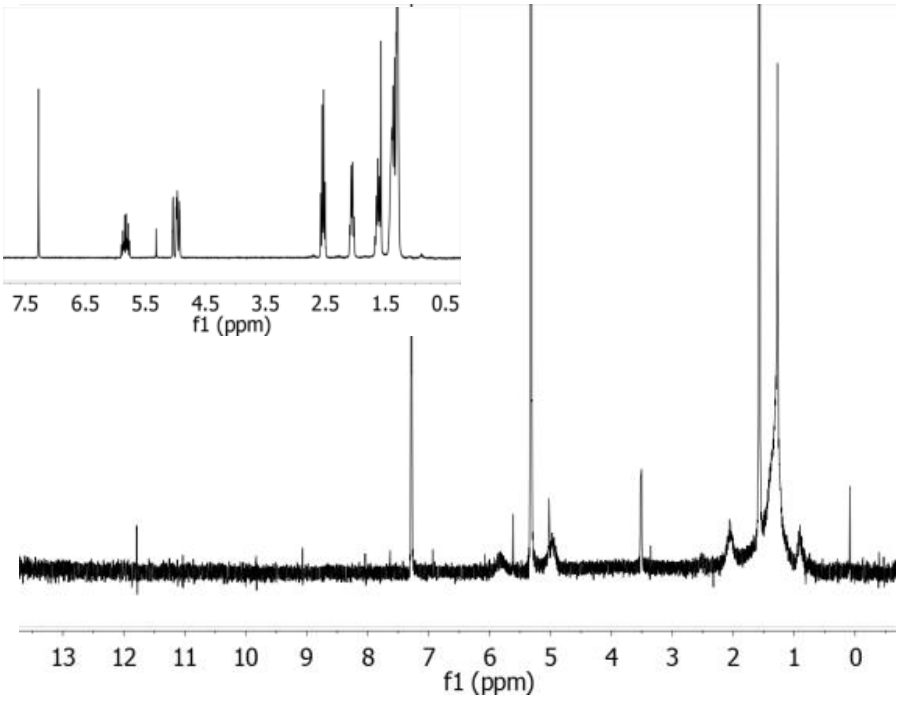

Figure A2. ^{1}H NMR of UDT AuNPs in $CDCl_3$. Inset shows the free 10-undecene-1-thiol ligand in $CDCl_3$.

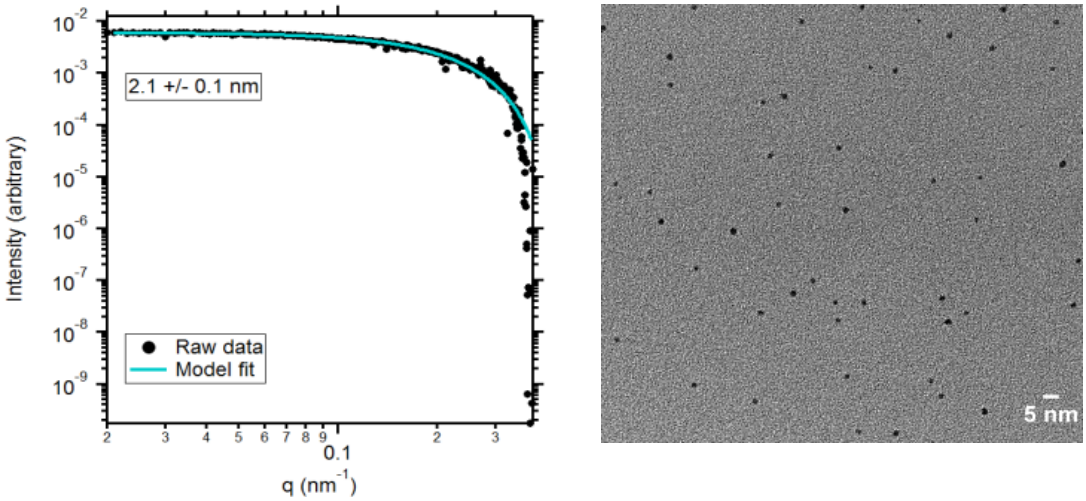

Figure A3. SAXS pattern and model fit of UDT AuNPs dispersed in heptane (left). Bright field TEM image of UDT AuNPs to corroborate the SAXS data (right).

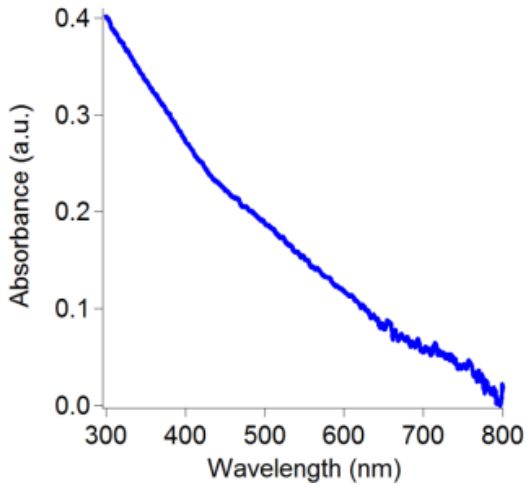

Figure A4. UV-Vis spectrum of UDT AuNPs dispersed in heptane at the concentration used for grafting experiments, showing the absence of a sharp plasmon feature.

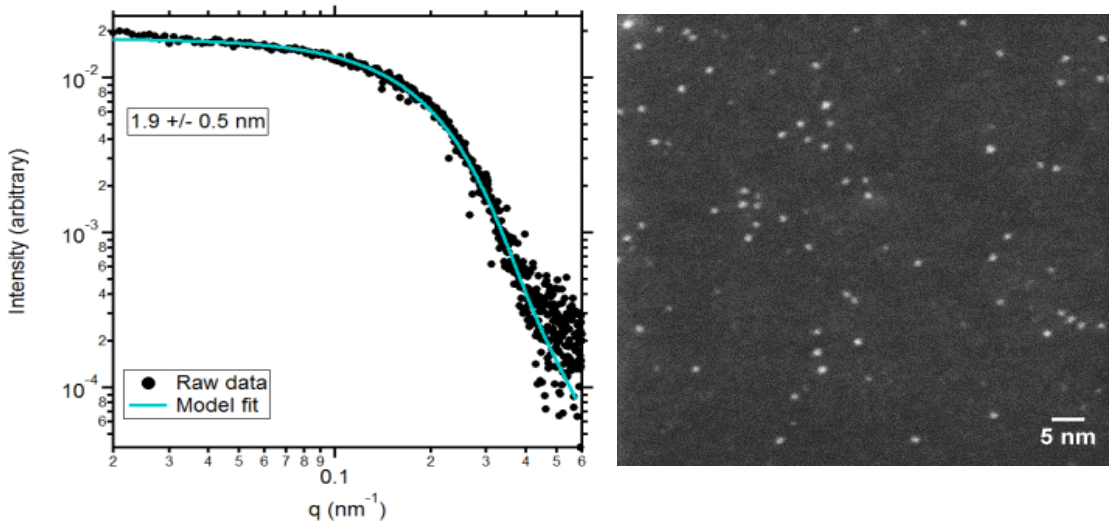

Figure A5. SAXS pattern and model fit of $Au_{101}(PPh_3)_{21}Cl_5$ dispersed in THF (left). STEM image of $Au_{101}(PPh_3)_{21}Cl_5$ to corroborate the SAXS measurement (right).

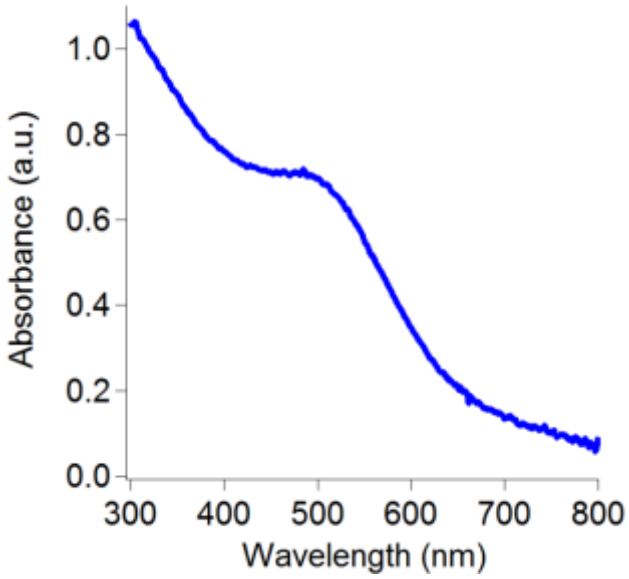

Figure A6. UV-vis spectra of $Au_{101}(PPh_3)_{21}Cl_5$ dispersed in CH_2Cl_2.

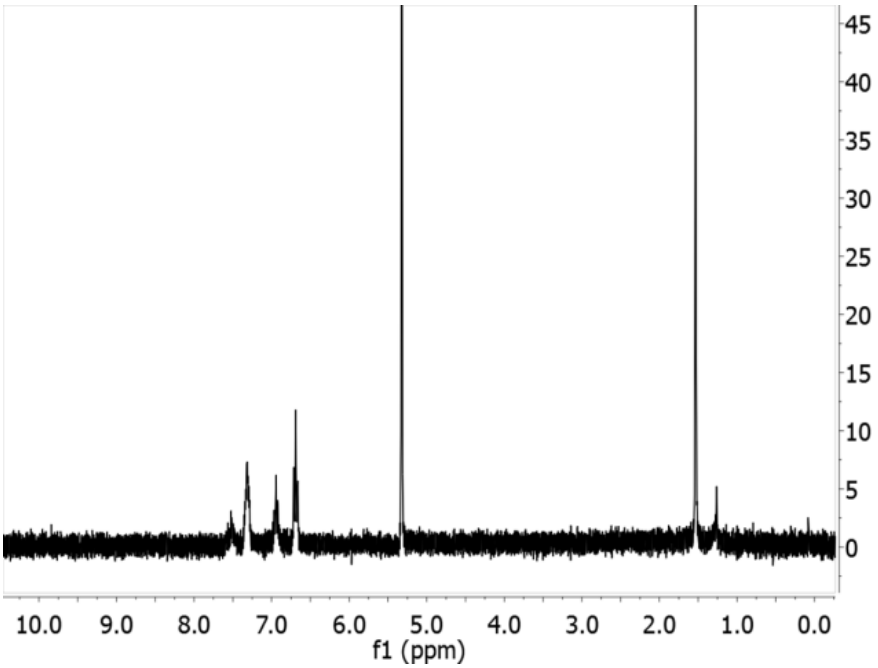

Figure A7. ^{1}H NMR of $Au_{11}(PPh_3)_8Cl_3$ in CD_2Cl_2.

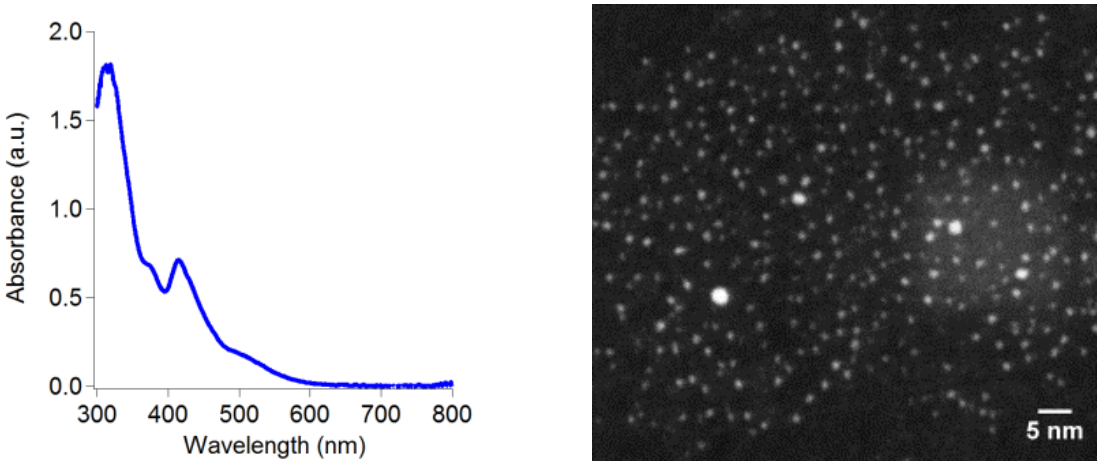

Figure A8. UV-vis of $Au_{11}(PPh_3)_8Cl_3$ in CH_2Cl_2 (left). STEM image of $Au_{11}(PPh_3)_8Cl_3$.

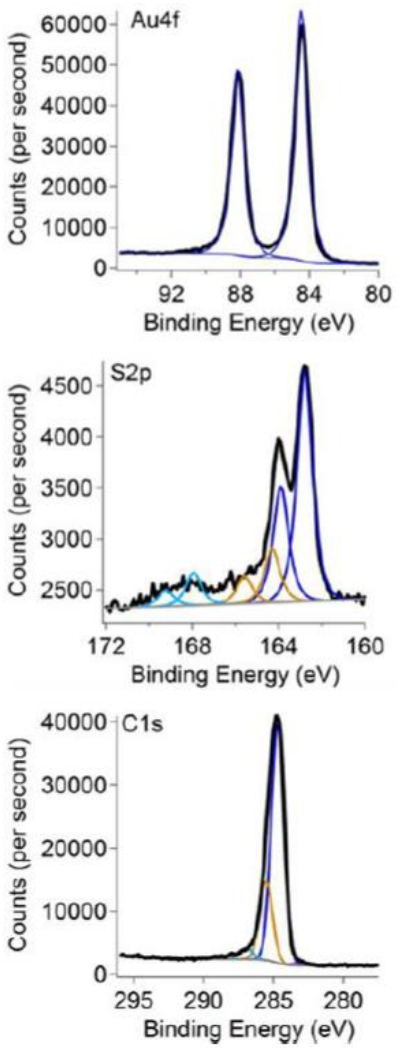

Figure A9. XPS elemental spectra (Au4f, S2p, and C1s) of **Graft-UDT-AuNP**, black trace is the experimental data and the other colored traces show the peak fitting.

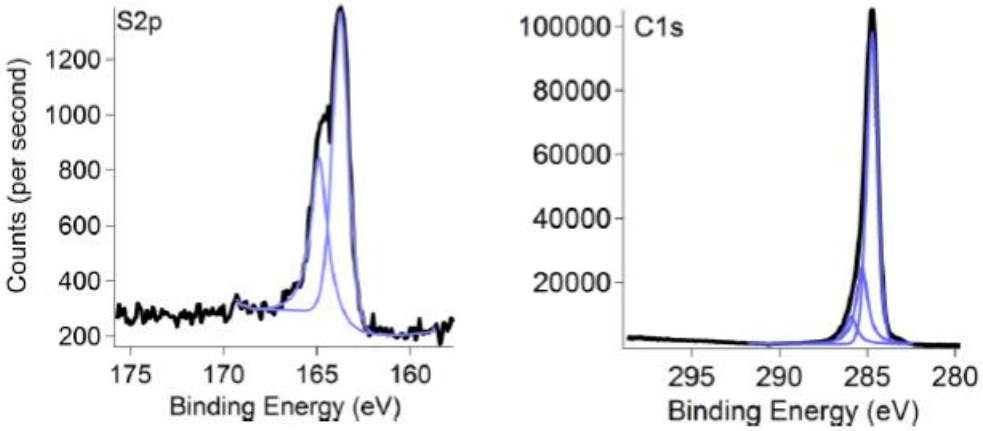

Figure A10. XPS elemental spectra (S2p and C1s) **UDTA-BDD**, black trace is the experimental data and the other colored traces show peak fitting.

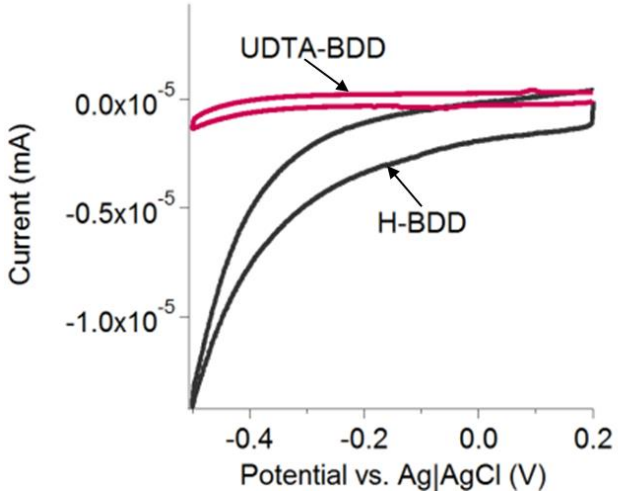

Figure A11. Cyclic voltammograms of hydrogen terminated BDD (H-BDD) and **UDTA-BDD** in 1 M KCl. The reduction in the capacitive current and suppression of the oxygen reduction current indicated that the BDD surface was functionalized by a molecular monolayer. All scans taken at 100 mV/s.

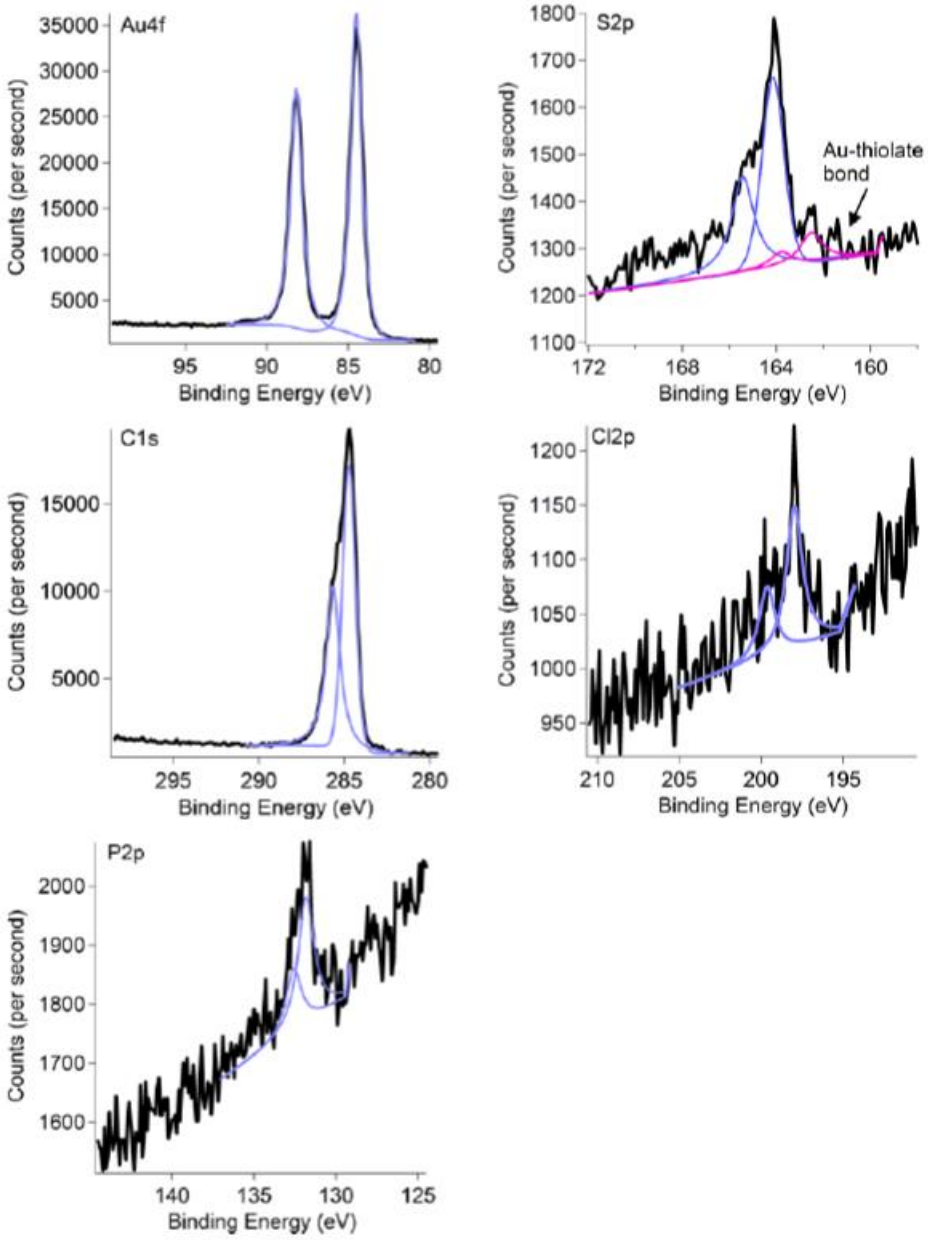

Figure A12. XPS elemental spectra (Au4f, C1s, S2p, P2p, and Cl2p of **TPP-Au$_{101}$-UDT**, black trace is the experimental data and the other colored traces show the peak fitting. The main S2p peak at 164.3 eV arises from thioacetate while the small broad hump at higher binding energy are due to a small amount of oxidized sulfur. The S2p peak could not be appropriately fit without the incorporation of the pink trace at 162.8 eV, which is indicative of a gold-thiolate bond.

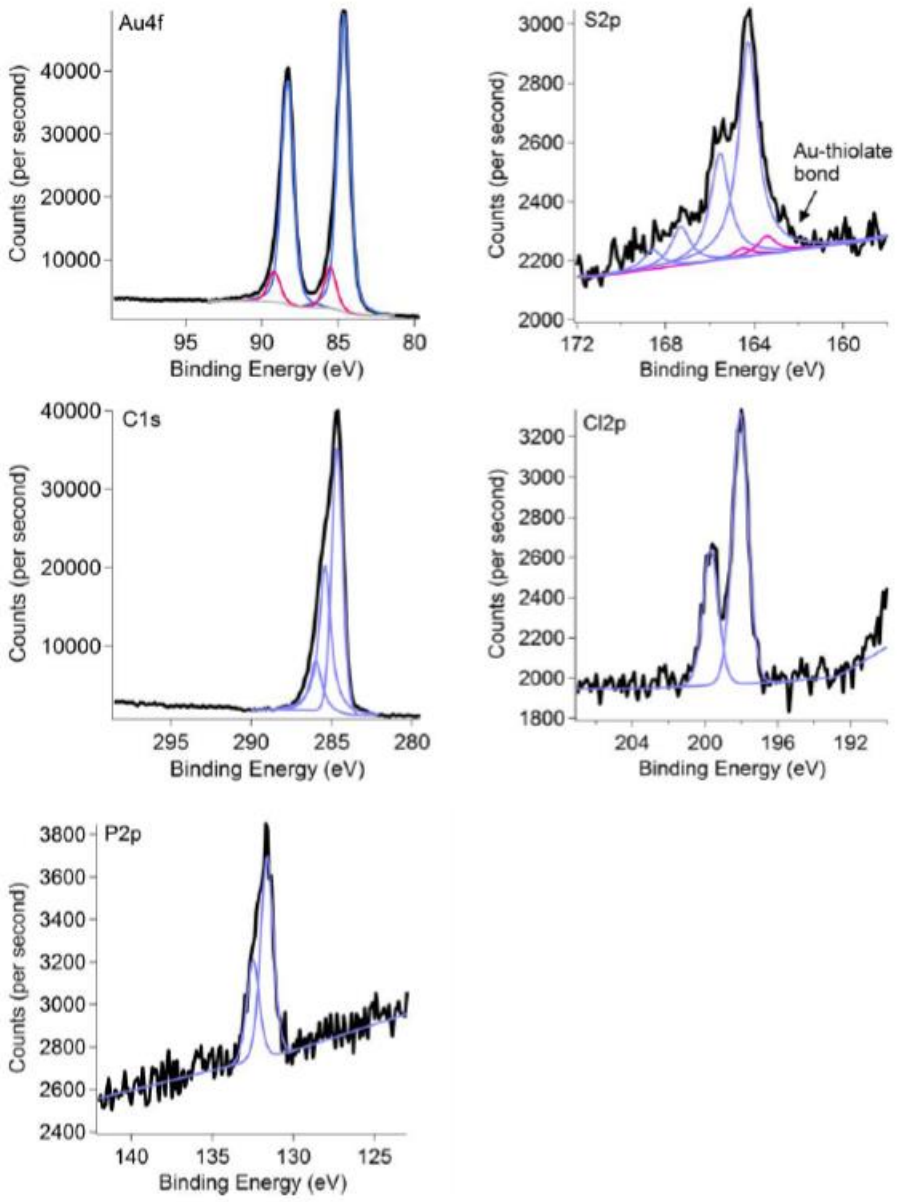

Figure A13. XPS elemental spectra (Au4f, S2p, C1s, P2p, and Cl2p) of **TPP-Au$_{11}$-UDT**, black trace is the experimental data and the other colored traces show the peak fitting. The main S2p peak at 164.3 eV arises from thioacetate while the small peaks at higher binding energy are due to a small amount of oxidized sulfur. The S2p peak could not be appropriately fit without the incorporation of the pink trace at 163.8 eV, which is indicative of a gold-thiolate bond.

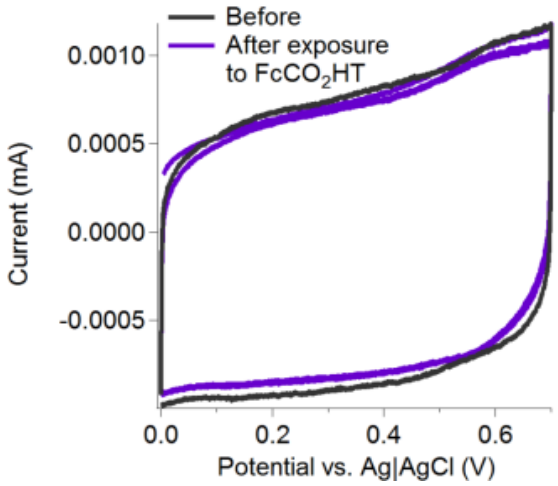

Figure A14. Cyclic voltammogram of a bare BDD substrate before (purple trace) and after treatment with dilute ozone and exposure to 1 mM $FcCO_2HT$ (gray trace), showing that $FcCO_2HT$ is not physiadsorbed to BDD. Scans in 0.1 M $HClO_4$ at 100 mV/s.

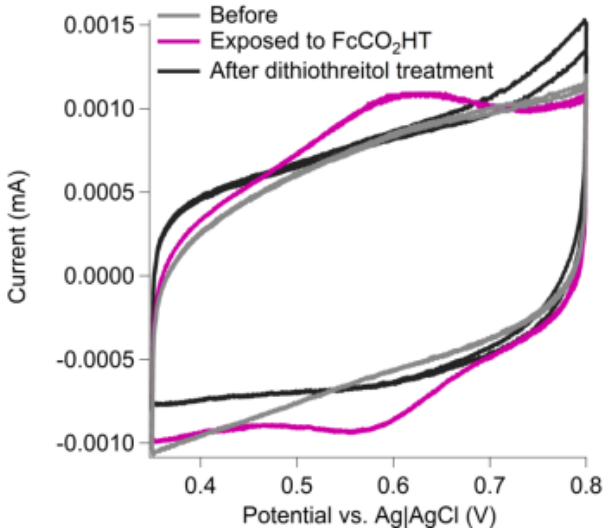

Figure A15. Cyclic voltammograms of **UDTA-BDD** (gray), after exposure to $FcCO_2HT$ (purple), then after exposing that sample to dithiothreitol (black). The small current observed after **UDTA-BDD** was exposed to $FcCO_2HT$ (purple trace), presumably due to formation of disulfide bonds between the thioacetate and the ferrocenated thiol. This hypothesis was supported by treating the sample with dithiothreitol, a disulfide reducing agent, which resulted in the suppression of the $FcCO_2HT$ current (black trace). All scans taken in 0.1 M $HClO_4$ at 100 mV/s.

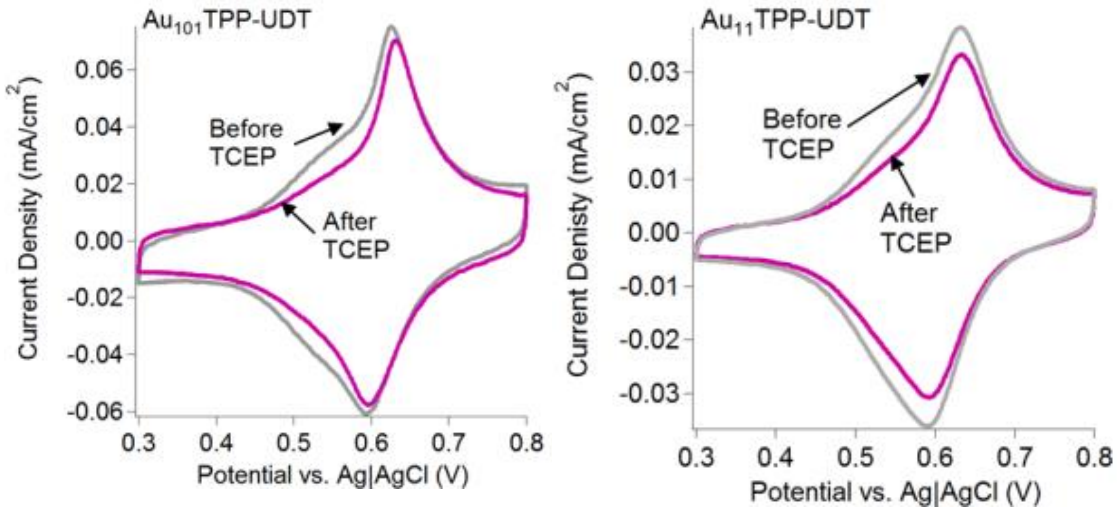

Figure A16. Cyclic voltammograms of **TPP-Au$_{11}$-UDT** (left) and **TPP-Au$_{101}$-UDT** (right) before and after treatment with TCEP. The suppression of the anodic shoulder and narrowing of the redox peaks after treatment with TCEP suggests that disulfide bonds that formed between $FcCO_2HT$ and the UDT monolayer were responsible for those features in the initial CVs.

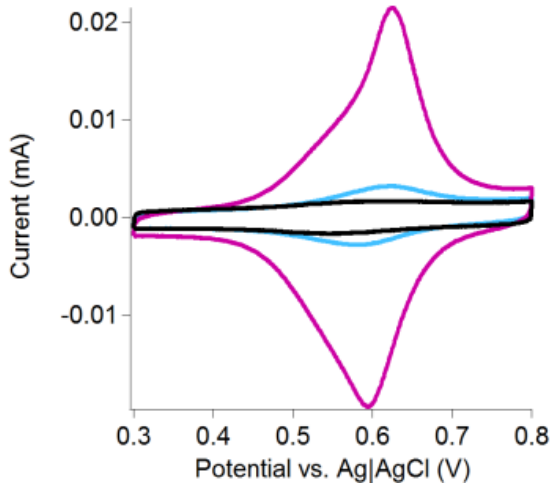

Figure A17. Overlay of cyclic voltammograms of **Graft-UDT-AuNP** as the sample went through treatments with 0.1 M KCN to decompose the AuNPs and dithiothreitol to reduce the resulting disulfide bonds. The $FcCO_2HT$ signal of the initial **Graft-UDT-AuNP** sample (purple trace) was mostly lost after treatment with 0.1 M KCN (blue trace) which indicated that the majority of the $FcCO_2HT$ is bound to the AuNP surface. The further loss of $FcCO_2HT$ signal after treatment with dithiothreitol (black trace) suggested that the signal remaining after cyanide treatment originated from disulfide bonds formed between the thiol redox probe and the undecanethiol monolayer, presumably a product of the cyanide decomposition. All scans in 0.1 M HClO4 at 100 mV/s.

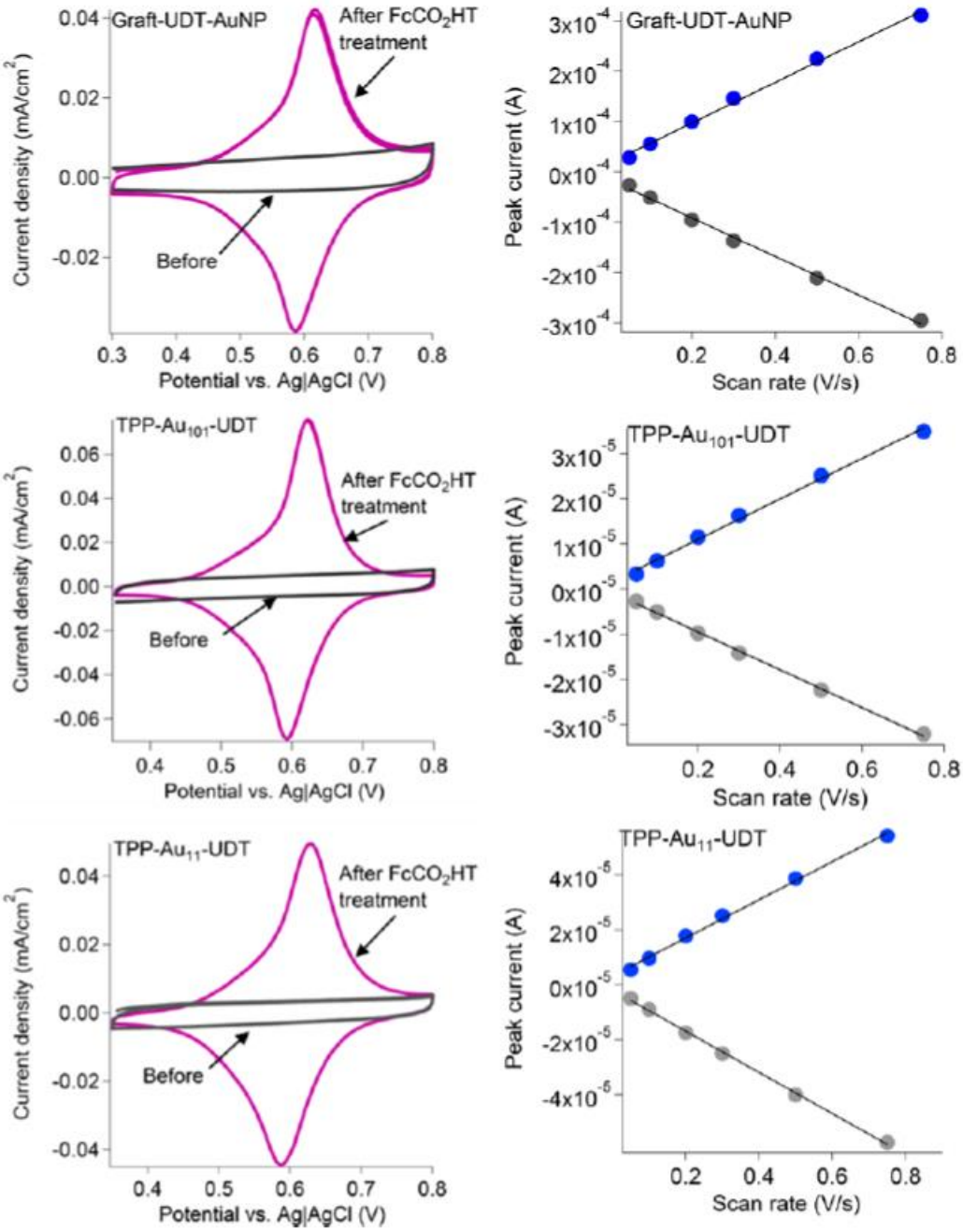

Figure A18. (Left column) Cyclic voltammograms of **Graft-UDT-AuNP**, **TPP-Au$_{101}$-UDT** and **TPP-Au$_{11}$-UDT** before (gray trace) and after attaching $FcCO_2HT$ (purple trace). Scans in 0.1 M $HClO_4$ at 100 mV/s. (Right column) Plot of the peak current as a function of scan rate for the AuNP samples treated with $FcCO_2HT$, anodic peak current (blue), cathodic peak current (gray). The linear fit is indicative of a surface bound redox probe.

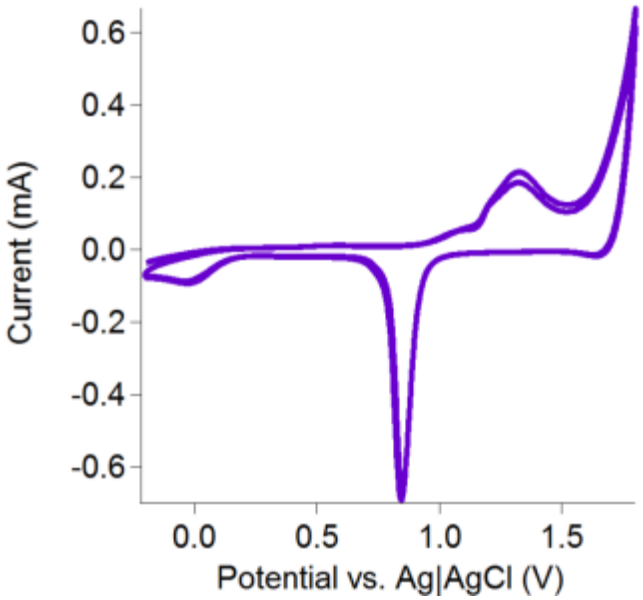

Figure A19. Representative cyclic voltammogram used to determine electrochemically active gold surface area. Scan taken in 0.5 M H_2SO_4 at 100 mV/s.

APPENDIX B

SUPPORTING INFORMATION FOR CHAPTER V: SURFACE PASSIVATION, NOT CORE COMPOSITION, DRIVE METAL OXIDE NANOPARTICLE *IN VIVO* BIOCOMPATABILITY

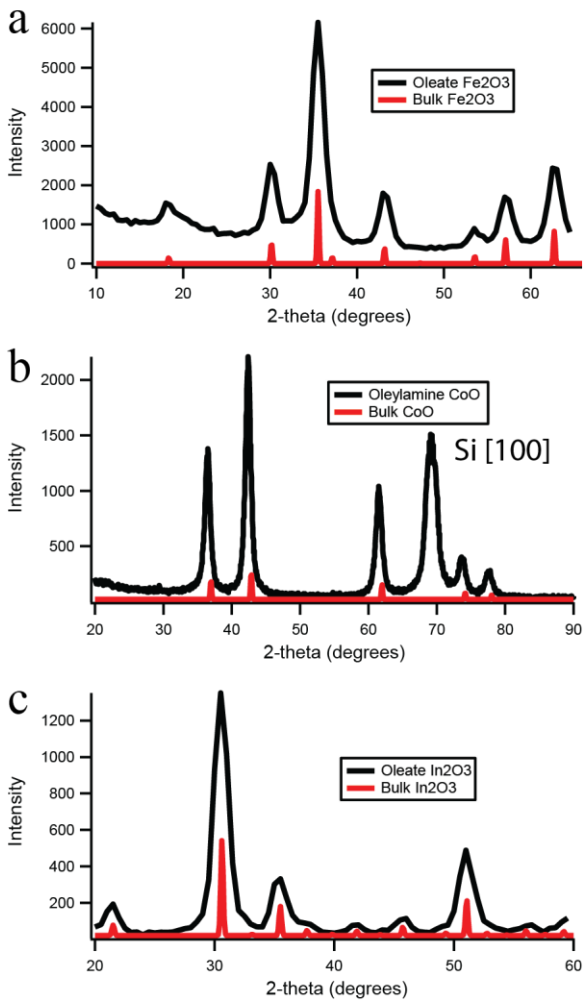

Figure B1: Powder X-ray diffraction spectra of α-Fe_2O_3 (a), CoO (b), and In_2O_3 (c) nanoparticles with refence spectra in red.

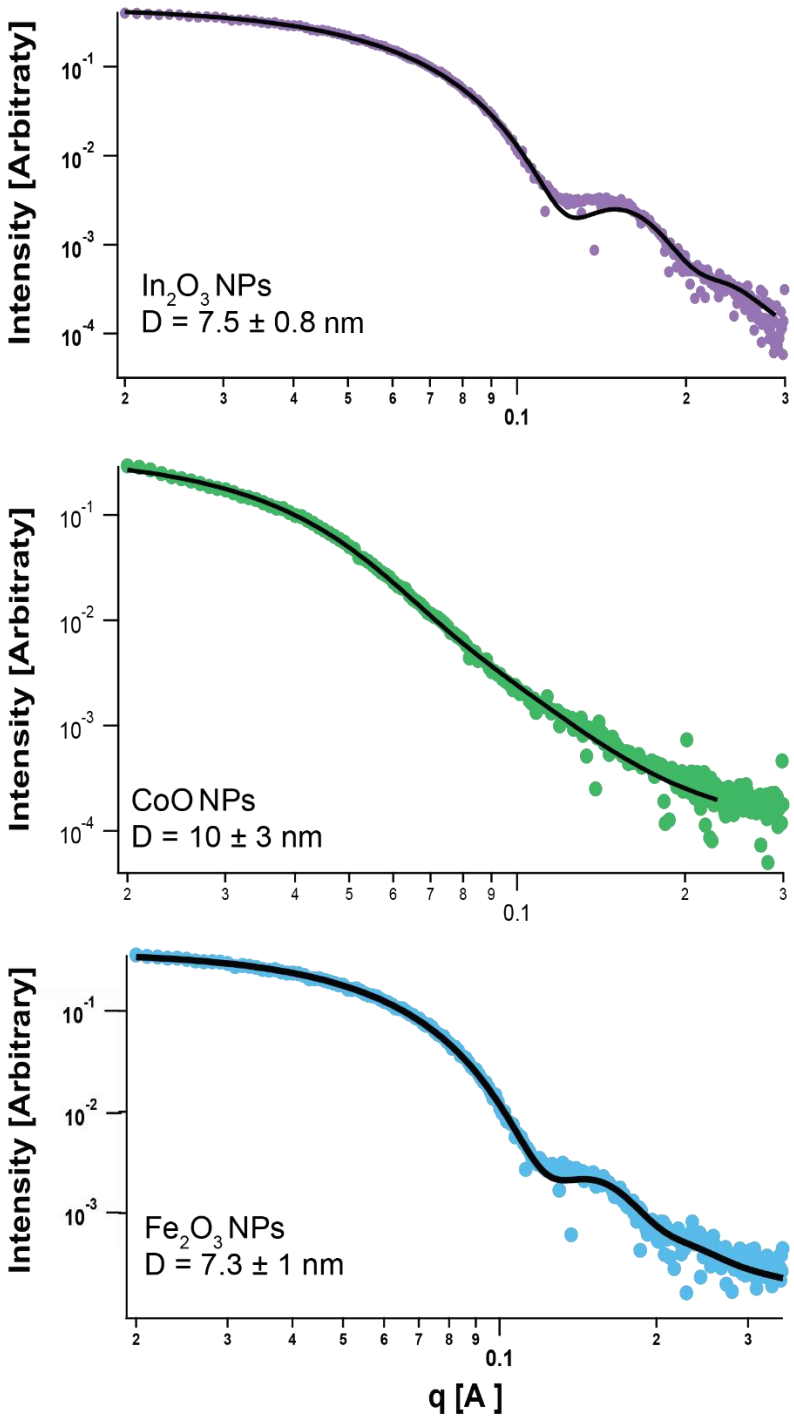

Figure B2: Small Angle X-ray Scattering (SAXS) patterns of the oleate-In_2O_3, oleylamine-CoO and oleate-α-Fe_2O_3. The colored circles are the raw data and the black line is the fit. Modelled core diameters and standard deviations are displayed within each SAXS pattern.

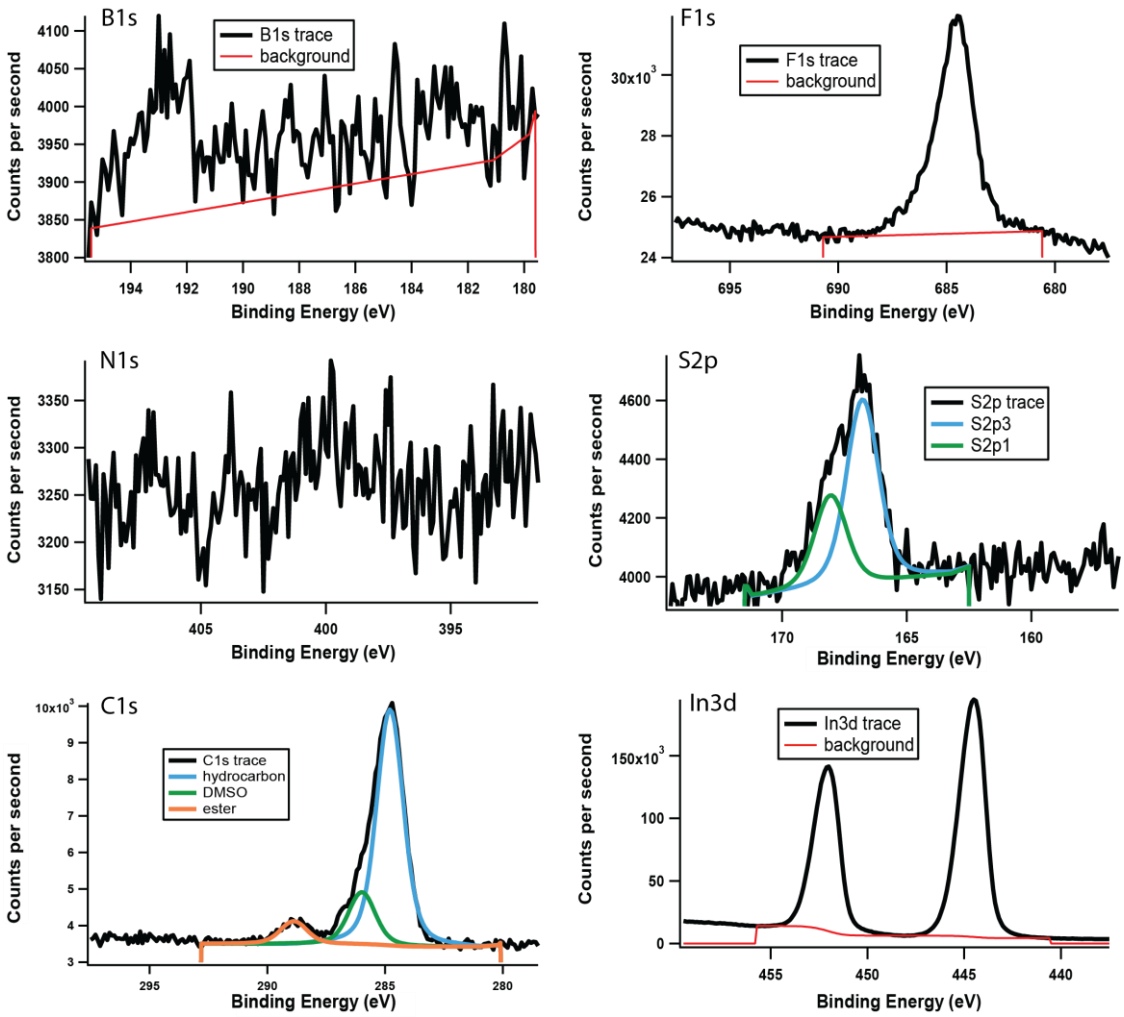

Figure B3: XPS spectra of the un-passivated In_2O_3 NPs.

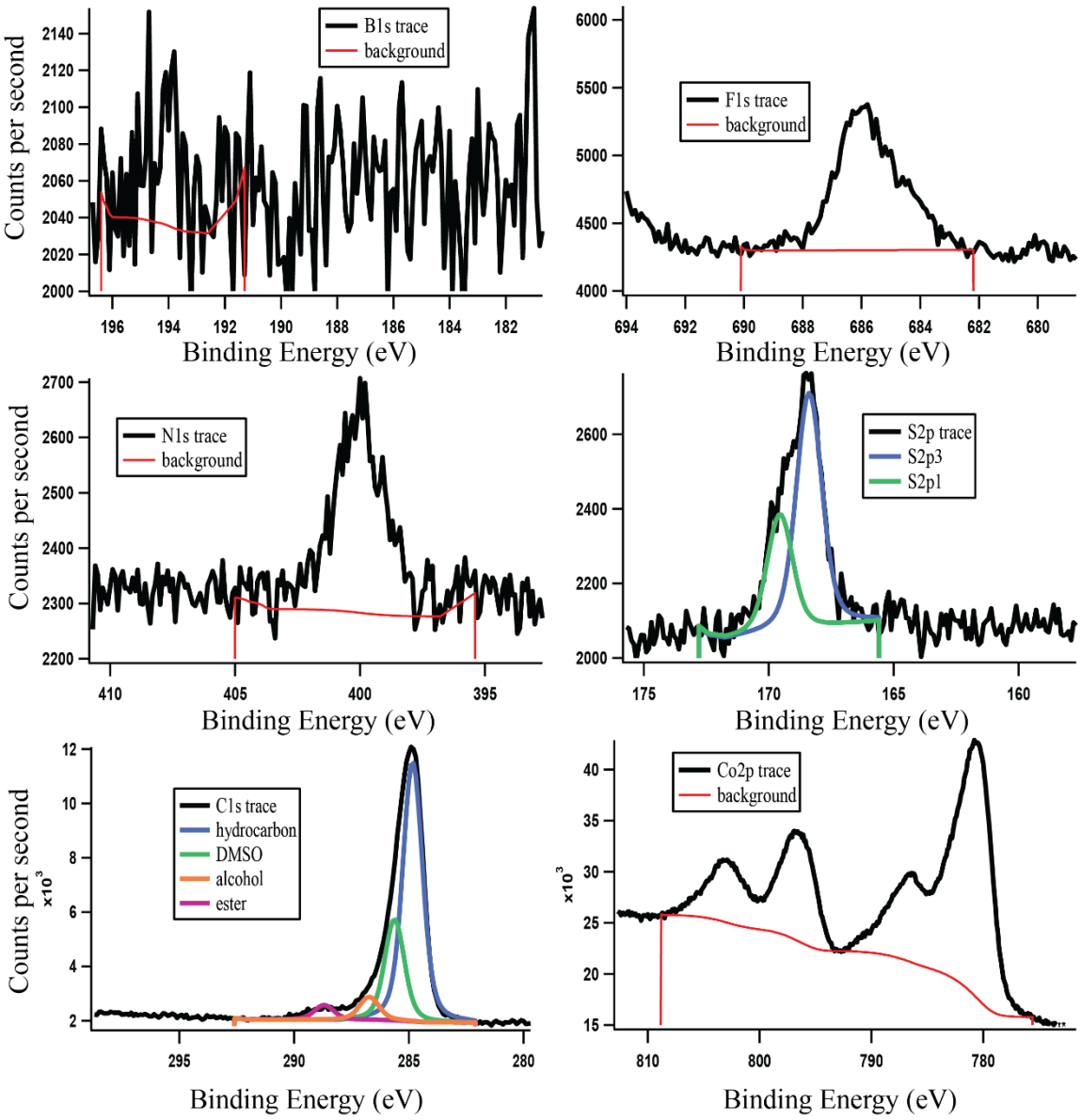

Figure B4: X-ray photoelectron spectra of the un-passivated CoO NPs. The N1s peak is from remaining oleylamine ligands.

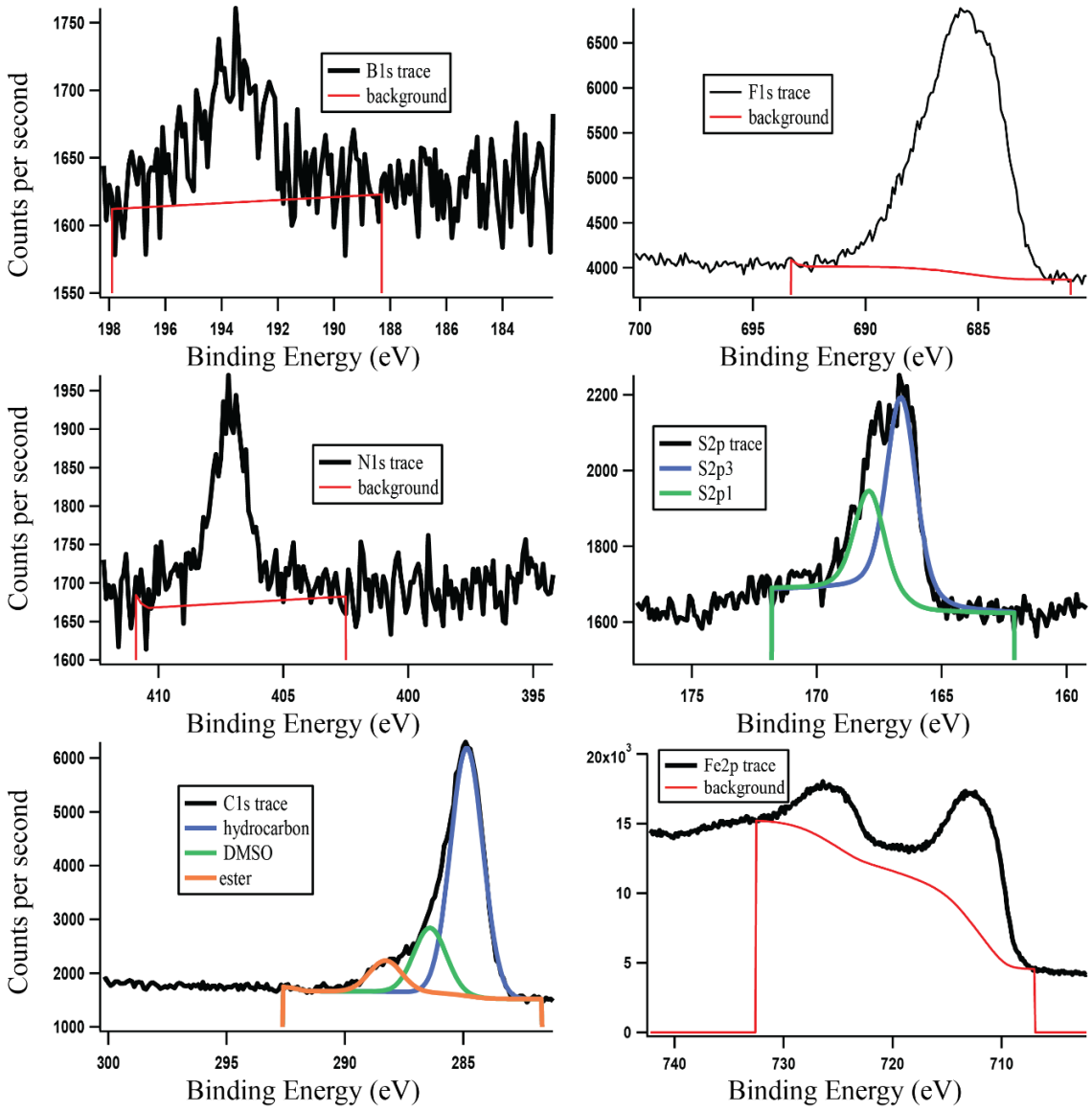

Figure B5: X-ray photoelectron spectra of the un-passivated α-Fe_2O_3 NPs. The N1s peak is from nitrate ions that were not removed in the initial rinse.

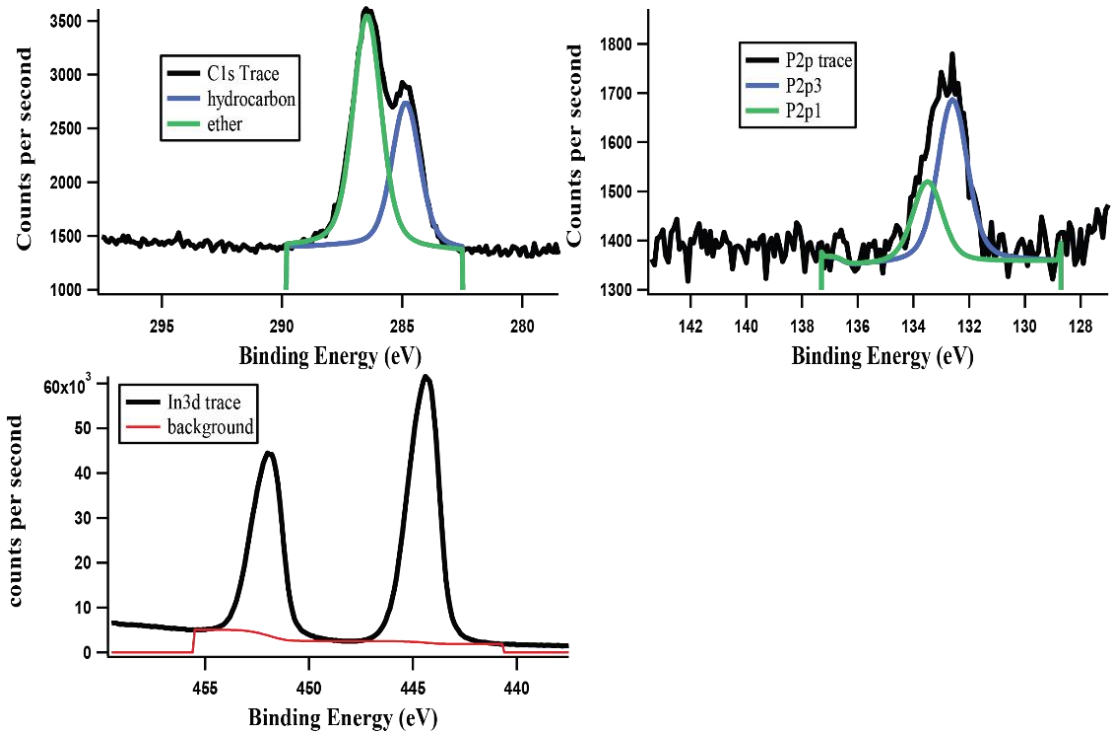

Figure B6: XPS spectra of the passivated In_2O_3 NPs.

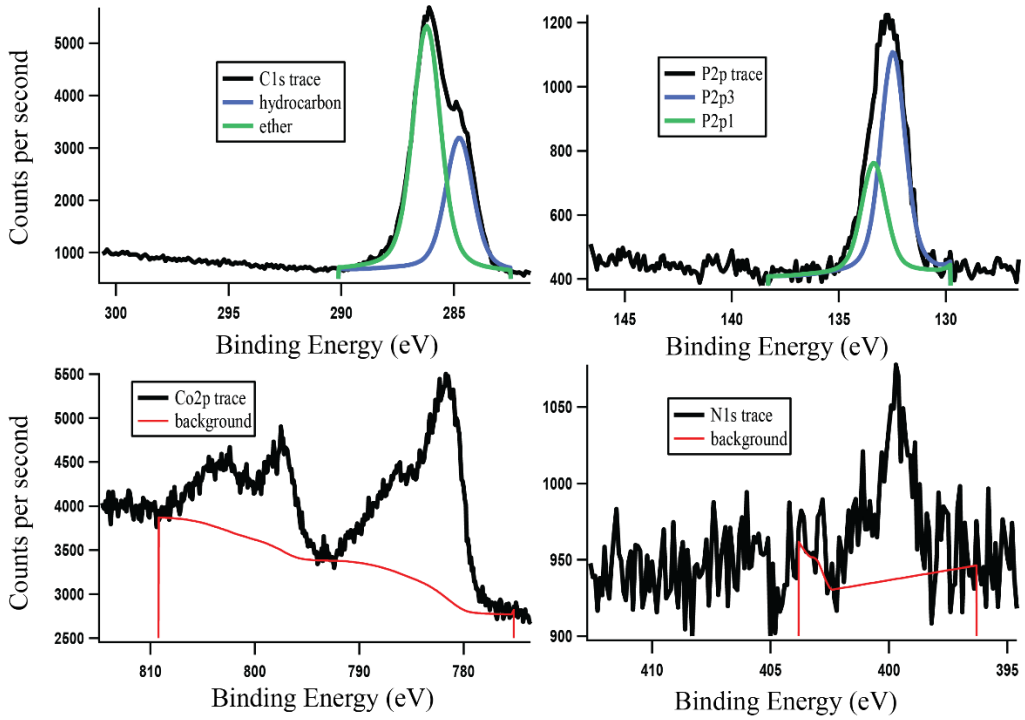

Figure B7: XPS spectra of the passivated CoO NPs. The N1s peak is from remaining oleylamine ligands.

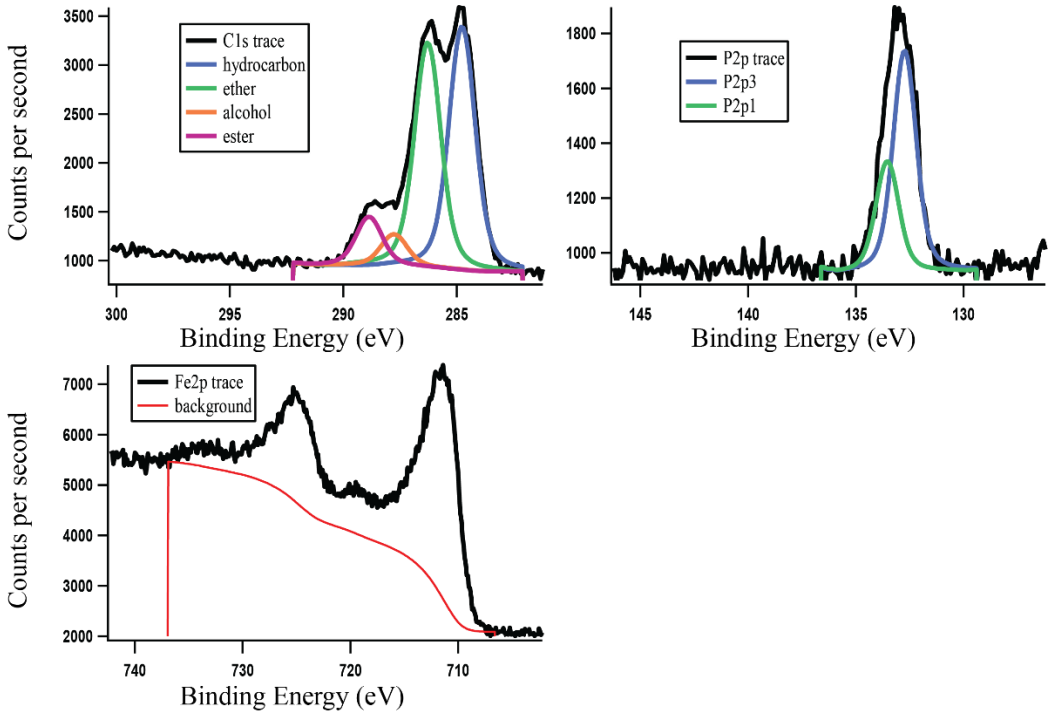

Figure B8: XPS spectra of the passivated Fe_2O_3 NPs.

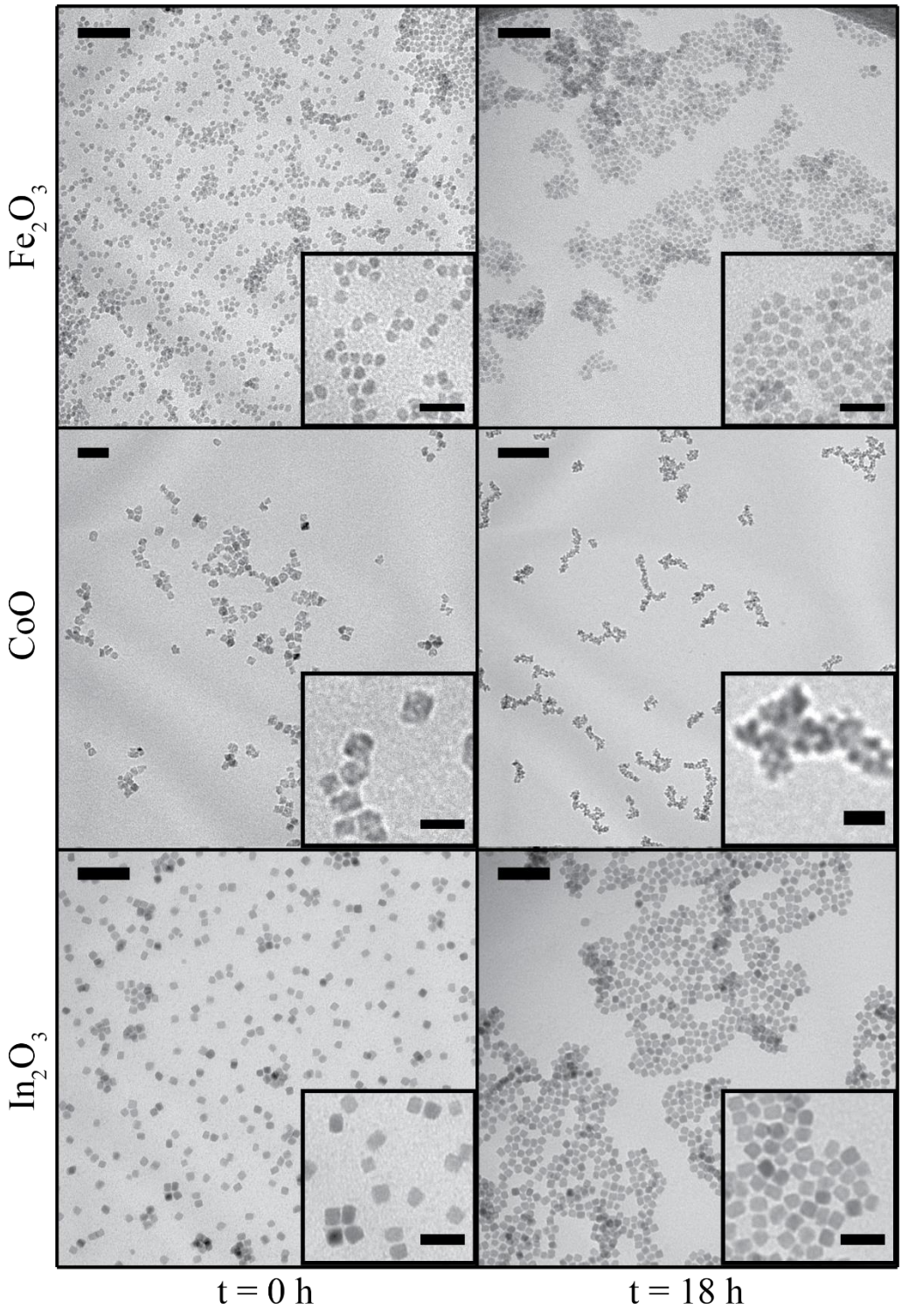

Figure B9: Transmission electron micrographs of the un-passivated NP cores under initial exposure conditions, t = 0 h, and after 18 hours. Scale bars are 50 nm, scale bars for insets are 20 nm.

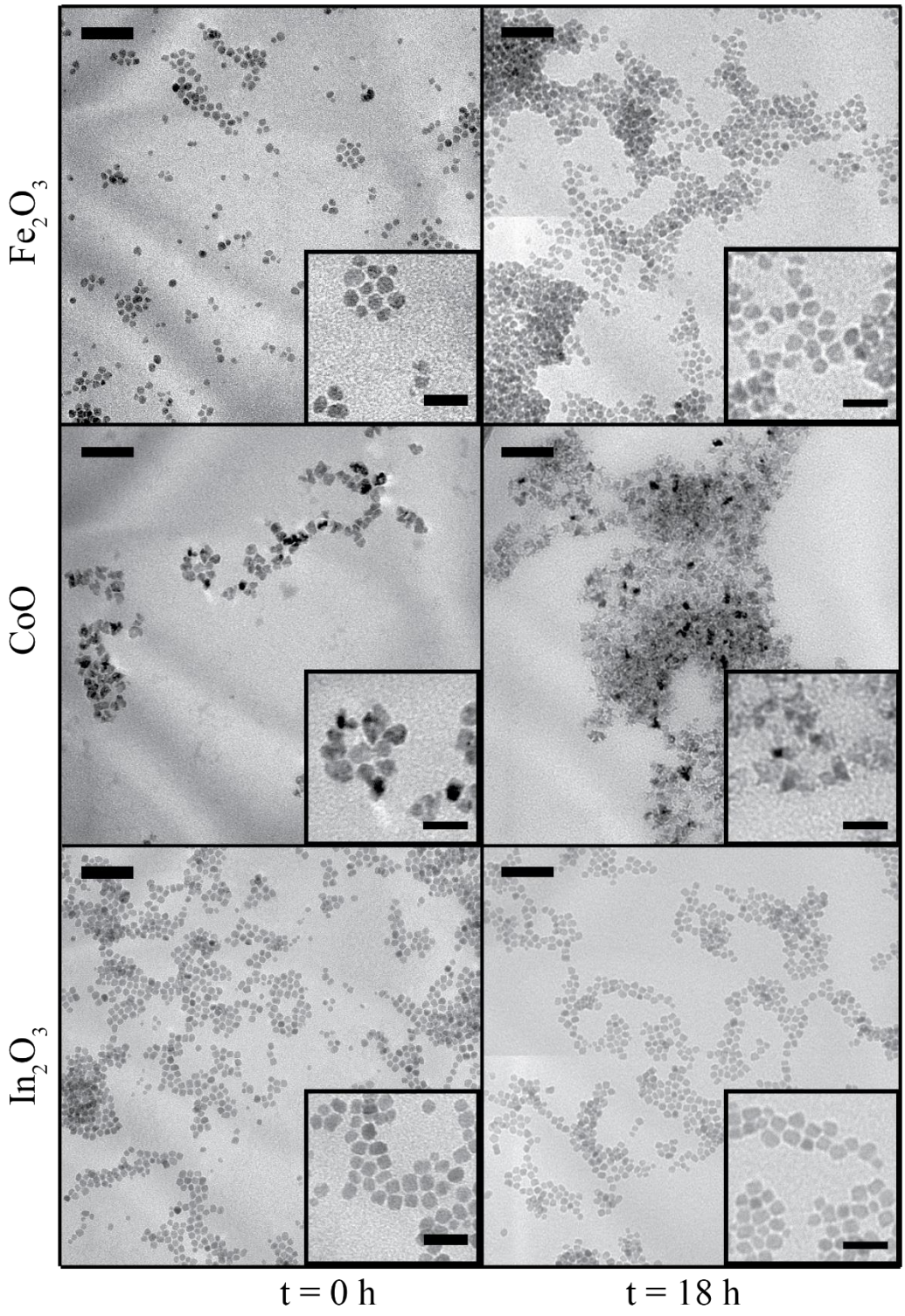

Figure B10: Transmission electron micrographs of the passivated NP cores under initial exposure conditions, t = 0 h, and after 18 hours. Scale bars are 50 nm, scale bars for insets are 20 nm.

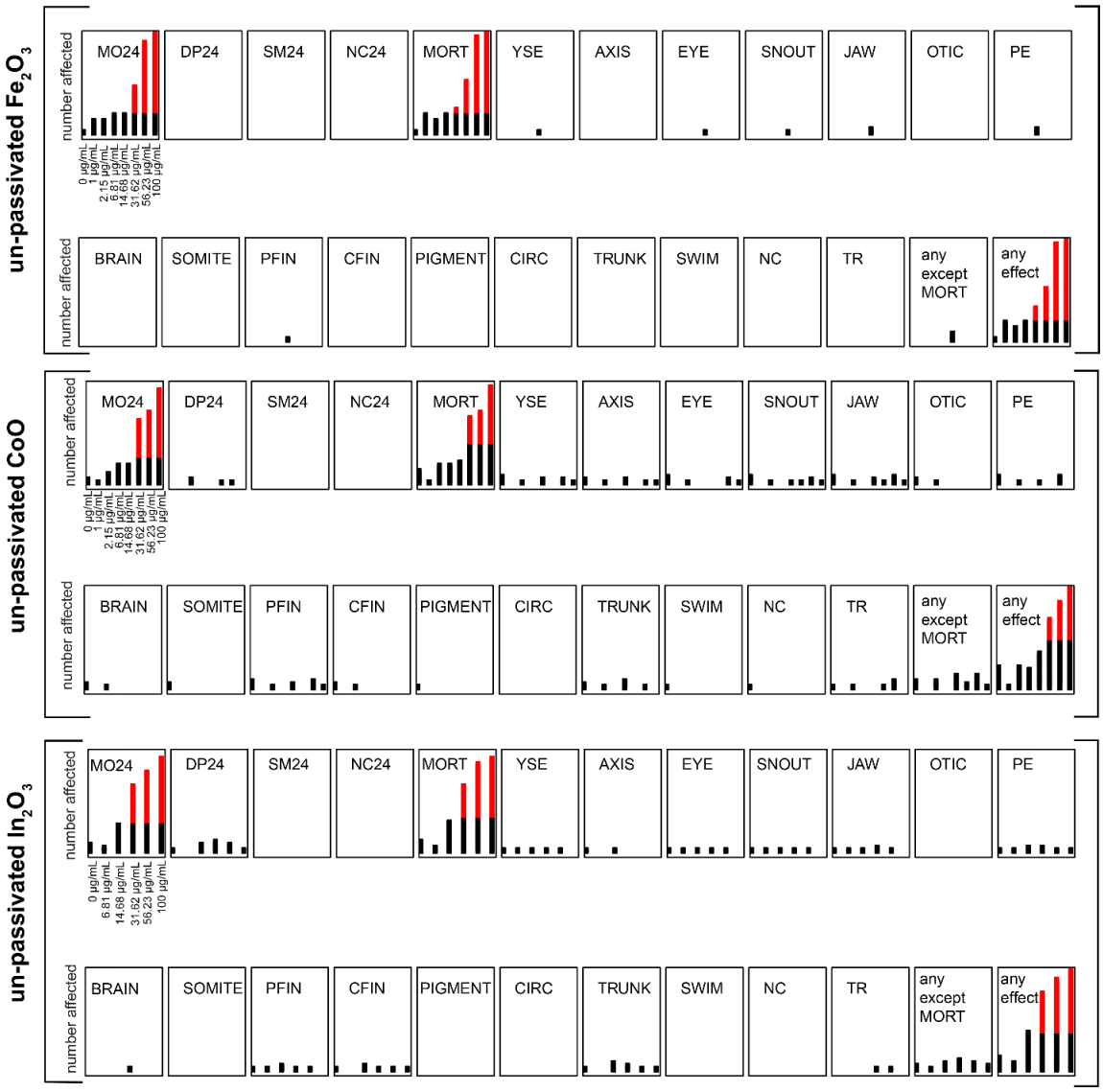
un-passivated Fe_2O_3
un-passivated CoO
un-passivated In_2O_3
number affected
MO24
DP24
SM24
NC24
MORT
YSE
AXIS
EYE
SNOUT
JAW
OTIC
PE
0 µg/mL
1 µg/mL
2.15 µg/mL
6.81 µg/mL
14.68 µg/mL
31.62 µg/mL
56.23 µg/mL
100 µg/mL
BRAIN
SOMITE
PFIN
CFIN
PIGMENT
CIRC
TRUNK
SWIM
NC
TR
any except MORT
any effect

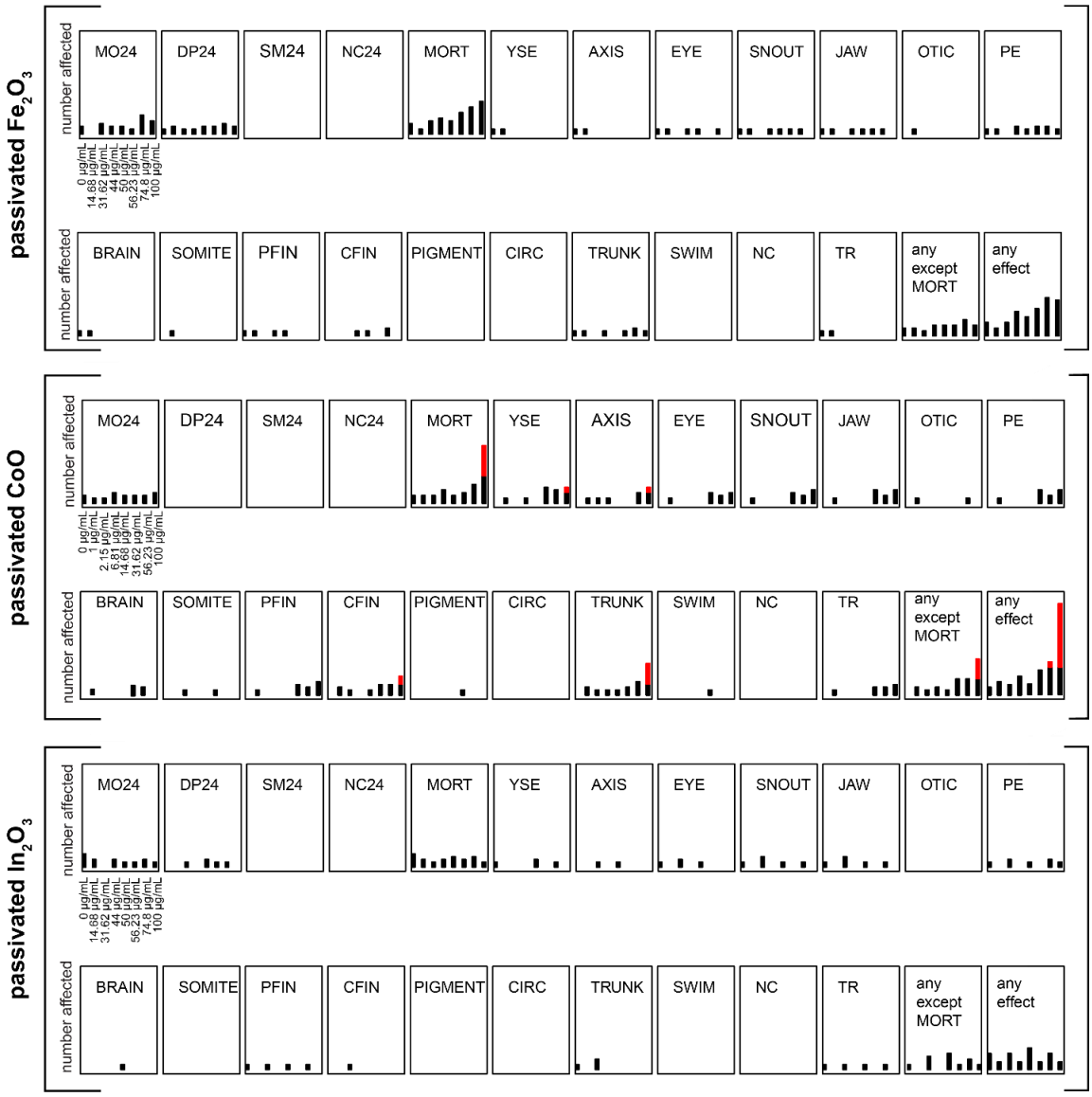

Figure B11: Developmental profile of un-passivated (**a**) and passivated (**b**) α-Fe_2O_3, CoO and In_2O_3 nanoparticles. Embryonic zebrafish are developmentally exposed to 6 concentrations from 6 to 120 hours post fertilization (hpf). At 24 hpf, each embryo was assessed for 4 endpoints (MO24 = mortality at 24, DP24 = delay in developmental progression, SM24 = spontaneous movement, and NC24 = notochord defects). At 120 hpf, each embryo was assessed for 18 endpoints (MORT = total mortality, YSE = yolk sac edema, AXIS = axis defect, EYE = eye malformation, SNOUT = snout defect, JAW = jaw abnormality, OTIC = otic vesicle, PE = pericardial edema, BRAIN = abnormal brain, SOMITE = defect in somite, PFIN = pectoral fin, CFIN = caudal fin, PIGMENT = abnormal pigmentation, CIRC = circulation defects, TRUNK = trunk malformation, SWIM = swim bladder no formed, NC = notochord defects). These endpoints were evaluated as present/absent for each embryo. Each embryo with a noted defect at a

certain concentration is represented as a datapoint. Once a statistical threshold is met ($p<0.01$, Fishers Exact Test compared to the control for each endpoint), the additional affected individuals are denoted as red. Two summary endpoints (any.except.mortality = sublethal effects, any.effect = presence of any of the endpoints) is also computed to assess for overall bioactivity.

REFERENCES CITED

Chapter I

(1) Sang, L.; Liao, M.; Sumiya, M. A Comprehensive Review of Semiconductor Ultraviolet Photodetectors: From Thin Film to One-Dimensional Nanostructures. Sensors (Switzerland) 2013, 13, 10482–10518.

(2) Golder, M. R.; Jasti, R. Syntheses of the Smallest Carbon Nanohoops and the Emergence of Unique Physical Phenomena. Acc. Chem. Res. 2015, 48, 557–566.

(3) Horn, D.; Rieger, J. Organic Nanoparticles in Aqueous Phase. Angew. Chem 2001, 40, 4330–4361.

(4) Sardar, R.; Funston, A. M.; Mulvaney, P.; Murray, R. W. Gold Nanoparticles: Past, Present, and Future. Langmuir 2009, 25, 13840–13851.

(5) Stoimenov, P. K.; Klinger, R. L.; Marchin, G. L.; Klabunde, K. J. Metal Oxide Nanoparticles as Bactericidal Agents. Langmuir 2002, 18, 6679–6686.

(6) Li, G.; Jin, R. Atomically Precise Gold Nanoclusters as New Model Catalysts. Acc. Chem. Res. 2013, 46, 1749–1758.

(7) Lane, L. A.; Qian, X.; Nie, S. SERS Nanoparticles in Medicine: From Label-Free Detection to Spectroscopic Tagging. Chem. Rev. 2015, 115, 10489–10529.

(8) Li, J.; Hu, H.; Li, H.; Yao, C. Recent Developments in Electrochemical Sensors Based on Nanomaterials for Determining Glucose and Its Byproduct H2O2. J. Mater. Sci. 2017, 52, 10455–10469.

(9) Mohammed, L.; Gomaa, H. G.; Ragab, D.; Zhu, J. Magnetic Nanoparticles for Environmental and Biomedical Applications: A Review. Particuology 2017, 30, 1–14.

(10) Tang, Z.; Ma, Z. Multiple Functional Strategies for Amplifying Sensitivity of Amperometric Immunoassay for Tumor Markers: A Review. Biosens. Bioelectron. 2017, 98, 100–112.

(11) Liu, G.; Qi, M.; Zhang, Y.; Cao, C.; Goldys, E. M. Nanocomposites of Gold Nanoparticles and Graphene Oxide towards an Stable Label-Free Electrochemical Immunosensor for Detection of Cardiac Marker Troponin-I. Anal. Chim. Acta 2016, 909, 1–8.

(12) Neouze, M. A.; Schubert, U. Surface Modification and Functionalization of Metal and Metal Oxide Nanoparticles by Organic Ligands. Monatshefte fur Chemie 2008, 139, 183–195.

(13) Damos, F. S.; Luz, R. C. S.; Tanaka, A. A.; Kubota, L. T. Development of an Electroactive Layer-by-Layer Assembly Based on Host-Guest Supramolecular Interactions. J. Electroanal. Chem. 2010, 639, 36–42.

(14) Hu, Q. Da; Tang, G. P.; Chu, P. K. Cyclodextrin-Based Host-Guest Supramolecular Nanoparticles for Delivery: From Design to Applications. Acc. Chem. Res. 2014, 47, 2017–2025.

(15) Zuo, F.; Luo, C.; Zheng, Z.; Ding, X.; Peng, Y. Supramolecular Assembly of ?-Cyclodextrin-Capped Gold Nanoparticles on Ferrocene-Functionalized ITO Surface for Enhanced Voltammetric Analysis of Ascorbic Acid. Electroanalysis 2008, 20, 894–899.

(16) Elliott, E. W.; Ginzburg, A. L.; Kennedy, Z. C.; Feng, Z.; Hutchison, J. E. Single-Step Synthesis of Small, Azide-Functionalized Gold Nanoparticles: Versatile, Water-Dispersible Reagents for Click Chemistry. Langmuir 2017, 33, 5796–5802.

(17) Matyjewicz, J.; Lesniewski, A.; Niedziolka-Jonsson, J. Click Chemistry Modification of Glassy Carbon Electrode with Gold Nanoparticles for Electroactive Ion Discrimination. Electrochem. commun. 2014, 48, 73–76.

(18) Stavis, C.; Clare, T. L.; Butler, J. E.; Radadia, A. D.; Carr, R.; Zeng, H.; King, W. P.; Carlisle, J. A.; Aksimentiev, A.; Bashir, R.; et al. Surface Functionalization of Thin-Film Diamond for Highly Stable and Selective Biological Interfaces. Proc. Natl. Acad. Sci. 2011, 108, 983–988.

(19) Menanteau, T.; Dias, M.; Levillain, E.; Downard, A. J.; Breton, T. Electrografting via Diazonium Chemistry: The Key Role of the Aryl Substituent in the Layer Growth Mechanism. J. Phys. Chem. C 2016, 120, 4423–4429.

(20) Delamar, M.; Hitmi, R.; Pinson, J.; Savéant, J. Covalent Modification of Carbon Surfaces by Grafting of Functionalized Aryl Radicals Produced from Electrochemical Reduction of Diazonium Salts. J. Am. Chem. Soc. 1992, 114, 5883–5884.

(21) Yu, S. S. C.; Downard, A. J. Photochemical Grafting and Activation of Organic Layers on Glassy Carbon and Pyrolyzed Photoresist Films. Langmuir 2007, 23, 4662–4668.

(22) Hak, S.; Helgesen, E.; Hektoen, H. H.; Huuse, E. M.; Jarzyna, P. A.; Mulder, W. J. M.; Haraldseth, O.; Davies, C. D. L. The Effect of Nanoparticle Polyethylene Glycol Surface Density on Ligand-Directed Tumor Targeting Studied in Vivo by Dual Modality Imaging. ACS Nano 2012, 6, 5648–5658.

(23) Cho, W. S.; Cho, M.; Jeong, J.; Choi, M.; Han, B. S.; Shin, H. S.; Hong, J.; Chung, B. H.; Jeong, J.; Cho, M. H. Size-Dependent Tissue Kinetics of PEG-Coated Gold Nanoparticles. Toxicol. Appl. Pharmacol. 2010, 245, 116–123.

(24) Yu, M.; Huang, S.; Yu, K. J.; Clyne, A. M. Dextran and Polymer Polyethylene Glycol (PEG) Coating Reduce Both 5 and 30 Nm Iron Oxide Nanoparticle Cytotoxicity in 2D and 3D Cell Culture. Int. J. Mol. Sci. 2012, 13, 5554–5570.

(25) Zhao, J.; Bradbury, C. R.; Fermín, D. J. Long-Range Electronic Communication between Metal Nanoparticles and Electrode Surfaces Separated by Polyelectrolyte Multilayer Films. J. Phys. Chem. C 2008, 112, 6832–6841.

(26) Li, F.; Ciani, I.; Bertoncello, P.; Unwin, P. R.; Zhao, J.; Bradbury, C. R.; Fermin, D. J. Scanning Electrochemical Microscopy of Redox-Mediated Hydrogen Evolution Catalyzed by Two-Dimensional Assemblies of Palladium Nanoparticles. J. Phys. Chem. C 2008, 112, 9686–9694.

(27) Zhang, Y.; Kohler, N.; Zhang, M. Surface Modification of Superparamagnetic Magnetite Nanoparticles and Their Intracellular Uptake. Biomaterials 2002, 23, 1553–1561.

(28) Dong, A.; Ye, X.; Chen, J.; Kang, Y.; Gordon, T.; Kikkawa, J. M.; Murray, C. B. A Generalized Ligand-Exchange Strategy Enabling Sequential Surface Functionalization of Colloidal Nanocrystals. J. Am. Chem. Soc. 2011, 133, 998–1006.

(29) Woehrle, G. H.; Brown, L. O.; Hutchison, J. E. Thiol-Functionalized, 1.5-Nm Gold Nanoparticles through Ligand Exchange Reactions: Scope and Mechanism of Ligand Exchange. J. Am. Chem. Soc. 2005, 127, 2172–2183.

(30) Karlsson, H. L.; Cronholm, P.; Gustafsson, J.; Moeller, L. Copper Oxide Nanoparticles Are Highly Toxic: A Comparison between Metal Oxide Nanoparticles and Carbon Nanotubes. Chem. Res. Toxicol. 2008, 21, 1726–1732.

(31) Zhang, H.; Ji, Z.; Xia, T.; Meng, H.; Low-Kam, C.; Liu, R.; Pokhrel, S.; Lin, S.; Wang, X.; Liao, Y. P.; et al. Use of Metal Oxide Nanoparticle Band Gap to Develop a Predictive Paradigm for Oxidative Stress and Acute Pulmonary Inflammation. ACS Nano 2012, 6, 4349–4368.

(32) Gunsolus, I. L.; Mousavi, M. P. S.; Hussein, K.; Bühlmann, P.; Haynes, C. L. Effects of Humic and Fulvic Acids on Silver Nanoparticle Stability, Dissolution, and Toxicity. Environ. Sci. Technol. 2015, 49, 8078–8086.

(33) Elliott, E. W.; Glover, R. D.; Hutchison, J. E. Removal of Thiol Ligands from Surface-Confined Nanoparticles without Particle Growth or Desorption. ACS Nano 2015, 9, 3050–3059.

(34) Chen, W.; Chen, S. Oxygen Electroreduction Catalyzed by Gold Nanoclusters: Strong Core Size Effects. Angew. Chemie - Int. Ed. 2009, 48, 4386–4389.

(35) Kleijn, S. E. F.; Lai, S. C. S.; Koper, M. T. M.; Unwin, P. R. Electrochemistry of Nanoparticles. Angew. Chemie - Int. Ed. 2014, 53, 3558–3586.

(36) Xiao, F.; Song, J.; Gao, H.; Zan, X.; Xu, R.; Duan, H. Coating Graphene Paper with 2D-Assembly of Electrocatalytic Nanoparticles: A Modular Approach toward High-Performance Flexible Electrodes. ACS Nano 2012, 6, 100–110.

(37) Kau, D. R.; Ohodnicki, P. R.; Kail, B. W.; Matranga, C. Selective Electrocatalytic Activity of Ligand Stabilized Copper. 2011, 2038–2043.

(38) Gooding, J. J. Advances in Interfacial Design for Electrochemical Biosensors and Sensors: Aryl Diazonium Salts for Modifying Carbon and Metal Electrodes. Electroanalysis 2008, 20, 573–582.

(39) Huang, X.; Du, D.; Gong, X.; Cai, J.; Tu, H.; Xu, X.; Zhang, A. Composite Assembly of Silver Nanoparticles with Avidin and Biotinylated AChE on Gold for the Pesticidal Electrochemical Sensing. Electroanalysis 2008, 20, 402–409.

(40) Gwo, S.; Wang, C. Y.; Chen, H. Y.; Lin, M. H.; Sun, L.; Li, X.; Chen, W. L.; Chang, Y. M.; Ahn, H. Plasmonic Metasurfaces for Nonlinear Optics and Quantitative SERS. ACS Photonics 2016, 3, 1371–1384.

(41) Oszajca, M. F.; Bodnarchuk, M. I.; Kovalenko, M. V. Precisely Engineered Colloidal Nanoparticles and Nanocrystals for Li- Ion and Na-Ion Batteries: Model Systems or Practical Solutions? Chem. Mater. 2014, 26, 5422–5432.

(42) Jiang, L.; Hsu, A.; Chu, D.; Chen, R. Size-Dependent Activity of Palladium Nanoparticles for Oxygen Electroreduction in Alkaline Solutions. J. Electrochem. Soc. 2009, 156, 10515–10519.

(43) Wang, J. X.; Inada, H.; Wu, L.; Zhu, Y.; Choi, Y.; Liu, P.; Zhou, W. P.; Adzic, R. R. Oxygen Reduction on Well-Defined Core-Shell Nanocatalysts: Particle Size, Facet, and Pt Shell Thickness Effects. J. Am. Chem. Soc. 2009, 131, 17299–17302.

(44) Young, S. L.; Kellon, J. E.; Hutchison, J. E. Small Gold Nanoparticles Interfaced to Electrodes through Molecular Linkers: A Platform to Enhance Electron Transfer and Increase Electrochemically Active Surface Area. J. Am. Chem. Soc. 2016, 138, 13975–13984.

(45) Liu, F.; Khan, K.; Liang, J. H.; Yan, J. W.; Wu, D. Y.; Mao, B. W.; Jensen, P. S.; Zhang, J.; Ulstrup, J. On the Hopping Efficiency of Nanoparticles in the Electron Transfer across Self-Assembled Monolayers. ChemPhysChem 2013, 14, 952–957.

(46) Bradbury, C. R.; Zhao, J.; Fermín, D. J. Distance-Independent Charge-Transfer Resistance at Gold Electrodes Modified by Thiol Monolayers and Metal Nanoparticles. J. Phys. Chem. C 2008, 112, 10153–10160.

(47) Kellon, J. E.; Young, S. L.; Hutchison, J. E. Engineering the Nanoparticle-Electrode Interface. Chem. Mater. 2019, 31, 2685–2701.

(48) El- Deab, M. S.; Ohsaka, T. An Extraordinary Electrocatalytic Reduction of Oxygen on Gold Nanoparticles-Electrodeposited Gold Electrodes. Electrochem. commun. 2002, 4, 288–292.

(49) Karimzadeh, I.; Aghazadeh, M.; Reza, M.; Norouzi, P. A Novel Method for Preparation of Bare and Poly (Vinylpyrrolidone) Coated Superparamagnetic Iron Oxide Nanoparticles for Biomedical Applications. 2016, 179, 5–8.

(50) Cross, C. E.; Hemminger, J. C.; Penner, R. M. Physical Vapor Deposition of One-Dimensional Nanoparticle Arrays on Graphite: Seeding the Electrodeposition of Gold Nanowires. Langmuir 2007, 23, 10372–10379.

(51) Montes De Oca, M. G.; Fermín, D. J. Electrochemical Deposition of Te Adlayers onto 3D Networks of Gold Nanoparticles. Electrochim. Acta 2010, 55, 8986–8991.

(52) Yoshii, K.; Tsuda, T.; Arimura, T.; Imanishi, A.; Torimoto, T.; Kuwabata, S. Platinum Nanoparticle Immobilization onto Carbon Nanotubes Using Pt-Sputtered Room-Temperature Ionic Liquid. RSC Adv. 2012, 2, 8262–8264.

(53) Ivanova, O. S.; Zamborini, F. P. Electrochemical Size Discrimination of Gold Nanoparticles Attached to Glass/Indium-Tin-Oxide Electrodes by Oxidation in Bromide-Containing Electrolyte. Anal. Chem. 2010, 82, 5844–5850.

(54) Bayati, M.; Abad, J. M.; Nichols, R. J.; Schiffrin, D. J. Substrate Structural Effects on the Synthesis and Electrochemical Properties of Platinum Nanoparticles on Highly Oriented Pyrolytic Graphite. J. Phys. Chem. C 2010, 114, 18439–18448.

(55) Guo, S.; Zhang, X.; Zhu, W.; He, K.; Su, D.; Mendoza-Garcia, A.; Ho, S. F.; Lu, G.; Sun, S. Nanocatalyst Superior to Pt for Oxygen Reduction Reactions: The Case of Core/Shell Ag(Au)/CuPd Nanoparticles. J. Am. Chem. Soc. 2014, 136, 15026–15033.

(56) Huang, J.; Liu, W.; Dolzhnikov, D. S.; Protesescu, L.; Kovalenko, M. V.; Koo, B.; Chattopadhyay, S.; Shenchenko, E. V.; Talapin, D. V. Surface Functionalization of Semiconductor and Oxide Nanocrystals with Small Inorganic Oxoanions (PO43-, MoO42-) and Polyoxometalate Ligands. ACS Nano 2014, 8, 9388–9402.

(57) Reske, R.; Mistry, H.; Behafarid, F.; Roldan Cuenya, B.; Strasser, P. Particle Size Effects in the Catalytic Electroreduction of CO_2 on Cu Nanoparticles. J. Am. Chem. Soc. 2014, 136, 6978–6986.

(58) Nguyen, T. A. H.; Hampton, M. A.; Nguyen, A. V. Evaporation of Nanoparticle Droplets on Smooth Hydrophobic Surfaces: The Inner Coffee Ring Deposits. J. Phys. Chem. C 2013, 117, 4707–4716.

(59) Koza, J. A.; He, Z.; Miller, A. S.; Switzer, J. A. Electrodeposition of Crystalline Co_3O_4 - A Catalyst for the Oxygen Evolution Reaction. Chem. Mater. 2012, 24, 3567–3573.

(60) Liang, X.; Bai, S.; Wang, X.; Dai, X.; Gao, F.; Sun, B.; Ning, Z.; Ye, Z.; Jin, Y. Colloidal Metal Oxide Nanocrystals as Charge Transporting Layers for Solution-Processed Light-Emitting Diodes and Solar Cells. Chem. Soc. Rev. 2017, 46, 1730–1759.

(61) Kovalenko, M. V.; Manna, L.; Cabot, A.; Hens, Z.; Talapin, D. V.; Kagan, C. R.; Klimov, V. I.; Rogach, A. L.; Reiss, P.; Milliron, D. J.; et al. Prospects of Nanoscience with Nanocrystals. ACS Nano 2015, 9, 1012–1057.

(62) Wang, J.; Cui, W.; Liu, Q.; Xing, Z.; Asiri, A. M.; Sun, X. Recent Progress in Cobalt-Based Heterogeneous Catalysts for Electrochemical Water Splitting. Adv. Mater. 2016, 28, 215–230

(63) Kriegel, I.; Scotognella, F.; Manna, L. Plasmonic Doped Semiconductor Nanocrystals: Properties, Fabrication, Applications and Perspectives. Phys. Rep. 2017, 674, 1–52.

(64) Ito, D.; Yokoyama, S.; Zaikova, T.; Masuko, K.; Hutchison, J. E. Synthesis of Ligand-Stabilized Metal Oxide Nanocrystals and Epitaxial Core / Shell Nanocrystals via a Lower- Temperature Esteri Fi Cation Process. ACS Nano 2014, 8, 64–75.

(65) Jansons, A. W.; Plummer, L. K.; Hutchison, J. E. Living Nanocrystals. Chem. Mater. 2017, 29, 5415–5425.

(66) Xie, X.; Shen, W. Morphology Control of Cobalt Oxide Nanocrystals for Promoting Their Catalytic Performance. Nanoscale 2009, 1, 50–60.

(67) Leung, Y. H.; Chan, C. M. N.; Ng, A. M. C.; Chan, H. T.; Chiang, M. W. L.; Djuriši?, A. B.; Ng, Y. H.; Jim, W. Y.; Guo, M. Y.; Leung, F. C. C.; et al. Antibacterial Activity of ZnO Nanoparticles with a Modified Surface under Ambient Illumination. Nanotechnology 2012, 23.

(68) Crockett, B. M.; Jansons, A. W.; Koskela, K. M.; Johnson, D. W.; Hutchison, J. E. Radial Dopant Placement for Tuning Plasmonic Properties in Metal Oxide Nanocrystals. ACS Nano 2017, 11, 7719–7728.

(69) Crockett, B. M.; Jansons, A. W.; Koskela, K. M.; Sharps, M. C.; Johnson, D. W.; Hutchison, J. E. Influence of Nanocrystal Size on the Optoelectronic Properties of Thin, Solution-Cast Sn-Doped In2O3 Films. Chem. Mater. 2019, 31, 3370–3380.

(70) Cooper, S. R.; Plummer, L. K.; Cosby, A. G.; Lenox, P.; Jander, A.; Dhagat, P.; Hutchison, J. E. Insights into the Magnetic Properties of Sub-10 Nm Iron Oxide Nanocrystals through the Use of a Continuous Growth Synthesis. Chem. Mater. 2018, 30, 6053–6062.

(71) Punnoose, A.; Dodge, K.; Rasmussen, J. W.; Chess, J.; Wingett, D.; Anders, C. Cytotoxicity of ZnO Nanoparticles Can Be Tailored by Modifying Their Surface Structure: A Green Chemistry Approach for Safer Nanomaterials. ACS Sustain. Chem. Eng. 2014, 2, 1666–1673.

(72) Runnerstrom, E. L.; Bergerud, A.; Agrawal, A.; Johns, R. W.; Dahlman, C. J.; Singh, A.; Selbach, S. M.; Milliron, D. J. Defect Engineering in Plasmonic Metal Oxide Nanocrystals. Nano Lett. 2016, 16, 3390–3398.

(73) Matijevi?, E. Monodispersed Metal (Hydrous) Oxides-A Fascinating Field of Colloid Science. Acc. Chem. Res. 1981, 14, 22–29.

(74) Matijevi?, E. Preparation and Properties of Uniform Size Colloids. Chem. Mater. 1993, 5, 412–426.

(75) Garnweitner, G.; Niederberger, M. Nonaqueous and Surfactant-Free Synthesis Routes to Metal Oxide Nanoparticles. J. Am. Ceram. Soc. 2006, 89, 1801–1808.

(76) Niederberger, M. Nonaqueous Sol-Gel Routes to Metal Oxide Nanoparticles. Acc. Chem. Res. 2007, 40, 793–800.

(77) Niederberger, M.; Garnweitner, G.; Pinna, N.; Neri, G. Non-Aqueous Routes to Crystalline Metal Oxide Nanoparticles: Formation Mechanisms and Applications. Prog. Solid State Chem. 2005, 33, 59–70.

(78) Garnweitner, G.; Niederberger, M. Organic Chemistry in Inorganic Nanomaterials Synthesis. J. Mater. Chem. 2008, 18, 1171–1182.

(79) Debecker, D. P.; Mutin, P. H. Non-Hydrolytic Sol-Gel Routes to Heterogeneous Catalysts. Chem. Soc. Rev. 2012, 41, 3624–3650.

(80) Sun, S.; Zeng, H.; Robinson, D. B.; Raoux, S.; Rice, P. M.; Wang, S. X.; Li, G. Monodisperse MFe2O4 (M = Fe, Co, Mn) Nanoparticles. J. Am. Chem. Soc. 2003, 4, 126–132.

(81) Adireddy, S.; Lin, C.; Palshin, V.; Dong, Y.; Cole, R.; Caruntu, G. Size-Controlled Synthesis of Quasi-Monodisperse Transition-Metal Ferrite Nanocrystals in Fatty Alcohol Solutions. J. Phys. Chem. C 2009, 113, 20800–20811.

(82) Plummer, L. K.; Crockett, B. M.; Pennel, M. L.; Jansons, A. W.; Koskela, K. M.; Hutchison, J. E. Influence of Monomer Flux and Temperature on Morphology of Indium Oxide Nanocrystals during a Continuous Growth Synthesis. Chem. Mater. 2019, 31, 7638–7649.

(83) Jansons, A. W.; Hutchison, J. E. Continuous Growth of Metal Oxide Nanocrystals: Enhanced Control of Nanocrystal Size and Radial Dopant Distribution. ACS Nano 2016, 10, 6942–6951.

(84) Simon-Deckers, a. Size-, Composition-and Shape-Dependent Toxicological Impact of Metal Oxide Nanoparticles and Carbon Nanotubes toward Bacteria. … Sci. Technol. 2009, 1–6.

(85) Karlsson, H. L.; Gustafsson, J.; Cronholm, P.; Möller, L. Size-Dependent Toxicity of Metal Oxide Particles-A Comparison between Nano- and Micrometer Size. Toxicol. Lett. 2009, 188, 112–118.

(86) Truong, L.; Zaikova, T.; Baldock, B. L.; Balik-Meisner, M.; To, K.; Reif, D. M.; Kennedy, Z. C.; Hutchison, J. E.; Tanguay, R. L. Systematic Determination of the Relationship between Nanoparticle Core Diameter and Toxicity for a Series of Structurally Analogous Gold Nanoparticles in Zebrafish. Nanotoxicology 2019, 13, 879–893.

(87) Wehmas, L. C.; Anders, C.; Chess, J.; Punnoose, A.; Pereira, C. B.; Greenwood, J. A.; Tanguay, R. L. Comparative Metal Oxide Nanoparticle Toxicity Using Embryonic Zebrafish. Toxicol. Reports 2015, 2, 702–715.

(88) Jiang, J.; Oberdörster, G.; Biswas, P. Characterization of Size, Surface Charge, and Agglomeration State of Nanoparticle Dispersions for Toxicological Studies. J. Nanoparticle Res. 2009, 11, 77–89.

(89) Albanese, A.; Tang, P. S.; Chan, W. C. W. The Effect of Nanoparticle Size, Shape, and Surface Chemistry on Biological Systems. Annu. Rev. Biomed. Eng. 2012, 14, 1–16.

(90) Suresh, A. K.; Pelletier, D. A.; Doktycz, M. J. Relating Nanomaterial Properties and Microbial Toxicity. Nanoscale 2013, 5, 463–474.

(91) Ginzburg, A. L.; Truong, L.; Tanguay, R. L.; Hutchison, J. E. Synergistic Toxicity Produced by Mixtures of Biocompatible Gold Nanoparticles and Widely Used Surfactants. ACS Nano 2018, 12, 5312–5322.

(92) Truong, L.; Zaikova, T.; Schaeublin, N. M.; Kim, K. T.; Hussain, S. M.; Hutchison, J. E.; Tanguay, R. L. Residual Weakly Bound Ligands Influence Biological Compatibility of Mixed Ligand Shell, Thiol-Stabilized Gold Nanoparticles. Environ. Sci. Nano 2017, 4, 1634–1646.

(93) Alkilany, A. M.; Lohse, S. E.; Murphy, C. J. The Gold Standard: Gold Nanoparticle Libraries to Understand the Nano-Bio Interface. Acc. Chem. Res. 2013, 46, 650–661.

(94) Gref, R.; Lück, M.; Quellec, P.; Marchand, M.; Dellacherie, E.; Harnisch, S.; Blunk, T.; Müller, R. H. "Stealth" Corona-Core Nanoparticles Surface Modified by Polyethylene Glycol (PEG): Influences of the Corona (PEG Chain Length and Surface Density) and of the Core Composition on Phagocytic Uptake and Plasma Protein Adsorption. Colloids Surfaces B Biointerfaces 2000, 18, 301–313.

(95) Wang, D.; Lin, Z.; Wang, T.; Yao, Z.; Qin, M.; Zheng, S.; Lu, W. Where Does the Toxicity of Metal Oxide Nanoparticles Come from: The Nanoparticles, the Ions, or a Combination of Both? J. Hazard. Mater. 2016, 308, 328–334.

(96) Davis, K.; Cole, B.; Ghelardini, M.; Powell, B. A.; Mefford, O. T. Quantitative Measurement of Ligand Exchange with Small-Molecule Ligands on Iron Oxide Nanoparticles via Radioanalytical Techniques. Langmuir 2016, 32, 13716–13727.

(97) Davis, K.; Qi, B.; Witmer, M.; Kitchens, C. L.; Powell, B. A.; Mefford, O. T. Quantitative Measurement of Ligand Exchange on Iron Oxides via Radiolabeled Oleic Acid. Langmuir 2014, 30, 10918–10925.

Chapter II

(1) Murray, R. W. Chemically Modified Electrodes. *Acc. Chem. Res.* **1980**, *13* (5), 135–141.

(2) Hutchison, J. E.; Postlethwaite, T. A.; Chen, C. H.; Hathcock, K. W.; Ingram, R. S.; Ou, W.; Linton, R. W.; Murray, R. W.; Tyvoll, D. A.; Chng, L. L.; et al. Electrocatalytic Activity of an Immobilized Cofacial Diporphyrin Depends on the Electrode Material. *Langmuir* **1997**, *13* (7), 2143–2148.

(3) Ulgut, B.; Abruña, H. D. Electron Transfer through Molecules and Assemblies at Electrode Surfaces. *Chem. Rev.* **2008**, *108* (7), 2721–2736.

(4) Yao, S. A.; Ruther, R. E.; Zhang, L.; Franking, R. A.; Hamers, R. J.; Berry, J. F. Covalent Attachment of Catalyst Molecules to Conductive Diamond: CO2 Reduction Using "Smart" Electrodes. *J. Am. Chem. Soc.* **2012**, *134* (38), 15632–15635.

(5) Bradbury, C. R.; Kuster, L.; Fermín, D. J. Electrochemical Reactivity of HOPG Electrodes Modified by Ultrathin Films and Two-Dimensional Arrays of Metal Nanoparticles. *J. Electroanal. Chem.* **2010**, *646* (1–2), 114–123.

(6) Cho, K. C.; Cham, P. M.; Che, C. M. Kinetics of Electron Transfer between Metal Hexacyanide Complexes. *Chem. Phys. Lett.* **1990**, *168* (3–4), 361–364.

(7) Rahman, M. A.; Won, M. S.; Shim, Y. B. Characterization of an EDTA Bonded Conducting Polymer Modified Electrode: Its Application for the Simultaneous Determination of Heavy Metal Ions. *Anal. Chem.* **2003**, *75* (5), 1123–1129.

(8) Willman, K. W.; Murray, R. W. Viologen Homopolymer, Polymer Mixture and Polymer Bilayer Films on Electrodes. *J. Electroanal. Chem. Interfacial Electrochem.* **1982**, *133* (2), 211–231.

(9) Hicks, J. F.; Zamborini, F. P.; Murray, R. W. Dynamics of Electron Transfers between Electrodes and Monolayers of Nanoparticles. *J. Phys. Chem. B* **2002**, *106* (32), 7751–7757.

(10) Katz, E.; Baron, R.; Willner, I. Magnetoswitchable Electrochemistry Gated by Alkyl-Chain-Functionalized Magnetic Nanoparticles: Control of Diffusional and Surface-Confined Electrochemical Processes. *J. Am. Chem. Soc.* **2005**, *127* (11), 4060–4070.

(11) Stiles, R. L.; Balasubramanian, R.; Feldberg, S. W.; Murray, R. W. Anion-Induced Adsorption of Ferrocenated Nanoparticles. *J. Am. Chem. Soc.* **2008**, *130* (6), 1856–1865.

(12) Xiao, W.; Lei, W.; Gong, M.; Xin, H. L.; Wang, D. Recent Advances of Structurally Ordered Intermetallic Nanoparticles for Electrocatalysis. *ACS Catal.* **2018**, *8* (4), 3237–3256.

(13) Tang, Z.; Ma, Z. Multiple Functional Strategies for Amplifying Sensitivity of Amperometric Immunoassay for Tumor Markers: A Review. *Biosens. Bioelectron.* **2017**, *98* (June), 100–112.

(14) Cardoso, D. S. P.; Šljukić, B.; Santos, D. M. F.; Sequeira, C. A. C. Organic Electrosynthesis: From Laboratorial Practice to Industrial Applications. *Org. Process Res. Dev.* **2017**, *21* (9), 1213–1226.

(15) Mistry, H.; Reske, R.; Zeng, Z.; Zhao, Z.-J.; Greeley, J.; Strasser, P.; Cuenya, B. R. Exceptional Size-Dependent Activity Enhancement in the Electroreduction of CO2 over Au Nanoparticles. *J. Am. Chem. Soc.* **2014**, *136* (47), 16473–16476.

(16) Cao, Z.; Kim, D.; Hong, D.; Yu, Y.; Xu, J.; Lin, S.; Wen, X.; Nichols, E. M.; Jeong, K.; Reimer, J. A.; et al. A Molecular Surface Functionalization Approach to Tuning Nanoparticle Electrocatalysts for Carbon Dioxide Reduction. *J. Am. Chem. Soc.* **2016**, *138* (26), 8120–8125.

(17) Rossi, L. M.; Fiorio, J. L.; Garcia, M. A. S.; Ferraz, C. P. The Role and Fate of Capping Ligands in Colloidally Prepared Metal Nanoparticle Catalysts. *Dalt. Trans.* **2018**, *47* (17), 5889–5915.

(18) Wan, X.-K.; Wang, J.-Q.; Nan, Z.-A.; Wang, Q.-M. Ligand Effects in Catalysis by Atomically Precise Gold Clusters. *Sci. Adv.* **2017**, *3*, e1701823.

(19) Mistry, H.; Behafarid, F.; Reske, R.; Varela, A. S.; Strasser, P.; Roldan Cuenya, B. Tuning Catalytic Selectivity at the Mesoscale via Interparticle Interactions. *ACS Catal.* **2016**, *6* (2), 1075–1080.

(20) Seidel, Y. E.; Schneider, A.; Jusys, Z.; Wickman, B.; Kasemo, B.; Behm, R. J. Mesoscopic Mass Transport Effects in Electrocatalytic Processes. *Faraday Discuss.* **2009**, *140*, 167–184.

(21) Young, S. L.; Kellon, J. E.; Hutchison, J. E. Small Gold Nanoparticles Interfaced to Electrodes through Molecular Linkers: A Platform to Enhance Electron Transfer and Increase Electrochemically Active Surface Area. *J. Am. Chem. Soc.* **2016**, *138* (42), 13975–13984.

(22) Carducci, T. M.; Murray, R. W. Kinetics and Low Temperature Studies of Electron Transfers in Films of Small (<2 Nm) Au Monolayer Protected Clusters. *J. Am. Chem. Soc.* **2013**, *135* (30), 11351–11356.

(23) Gambardella, A. a; Feldberg, S. W.; Murray, R. W. Electron Transfer Dynamics of Iridium Oxide Nanoparticles Attached to Electrodes by Self-Assembled Monolayers. *J. Am. Chem. Soc.* **2012**, *134* (13), 5774–5777.

(24) Holland, J. T.; Lau, C.; Brozik, S.; Atanassov, P.; Banta, S. Engineering of Glucose Oxidase for Direct Electron Transfer via Site-Specific Gold Nanoparticle Conjugation. *J. Am. Chem. Soc.* **2011**, *133* (48), 19262–19265.

(25) Kim, D.; Kley, C. S.; Li, Y.; Yang, P. Copper Nanoparticle Ensembles for Selective Electroreduction of CO2 to C2 –C3 Products. *Proc. Natl. Acad. Sci.* **2017**, *114* (40), 10560–10565.

(26) Zhang, S.; Kang, P.; Meyer, T. J. Nanostructured Tin Catalysts for Selective Electrochemical Reduction of Carbon Dioxide to Formate. *J. Am. Chem. Soc.* **2014**, *136* (5), 1734–1737.

(27) Zhu, W.; Michalsky, R.; Metin, Ö.; Lv, H.; Guo, S.; Wright, C. J.; Sun, X.; Peterson, A. A.; Sun, S. Monodisperse Au Nanoparticles for Selective Electrocatalytic Reduction of CO2 to CO. *J. Am. Chem. Soc.* **2013**, *135* (45), 16833–16836.

(28) Waheed, A.; Mansha, M.; Ullah, N. Nanomaterials-Based Electrochemical Detection of Heavy Metals in Water: Current Status, Challenges and Future Direction. *TrAC - Trends Anal. Chem.* **2018**, *105*, 37–51.

(29) Miao, P.; Tang, Y.; Wang, L. DNA Modified Fe3O4@Au Magnetic Nanoparticles as Selective Probes for Simultaneous Detection of Heavy Metal Ions. *ACS Appl. Mater. Interfaces* **2017**, *9* (4), 3940–3947.

(30) Li, J.; Hu, H.; Li, H.; Yao, C. Recent Developments in Electrochemical Sensors Based on Nanomaterials for Determining Glucose and Its Byproduct H2O2. *J. Mater. Sci.* **2017**, *52* (17), 10455–10469.

(31) Bayati, M.; Abad, J. M.; Nichols, R. J.; Schiffrin, D. J. Substrate Structural Effects on the Synthesis and Electrochemical Properties of Platinum Nanoparticles on Highly Oriented Pyrolytic Graphite. *J. Phys. Chem. C* **2010**, *114* (43), 18439–18448.

(32) El- Deab, M. S.; Ohsaka, T. An Extraordinary Electrocatalytic Reduction of Oxygen on Gold Nanoparticles-Electrodeposited Gold Electrodes. *Electrochem. Commun.* **2002**, *4* (4), 288–292.

(33) Ivanova, O. S.; Zamborini, F. P. Electrochemical Size Discrimination of Gold Nanoparticles Attached to Glass/Indium-Tin-Oxide Electrodes by Oxidation in Bromide-Containing Electrolyte. *Anal. Chem.* **2010**, *82* (13), 5844–5850.

(34) Mohanty, U. S. Electrodeposition: A Versatile and Inexpensive Tool for the Synthesis of Nanoparticles, Nanorods, Nanowires, and Nanoclusters of Metals. *J. Appl. Electrochem.* **2011**, *41* (3), 257–270.

(35) Penner, R. M. Mesoscopic Metal Particles and Wires by Electrodeposition. *J. Phys. Chem. B* **2002**, *106* (13), 3339–3353.

(36) Penner, R. M. A Nose for Hydrogen Gas: Fast, Sensitive H2 Sensors Using Electrodeposited Nanomaterials. *Acc. Chem. Res.* **2017**, *50* (8), 1902–1910.

(37) Luo, Z.; Somers, L. A.; Dan, Y.; Ly, T.; Kybert, N. J.; Mele, E. J.; Johnson, A. T. C. Size-Selective Nanoparticle Growth on Few-Layer Graphene Films. *Nano Lett.* **2010**, *10* (3), 777–781.

(38) Masuda, H.; Yasui, K.; Nishio, K. Fabrication of Ordered Arrays of Multiple Nanodots Using Anodic Porous Alumina as an Evaporation Mask. *Adv. Mater.* **2000**, *12* (14), 1031–1033.

(39) Cross, C. E.; Hemminger, J. C.; Penner, R. M. Physical Vapor Deposition of One-Dimensional Nanoparticle Arrays on Graphite: Seeding the Electrodeposition of Gold Nanowires. *Langmuir* **2007**, *23* (20), 10372–10379.

(40) Deligianni, H. Electrodeposition and Microelectronics. *Electrochem. Soc. Interface* **2006**, *250* (6), 32–35.

(41) Chen, W.; Chen, S. Oxygen Electroreduction Catalyzed by Gold Nanoclusters: Strong Core Size Effects. *Angew. Chemie Int. Ed.* **2009**, *48* (24), 4386–4389.

(42) Guo, S.; Zhang, X.; Zhu, W.; He, K.; Su, D.; Mendoza-Garcia, A.; Ho, S. F.; Lu, G.; Sun, S. Nanocatalyst Superior to Pt for Oxygen Reduction Reactions: The Case of Core/Shell Ag(Au)/CuPd Nanoparticles. *J. Am. Chem. Soc.* **2014**, *136* (42), 15026–15033.

(43) Huang, J.; Liu, W.; Dolzhnikov, D.; Protesescu, L.; Kovalenko, M. V.; Koo, B.; Chattopadhyay, S.; Shenchenko, E. V.; Talapin, D. V. Surface Functionalization of Semiconductor and Oxide Nanocrystals with Small Inorganic Oxoanions (PO43-, MoO42-) and Polyoxometalate Ligands. *ACS Nano* **2014**, *8* (9), 9388–9402.

(44) Jiang, L.; Hsu, A.; Chu, D.; Chen, R. Size-Dependent Activity of Palladium Nanoparticles for Oxygen Electroreduction in Alkaline Solutions. *J. Electrochem. Soc.* **2009**, *156* (5), 10515–10519.

(45) Reske, R.; Mistry, H.; Behafarid, F.; Cuenya, B. R.; Strasser, P. Particle Size Effects in the Catalytic Electroreduction of CO2 on Cu Nanoparticles. *J. Am. Chem. Soc.* **2014**, *136*, 6978–6986.

(46) Xiao, F.; Song, J.; Gao, H.; Zan, X.; Xu, R.; Duan, H. Coating Graphene Paper with 2D-Assembly of Electrocatalytic Nanoparticles: A Modular Approach toward High-Performance Flexible Electrodes. *ACS Nano* **2012**, *6* (1), 100–110.

(47) Nguyen, T. A. H.; Hampton, M. A.; Nguyen, A. V. Evaporation of Nanoparticle Droplets on Smooth Hydrophobic Surfaces: The Inner Coffee Ring Deposits. *J. Phys. Chem. C* **2013**, *117* (9), 4707–4716.

(48) Kleijn, S. E. F.; Lai, S. C. S.; Koper, M. T. M.; Unwin, P. R. Electrochemistry of Nanoparticles. *Angew. Chemie Int. Ed.* **2014**, *53* (14), 3558–3586.

(49) Simon, U. Charge Transport in Nanoparticle Arrangements. *Adv. Mater.* **1998**, *10* (17), 1487–1492.

(50) Claridge, S. A.; Liao, W. S.; Thomas, J. C.; Zhao, Y.; Cao, H. H.; Cheunkar, S.; Serino, A. C.; Andrews, A. M.; Weiss, P. S. From the Bottom up: Dimensional Control and Characterization in Molecular Monolayers. *Chem. Soc. Rev.* **2013**, *42* (7), 2725–2745.

(51) Strother, T.; Knickerbocker, T.; Russell, J. N.; Butler, J. E.; Smith, L. M.; Hamers, R. J. Photochemical Functionalization of Diamond Films. *Langmuir* **2002**, *18* (4), 968–971.

(52) Love, J. C.; Estroff, L. A.; Kriebel, J. K.; Nuzzo, R. G.; Whitesides, G. M. Self-Assembled Monolayers of Thiolates on Metals as a Form of Nanotechnology. *Chem. Rev.* **2005**, *105* (4), 1103–1170.

(53) Li, G.; Jin, R. Atomically Precise Gold Nanoclusters as New Model Catalysts. *Acc. Chem. Res.* **2013**, *46* (8), 1749–1758.

(54) Mourdikoudis, S.; Liz-Marzán, L. M. Oleylamine in Nanoparticle Synthesis. *Chem. Mater.* **2013**, *25* (9), 1465–1476.

(55) Niu, Z.; Li, Y. Removal and Utilization of Capping Agents in Nanocatalysis. *Chem. Mater.* **2014**, *26*, 72–83.

(56) Sardar, R.; Funston, A. M.; Mulvaney, P.; Murray, R. W. Gold Nanoparticles: Past, Present, and Future. *Langmuir* **2009**, *25* (24), 13840–13851.

(57) Smith, B. L.; Hutchison, J. E. Transformations during Sintering of Small (Dcore< 2 Nm) Ligand-Stabilized Gold Nanoparticles: Influence of Ligand Functionality and Core Size. *J. Phys. Chem. C* **2013**, *117* (47), 25127–25137.

(58) Jansons, A. W.; Plummer, L. K.; Hutchison, J. E. Living Nanocrystals. *Chem. Mater.* **2017**, *29* (13), 5415–5425.

(59) Kissling, G. P.; Miles, D. O.; Fermín, D. J. Electrochemical Charge Transfer Mediated by Metal Nanoparticles and Quantum Dots. *Phys. Chem. Chem. Phys.* **2011**, *13* (48), 21175–21185.

(60) Adams, D.; Brus, L.; Chidsey, C.; Creager, S.; Creutz, C.; Kagan, C.; Kamat, P.; Lieberman, M.; Lindsay, S.; Marcus, R.; et al. Charge Transfer on the Nanoscale: Current Status. *J. Phys. Chem. B* **2003**, *107* (28), 6668–6697.

(61) Liu, F.; Khan, K.; Liang, J.-H.; Yan, J.-W.; Wu, D.-Y.; Mao, B.-W.; Jensen, P. S.; Zhang, J.; Ulstrup, J. On the Hopping Efficiency of Nanoparticles in the Electron Transfer across Self-Assembled Monolayers. *ChemPhysChem* **2013**, *14* (5), 952–957.

(62) Gittins, D. I.; Bethell, D.; Nichols, R. J.; Schiffrin, D. J. Redox-Connected Multilayers of Discrete Gold Particles: A Novel Electroactive Nanomaterial. *Adv. Mater.* **1999**, *11* (9), 737–740.

(63) Gittins, D. I.; Bethell, D.; Schiffrin, D. J.; Nichols, R. J. A Nanometre-Scale Electronic Switch Consisting of a Metal Cluster and Redox-Addressable Groups. *Nature* **2000**, *408* (6808), 67–69.

(64) Chou, A.; Eggers, P. K.; Paddon-Row, M. N.; Gooding, J. J. Self-Assembled Carbon Nanotube Electrode Arrays: Effect of Length of the Linker between Nanotubes and Electrode. *J. Phys. Chem. C* **2009**, *113* (8), 3203–3211.

(65) Shein, J. B.; Lai, L. M. H.; Eggers, P. K.; Paddon-Row, M. N.; Gooding, J. J. Formation of Efficient Electron Transfer Pathways by Adsorbing Gold Nanoparticles to Self-Assembled Monolayer Modified Electrodes. *Langmuir* **2009**, *25* (18), 11121–11128.

(66) Suk, J.; Lee, J.; Kwak, J. Electrochemistry on Alternate Structures of Gold Nanoparticles and Ferrocene-Tethered Polyamidoamine Dendrimers. *Bull. Korean Chem. Soc.* **2004**, *25* (11), 1681–1686.

(67) Chirea, M.; Cruz, A.; Pereira, C. M.; Silva, A. F. Size-Dependent Electrochemical Properties of Gold Nanorods. *J. Phys. Chem. C* **2009**, *113* (30), 13077–13087.

(68) Jensen, P. S.; Chi, Q.; Zhang, J.; Ulstrup, J. Long-Range Interfacial Electrochemical Electron Transfer of Pseudomonas Aeruginosa Azurin−Gold Nanoparticle Hybrid Systems. *J. Phys. Chem. C* **2009**, *113* (31), 13993–14000.

(69) Bakkers, E. P. A. M.; Roest, A. L.; Marsman, A. W.; Jenneskens, L. W.; de Jong-van Steensel, L. I.; Kelly, J. J.; Vanmaekelbergh, D. Characterization of Photoinduced Electron Tunneling in Gold/SAM/Q-CdSe Systems by Time-Resolved Photoelectrochemistry. *J. Phys. Chem. B* **2000**, *104* (31), 7266–7272.

(70) Baum, T.; Bethell, D.; Brust, M.; Schiffrin, D. J. Electrochemical Charge Injection into Immobilized Nanosized Gold Particle Ensembles: Potential Modulated Transmission and Reflectance Spectroscopy. *Langmuir* **1999**, *15* (3), 866–871.

(71) Musick, M. D.; Peña, D. J.; Botsko, S. L.; McEvoy, T. M.; Richardson, J. N.; Natan, M. J. Electrochemical Properties of Colloidal Au-Based Surfaces: Multilayer Assemblies and Seeded Colloid Films. *Langmuir* **1999**, *15* (3), 844–850.

(72) Ballarin, B.; Cassani, M. C.; Scavetta, E.; Tonelli, D. Self-Assembled Gold Nanoparticles Modified ITO Electrodes: The Monolayer Binder Molecule Effect. *Electrochim. Acta* **2008**, *53* (27), 8034–8044.

(73) Cheng, W.; Dong, S.; Wang, E. Colloid Chemical Approach to Nanoelectrode Ensembles with Highly Controllable Active Area Fraction. *Anal. Chem.* **2002**, *74* (15), 3599–3604.

(74) Doron, A.; Katz, E.; Willner, I. Organization of Au Colloids as Monolayer Films onto ITO Glass Surfaces: Application of the Metal Colloid Films as Base Interfaces To Construct Redox-Active Monolayers. *Langmuir* **1995**, *11* (4), 1313–1317.

(75) Tseng, J. Y.; Lin, M. H.; Chau, L. K. Preparation of Colloidal Gold Multilayers with 3-(Mercaptopropyl)-Trimethoxysilane as a Linker Molecule. *Colloids Surfaces A Physicochem. Eng. Asp.* **2001**, *182* (1–3), 239–245.

(76) Kondo, T.; Aoshima, S.; Honda, K.; Einaga, Y.; Fujishima, A.; Kawai, T. Fabrication of Covalent SAM/Au Nanoparticle/Boron-Doped Diamond Configurations with a Sequential Self-Assembly Method. *J. Phys. Chem. C* **2007**, *111* (34), 12650–12657.

(77) Cheng, W.; Dong, S.; Wang, E. Gold Nanoparticles as Fine Tuners of Electrochemical Properties of the Electrode/Solution Interface. *Langmuir* **2002**, *18* (25), 9947–9952.

(78) Brust, M.; Bethell, D.; Kiely, C. J.; Schiffrin, D. J. Self-Assembled Gold Nanoparticle Thin Films with Nonmetallic Optical and Electronic Properties. *Langmuir* **1998**, *14* (19), 5425–5429.

(79) Cao, C.; Zhang, Y.; Jiang, C.; Qi, M.; Liu, G. Advances on Aryldiazonium Salt Chemistry Based Interfacial Fabrication for Sensing Applications. *ACS Appl. Mater. Interfaces* **2017**, *9* (6), 5031–5049.

(80) Gooding, J. J. Advances in Interfacial Design for Electrochemical Biosensors and Sensors: Aryl Diazonium Salts for Modifying Carbon and Metal Electrodes. *Electroanalysis* **2008**, *20* (6), 573–582.

(81) Lesniewski, A.; Matyjewicz, J.; Palys, B.; Niedziolka-Jonsson, J. Electroassisted Click Chemistry Immobilisation of Gold Nanoparticles on a Solid Substrate. *Electrochem. Commun.* **2015**, *53*, 20–23.

(82) Liu, G.; Luais, E.; Gooding, J. J. The Fabrication of Stable Gold Nanoparticle-Modified Interfaces for Electrochemistry. *Langmuir* **2011**, *27* (7), 4176–4183.

(83) Lee, H. E.; Kang, Y. O.; Choi, S. H. Electrochemical-DNA Biosensor Development Based on a Modified Carbon Electrode with Gold Nanoparticles for Influenza A (H1N1) Detection: Effect of Spacer. *Int. J. Electrochem. Sci.* **2014**, *9* (12), 6793–6808.

(84) Delamar, M.; Hitmi, R.; Pinson, J.; Savéant, J. Covalent Modification of Carbon Surfaces by Grafting of Functionalized Aryl Radicals Produced from Electrochemical Reduction of Diazonium Salts. *J. Am. Chem. Soc.* **1992**, *114* (14), 5883–5884.

(85) González, M. C. R.; Orive, A. G.; Salvarezza, R. C.; Creus, A. H. Electrodeposition of Gold Nanoparticles on Aryl Diazonium Monolayer Functionalized HOPG Surfaces. *Phys. Chem. Chem. Phys.* **2016**, *18* (3), 1953–1960.

(86) Liu, G.; Liu, J.; Davis, T. P.; Gooding, J. J. Electrochemical Impedance Immunosensor Based on Gold Nanoparticles and Aryl Diazonium Salt Functionalized Gold Electrodes for the Detection of Antibody. *Biosens. Bioelectron.* **2011**, *26* (8), 3660–3665.

(87) Barfidokht, A.; Ciampi, S.; Luais, E.; Darwish, N.; Gooding, J. J. Distance-Dependent Electron Transfer at Passivated Electrodes Decorated by Gold Nanoparticles. *Anal. Chem.* **2013**, *85* (2), 1073–1080.

(88) Wang, X.; Colavita, P. E.; Streifer, J. a.; Butler, J. E.; Hamers, R. J. Photochemical Grafting of Alkenes onto Carbon Surfaces: Identifying the Roles of Electrons and Holes. *J. Phys. Chem. C* **2010**, *114* (111), 4067–4074.

(89) Wang, X.; Landis, E. C.; Franking, R.; Hamers, R. J. Surface Chemistry for Stable and Smart Molecular and Biomolecular Interfaces via Photochemical Grafting of Alkenes. *Acc. Chem. Res.* **2010**, *43* (9), 1205–1215.

(90) Tian, R.; Rao, T. N.; Einaga, Y.; Zhi, J. Construction of Two-Dimensional Arrays Gold Nanoparticles Monolayer onto Boron-Doped Diamond Electrode Surfaces. *Chem. Mater.* **2006**, *18* (4), 939–945.

(91) Nakamura, T.; Ohana, T. Surface Functionalization of Diamond Films by Photoreaction of Elemental Sulfur and Their Surface Properties. *Jpn. J. Appl. Phys.* **2012**, *51*, 085201.

(92) Le Saux, G.; Ciampi, S.; Gaus, K.; Gooding, J. J. Electrochemical Behavior of Gold Colloidal Alkyl Modified Silicon Surfaces. *ACS Appl. Mater. Interfaces* **2009**, *1* (11), 2477–2483.

(93) Kashi, M. B.; Wu, Y.; Gonçales, V. R.; Choudhury, M. H.; Ciampi, S.; Gooding, J. J. Silicon–SAM–AuNP Electrodes: Electrochemical "Switching" and Stability. *Electrochem. Commun.* **2016**, *70*, 28–32.

(94) Hongthani, W.; Fox, N. A.; Fermín, D. J. Electrochemical Properties of Two Dimensional Assemblies of Insulating Diamond Particles. *Langmuir* **2011**, *27* (8), 5112–5118.

(95) Montes de Oca, M. G.; Kumarakuru, H.; Cherns, D.; Fermín, D. J. Hydrogen Adsorption at Strained Pd Nanoshells. *J. Phys. Chem. C* **2011**, *115* (21), 10489–10496.

(96) Montes de Oca, M. G.; Fermín, D. J. Electrochemical Deposition of Te Adlayers onto 3D Networks of Gold Nanoparticles. *Electrochim. Acta* **2010**, *55* (28), 8986–8991.

(97) Kissling, G. P.; Bünzli, C.; Fermín, D. J. Tuning Electrochemical Rectification via Quantum Dot Assemblies. *J. Am. Chem. Soc.* **2010**, *132* (47), 16855–16861.

(98) Bradbury, C. R.; Zhao, J.; Fermín, D. J. Distance-Independent Charge-Transfer Resistance at Gold Electrodes Modified by Thiol Monolayers and Metal Nanoparticles. *J. Phys. Chem. C* **2008**, *112* (27), 10153–10160.

(99) Zhao, J.; Bradbury, C. R.; Fermín, D. J. Long-Range Electronic Communication between Metal Nanoparticles and Electrode Surfaces Separated by Polyelectrolyte Multilayer Films. *J. Phys. Chem. C* **2008**, *112* (17), 6832–6841.

(100) Chirea, M.; García-Morales, V.; Manzanares, J. A.; Pereira, C.; Gulaboski, R.; Silva, F. Electrochemical Characterization of Polyelectrolyte/Gold Nanoparticle Multilayers Self-Assembled on Gold Electrodes. *J. Phys. Chem. B* **2005**, *109* (46), 21808–21817.

(101) Ottakam Thotiyl, M. M.; Basit, H.; Sánchez, J. A.; Goyer, C.; Coche-Guerente, L.; Dumy, P.; Sampath, S.; Labbé, P.; Moutet, J. C. Multilayer Assemblies of Polyelectrolyte-Gold Nanoparticles for the Electrocatalytic Oxidation and Detection of Arsenic(III). *J. Colloid Interface Sci.* **2012**, *383* (1), 130–139.

(102) Bradbury, C. R.; Bünzli, C.; Zhao, J.; Carrara, M.; Kissling, G. P.; Aslan-Guerel, E.; Fermín, D. J. Modulating the Reactivity of Electrode Surfaces by Electrostatic Assembly of Metal Nanoparticles and Quantum Dots. *Chimia (Aarau).* **2008**, *62* (10), 841–846.

(103) Zhao, J.; Bradbury, C. R.; Huclova, S.; Potapova, I.; Carrara, M.; Fermín, D. J. Nanoparticle-Mediated Electron Transfer Across Ultrathin Self-Assembled Films. *J. Phys. Chem. B* **2005**, *109* (48), 22985–22994.

(104) Chirea, M.; Pereira, C. M.; Silva, F. Catalytic Effect of Gold Nanoparticles Self-Assembled in Multilayered Polyelectrolyte Films. *J. Phys. Chem. C* **2007**, *111* (26), 9255–9266.

(105) Li, F.; Ciani, I.; Bertoncello, P.; Unwin, P. R.; Zhao, J.; Bradbury, C. R.; Fermin, D. J. Scanning Electrochemical Microscopy of Redox-Mediated Hydrogen Evolution Catalyzed by Two-Dimensional Assemblies of Palladium Nanoparticles. *J. Phys. Chem. C* **2008**, *112* (26), 9686–9694.

(106) Tang, Y.; Cheng, W. Nanoparticle-Modified Electrode with Size- and Shape-Dependent Electrocatalytic Activities. *Langmuir* **2013**, *29* (9), 3125–3132.

(107) Xi, Q.; Chen, X.; Evans, D. G.; Yang, W. Gold Nanoparticle-Embedded Porous Graphene Thin Films Fabricated via Layer-by-Layer Self-Assembly and Subsequent Thermal Annealing for Electrochemical Sensing. *Langmuir* **2012**, *28* (25), 9885–9892.

(108) Kolb, H. C.; Finn, M. G.; Sharpless, K. B. Click Chemistry: Diverse Chemical Function from a Few Good Reactions. *Angew. Chemie Int. Ed.* **2001**, *40* (11), 2004–2021.

(109) Matyjewicz, J.; Lesniewski, A.; Niedziolka-Jonsson, J. Click Chemistry Modification of Glassy Carbon Electrode with Gold Nanoparticles for Electroactive Ion Discrimination. *Electrochem. Commun.* **2014**, *48*, 73–76.

(110) Upadhyay, A. P.; Behara, D. K.; Sharma, G. P.; Bajpai, A.; Sharac, N.; Ragan, R.; Pala, R. G. S.; Sivakumar, S. Generic Process for Highly Stable Metallic Nanoparticle-Semiconductor Heterostructures via Click Chemistry for Electro/Photocatalytic Applications. *ACS Appl. Mater. Interfaces* **2013**, *5* (19), 9554–9562.

(111) Fratila, R. M.; Navascuez, M.; Idiago-López, J.; Eceiza, M.; Miranda, J. I.; Aizpurua, J. M.; de la Fuente, J. M. Covalent Immobilisation of Magnetic Nanoparticles on Surfaces via Strain-Promoted Azide–alkyne Click Chemistry. *New J. Chem.* **2017**, 10835–10840.

(112) Jensen, P. S.; Chi, Q.; Grumsen, F. B.; Abad, J. M.; Horsewell, A.; Schiffrin, D. J.; Ulstrup, J. Gold Nanoparticle Assisted Assembly of a Heme Protein for Enhancement of Long-Range Interfacial Electron Transfer. *J. Phys. Chem.* **2007**, *111*, 6124–6132.

(113) Nguyen, T. T.; Sly, K. L.; Conboy, J. C. Comparison of the Energetics of Avidin, Streptavidin, NeutrAvidin, and Anti-Biotin Antibody Binding to Biotinylated Lipid Bilayer Examined by Second-Harmonic Generation. *Anal. Chem.* **2012**, *84* (1), 201–208.

(114) Kar, P.; Tatard, F.; Lamblin, G.; Banet, P.; Aubert, P. H.; Plesse, C.; Chevrot, C. Silver Nanoparticles to Improve Electron Transfer at Interfaces of Gold Electrodes Modified by Biotin or Avidin. *J. Electroanal. Chem.* **2013**, *692*, 17–25.

(115) Huang, X.; Du, D.; Gong, X.; Cai, J.; Tu, H.; Xu, X.; Zhang, A. Composite Assembly of Silver Nanoparticles with Avidin and Biotinylated AChE on Gold for the Pesticidal Electrochemical Sensing. *Electroanalysis* **2008**, *20* (4), 402–409.

(116) Damos, F. S.; Luz, R. C. S.; Tanaka, A. A.; Kubota, L. T. Development of an Electroactive Layer-by-Layer Assembly Based on Host-Guest Supramolecular Interactions. *J. Electroanal. Chem.* **2010**, *639* (1–2), 36–42.

(117) Zuo, F.; Luo, C.; Zheng, Z.; Ding, X.; Peng, Y. Supramolecular Assembly of β-Cyclodextrin-Capped Gold Nanoparticles on Ferrocene-Functionalized ITO Surface for Enhanced Voltammetric Analysis of Ascorbic Acid. *Electroanalysis* **2008**, *20* (8), 894–899.

(118) Yamanoi, Y.; Shirahata, N.; Yonezawa, T.; Terasaki, N.; Yamamoto, N.; Matsui, Y.; Nishio, K.; Masuda, H.; Ikuhara, Y.; Nishihara, H. Detailed Structural Examinations of Covalently Immobilized Gold Nanoparticles onto Hydrogen-Terminated Silicon Surfaces. *Chem. - A Eur. J.* **2006**, *12* (1), 314–323.

(119) Liu, G.; Qi, M.; Zhang, Y.; Cao, C.; Goldys, E. M. Nanocomposites of Gold Nanoparticles and Graphene Oxide towards an Stable Label-Free Electrochemical Immunosensor for Detection of Cardiac Marker Troponin-I. *Anal. Chim. Acta* **2016**, *909*, 1–8.

(120) Chazalviel, J. N.; Allongue, P. On the Origin of the Efficient Nanoparticle Mediated Electron Transfer across a Self-Assembled Monolayer. *J. Am. Chem. Soc.* **2011**, *133*, 762–764.

(121) Macpherson, J. V. A Practical Guide to Using Boron Doped Diamond in Electrochemical Research. *Phys. Chem. Chem. Phys.* **2015**, *17* (5), 2935–2949.

(122) Ruther, R. E.; Rigsby, M. L.; Gerken, J. B.; Hogendoorn, S. R.; Landis, E. C.; Stahl, S. S.; Hamers, R. J. Highly Stable Redox-Active Molecular Layers by Covalent Grafting to Conductive Diamond. *J. Am. Chem. Soc.* **2011**, *133*, 5692–5694.

(123) Widrig, C. A.; Chung, C.; Porter, M. D. The Electrochemical Desorption of N-Alkanethiol Monolayers from Polycrystalline Au and Ag Electrodes. *J. Electroanal. Chem.* **1991**, *310* (1–2), 335–359.

(124) Muglali, M. I.; Erbe, A.; Chen, Y.; Barth, C.; Koelsch, P.; Rohwerder, M. Modulation of Electrochemical Hydrogen Evolution Rate by Araliphatic Thiol Monolayers on Gold. *Electrochim. Acta* **2013**, *90*, 17–26.

(125) Strong, L.; Whitesides, G. M. Structures of Self-Assembled Monolayer Films of Organosulfur Compounds Adsorbed on Gold Single Crystals: Electron Diffraction Studies. *Langmuir* **1988**, *4* (3), 546–558.

(126) Laibinis, P. E.; Whitesides, G. M.; Allara, D. L.; Tao, Y. T.; Parikh, A. N.; Nuzzo, R. G. Comparison of the Structures and Wetting Properties of Self-Assembled Monolayers of n-Alkanethiols on the Coinage Metal Surfaces, Copper, Silver, and Gold. *J. Am. Chem. Soc.* **1991**, *113* (19), 7152–7167.

(127) Zamborini, F. P.; Crooks, R. M. Corrosion Passivation of Gold by n -Alkanethiol Self-Assembled Monolayers : Effect of Chain Length and End Group. **1998**, *7463* (4), 3279–3286.

(128) Schoenenberger, C.; Sondag-Huethorst, J. A. M.; Jorritsma, J.; Fokkink, L. G. J. What Are the "Holes" in Self-Assembled Monolayers of Alkanethiols on Gold? *Langmuir* **1994**, *10* (3), 611–614.

(129) Edinger, K.; Goelzhaeuser, A.; Demota, K.; Woell, C.; Grunze, M. Formation of Self-Assembled Monolayers of n-Alkanethiols on Gold: A Scanning Tunneling Microscopy Study on the Modification of Substrate Morphology. *Langmuir* **1993**, *9* (1), 4–8.

(130) Ruther, R. E.; Cui, Q.; Hamers, R. J. Conformational Disorder Enhances Electron Transfer through Alkyl Monolayers: Ferrocene on Conductive Diamond. *J. Am. Chem. Soc.* **2013**, *135* (15), 5751–5761.

(131) Adenier, A.; Combellas, C.; Kanoufi, F.; Pinson, J.; Podvorica, F. I. Formation of Polyphenylene Films on Metal Electrodes by Electrochemical Reduction of Benzenediazonium Salts. *Chem. Mater.* **2006**, *18* (8), 2021–2029.

(132) Menanteau, T.; Dias, M.; Levillain, E.; Downard, A. J.; Breton, T. Electrografting via Diazonium Chemistry: The Key Role of the Aryl Substituent in the Layer Growth Mechanism. *J. Phys. Chem. C* **2016**, *120* (8), 4423–4429.

(133) Menanteau, T.; Levillain, E.; Downard, A. J.; Breton, T. Evidence of Monolayer Formation via Diazonium Grafting with a Radical Scavenger: Electrochemical, AFM and XPS Monitoring. *Phys. Chem. Chem. Phys.* **2015**, *17* (19), 13137–13142.

(134) Leroux, Y. R.; Fei, H.; Noël, J. M.; Roux, C.; Hapiot, P. Efficient Covalent Modification of a Carbon Surface: Use of a Silyl Protecting Group to Form an Active Monolayer. *J. Am. Chem. Soc.* **2010**, *132* (40), 14039–14041.

(135) Lee, L.; Ma, H.; Brooksby, P. A.; Brown, S. A.; Leroux, Y. R.; Hapiot, P.; Downard, A. J. Covalently Anchored Carboxyphenyl Monolayer via Aryldiazonium Ion Grafting: A Well-Defined Reactive Tether Layer for on-Surface Chemistry. *Langmuir* **2014**, *30* (24), 7104–7111.

(136) Combellas, C.; Kanoufi, F.; Pinson, J.; Podvorica, F. I. Sterically Hindered Diazonium Salts for the Grafting of a Monolayer on Metals. *J. Am. Chem. Soc.* **2008**, *130* (27), 8576–8577.

(137) Chirea, M.; Borges, J.; Pereira, C. M.; Silva, A. F. Density-Dependent Electrochemical Properties of Vertically Aligned Gold Nanorods. *J. Phys. Chem. C* **2010**, *114* (20), 9478–9488.

(138) Raj, C. R.; Okajima, T.; Ohsaka, T. Gold Nanoparticle Arrays for the Voltammetric Sensing of Dopamine. *J. Electroanal. Chem.* **2003**, *543* (2), 127–133.

(139) Castañeda, A. D.; Alligrant, T. M.; Loussaert, J. A.; Crooks, R. M. Electrocatalytic Amplification of Nanoparticle Collisions at Electrodes Modified with Polyelectrolyte Multilayer Films. *Langmuir* **2015**, *31* (2), 876–885.

(140) Mirkhalaf, F.; Graves, J. E. Nanostructured Electrocatalysts Immobilised on Electrode Surfaces and Organic Film Templates. *Chem. Pap.* **2012**, *66* (5), 472–483.

(141) Lee, J.; Hwang, S.; Lee, H.; Kwak, J. Bimetallic Clusters by Underpotential Deposition on Layered Au Nanoparticle Films. *J. Phys. Chem. B* **2004**, *108* (17), 5372–5379.

(142) Young, S. L.; Hutchison, J. E. Selective Deposition of Metals onto Molecularly Tethered Gold Nanoparticles: The Influence of Silver Deposition on Oxygen Electroreduction. *Chem. Mater.* Under Review.

(143) Jansons, A. W.; Hutchison, J. E. Continuous Growth of Metal Oxide Nanocrystals: Enhanced Control of Nanocrystal Size and Radial Dopant Distribution. *ACS Nano* **2016**, *10* (7), 6942–6951.

(144) Price, S. W. T.; Speed, J. D.; Kannan, P.; Russell, A. E. Exploring the First Steps in Core-Shell Electrocatalyst Preparation: In Situ Characterization of the Underpotential Deposition of Cu on Supported Au Nanoparticles. *J. Am. Chem. Soc.* **2011**, *133* (48), 19448–19458.

(145) Weber, K.; Creager, S. E. Voltammetry of Redox-Active Groups Irreversibly Adsorbed onto Electrodes. Treatment Using the Marcus Relation between Rate and Overpotential. *Anal. Chem.* **1994**, *66* (19), 3164–3172.

(146) Zhang, X.; Su, Z. Polyelectrolyte-Multilayer-Supported Au@Ag Core-Shell Nanoparticles with High Catalytic Activity. *Adv. Mater.* **2012**, *24* (33), 4574–4577.

(147) Minguzzi, A.; Lugaresi, O.; Achilli, E.; Locatelli, C.; Vertova, A.; Ghigna, P.; Rondinini, S. Observing the Oxidation State Turnover in Heterogeneous Iridium-Based Water Oxidation Catalysts. *Chem. Sci.* **2014**, *5* (9), 3591.

(148) Cortes, F. J. Q.; Boebinger, M. G.; Xu, M.; Ulvestad, A.; McDowell, M. T. Operando Synchrotron Measurement of Strain Evolution in Individual Alloying Anode Particles within Lithium Batteries. *ACS Energy Lett.* **2018**, *3* (2), 349–355.

(149) Chapman, K. W. Emerging Operando and X-Ray Pair Distribution Function Methods for Energy Materials Development. *MRS Bull.* **2016**, *41* (3), 231–238.

(150) Zhang, C.; Grass, M. E.; Yu, Y.; Gaskell, K. J.; Decaluwe, S. C.; Chang, R.; Jackson, G. S.; Hussain, Z.; Bluhm, H.; Eichhorn, B. W.; et al. Multielement Activity Mapping and Potential Mapping in Solid Oxide Electrochemical Cells through the Use of Operando XPS. *ACS Catal.* **2012**, *2* (11), 2297–2304.

(151) Mehdi, B. L.; Gu, M.; Parent, L. R.; Xu, W.; Nasybulin, E. N.; Chen, X.; Unocic, R. R.; Xu, P.; Welch, D. A.; Abellan, P.; et al. In-Situ Electrochemical Transmission Electron Microscopy for Battery Research. *Microsc. Microanal.* **2014**, *20* (2), 484–492.

Chapter III

(1) Saha, K.; Agasti, S. S.; Kim, C.; Li, X.; Rotello, V. M. *Chem. Rev.* **2012**, *112*, 2739–2779.

(2) Segev-Bar, M.; Haick, H. ACS Nano 2013, 7, 8366–8378.

(3) Oszajca, M. F.; Bodnarchuk, M. I.; Kovalenko, M. V. Chem. Mater. 2014, 26, 5422–5432.

(4) Oezaslan, M.; Hasché, F.; Strasser, P. J. Phys. Chem. Lett. 2013, 4, 3273–3291.

(5) Corma, A.; Garcia, H. Chem. Soc. Rev. 2008, 37, 2096–2126.

(6) Kleijn, S. E. F.; Lai, S. C. S.; Koper, M. T. M.; Unwin, P. R. Angew. Chemie Int. Ed. 2014, 53, 3558–3586.

(7) Schünemann, S.; Dodekatos, G.; Tüysüz, H. Chem. Mater. 2015, 27, 7743–7750.

(8) Zhu, M.; Diao, G. J. Phys. Chem. C 2011, 115, 24743–24749.

(9) Taniguchi, K.; Jin, X.; Yamaguchi, K.; Mizuno, N. Chem. Commun. 2015, 51, 14969–15082.

(10) Willner, I.; Willner, B. Nano Lett. 2010, 10, 3805–3815.

(11) Yu, A.; Liang, Z.; Cho, J.; Caruso, F. Nano Lett. 2003, 3, 1203–1207.

(12) Tsukamoto, D.; Shiraishi, Y.; Sugano, Y.; Ichikawa, S.; Tanaka, S.; Hirai, T. J. Am. Chem. Soc. 2012, 134, 6309–6315.

(13) Tang, Y.; Cheng, W. Langmuir 2013, 29, 3125–3132.

(14) Barfidokht, A.; Ciampi, S.; Luais, E.; Darwish, N.; Gooding, J. J. Anal. Chem. 2013, 85, 1073–1080.

(15) Bradbury, C. R.; Zhao, J.; Fermín, D. J. J. Phys. Chem. C 2008, 112, 10153–10160.

(16) Kauffman, D. R.; Alfonso, D.; Matranga, C.; Qian, H.; Jin, R. J. Am. Chem. Soc. 2012, 134, 10237–10243.

(17) Cao, Z.; Kim, D.; Hong, D.; Yu, Y.; Xu, J.; Lin, S.; Wen, X.; Nichols, E. M.; Jeong, K.; Reimer, J. A.; Yang, P.; Chang, C. J. J. Am. Chem. Soc. 2016, 138, 8120–8125.

(18) Zhu, W.; Michalsky, R.; Metin, O.; Lv, H.; Guo, S.; Wright, C. J.; Sun, X.; Peterson, A. A.; Sun, S. J. Am. Chem. Soc. 2013, 135, 16833–16836.

(19) Wang, J. X.; Inada, H.; Wu, L.; Zhu, Y.; Choi, Y.; Liu, P.; Zhou, W. P.; Adzic, R. R. J. Am. Chem. Soc. 2009, 131, 17298–17302.

(20) Padayachee, D.; Golovko, V.; Ingham, B.; Marshall, A. T. Electrochim. Acta 2014, 120, 398–407.

(21) Lee, H. RSC Adv. 2014, 4, 41017–41027.

(22) Seidel, Y. E.; Schneider, A.; Jusys, Z.; Wickman, B.; Kasemo, B.; Behm, R. J. Langmuir 2010, 26, 3569–3578.

(23) Diao, P.; Guo, M.; Zhang, Q. J. Phys. Chem. C 2008, 112, 7036–7046.

(24) Sun, X.; Guo, S.; Liu, Y.; Sun, S. Nano Lett. 2012, 12, 4859–4863.

(25) Weng, Z.; Liu, W.; Yin, L. C.; Fang, R.; Li, M.; Altman, E. I.; Fan, Q.; Li, F.; Cheng, H. M.; Wang, H. Nano Lett. 2015, 15, 7704–7710.

(26) Diao, P.; Zhang, D.; Wang, J.; Zhang, Q. Electrochem. Commun. 2010, 12, 1622–1625.

(27) Tang, Y.; Cheng, W. Nanoscale 2015, 7, 16151–16164.

(28) Chen, W.; Chen, S. Angew. Chem. Int. Ed. Engl. 2009, 48, 4386–4389.

(29) Reske, R.; Mistry, H.; Behafarid, F.; Cuenya, B. R.; Strasser, P. J. Am. Chem. Soc. 2014, 136, 6978–6986.

(30) Salehi-Khojin, A.; Jhong, H. R. M.; Rosen, B. A.; Zhu, W.; Ma, S.; Kenis, P. J. A.; Masel, R. I. J. Phys. Chem. C 2013, 117, 1627–1632.

(31) Masuda, H.; Yasui, K.; Nishio, K. Adv. Mater. 2000, 12, 1031–1033.

(32) Penner, R. M. J. Phys. Chem. B 2002, 106, 3339–3353.

(33) Ivanova, O. S.; Zamborini, F. P. Anal. Chem. 2010, 82, 5844–5850.

(34) Lopez-Serrano, A.; Olivas, R. M.; Landaluze, J. S.; Camara, C. Anal. Methods 2014, 6, 38–56.

(35) Smith, B. L.; Hutchison, J. E. J. Phys. Chem. C 2013, 117, 25127–25137.

(36) Lopez-Sanchez, J. A.; Dimitratos, N.; Hammond, C.; Brett, G. L.; Kesavan, L.; White, S.; Miedziak, P.; Tiruvalam, R.; Jenkins, R. L.; Carley, A. F.; Knight, D.; Kiely, C. J.; Hutchings, G. J. Nat. Chem. 2011, 3, 551–556.

(37) Kilmartin, J.; Sarip, R.; Grau-Crespo, R.; Di Tommaso, D.; Hogarth, G.; Prestipino, C.; Sankar, G. ACS Catal. 2012, 2, 957–963.

(38) Shein, J. B.; Lai, L. M. H.; Eggers, P. K.; Paddon-Row, M. N.; Gooding, J. J. Langmuir 2009, 25, 11121–11128.

(39) Jensen, P. S.; Chi, Q.; Grumsen, F. B.; Abad, J. M.; Horsewell, A.; Schiffrin, D. J.; Ulstrup, J. J. Phys. Chem. 2007, 111, 6124–6132.

(40) Liu, F.; Khan, K.; Liang, J.-H.; Yan, J.-W.; Wu, D.-Y.; Mao, B.-W.; Jensen, P. S.; Zhang, J.; Ulstrup, J. ChemPhysChem 2013, 14, 952–957.

(41) Liu, G.; Luais, E.; Gooding, J. J. Langmuir 2011, 27, 4176–4183.

(42) Matyjewicz, J.; Lesniewski, A.; Niedziolka-Jonsson, J. Electrochem. Commun. 2014, 48, 73–76.

(43) Le Saux, G.; Ciampi, S.; Gaus, K.; Gooding, J. J. ACS Appl. Mater. Interfaces 2009, 1, 2477–2483.

(44) Tian, R.; Rao, T. N.; Einaga, Y.; Zhi, J. Chem. Mater. 2006, 18, 939–945.

(45) Kondo, T.; Aoshima, S.; Honda, K.; Einaga, Y.; Fujishima, A.; Kawai, T. J. Phys. Chem. C 2007, 111, 12650–12657.

(46) Widrig, C. A.; Chung, C.; Porter, M. D. J. Electroanal. Chem. 1991, 310, 335–359.

(47) Boubour, E.; Lennox, R. B. Langmuir 2000, 16, 7464–7470.

(48) Mattiuzzi, A.; Jabin, I.; Mangeney, C.; Roux, C.; Reinaud, O.; Santos, L.; Bergamini, J.-F.; Hapiot, P.; Lagrost, C. Nat. Commun. 2012, 3, 1130.

(49) McCreery, R. L. Chem. Rev. 2008, 108, 2646–2687.

(50) Li, G.; Jin, R. Acc. Chem. Res. 2013, 46, 1749–1758.

(51) Mckenzie, L. C.; Zaikova, T. O.; Hutchison, J. E. J. Am. Chem. Soc. 2014, 136, 13426–13435.

(52) Hicks, J. F.; Zamborini, F. P.; Murray, R. W. J. Phys. Chem. B 2002, 106, 7751–7757.

(53) Strother, T.; Knickerbocker, T.; Russell, J. N.; Butler, J. E.; Smith, L. M.; Hamers, R. J. Langmuir 2002, 18, 968–971.

(54) Ilavsky, J.; Jemian, P. R. J. Appl. Crystallogr. 2009, 42, 347–353.

(55) Yamanoi, Y.; Shirahata, N.; Yonezawa, T.; Terasaki, N.; Yamamoto, N.; Matsui, Y.; Nishio, K.; Masuda, H.; Ikuhara, Y.; Nishihara, H. Chem. - A Eur. J. 2006, 12, 314–323.

(56) Weare, W. W.; Reed, S. M.; Warner, M. G.; Hutchison, J. E. J. Am. Chem. Soc. 2000, 122, 12890–12891.

(57) Seshan, V.; Ullien, D.; Castellanos-Gomez, A.; Sachdeva, S.; Murthy, D. H. K.; Savenije, T. J.; Ahmad, H. A.; Nunney, T. S.; Janssens, S. D.; Haenen, K.; Nesládek, M.; van der Zant, H. S. J.; Sudhölter, E. J. R.; de Smet, L. C. P. M. J. Chem. Phys. 2013, 138, 234707.

(58) Nichols, B. M.; Butler, J. E.; Russell, J. N.; Hamers, R. J. J. Phys. Chem. B 2005, 109, 20938–20947.

(59) Woehrle, G. H.; Hutchison, J. E. Inorg. Chem. 2005, 44, 6149–6158.

(60) Chidsey, C. E. D.; Bertozzi, C. R.; Putvinski, T. M.; Mujsce, A. M. J. Am. Chem. Soc. 1990, 112, 4301–4306.

(61) Elliott, E. W.; Glover, R. D.; Hutchison, J. E. ACS Nano 2015, 9, 3050–3059.

(62) Macpherson, J. V. Phys. Chem. Chem. Phys. 2015, 17, 2935–2949.

(63) Woehrle, G. H.; Brown, L. O.; Hutchison, J. E. J. Am. Chem. Soc. 2005, 127, 2172–2183.

(64) Woehrle, G. H.; Warner, M. G.; Hutchison, J. E. J. Phys. Chem. B 2002, 106, 9979–9981.

(65) Ingram, R. S.; Hostetler, M. J.; Murray, R. W. J. Am. Chem. Soc. 1997, 119, 9175–9178.

(66) Chazalviel, J.; Allongue, P. J. Am. Chem. Soc. 2011, 133, 762–764.

(67) Patten, H. V.; Lai, S. C. S.; MacPherson, J. V.; Unwin, P. R. Anal. Chem. 2012, 84, 5427–5432.

(68) Patten, H. V.; Meadows, K. E.; Hutton, L. A.; Iacobini, J. G.; Battistel, D.; McKelvey, K.; Colburn, A. W.; Newton, M. E.; MacPherson, J. V.; Unwin, P. R. Angew. Chemie - Int. Ed. 2012, 51, 7002–7006.

(69) Ruther, R. E.; Cui, Q.; Hamers, R. J. J. Am. Chem. Soc. 2013, 135, 5751–5761.

(70) Li, Y.; Huang, W.; Sun, S. Angew. Chemie 2006, 118, 2599–2601.

(71) Reincke, F.; Hickey, S. G.; Kegel, W. K.; Vanmaekelbergh, D. Angew. Chemie 2004, 116, 464–468.

(72) Chen, S. Langmuir 2001, 17, 6664–6668.

(73) Trasatti, S.; Petrii, O. Pure Appl. Chem. 1991, 63, 711–734.

(74) Wang, X.; Ruther, R. E.; Streifer, J. A.; Hamers, R. J. J. Am. Chem. Soc. 2010, 132, 4048–4049.

(75) Maat, J. Ter; Regeling, R.; Yang, M.; Mullings, M. N.; Bent, S. F.; Zuilhof, H. Langmuir 2009, 25, 11592–11597.

(76) Franking, R.; Kim, H.; Chambers, S. A.; Mangham, A. N.; Hamers, R. J. Langmuir 2012, 28, 12085–12093.

(77) Colavita, P. E.; Sun, B.; Tse, K. Y.; Hamers, R. J. J. Am. Chem. Soc. 2007, 129, 13554–13565.

Chapter IV

(1) Cooper, S. R.; Plummer, L. K.; Cosby, A. G.; Lenox, P.; Jander, A.; Dhagat, P.; Hutchison, J. E. Insights into the Magnetic Properties of Sub-10 Nm Iron Oxide Nanocrystals through the Use of a Continuous Growth Synthesis. Chem. Mater. 2018, 30, 6053–6062.

(2) Kruse, N. Catalytic CO Oxidation over Well-Defined Cobalt Oxide Nanoparticles: Size-Reactivity Correlation. ACS Catal. 2015, 5714–5718.

(3) Mocatta, D.; Cohen, G.; Schattner, J.; Millo, O.; Rabani, E.; Banin, U. Heavily Doped Semiconductor Nanocrystal Quantum Dots. Science (80-.). 2011, 332, 77–81.

(4) Johns, R. W.; Bechtel, H. A.; Runnerstrom, E. L.; Agrawal, A.; Lounis, S. D.; Milliron, D. J. Direct Observation of Narrow Mid-Infrared Plasmon Linewidths of Single Metal Oxide Nanocrystals. Nat. Commun. 2016, No. May, 1–6.

(5) Runnerstrom, E. L.; Bergerud, A.; Agrawal, A.; Johns, R. W.; Dahlman, C. J.; Singh, A.; Selbach, S. M.; Milliron, D. J. Defect Engineering in Plasmonic Metal Oxide Nanocrystals. Nano Lett. 2016, 16, 3390–3398.

(6) De Roo, J.; Van Den Broeck, F.; De Keukeleere, K.; Martins, J. C.; Van Driessche, I.; Hens, Z. Unravelling the Surface Chemistry of Metal Oxide Nanocrystals, the Role of Acids and Bases. J. Am. Chem. Soc. 2014, 136, 9650–9657.

(7) Auffan, M.; Rose, J.; Proux, O.; Borschneck, D.; Masion, A.; Chaurand, P.; Hazemann, J. L.; Chaneac, C.; Jolivet, J. P.; Wiesner, M. R.; et al. Enhanced Adsorption of Arsenic onto Maghemites Nanoparticles: As(III) as a Probe of the Surface Structure and Heterogeneity. Langmuir 2008, 24, 3215–3222.

(8) Kumar, M.; Kumar, A.; Abhyankar, A. C. Influence of Texture Coefficient on Surface Morphology and Sensing Properties of W-Doped Nanocrystalline Tin Oxide Thin Films. ACS Appl. Mater. Interfaces 2015, 7, 3571–3580.

(9) Qiao, L.; Swihart, M. T. Solution-Phase Synthesis of Transition Metal Oxide Nanocrystals: Morphologies, Formulae, and Mechanisms. Adv. Colloid Interface Sci. 2017, 244, 199–266.

(10) Liu, J.; Wu, Z.; Tian, Q.; Wu, W.; Xiao, X. Shape-Controlled Iron Oxide Nanocrystals: Synthesis, Magnetic Properties and Energy Conversion Applications. CrystEngComm 2016, 18, 6303–6326.

(11) Auffan, M.; Rose, J.; Bottero, J. Y.; Lowry, G. V.; Jolivet, J. P.; Wiesner, M. R. Towards a Definition of Inorganic Nanoparticles from an Environmental, Health and Safety Perspective. Nat. Nanotechnol. 2009, 4, 634–641.

(12) Ito, D.; Yokoyama, S.; Zaikova, T.; Masuko, K.; Hutchison, J. E. Synthesis of Ligand-Stabilized Metal Oxide Nanocrystals and Epitaxial Core / Shell Nanocrystals via a Lower- Temperature Esteri Fi Cation Process. ACS Nano 2014, 8, 64–75.

(13) Jansons, A. W.; Plummer, L. K.; Hutchison, J. E. Living Nanocrystals. Chem. Mater. 2017, 29, 5415–5425.

(14) Jansons, A. W.; Hutchison, J. E. Continuous Growth of Metal Oxide Nanocrystals: Enhanced Control of Nanocrystal Size and Radial Dopant Distribution. ACS Nano 2016, 10, 6942–6951.

(15) Crockett, B. M.; Jansons, A. W.; Koskela, K. M.; Johnson, D. W.; Hutchison, J. E. Radial Dopant Placement for Tuning Plasmonic Properties in Metal Oxide Nanocrystals. ACS Nano 2017, 11, 7719–7728.

(16) Xu, J. M.; Cheng, J. P. The Advances of Co3O4as Gas Sensing Materials: A Review. J. Alloys Compd. 2016, 686, 753–768.

(17) Poizot, P.; Laruelle, S.; Grugeon, S.; Dupont, L.; Tarascon, J. Nano-Sized Transition-Metaloxides as Negative Electrode Materials for Lithium-Ion Batteries. 2000, 407.

(18) Wang, J.; Cui, W.; Liu, Q.; Xing, Z.; Asiri, A. M.; Sun, X. Recent Progress in Cobalt-Based Heterogeneous Catalysts for Electrochemical Water Splitting. Adv. Mater. 2016, 28, 215–230.

(19) Siddall, M.; Rohling, E. J.; Almogi-Labin, A.; Hemleben, C.; Meischner, D.; Schmeizer, I.; Smeed, D. A. Beating the Superparamagnetic Limit with Exchange Bias. Nature 2003, 423, 850–853.

(20) Nam, K. M.; Seo, W. S.; Song, H.; Park, J. T. Non-Native Transition Metal Monoxide Nanostructures: Unique Physicochemical Properties and Phase Transformations of CoO, MnO and ZnO. NPG Asia Mater. 2017, 9, e364-15.

(21) Seo, W. S.; Shim, J. H.; Oh, S. J.; Lee, E. K.; Hur, N. H.; Park, J. T. Phase- and Size-Controlled Synthesis of Hexagonal and Cubic CoO Nanocrystals. J. Am. Chem. Soc. 2005, 47, 6188–6189.

(22) Xie, X.; Shen, W. Morphology Control of Cobalt Oxide Nanocrystals for Promoting Their Catalytic Performance. Nanoscale 2009, 1, 50–60.

(23) Indra, A.; Menezes, P. W.; Das, C.; Göbel, C.; Tallarida, M.; Schmei?er, D.; Driess, M. A Facile Corrosion Approach to the Synthesis of Highly Active CoOx Water Oxidation Catalysts. J. Mater. Chem. A 2017, 5, 5171–5177.

(24) Buck, M. R.; Biacchi, A. J.; Schaak, R. E. Insights into the Thermal Decomposition of Co(II) Oleate for the Shape-Controlled Synthesis of Wurtzite-Type CoO Nanocrystals. 2014, No. Ii.

(25) Yiliguma; Xu, W.; Wang, Z.; Shang, L.; Zhang, H.; Al-Enizi, A. M.; Tang, Y.; Zheng, G. Unconventional Morphologies of CoO Nanocrystals: Via Controlled Oxidation of Cobalt Oleate Precursors. Chem. Commun. 2018, 54, 3867–3870.

(26) Zhang, Y.; Zhong, X.; Zhu, J.; Song, X. Alcoholysis Route to Monodisperse CoO Nanotetrapods with Tunable Size. Nanotechnology 2007, 18.

(27) Ghosh, M.; Sampathkumaran, E. V.; Rao, C. N. R. Synthesis and Magnetic Properties of CoO Nanoparticles. Chem. Mater. 2005, 17, 2345–2352.

(28) Nam, K. M.; Shim, J. H.; Han, D.; Kwon, H. S.; Kang, Y.; Li, Y.; Song, H.; Seo, W. S.; Park, J. T. Syntheses and Characterization of Wurtzite CoO , Rocksalt CoO , and Spinel Co3O4 Nanocrystals?: Their Interconversion and Tuning of Phase and Morphology. 2010, 4446–4454.

(29) Zhang, Y.; Zhu, J.; Song, X.; Zhong, X. Controlling the Synthesis of CoO Nanocrystals with Various Morphologies. J. Phys. Chem. C 2008, 112, 5322–5327.

(30) Mehandjiev, D.; Nikolova-Zhecheva, E. Mechanism of the Decomposition of Cobaltous Compounds in Vacuo. Thermochim. Acta 1980, 37, 145–154.

Chapter V

(1) Mocatta, D.; Cohen, G.; Schattner, J.; Millo, O.; Rabani, E.; Banin, U. Heavily Doped Semiconductor Nanocrystal Quantum Dots. Science (80). 2011, 332, 77–81.

(2) Kriegel, I.; Scotognella, F.; Manna, L. Plasmonic Doped Semiconductor Nanocrystals: Properties, Fabrication, Applications and Perspectives. Phys. Rep. 2017, 674, 1–52.

(3) Runnerstrom, E. L.; Bergerud, A.; Agrawal, A.; Johns, R. W.; Dahlman, C. J.; Singh, A.; Selbach, S. M.; Milliron, D. J. Defect Engineering in Plasmonic Metal Oxide Nanocrystals. Nano Lett. 2016, 16, 3390–3398.

(4) Mulvaney, P. Surface Plasmon Spectroscopy of Nanosized Metal Particles. Langmuir 2002, 12, 788–800.

(5) Link, S.; El-Sayed, M. A. Spectral Properties and Relaxation Dynamics of Surface Plasmon Electronic Oscillations in Gold and Silver Nanodots and Nanorods. J. Phys. Chem. B 2002, 103, 8410–8426.

(6) Liang, X.; Bai, S.; Wang, X.; Dai, X.; Gao, F.; Sun, B.; Ning, Z.; Ye, Z.; Jin, Y. Colloidal Metal Oxide Nanocrystals as Charge Transporting Layers for Solution-Processed Light-Emitting Diodes and Solar Cells. Chem. Soc. Rev. 2017, 46, 1730–1759.

(7) Kovalenko, M. V.; Manna, L.; Cabot, A.; Hens, Z.; Talapin, D. V.; Kagan, C. R.; Klimov, V. I.; Rogach, A. L.; Reiss, P.; Milliron, D. J.; et al. Prospects of Nanoscience with Nanocrystals. ACS Nano 2015, 9, 1012–1057.

(8) Nakhleh, M. K.; Amal, H.; Jeries, R.; Broza, Y. Y.; Aboud, M.; Gharra, A.; Ivgi, H.; Khatib, S.; Badarneh, S.; Har-Shai, L.; et al. Diagnosis and Classification of 17 Diseases from 1404 Subjects via Pattern Analysis of Exhaled Molecules. ACS Nano 2017, 11, 112–125.

(9) Hua, M.; Zhang, S.; Pan, B.; Zhang, W.; Lv, L.; Zhang, Q. Heavy Metal Removal from Water/Wastewater by Nanosized Metal Oxides: A Review. J. Hazard. Mater. 2012, 211–212, 317–331.

(10) Cong, Y.; Zhang, J.; Chen, F.; Anpo, M.; He, D. Preparation, Photocatalytic Activity, and Mechanism of Nano-TiO2 Co-Doped with Nitrogen and Iron (III). J. Phys. Chem. C 2007, 111, 10618–10623.

(11) Xu, A. W.; Gao, Y.; Liu, H. Q. The Preparation, Characterization, and Their Photocatalytic Activities of Rare-Earth-Doped TiO2 Nanoparticles. J. Catal. 2002, 207, 151–157.

(12) Albanese, A.; Tang, P. S.; Chan, W. C. W. The Effect of Nanoparticle Size, Shape, and Surface Chemistry on Biological Systems. Annu. Rev. Biomed. Eng. 2012, 14, 1–16.

(13) Suresh, A. K.; Pelletier, D. A.; Doktycz, M. J. Relating Nanomaterial Properties and Microbial Toxicity. Nanoscale 2013, 5, 463–474.

(14) Mourdikoudis, S.; Liz-marza, L. M. Oleylamine in Nanoparticle Synthesis. 2013.

(15) Truong, L.; Zaikova, T.; Schaeublin, N. M.; Kim, K. T.; Hussain, S. M.; Hutchison, J. E.; Tanguay, R. L. Residual Weakly Bound Ligands Influence Biological Compatibility of Mixed Ligand Shell, Thiol-Stabilized Gold Nanoparticles. Environ. Sci. Nano 2017, 4, 1634–1646.

(16) Jiang, J.; Oberdörster, G.; Biswas, P. Characterization of Size, Surface Charge, and Agglomeration State of Nanoparticle Dispersions for Toxicological Studies. J. Nanoparticle Res. 2009, 11, 77–89.

(17) Alkilany, A. M.; Lohse, S. E.; Murphy, C. J. The Gold Standard: Gold Nanoparticle Libraries to Understand the Nano-Bio Interface. Acc. Chem. Res. 2013, 46, 650–661.

(18) Punnoose, A.; Dodge, K.; Rasmussen, J. W.; Chess, J.; Wingett, D.; Anders, C. Cytotoxicity of ZnO Nanoparticles Can Be Tailored by Modifying Their Surface Structure: A Green Chemistry Approach for Safer Nanomaterials. ACS Sustain. Chem. Eng. 2014, 2, 1666–1673.

(19) Zhang, H.; Ji, Z.; Xia, T.; Meng, H.; Low-Kam, C.; Liu, R.; Pokhrel, S.; Lin, S.; Wang, X.; Liao, Y. P.; et al. Use of Metal Oxide Nanoparticle Band Gap to Develop a Predictive Paradigm for Oxidative Stress and Acute Pulmonary Inflammation. ACS Nano 2012, 6, 4349–4368.

(20) Kaweeteerawat, C.; Ivask, A.; Liu, R.; Zhang, H.; Chang, C. H.; Low-Kam, C.; Fischer, H.; Ji, Z.; Pokhrel, S.; Cohen, Y.; et al. Toxicity of Metal Oxide Nanoparticles in Escherichia Coli Correlates with Conduction Band and Hydration Energies. Environ. Sci. Technol. 2015, 49, 1105–1112.

(21) Burello, E.; Worth, A. P. A Theoretical Framework for Predicting the Oxidative Stress Potential of Oxide Nanoparticles. Model. Nanotoxicology 2011, 5, 228–235.

(22) Song, W.; Zhang, J.; Guo, J.; Zhang, J.; Ding, F.; Li, L.; Sun, Z. Role of the Dissolved Zinc Ion and Reactive Oxygen Species in Cytotoxicity of ZnO Nanoparticles. Toxicol. Lett. 2010, 199, 389–397.

(23) Shi, M.; Kwon, H. S.; Peng, Z.; Elder, A.; Yang, H. Effects of Surface Chemistry on the Generation of Reactive Oxygen Species by Copper Nanoparticles. ACS Nano 2012, 6, 2157–2164.

(24) Shi, M.; Kwon, H. S. H.; Peng, Z.; Elder, A.; Yang, H. Effects of Surface Chemistry on the Generation of Reactive Oxygen Species by Copper Nanoparticles. ACS Nano 2012, 6, 2157–2164.

(25) Ng, Y. H.; Leung, Y. H.; Liu, F. Z.; Ng, A. M. C.; Gao, M. H.; Chan, C. M. N.; Djuriši?, A. B.; Leung, F. C. C.; Chan, W. K. Antibacterial Activity of ZnO Nanoparticles under Ambient Illumination - The Effect of Nanoparticle Properties. Thin Solid Films 2013, 542, 368–372.

(26) Leung, Y. H.; Chan, C. M. N.; Ng, A. M. C.; Chan, H. T.; Chiang, M. W. L.; Djuriši, A. B.; Ng, Y. H.; Jim, W. Y.; Guo, M. Y.; Leung, F. C. C.; et al. Antibacterial Activity of ZnO Nanoparticles with a Modified Surface under Ambient Illumination. Nanotechnology 2012, 23.

(27) Wang, D.; Lin, Z.; Wang, T.; Yao, Z.; Qin, M.; Zheng, S.; Lu, W. Where Does the Toxicity of Metal Oxide Nanoparticles Come from: The Nanoparticles, the Ions, or a Combination of Both? J. Hazard. Mater. 2016, 308, 328–334.

(28) Liu, J.; Sonshine, D. A.; Shervani, S.; Hurt, R. H. Controlled Release of Biologically Active Silver from Nanosilver Surfaces. ACS Nano 2010, 4, 6903–6913.

(29) Horie, M.; Fujita, K.; Kato, H.; Endoh, S.; Nishio, K.; Komaba, L. K.; Nakamura, A.; Miyauchi, A.; Kinugasa, S.; Hagihara, Y.; et al. Association of the Physical and Chemical Properties and the Cytotoxicity of Metal Oxide Nanoparticles: Metal Ion Release, Adsorption Ability and Specific Surface Area. Metallomics 2012, 4, 350–360.

(30) Alkilany, A. M.; Murphy, C. J. Toxicity and Cellular Uptake of Gold Nanoparticles: What We Have Learned so Far? J. Nanoparticle Res. 2010, 12, 2313–2333.

(31) Mahmoudi, M.; Simchi, A.; Imani, M.; Milani, A. S.; Stroeve, P. An in Vitro Study of Bare and Poly(Ethylene Glycol)-Co-Fumarate-Coated Superparamagnetic Iron Oxide Nanoparticles: A New Toxicity Identification Procedure. Nanotechnology 2009, 20, 225104.

(32) Mahmoudi, M.; Simchi, A.; Vali, H.; Imani, M.; Shokrgozar, M. A.; Azadmanesh, K.; Azari, F. Cytotoxicity and Cell Cycle Effects of Bare and Poly(Vinyl Alcohol)-Coated Iron Oxide Nanoparticles in Mouse Fibroblasts. Adv. Eng. Mater. 2009, 11, 243–250.

(33) Mahmoudi, M.; Simchi, A.; Imani, M.; Milani, A. S.; Stroeve, P. An in Vitro Study of Bare and Poly (Ethylene Glycol)-Co-Fumarate-Coated Superparamagnetic Iron Oxide Nanoparticles: A New Toxicity Identification. Nanotechnology 2009, 20, 225104–225112.

(34) Hsu, A.; Liu, F.; Leung, Y. H.; Ma, A. P. Y.; Djuriši, A. B.; Leung, F. C. C.; Chan, W. K.; Lee, H. K. Is the Effect of Surface Modifying Molecules on Antibacterial Activity Universal for a given Material? Nanoscale 2014, 6, 10323–10331.

(35) Perreault, F.; Popovic, R.; Dewez, D. Different Toxicity Mechanisms between Bare and Polymer-Coated Copper Oxide Nanoparticles in Lemna Gibba. Environ. Pollut. 2014, 185, 219–227.

(36) Yu, M.; Huang, S.; Yu, K. J.; Clyne, A. M. Dextran and Polymer Polyethylene Glycol (PEG) Coating Reduce Both 5 and 30 Nm Iron Oxide Nanoparticle Cytotoxicity in 2D and 3D Cell Culture. Int. J. Mol. Sci. 2012, 13, 5554–5570.

(37) Baumann, J.; Köser, J.; Arndt, D.; Filser, J. The Coating Makes the Difference: Acute Effects of Iron Oxide Nanoparticles on Daphnia Magna. Sci. Total Environ. 2014, 484, 176–184.

(38) Huang, Y. W.; Wu, C. H.; Aronstam, R. S. Toxicity of Transition Metal Oxide Nanoparticles: Recent Insights from in Vitro Studies. Materials (Basel). 2010, 3, 4842–4859.

(39) Wang, R.; Hughes, T.; Beck, S.; Vakil, S.; Li, S.; Pantano, P.; Draper, R. K. Generation of Toxic Degradation Products by Sonication of Pluronic Dispersants: Implications for Nanotoxicity Testing. Nanotoxicology 2013, 7, 1272–1281.

(40) Djuriši, A. B.; Leung, Y. H.; Ng, A. M. C.; Xu, X. Y.; Lee, P. K. H.; Degger, N.; Wu, R. S. S. Toxicity of Metal Oxide Nanoparticles: Mechanisms, Characterization, and Avoiding Experimental Artefacts. Small 2015, 11, 26–44.

(41) Pino, P. Del; Pelaz, B.; Zhang, Q.; Maffre, P.; Nienhaus, G. U.; Parak, W. J. Protein Corona Formation around Nanoparticles - From the Past to the Future. Mater. Horizons 2014, 1, 301–313.

(42) Burello, E.; Worth, A. QSAR Modeling of Nanomaterials. Adv. Rev. 2011, 3, 298–306.

(43) Puzyn, T.; Rasulev, B.; Gajewicz, A.; Hu, X.; Dasari, T. P.; Michalkova, A.; Hwang, H.-M.; Toropov, A.; Leszczynska, D.; Leszczynski, J. Using Nano-QSAR to Predict the Cytotoxicity of Metal Oxide Nanoparticles. Nat. Nanotechnol. 2011, 6, 175–178.

(44) Gajewicz, A.; Schaeublin, N.; Rasulev, B.; Hussain, S.; Leszczynska, D.; Puzyn, T.; Leszczynski, J. Towards Understanding Mechanisms Governing Cytotoxicity of Metal Oxides Nanoparticles: Hints from Nano-QSAR Studies. Nanotoxicology 2015, 9, 313–325.

(45) Puzyn, T.; Rasulev, B.; Gajewicz, A.; Hu, X.; Dasari, T. P.; Michalkova, A.; Hwang, H. M.; Toropov, A.; Leszczynska, D.; Leszczynski, J. Using Nano-QSAR to Predict the Cytotoxicity of Metal Oxide Nanoparticles. Nat. Nanotechnol. 2011, 6, 175–178.

(46) Pan, Y.; Li, T.; Cheng, J.; Telesca, D.; Zink, J. I.; Jiang, J. Nano-QSAR Modeling for Predicting the Cytotoxicity of Metal Oxide Nanoparticles Using Novel Descriptors. RSC Adv. 2016, 6, 25766–25775.

(47) Singh, K. P.; Gupta, S. Nano-QSAR Modeling for Predicting Biological Activity of Diverse Nanomaterials. RSC Adv. 2014, 4, 13215–13230.

(48) Cooper, S. R.; Plummer, L. K.; Cosby, A. G.; Lenox, P.; Jander, A.; Dhagat, P.; Hutchison, J. E. Insights into the Magnetic Properties of Sub-10 Nm Iron Oxide Nanocrystals through the Use of a Continuous Growth Synthesis. Chem. Mater. 2018, 30, 6053–6062.

(49) Dong, A.; Ye, X.; Chen, J.; Kang, Y.; Gordon, T.; Kikkawa, J. M.; Murray, C. B. A Generalized Ligand-Exchange Strategy Enabling Sequential Surface Functionalization of Colloidal Nanocrystals. J. Am. Chem. Soc. 2011, 133, 998–1006.

(50) Davis, K.; Qi, B.; Witmer, M.; Kitchens, C. L.; Powell, B. A.; Mefford, O. T. Quantitative Measurement of Ligand Exchange on Iron Oxides via Radiolabeled Oleic Acid. Langmuir 2014, 30, 10918–10925.

(51) Davis, K.; Cole, B.; Ghelardini, M.; Powell, B. A.; Mefford, O. T. Quantitative Measurement of Ligand Exchange with Small-Molecule Ligands on Iron Oxide Nanoparticles via Radioanalytical Techniques. Langmuir 2016, 32, 13716–13727.

(52) Ginzburg, A. L.; Truong, L.; Tanguay, R. L.; Hutchison, J. E. Synergistic Toxicity Produced by Mixtures of Biocompatible Gold Nanoparticles and Widely Used Surfactants. ACS Nano 2018, 12, 5312–5322.

(53) Truong, L.; Reif, D. M.; Mary, L. S.; Geier, M. C.; Truong, H. D.; Tanguay, R. L. Multidimensional in Vivo Hazard Assessment Using Zebrafish. Toxicol. Sci. 2014, 137, 212–233.

(54) Ito, D.; Yokoyama, S.; Zaikova, T.; Masuko, K.; Hutchison, J. E. Synthesis of Ligand-Stabilized Metal Oxide Nanocrystals and Epitaxial Core / Shell Nanocrystals via a Lower- Temperature Esteri Fi Cation Process. ACS Nano 2014, 8, 64–75.

(55) Seo, W. S.; Shim, J. H.; Oh, S. J.; Lee, E. K.; Hur, N. H.; Park, J. T. Phase- and Size-Controlled Synthesis of Hexagonal and Cubic CoO Nanocrystals. J. Am. Chem. Soc. 2005, 47, 6188–6189.

(56) Jansons, A. W.; Hutchison, J. E. Continuous Growth of Metal Oxide Nanocrystals: Enhanced Control of Nanocrystal Size and Radial Dopant Distribution. ACS Nano 2016, 10, 6942–6951.

(57) Zhang, Y.; Zhu, J.; Song, X.; Zhong, X. Controlling the Synthesis of CoO Nanocrystals with Various Morphologies. J. Phys. Chem. C 2008, 112, 5322–5327.

(58) Kimmel, C. B.; Ballard, W. M.; Kimmel, S. R.; Ullmann, B.; Schilling, Thomas, R. Stages of Embryonic Developmental of the Zebrafish. Dev. Dyn. 1995, 10, 253–310.

(59) Mandrell, D.; Truong, L.; Jephson, C.; Sarker, M. R.; Moore, A.; Land, C.; Simonich, M. T.; Tanguay, R. L. Automated Zebrafish Chorion Removal and Single Embryo Placement: Optimizing Throughput of Zebrafish Developmental Toxicity Screens. J. Lab Autom. 2012, 17, 66–74.

(60) Truong, L.; Zaikova, T.; Baldock, B. L.; Balik-Meisner, M.; To, K.; Reif, D. M.; Kennedy, Z. C.; Hutchison, J. E.; Tanguay, R. L. Systematic Determination of the Relationship between Nanoparticle Core Diameter and Toxicity for a Series of Structurally Analogous Gold Nanoparticles in Zebrafish. Nanotoxicology 2019, 13, 879–893.

(61) Oberdörster, G.; Maynard, A.; Donaldson, K.; Castranova, V.; Fitzpatrick, J.; Ausman, K.; Carter, J.; Karn, B.; Kreyling, W.; Lai, D.; et al. Principles for Characterizing the Potential Human Health Effects from Exposure to Nanomaterials: Elements of a Screening Strategy. Part. Fibre Toxicol. 2005, 2, 1–35.

(62) Ling, D.; Lee, N.; Hyeon, T. Chemical Synthesis and Assembly of Uniformly Sized Iron Oxide Nanoparticles for Medical Applications. Acc. Chem. Res. 2015, 48, 1276–1285.

(63) Bárcena, C.; Sra, A. K.; Gao, J. Applications of Magnetic Nanoparticles in Biomedicine. Nanoscale Magn. Mater. Appl. 2009, 591–626.

(64) Mohammed, L.; Gomaa, H. G.; Ragab, D.; Zhu, J. Magnetic Nanoparticles for Environmental and Biomedical Applications: A Review. Particuology 2017, 30, 1–14.

(65) Lipka, J.; Semmler-Behnke, M.; Sperling, R. A.; Wenk, A.; Takenaka, S.; Schleh, C.; Kissel, T.; Parak, W. J.; Kreyling, W. G. Biodistribution of PEG-Modified Gold Nanoparticles Following Intratracheal Instillation and Intravenous Injection. Biomaterials 2010, 31, 6574–6581.

(66) Ryman-Rasmussen, J. P.; Riviere, J. E.; Monteiro-Riviere, N. A. Variables Influencing Interactions of Untargeted Quantum Dot Nanoparticles with Skin Cells and Identification of Biochemical Modulators. Nano Lett. 2007, 7, 1344–1348.

(67) Hak, S.; Helgesen, E.; Hektoen, H. H.; Huuse, E. M.; Jarzyna, P. A.; Mulder, W. J. M.; Haraldseth, O.; Davies, C. D. L. The Effect of Nanoparticle Polyethylene Glycol Surface Density on Ligand-Directed Tumor Targeting Studied in Vivo by Dual Modality Imaging. ACS Nano 2012, 6, 5648–5658.

(68) Gref, R.; Lück, M.; Quellec, P.; Marchand, M.; Dellacherie, E.; Harnisch, S.; Blunk, T.; Müller, R. H. "Stealth" Corona-Core Nanoparticles Surface Modified by Polyethylene Glycol (PEG): Influences of the Corona (PEG Chain Length and Surface Density) and of the Core Composition on Phagocytic Uptake and Plasma Protein Adsorption. Colloids Surfaces B Biointerfaces 2000, 18, 301–313.

(69) Dai, Q.; Walkey, C.; Chan, W. C. W. Polyethylene Glycol Backfilling Mitigates the Negative Impact of the Protein Corona on Nanoparticle Cell Targeting. Angew. Chemie - Int. Ed. 2014, 53, 5093–5096.